UNIVERSITY OF LIVERPOOL

Beam Quality Characterisation and the Optimisation of Next Generation Antimatter Facilities

Thesis submitted in accordance with the requirements of
the University of Liverpool for the degree of Doctor in Philosophy

by

James Robert Hunt

January 2019

Abstract

The Extra Low Energy Antiproton (ELENA) ring is a new upgrade to the antimatter facility at CERN. By further decelerating beams from the Antiproton Decelerator from energies of 5.3 MeV down to 100 keV, it will allow for increased antiproton trapping efficiencies by a factor of 10–100 for experiments. In order to guarantee the best possible beam quality from ELENA and for other next generation ultra-low energy antiproton and ion facilities, unique diagnostic solutions must be developed.

Two new algorithms have been developed for use with a scraper system to determine the transverse beam emittance within ELENA and machines facing similar diagnostic related challenges. These new methods improve the state of the art of beam scraping techniques for low energy ion and antiproton facilities. The algorithms are capable of accurately reconstructing the emittance in a region of non-zero dispersion. Additionally, an algorithm which combines scraping results from opposing directions is capable of the same task for non-Gaussian beams, which are expected due to more efficient electron cooling towards the core of the beam.

The new scraping algorithms have been tested through simulations and error tolerances have been established for a range of effects. They also have been shown to be capable of accurately estimating other beam quantities, such as the momentum-dependant closed orbit, and a quantity which indicates the magnitude of a correlation between the emittance of particles and their momentum offset.

Using the two scan algorithm, analysis of data taken during ELENA commissioning showed decreases of 28 ($\pm$2) % and 81 ($\pm$10) % in vertical and horizontal emittances respectively, during 6.7 s seconds of electron cooling along the intermediate energy plateau at 650 keV. At the extraction plateau of beam energy 100 keV, the vertical and horizontal emittances were reduced by 79 ($\pm$2) % and 78 ($\pm$10) %, respectively, when comparing with and without 3.9 seconds of electron cooling after deceleration. In both cases, non-Gaussian beam profiles were

observed. The emittance-momentum offset correlation coefficient showed a significant change towards a positive correlation during electron cooling.

To further determine and optimise beam quality at the experiments, a realistic 3D simulation of the electrostatic transport line from ELENA to the ALPHA experiment has been developed in the GEANT4 based beam transport code G4Beamline. Employing the use of realistic elements which include fringe fields and field maps from finite methods simulations, the transport lines have been optically tuned to the experimental handover point. Realistic beam distributions based on scraper measurements and profile measurements taken along an existing transport line from ELENA have been tracked to the target and error tolerances have been established. The development of the simulations has resulted in a comprehensive toolkit for simulating beam transport with electrostatic elements and laid the groundwork for further optimisation using machine learning methods.

Acknowledgements

First and foremost I would like to thank my supervisor Prof. Dr. Carsten Welsch for giving me the opportunity to carry out this exciting and interesting work, and for encouraging my professional and personal development. I would also like to extend my deepest gratitude to my supervisor Dr. Javier Resta-Lòpez for his unwavering patience and his friendly and valuable support over the years. I am grateful to have spent time as a part of the Quasar group and would like to thank every member I have been fortunate enough to call a friend and a colleague. Particularly, I would like to acknowledge Volodymyr Rodin who has been an absolute pleasure to work with and with whom I have shared many a laugh.

At CERN I would like to thank every member of the ELENA project for being so welcoming and helpful. In particular, I extend gratitude to Christian Carli who has provided many useful and interesting discussions, and helped me to understand so much. Thank you also to Tommy Eriksson for being so accommodating during my time there. This project would not have been possible without the help of Pierre Grandemange, Bruno Dupuy and Davide Gamba who have all enthusiastically provided their assistance and who have my equally enthusiastic gratitude.

I would like to thank my family and friends for their encouragement and understanding during my time working on this project. Thank you especially to my parents, the two Clares, Hanni, Peter, Alex, Hollie, and Ash. Last, and most certainly not least, I thank Bernie for the continuous support and inspiration she has given me, and for always keeping a smile on my face.

Contents

Chapter 1

Introduction

1.1 Introduction

For hundreds of thousands of years humans have sought to understand the world in which we find ourselves. It is widely regarded that this fervent pursuit of knowledge has been fuelled by the evolutionary battle to simply survive. Yet, to this day this lingering trait from our long and dark past manifests itself in one of the most important and profound human qualities – curiosity. Over millennia we have slowly pushed back the gloomy mists of the unknown, finding ourselves in an inconceivably vast and ancient universe, still wondering how it all began.

Modern cosmology tells us the universe burst into existence with a colossal growth rate from a singularity 13.8 billion years ago. After 10^{-37} seconds of rapid expansion and cooling, a phase change led to a period of extreme exponential growth known as cosmic inflation. Following this process the universe began to reheat, reaching temperatures high enough for the production of a quark-gluon plasma and the so called elementary particles we see around and within us today. It is in this state that it is believed particle and anti-particle pairs were being continuously created and destroyed through annihilation, resulting in a universe consisting of equal parts matter and anti-matter.

A sudden reaction causing an asymmetry between these two matter types, hypothetically known as baryogensis, is believed to have led to modern observations of matter dominance in the observable universe over antimatter – by a ratio of

30,000,000:1. This hypothesised symmetry breaking between matter and antimatter is arguably one of the biggest motivating factors for the antimatter experiments carried out today.

The purpose of this chapter is to provide context for the work presented in this thesis. An overview of the history of antimatter research is given with particular focus on the accelerators that have enabled such progress. Current antimatter experiments running today are introduced after which the Extra Low Energy Antiproton ring (ELENA) is presented. Finally, the goals of the project are presented with an overview of the contents of this thesis.

1.2 A Brief History of Antimatter Research

1.2.1 The Early Days

It took only four years after Dirac first predicted antimatter in 1928 [1] for the discovery of the first antiparticle, the positron, e^+. This discovery was made by Anderson whilst photographing cosmic ray tracks in a cloud chamber [2], confirming Dirac's suppositions. It took some 23 years and great leaps in particle accelerator technology before the first antiproton, $\overline{p}$, was observed in 1955 using the 6.2 GeV weakly focusing synchrotron named the Bevatron at Lawrence Berkeley National Laboratory, U.S. [3]. A year later the existance of the antineutron was confirmed using the same machine [4]. The successful pursuit of the constituents of the anti-atom had ushered in the age of accelerator physics, and with it, the field of high energy physics was expanding well beyond the confines of cosmic rays and cloud chambers.

Not long later in 1965 the first antinuclei, antideuterons, were produced from proton-beryllium collisions with the Proton Syncrotron (PS) at the European Organization for Nuclear Research (CERN) in Switzerland [5] and with the Alternating Gradient Synchrotron (AGS) at Brookhaven National Laboratory in New York [6]. These exciting achievements led to enthusiastic support from across the physics community to construct a purpose built storage ring for the production of high quality antiproton beams.

1.2.2 The AA era: Sp$\overline{\text{p}}$S and LEAR

The Super Proton-Antiproton Synchrotron (Sp$\overline{\text{p}}$S) was a yearly modification of the Super Proton Synchrotron (SPS) to allow for proton-antiproton (beam-beam) collision experiments with a centre of mass energy of 630 GeV, between the years of 1981 and 1991 [7]. Using a spectrometer, 2.7 GeV antiprotons were selected from the antiproton showers produced by directing 25 GeV protons from the PS onto a fixed iridium target. Proton-proton collisions over the kinetic energy threshold of 5.6 GeV allow for the production of antiprotons through the simple mechanism:

$$\mathrm{p} + \mathrm{p} \rightarrow \mathrm{p} + \mathrm{p} + \mathrm{p} + \overline{\mathrm{p}}. \tag{1.1}$$

The resultant antiproton beams were then injected into the Antiproton Accumulator (AA) where they were subject to stochastic cooling to reduce their transverse phase space and extremely large longitudinal momementum spreads [8]. A qualitative description of stochastic cooling is given in the following chapter. Through the use of RF to stack beams within the machine, the AA was capable of accumulating around $6{\times}10^{11}$ antiprotons over a period of 24 hours. Beams could then be injected into the Sp$\overline{\text{p}}$S where they were eventually led to the discovery of the $\mathrm{W}^{\pm}$ and Z^{0} bosons in 1983 [9].

In the same year the Low Energy Antiproton Ring (LEAR) began operation at CERN [10], a dedicated machine for antiproton physics with intense low energy beams. Beams also taken from the AA were injected into to LEAR for deceleration down to energies of around 5.3 MeV. LEAR employed the use of electron cooling to regulate the longitudinal and transverse phase space growth of the beam during deceleration [11, 12]. An additional upgrade to this facility came in 1986 when the Antiproton Collector (AC) was built around the AA providing a ten-fold increase in the production rate of antiprotons [13]. Over the next few years numerous experiments were performed including the investigation of interactions of matter and antimatter through proton-antiproton collisions [14, 15].

Finally the goal to combine antiprotons with positrons to create antihydrogen, $\overline{\mathrm{H}^{0}}$, was achieved by the PS210 collaboration at LEAR in 1995 [16], and again

two years later by the E862 collaboration with the Tevatron at Fermilab, US [17]. At LEAR, antihydrogen was created by antiprotons interacting with heavy atomic nuclei, xenon clusters, and binding with the positrons created from an electron positron pair generated through these interactions. Although this was a ground-breaking achievement, only 9 antihydrogen atoms were detected, quickly annihilating downstream from the target and providing little opportunity for further study. A new approach was needed, and in 1996 LEAR was shut down to be re-purposed as the currently operting Low Energy Ion Ring (LEIR), which began commissioning in 2005 [18]. The AC was shut down in 1997 to be re-purposed into the also currently operating Antiproton Decelerator (AD) which finished commissioning in 2000 [19, 20].

1.2.3 The Antiproton Decelerator

The 188m circumference AD was vital in bringing in the next era of antimatter research. Accepting beams of around 4×10^7 antiprotons at 2.8 GeV, generated from the PS in a similar manner to those for the AA, the AD is capable of decelerating to energies of 5.3 MeV. The beam is brought down in energy in three stages, in between which it uses a combination of electron cooling and stochastic cooling to counteract undesirable beam blow up (adiabatic expansion) during deceleration. A single cycle of the AD takes around 100 seconds after which beam is distributed to the experiments operating within the ring itself. Figure 1.2 below shows the latest planned layout, for reference. As opposed to the stacking methods used in the AA and AC, the AD transfers the beam directly to experiments which are then responsible for capturing, storing and stacking their own antiprotons.

The first experiment to operate at the AD was ATHENA [21] whose goal was to trap and perform laser spectroscopy on antihydrogen. Trapping was successfully achieved in 2002 resulting in headline articles in newspapers across the world [22]. Around 50,000 antihydrogen atoms were produced at extremely low energies by mixing positrons and antiprotons in cryogenically cooled penning traps. In order to trap antiprotons the 5.3 MeV beam from the AD was passed through a degrader foil which allowed them to lose energy via interaction with electrons. Over 99%

of antiprotons from the beam are lost during this process through annihilation or through large scattering angles resulting in an extremely low capturing efficiency. ATHENA was eventually reformed by some of its members into the Antihydrogen Laser Physics Apparatus (ALPHA) experiment, which began in 2008 to pursue its goal of spectroscopy on antihydrogen [23–25].

1.3 Current Antimatter Experiments

Currently there are five existing major antimatter experiments operating at the AD. ATRAP are the longest running experiment and also succeeded in trapping cold antihydrogen atoms shortly after ATHENA [26]. Due to limited space in the experimental area the two antiproton traps used by ATRAP are actually situated above one of the beam transport lines, requiring vertical deflectors. At the end of the same beamline is Atomic Spectroscopy and Collisions Using Slow Antiprotons (ASACUSA), which achieved antihydrogen beams in 2002 [26].

ASACUSA primarily aims to investigate investiagte the combined symmetry of charge conjugation, parity transformation and time reversal (CPT) symmetry between matter and antimatter by both measuring the antiproton-to-electron mass ratio through laser spectroscopy of antiprotonic helium [27] and by measuring the ground-state hyperfine structure of the antihydrogen atom using antihydrogen beams [28, 29]. ASACUSA uses a radio-frequency quadrupole (RFQ) decelerator to bring antiproton energies down to between around 10 keV and 120 keV [30]. RFQs are typically used in linear accelerators to bunch, focus and accelerate beams through the use of four electrodes, however the function here is reversed for deceleration. As well as being costly in its requirement of beam time for tuning, the resultant beam blow up from deceleration causes large beam losses and less than 3% goes on to be used in the experiment.

The ALPHA experiment also seeks to probe CPT invariance, albeit with different methods, and has been successfully trapping antihydrogen since 2010 [31], achieving confinement for 1000 seconds a year later [32] (as well as ATRAP the same year [33]). Much more recently the ALPHA experiment measured the 1S-2S transition of antihydrogen in 2016 [34] and the 1S-2P transition [35] in 2017.

Both measurements showed consistency with CPT invariance with the 2016 measurements reaching a precision of 2×10^{-10}. ALPHA also measured the hyperfine structure of antihydrogen in 2017 [36]. Currently ATRAP and ALPHA employ the use of degrader foils to obtain the low energy antiprotons required, and similarly to for ATHENA, passage of the beam through these foils causes beam losses of over 99%.

Other experiments at the AD include Antihydrogen Experiment: Gravity, Interferometry, Spectroscopy (AEGIS) which aims to perform direct measurements of the Earth's gravitational acceleration on antihydrogen [37] and the Baryon Antibaryon Symmetry Experiment (BASE) which succeeded in measuring the magnetic moment of the antiproton to a precision of the order of 10^{-9} in 2017 [38]. BASE is a unique user of the AD in that it is capable of storing tens of antiprotons within its reservoir trap for months at a time. A sixth new experiment, Gravitational Behaviour of Anti-Hydrogen at Rest (GBAR), is currently commissioning [39]. GBAR will attempt to measure the gravitational interaction of antimatter by ionising trapped antihydrogen ions ($e^+e^+\overline{p}$) and measuring their annihilation positions. Additionally the Antiproton Cell Experiment (ACE) has demonstrated the antiproton's effectiveness in cancer therapy treatment, showing an increase in cell killing capability by a factor of four over proton beams of the same energy [40, 41].

1.4 Extra Low Energy Antiproton Ring (ELENA)

From the vast array of ground-breaking research and monumental measurements achieved using AD beams it is clear to see why the facility has recently received its latest upgrade, the Extra Low Energy Antiproton ring (ELENA) [42–44]. ELENA is a 30.4 m magnetic syncrotron ring designed for the purpose of delivering high quality 100 keV antiproton beams to the experiments. ELENA commissioning came to an end at the start of CERN's second long shutdown (LS2) in November 2018.

ELENA is situated inside the circumference of the AD and receives 5.3 MeV antiprotons through a magnetic transport line. The antiprotons are decelerated in two stages allowing for an intermediate energy plateau where electron cooling

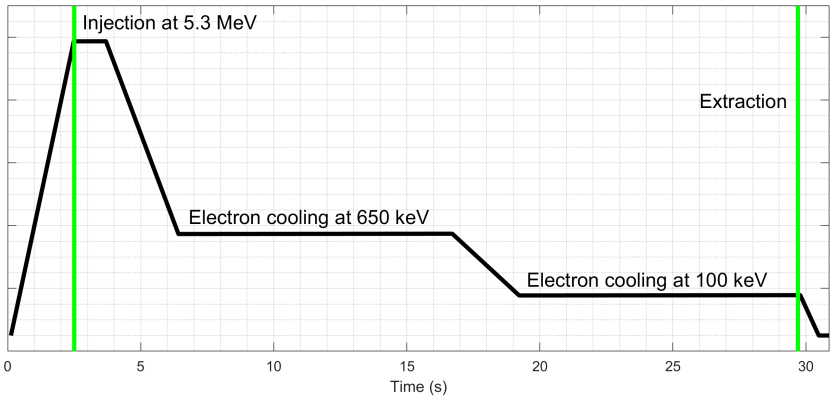

FIGURE 1.1: Example of a typical ELENA cycle. The y-axis does not have units due to it being representational based on the strengths of the bending dipoles, which are proportional to beam energy.

may be performed, as seen in Fig. 1.1. Electron cooling is also applied prior to extraction to achieve the highest quality beams of nominal intensity $\approx 1.8 \times 10^7$ [45]. ELENA's electron cooler is based on a design used by the S-LSR cooler ring at Kyoto University [46, 47].

With these extremely low energy 100 keV beams the experiments will be able to increase trapping efficiencies by the order of 10-100, for example by significantly decreasing the usage of degrader foils. The improved availability of trapped antiprotons will allow experiments to greatly improve measurement statistics and achieve their goals in a much shorter time frame. Currently AD beam time is divided by experiments in 8 hour shifts whereas ELENA will be capable of distributing four bunches amongst four experiments per AD shot, allowing for almost continuous beam time [48].

A series of electrostatic transport lines will carry the 100 keV antiprotons to the experimental areas. Figure 1.2 shows the ELENA ring situated within the AD and its network of beam transport lines. There are two main extraction points from ELENA, one, which is under construction during LS2, will lead to the original experimental area and a second which is already capable supplying beam to GBAR. It should be pointed out that in Fig. 1.2 the position of AEGIS is a proposed move from the empty space next to ATRAP.

ELENA also has a dedicated hydrogen ion, H^-, source which is used for commissioning when antiprotons are not available, for example to set up the magnetic

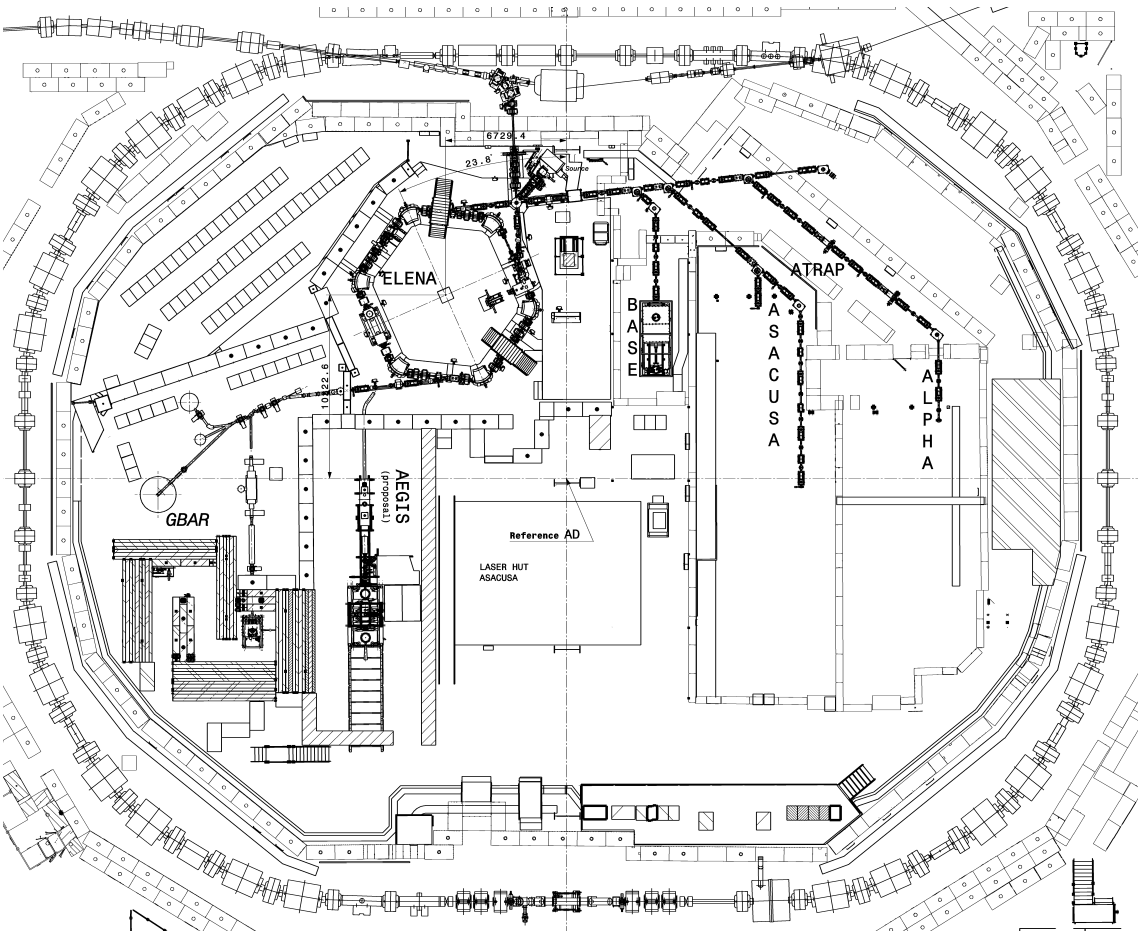

FIGURE 1.2: Planned layout of the AD hall. The AD is seen around the edges of the diagram.

system and measure beam optics. It has also been used to assist in the commissioning of the beam transport line to GBAR and is foreseen to be used similarly for the remaining transport lines.

To ensure the best possible beam quality during deceleration and distribution, diagnostics are essential. To monitor the closed orbit of the beam the ring is equipped with 20 stainless steel pickup beam position monitors (BPMs) which are mounted within dipoles and quadrupoles. The BPMs are also responsible for longitudinal Schottky measurements which may be performed on a bunching beam after summing signals and correcting for time-of-flight [49].

Two Gas Electron Multiplier (GEM) montiors (with two more to be added later) and a luminescent screen monitor (Beam Television, BTV) are installed along the beam transport line from the AD to ELENA. GEM montiors were previously effectively used along the AD beam distribution lines and so where chosen

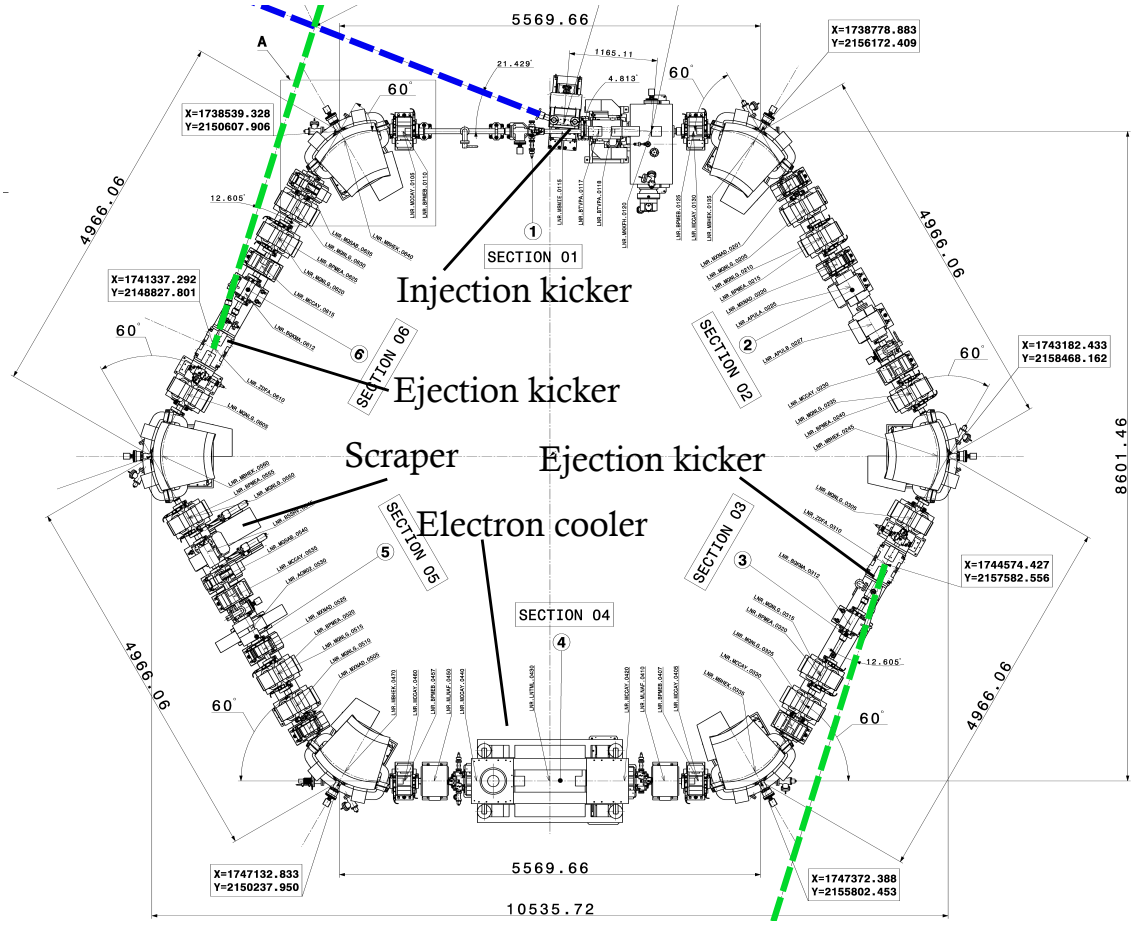

FIGURE 1.3: Layout of the ELENA ring.

for use here [50]. The BTV is a destructive device giving precise beam profile measurements by using a CCD camera to detect the photons generated when the beam interacts with a scintillating screen. The BTV is situated between the injection septum and the orbit correction kicker and is vital in checking incoming beam quality, particularly during commissioning.

Along the electrostatic transport lines micro-wire grid BPMs based on those used by ASACUSA are periodically placed to allow for online position measurements [42,51,52]. These BPMs, also known as secondary emission monitors (SEM), comprise of two micro-wire cathode arrays, arranged horizontally and vertically and held at ground potential. The wires are around 5-20 μm in diameter, spaced transversally 0.5–1.5 mm and made from gold coated tungsten. The arrays are sandwiched between 3 anode arrays with 2 mm longitudinal gaps. As a beam passes the cathode wires a small fraction of the antiprotons strikes them resulting in the emission of secondary electrons. The secondary electrons are then collected

by the anode arrays which are biased at around 100 V and a resultant position signal may be extracted from the induced amplified current within the cathode wire arrays.

For beam profile and emittance measurements within ELENA, a scraper system is used. Its position in section 5 of the ring is shown in Fig. 1.3. By measuring the secondary shower generated whilst intercepting the beam with an aluminium scraper blade, information on the transverse phase space may be obtained. Challenges relating to non-zero dispersion and non-Gaussian beam profiles have led to the development of novel emittance measurement algorithms for use with the scraper system which were recently published [53]. These techniques form the basis of a large part of this work and the scraper hardware as well as the challenges presented are well described in Section 3.3.

1.5 Project Goals and Overview

The primary goal of this project is the characterisation and optimisation of beam quality for extra low energy antiproton beams. The project is split into two main sections. The bulk of the work focuses on the development, testing and implementation of a novel emittance measurement technique within ELENA using the scraper blade system. Secondly, beam quality to the experiments is investigated using detailed and realistic simulations of the electrostatic transport lines.

Chapter 2 introduces the underlying theoretical concepts used for this work. In Chapter 3 emittance measurement techniques are introduced along with a detailed explanation of the scraper system in ELENA. Chapter 4 presents the underlying theory of the new scraper algorithms. The algorithms are tested using simulations in Chapter 5, followed by analysis of scraper data taken from ELENA in Chapter 6. Chapter 7 presents the transfer lines simulation, complete with expected beam quality and a discussion of optimisation techniques. Finally Chapter 8 gives a summary and outlook.

The work presented here is done in the context of the ELENA ring, but is generally of interest for future low energy ion and antimatter facilities. For example, the Facility for Low-energy Antiproton and Ion Research (FLAIR) is a

future addition to the Facility for Antiproton and Ion Research (FAIR) [54, 55]. FAIR is currently under construction at the GSI Helmholtz Centre for Heavy Ion Research in Darmstadt with FLAIR proposed as a phase 2 upgrade [56]. The use of scraper blades to characterise beams is not limited to such low energy machines and so the techniques may be adapted for use outside of the field of low energy antimatter and ion research. Furthermore, techniques for simulating the transport of extra low energy antiprotons and ions using electrostatic elements may also be built upon and adapted for future experimental, commercial and medical facilities in the future.

Chapter 2

Beam Dynamics

2.1 Introduction

Beam dynamics is the underpinning theory behind effective particle accelerator operation. The purpose of this chapter is to set up the theoretical framework for the development of the scraper algorithm and beam transport lines studies. Additionally, emittance growth due to deceleration and space charge effects is introduced, with a description of the effects expected in ELENA. The electron cooler and related simulation results are presented for context for the scraping algorithm.

2.2 Transverse Beam Dynamics

2.2.1 Co-ordinate System

We may consider two co-ordinate systems when describing a beam traversing a particle accelerator or transport line. In both systems the transverse plane is described by the horizontal co-ordinate x and the vertical position co-ordinate y. In all accelerators there is a single ideal path taken by a hypothetical perfectly centred particle with the design momentum and no initial divergence known as the reference particle. The path it traces out through the machine is called the closed orbit in the case of a ring (since it ends exactly where it began) or the reference orbit for a linear machine. This path defines $x = 0$ and $y = 0$ along the machine.

If we are in a frame of reference which travels with the reference particle, we may define a co-moving system x, y, z where the z component describes a particle's longitudinal offset from the reference particle. When considering a beam's position around a ring or along a transport line we may use x, y, s where s defines a distance along or around the machine from some arbitrary point, $s = 0$. Typically $s = 0$ will be at the injection point or the start of a beam transfer line and follows the path of the reference particle. The systems are represented in Fig 2.1. It should be noted that z is a curvilinear co-ordinate and is always parallel to the reference particle's closed orbit.

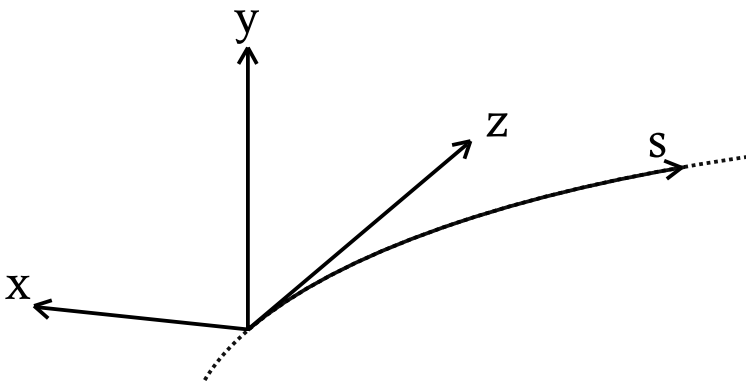

FIGURE 2.1: Simple representation of the co-ordinate systems used.

A particle may be described at any single point along s by a set of 6 phase space co-ordinates:

$$(x, x', y, y', z, \delta), \tag{2.1}$$

where $x' = \frac{dx}{ds}$, $y' = \frac{dy}{ds}$ and $\delta = \frac{p_i - p_0}{p_0}$, with p_i as the momentum of the particle and p_0 as the design momentum. δ is known as the (longitudinal) momentum offset.

2.2.2 Optical Elements

Modern particle accelerators typically use a series of magnetic or electrostatic dipoles and quadrupoles, commonly referred to as optical 'elements' which make up the electromagnetic architecture of the machine, called a 'lattice'. They are used to steer and focus a beam by exploiting the Lorentz force:

$$\vec{F} = \frac{\mathrm{d}\vec{p}}{\mathrm{d}t} = q\vec{E} + q\vec{v} \times \vec{B} \tag{2.2}$$

where q is the charge on the particle moving with velocity $\vec{v}$, $\vec{E}$ and $\vec{B}$ are the electric and magnetic fields, respectively and $\vec{F}$ is the force experienced by the particle, equal to the rate of change of momentum, $\vec{p}$. For example, the bending effect of a constant vertical magnetic field, B_0 on a particle may be described by:

$$\rho B_0 = \frac{p}{q} \tag{2.3}$$

where ρ is the bending radius and p is the longitudinal momentum of the particle. The quantity ρB_0 is called the magnetic rigidity and this relationship with the momentum of particles determines the field strength and length of bending dipole magnets to achieve the desired deflection angle.

As a beam traverses a lattice its horizontal and vertical widths are focused and controlled by quadrupoles. A quadrupole is designed such that it has zero field at the central axis $(x, y = 0)$ and applies some correcting kick to off-axis particles. This can only be done in one plane at a time, having the opposite effect in the other plane. A quadrupole whose polarity kicks off-axis horizontal particles towards $x = 0$ is conventionally known as a focusing quadrupole and when focusing vertically is called a defocusing quadrupole. A magnetic quadrupole's normalised focusing strength, k, may be given by:

$$k = \frac{G_M q}{p}, \tag{2.4}$$

where G_M is the magnetic field gradient, $\frac{\mathrm{d}B_y}{\mathrm{d}x}$. It is standard practice for a lattice to keep a beam focused in both planes by use of focusing and defocusing quadrupoles in an alternating arrangement, known as a FODO lattice.

2.2.3 Emittance

For a particle with no momentum offset, $\delta = 0$, its transverse motions around the closed orbit of an accelerator are given by Hill's equations [57]:

$$x''(s) + K_x(s)x(s) = 0, \tag{2.5}$$

$$y''(s) + K_y(s)x(s) = 0 \tag{2.6}$$

where $K_x(s) = (\frac{1}{\rho^2(s)} - k(s))$ and $K_y(s) = k(s)$, describe the focusing properties around the lattice. Since for a circular machine the lattice is a closed loop, the coefficients satisfy the periodicity conditions $K_{x,y}(s) = K_{x,y}(s+C)$ where C is the circumference of the machine. Looking for a solution for the horizontal equation we may arrive at:

$$x = \sqrt{\epsilon_x \beta_x(s)} \cos(\psi(s) - \psi_0). \tag{2.7}$$

Here we define some very important quantities. $\psi(s)$ is the phase advance with ψ_0 being its initial condition. ϵ_x is the horizontal emittance of the particle and is a constant around the machine. β_x is known as the beta function and varies around the ring as a result of the focusing properties of the elements. The derivative of the equation Eq. 2.7, may be written:

$$x' = -\sqrt{\frac{\epsilon_x}{\beta_x(s)}}\Big(\alpha_x(s)\cos(\psi(s) - \psi_0) + \sin(\psi(s) - \psi_0)\Big), \tag{2.8}$$

where we have defined $\alpha_x(s) = -\beta_x'(s)/2$, which is another parameter of the lattice.

Finally, we may combine the results for x and x' to arrive at an expression for the horizontal emittance:

$$\epsilon_x = \gamma_x(s)x^2 + 2\alpha_x(s)xx' + \beta_x(s)x'^2 \tag{2.9}$$

where $\gamma_x(s) = \frac{1+\alpha^2(s)}{\beta_x(s)}$, the final of the three lattice parameters $(\alpha_x(s), \beta_x(s), \gamma_x(s))$ known as the Twiss parameters. The vertical emittance and Twiss parameters may be derived similarly. Throughout this work the beta function is used frequently and so we drop the (s) notation simply writing β_x and β_y for brevity.

Plotting Eq. 2.9 gives an ellipse which a particle will trace out in phase space when measured many times at a given position s around the lattice. The ellipse will be centred around the closed orbit of the beam (x_0 or y_0) and has the properties shown in Fig. 2.2. As a particle moves through the machine the ellipse will change shape yet the area $\pi\epsilon_{x,y}$ will remain constant. The idea that emittance is conserved around the machine is known as Liouville's theorem and applies only for a closed system, not considering collective effects or acceleration forces, which will be described later [58].

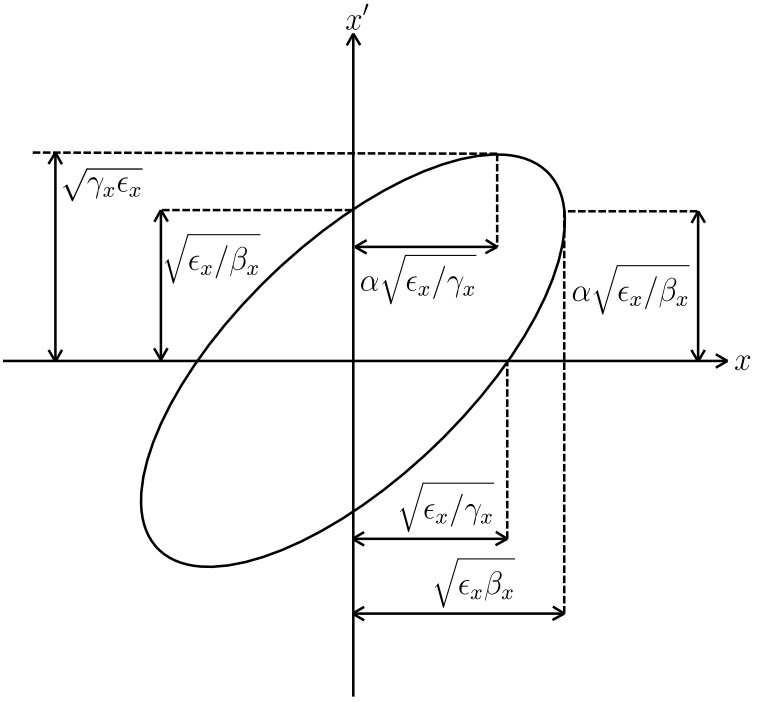

FIGURE 2.2: Properties of the horizontal phase space ellipse.

2.2.4 Dispersion and Momentum Spread

The horizontal Hill's equation must be modified when considering a particle with some small momentum deviation $\delta << 1$. An on axis yet off momentum particle will have some modified divergence x' after a sector bend due to its exit angle being slightly different from the design angle for the reference momentum p_0. We must then rewrite Eq. 2.5 as [57]:

$$x''(s) + K_x(s)x(s) = \frac{\delta}{\rho(s)}, \tag{2.10}$$

to account for this effect. The orbit of the particle is now adjusted and so we redefine the original on-momentum co-ordinate as the betatron position, x_β, which traces out the phase space ellipse as described. It is possible then to define a new closed orbit around which a hypothetical particle of $\delta = 1$ would follow, $D(s)$. Note: in reality particles with $\delta = 1$ would be immediately lost in the machine. $D(s)$ is known as the dispersion around the machine and is a property of the lattice. A particle with some small δ would then have a position:

$$x(s) = x_\beta(s) + D_x(s)\delta, \tag{2.11}$$

at some point s along the machine. The dispersive term $D_x\delta$ (again dropping (s) notation due to frequent use) causes a shift in the horizontal position of the ellipse traced out by x_β as seen in Fig. 2.3. The quantity $x_\beta(s) + D_x\delta$ may be thought of as the momentum-dependant closed orbit of a particle.

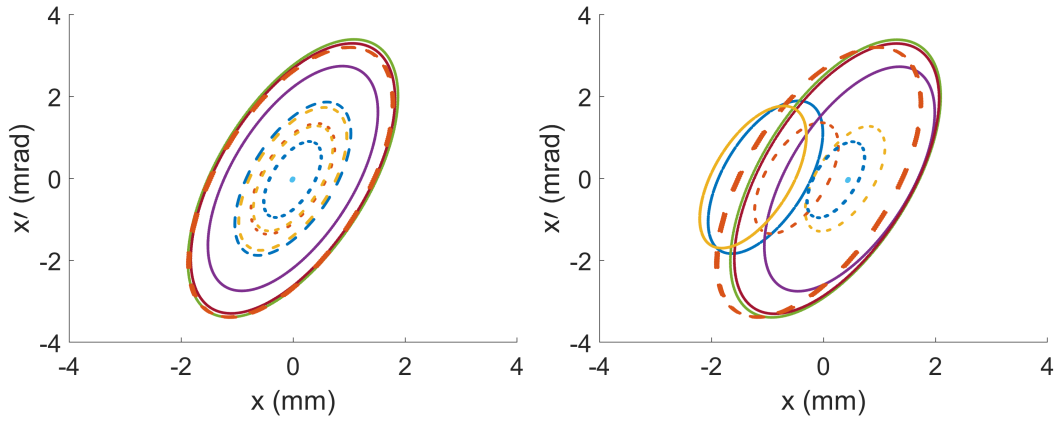

FIGURE 2.3: Horizontal phase space ellipses traced out by ten particles over many turns at fixed s in a region with $D_x \neq 0$. Particles in the left plot have zero momentum offset and in the right plot a range of positive and negative momentum offsets. Both sets of particles have the same emittances.

2.2.5 Statistical Emittance

In an accelerator a beam is made up of a number of particles all with different emittances and momentum offsets. Typically it is the case that the distribution of these two quantities can be approximated by Gaussian distributions. The overall emittance of a beam must be defined by how much of the beam distribution is being considered. For example, the phase space area of the 95% emittance contains 95% of the particles in the distribution. Here the RMS (root mean square) definition is used where we consider the area containing one standard deviation of the beam's particles. We may compute the statistical RMS emittance of a distribution of particles using:

$$\epsilon_x = \sqrt{\langle x^2 \rangle \langle x'^2 \rangle - \langle x x' \rangle^2} \tag{2.12}$$

where $\langle ... \rangle$ denotes the weighted averages and are the second order moments of the beam. Units of emittance are typically given in mm mrad. The momentum spread of the beam, σ_δ, is defined as the RMS width of the momentum offset distribution

and in unitless as is δ. In the case of a Gaussian beam the emittance at any point along s may be estimated from the RMS beam widths $\sigma_{x,y}$ with:

$$\epsilon_x = \frac{\sigma_x^2}{\beta_x} - \frac{\sigma_\delta^2 D_x^2}{\beta_x} \tag{2.13}$$

$$\epsilon_y = \frac{\sigma_y^2}{\beta_y} \tag{2.14}$$

where in the horizontal plane dispersive effects are accounted for by the second term. From these equations it is clear to see that the RMS beam width varies as a function of $\beta_{x,y}$. An example of this relation is given in Fig. 2.4 where a beam of $\epsilon_{x,y} = 1$ mm mrad and $\sigma_\delta = 0$ is being tracked through a FODO quadrupole arrangement.

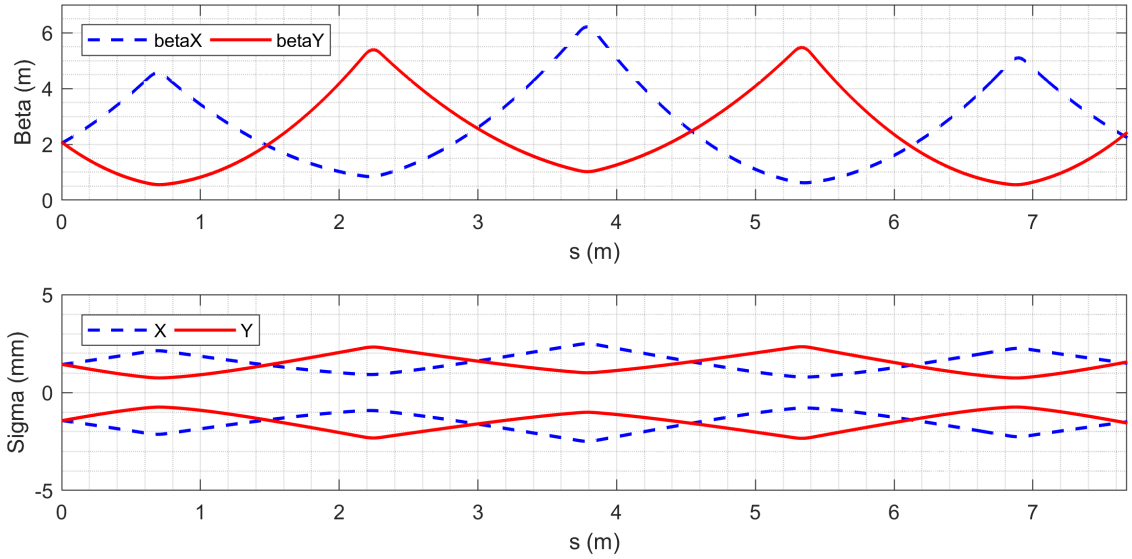

FIGURE 2.4: Example of the relationship between $\beta_{x,y}$ and $\sigma_{x,y}$.

As particles orbit a circular machine they undergo transverse oscillations around the reference particle known as betatron oscillations. The number of oscillations per turn, or phase advance, in each plane are known as the horizontal and vertical tunes of the lattice which may be calculated by:

$$Q_{x,y} = \frac{1}{2\pi} \oint_C \frac{1}{\beta_{x,y}(s)} \mathrm{d}s \tag{2.15}$$

where the integral is taken around the circumference of the ring, C [59]. Careful considerations must be made when adjusting the optics of a machine to avoid resonant tunes which lead to self-amplifying instabilities and result in beam losses.

2.3 Beam Cooling

2.3.1 Sources of Emittance Growth in ELENA

The beam in ELENA is decelerated from the injection energy of 5.3 MeV to an extraction energy of 100 keV in two stages to allow for an intermediate cooling plateau at 650 keV. The adiabatic blow up of the beam is an emittance increase inversely proportional to the change in momentum of the beam. The increase factor due to this effect, f_a, may be estimated using:

$$f_a = \frac{\beta_{\gamma,1}\gamma_{l,1}}{\beta_{\gamma,2}\gamma_{l,2}} = \frac{p_1}{p_2}, \tag{2.16}$$

where $\beta_\gamma = \frac{v}{c}$ and γ_l is the Lorentz factor [60]. Subscripts 1 and 2 refer to before and after deceleration respectively whilst p describes the momentum of the beam. This gives emittance increase factors of 2.86 and 2.56 along the first and second deceleration ramps, respectively. A direct deceleration from 5.3 MeV to 100 keV would result in $f_a =$ 7.3, likely resulting in beam losses and further emphasising the necessity for the intermediate cooling plateau to counteract emittance blow up mid way.

At the low energy region in which ELENA operates, dispersive effects become significant. The effect of rest gas scattering, whereby the beam interacts with residual particles in the beamline through multiple Coulomb scattering, was investigated and found to be negligible due to ELENA's nominal operating vacuum of 3×10^{-12} Torr [61]. However, a more considerable factor contributing to the necessity of electron cooling for low energy beams is intra-beam scattering (IBS).

IBS is a diffusion effect arising from the interaction of particles with each other in the beam through multiple small angle Coulomb scattering. IBS is well explained in literature with models developed by Piwinski [62, 63], Martini [64]

and later by Bjorken and Mtingwa [65]. Beam growth rates due to this effect may be approximated by:

$$\frac{1}{\tau_{x,y,p}} \propto \frac{r_p^2 c \lambda}{32\pi\sqrt{\pi}\beta_\gamma^3 \gamma_l^4 \epsilon_x \epsilon_y \sigma_\delta}, \tag{2.17}$$

where for coasting beams $\lambda = N/C$ and for bunched beams $\lambda = N_b/(2\sqrt{\pi}\sigma_s)$. N is the total particles in the beam and N_b in each bunch whilst σ_s gives the bunch length. C gives the circumference of the ring, c the speed of light in vacuum and r_p is the classical proton radius. The inverse dependence on γ_l^4 highlights the significance of this effect for low energy machines where γ_l approaches 1 and so understanding the magnitude of this effect is most crucial at an energy of 100 keV.

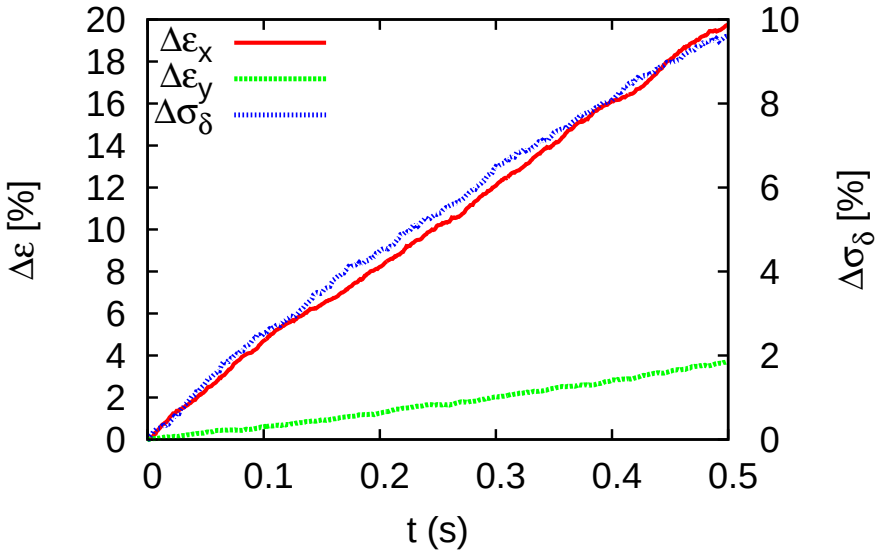

FIGURE 2.5: Rate of increase of emittance and longitudinal momentum spread due to the effects of IBS in a BETACOOL simulation of ELENA at 100 keV [53].

Using the code BETACOOL [66], IBS simulations were performed for the ELENA ring. BETACOOL is a multi-particle tracking code capable of simulating various space charge effects in the presence of electron cooling using Monte-Carlo methods. Here no electron cooling was used in order to obtain growth rates due to IBS based on Martini's model, which is an extension of the Piwinski model for strongly focusing machines and accounts for variations in beta functions and dispersion around the ring. The simulation was performed for a 100 keV beam with initial $\epsilon_{x,y} = 1$ mm mrad, $\sigma_\delta = 5 \times 10^{-4}$ and nominal intensity of 2.5×10^7 represented by 10^4 macroparticles. Figure 2.5 shows the evolution of the beam over

half a second. Whilst there is some small increase in momentum spread over this time, the emittance has grown by 20% indicating that even along energy plateaus the beam is growing significantly in phase space. The electron cooler will reduce the beam size until it finds an equilibrium with resistive IBS effects.

2.3.2 Stochastic Cooling

Stochastic cooling was invented by Simon van der Meer in 1972 [67], who then went on to win a Nobel Prize for the idea. It is used in the AD in but not in ELENA. The basic principle of stochastic cooling is well described in literature [68, 69] so here a simple qualitative explanation is given. Considering a hypothetical scenario with a single particle travelling in the machine, we may measure its horizontal displacement with a non-invasive pickup. The pickup may transmit the signal through an amplifier to a kicker further along the ring, delayed such that the resultant kick takes place upon arrival of the particle. If the system is configured to account for the horizontal oscillations of the particle then the resultant kick can be such that the horizontal oscillation amplitude of the particle is reduced.

A more realistic scenario would involve replacing the particle with a longitudinal or transverse phase space sample of a coasting beam and applying kicks in the appropriate plane. Careful planning can negate unwanted statistical effects, and the entire beam may be cooled over many turns. Whilst it is true that emittance is conserved around a ring in the absence of external effects, stochastic cooling may be thought of as a trick to move the empty space between particles towards the outer region of the beam.

2.3.3 Electron Cooling

Electron cooling was invented by Gersch Budker in 1967 at the Budker Institute of Nuclear Physics, Novosibirsk [70]. It has been used successfully in LEAR [11, 12] and the AD [19, 20] to reduce and maintain the emittance of low energy antiproton beams and so is employed in ELENA. Electron cooling is applied for a coasting beam at the intermediate plateau and along the extraction plateau for both

a coasting beam and during rebunching to control the longitudinal momentum spread.

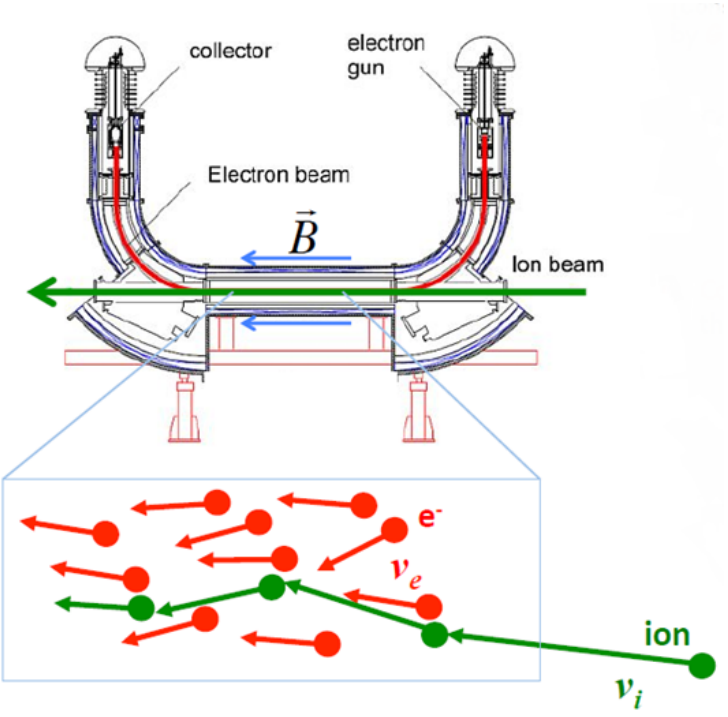

FIGURE 2.6: Working concept of an electron cooler.

Figure 2.6 gives a schematic representation of how electron cooling works. The ion (antiproton) beam passes through a parallel intense electron beam with similar velocity and Coulomb interactions of the ions with individual electrons takes place. The electrons are then collected at the other end of the cooler whilst the ions travel the ring and enter the cooler again, continuing the processes. The cooling effect is akin to the theory of ideal gasses, in the particle frame the electron beam may be thought of as a cold electron gas which interacts with the hot ion gas resulting in a net decrease in the ion gas temperature. In terms of beam dynamics, the result of this interaction results in a gradual reduction in the transverse emittance and momentum spread of the beam.

The cooling rate due to electron cooling depends on many factors as given in this approximation [42]:

$$\frac{1}{\tau} = \frac{1}{k}\frac{q^2}{A}\eta_c L_c r_e r_p \frac{j}{e}\frac{1}{\beta_\gamma^4 \gamma^5 \Theta^3} \tag{2.18}$$

where $k = 0.16$ is a constant depending on the distributions of ions and electrons, q is the charge of the ions, A the mass number, η_c is the fraction of the ring over which cooling takes place (in ELENA 0.7 m over 30.4 m, $\eta_c = 0.023$), $L_c \approx 10$ is the Coulomb logarithm and depends on the electron temperature (T_e), $r_e = 2.8 \times 10^{-15}$ m is the classical electron radius, $r_p = 1.54 \times 10^{-18}$ m is the classical proton radius, j is the current density of the electron beam and Θ is the RMS angular spread between the electron beam and the ion beam which is given by ion and electron transverse temperatures and misalignments. The electron cooler, pictured in Fig 2.7, is optimised by varying the parameters n_c, j, Θ and T_e. Table 2.1 shows the nominal electron cooler parameters for ELENA.

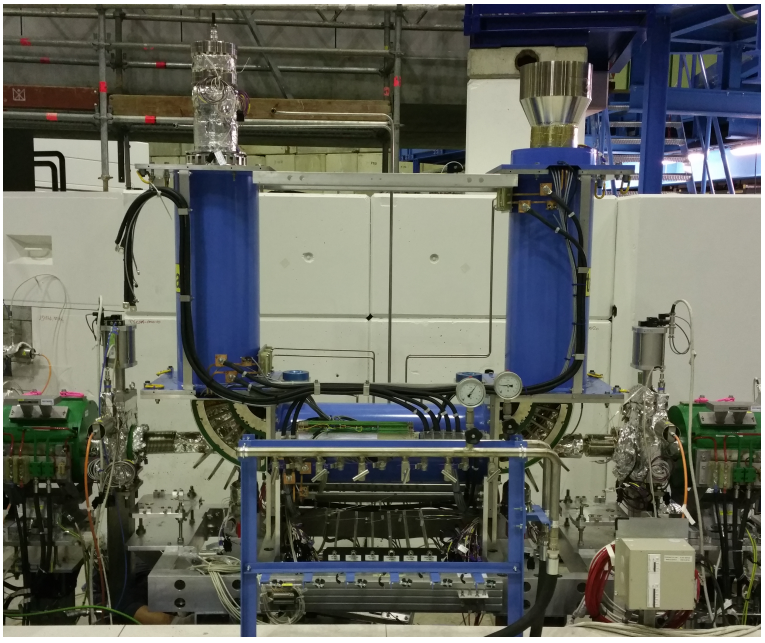

FIGURE 2.7: Picture of the electron cooler during installation in ELENA [71].

Studies into the long-term beam evolution were carried out to determine cooling rates and the equilibrium values of the emittance and momentum spread [60, 61]. Non-Gaussian beam profiles had previously been observed in the AD due to more efficient cooling at the core of the beam. The magnitude of this effect is dependent on the radial intensity of the electron beam which is non-uniform and tends to have a higher density around $x, y = 0$. In BETACOOL simulations for ELENA the same effect was observed. Figure 2.8 shows the results of one such simulation where the beam is well approximated by a bi-Gaussian distribution.

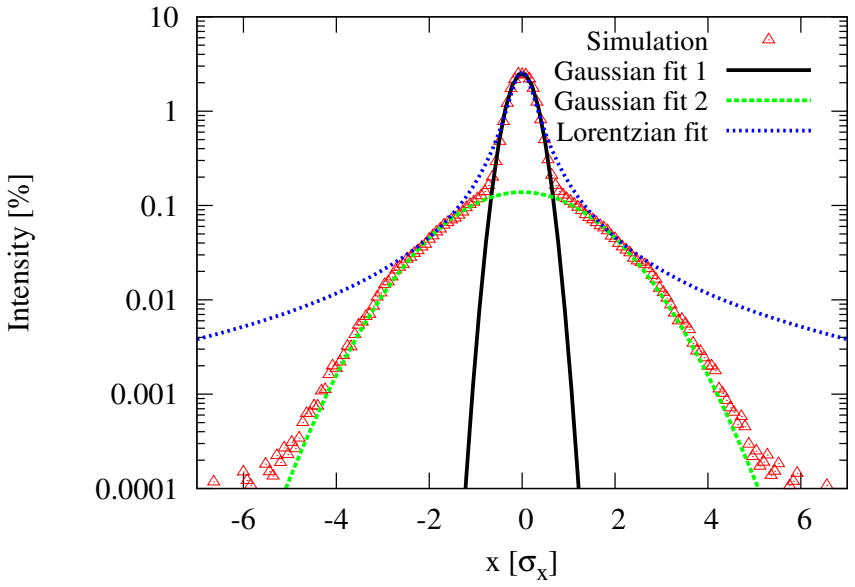

FIGURE 2.8: Expected bi-Gaussian beam distribution based on BETACOOL simulations.

TABLE 2.1: Nominal electron cooler parameters for ELENA.

	Intermediate plateau	Ejection Plateau
Electron beam energy (eV)	355	55
Electron current (mA)	5	2
Electron beam density (m^{-3})	1.38×10^{12}	1.41×10^{12}
B_{gun}(G)	1000	
B_{drift} (G)	100	
Expansion factor	10	
Cathode radius (mm)	8	
Electron beam radius (mm)	25	
Twiss parameters (m)	β_x=2.103, β_y=2.186, D_x=1.498	
Flange-to-flange length (mm)	2330	
Drift solenoid length (mm)	1000	
Effective length (mm)	700	

2.4 Summary

In this chapter important concepts such as emittance, beta functions, momentum spread, and dispersion have been introduced. Beam effects more specific to low energy storage rings such as ELENA have also been introduced. It has been shown that bi-Gaussian transverse beam distributions are expected in ELENA, based on BETACOOL simulations in the presence of IBS and electron cooling. In combination with non-zero dispersion around the ELENA ring, these non-Gaussian

beams pose a challenge for accurately measuring the emittance of the beam within the machine using the scraper system. In the following chapter diagnostic devices for measuring the emittance of a beam are introduced, including an introduction to beam scraping and details of the ELENA scraper system.

Chapter 3

Emittance Measurements

3.1 Introduction

The main purpose of this chapter is to provide context for the new scraping analysis algorithms which have been derived for meeting the challenges presented by the conditions in ELENA. Various techniques for emittance measurement are introduced, along with an explanation of the general concept of beam scraping. The specific hardware used in the ELENA scraping system will be described to provide some background for the algorithms. Additionally, the scraping challenges presented by ELENA will be discussed in detail to provide the context and motivation for the development of these new methods.

3.2 Emittance Measurement Techniques

In order to control and optimise beam quality it's essential to monitor the beam emittance in all accelerators, linear and circular and in some cases along transport lines. Here we focus on transverse emittance (ϵ_x, ϵ_y) measurements since it is the primary goal of the scraper to measure these quantities. Longitudinal emittance measurements are typically performed separately using different techniques. Because the transverse emittance and phase space density of a beam cannot be measured directly, they have to be inferred from other data such as beam profile measurements.

Since the applications and hence energy range of particle accelerators is so broad, many different techniques for measuring the emittance under various circumstances have been developed over the years. Unfortunately, there is no technique to fit all machine types and the pros and cons of each method must be weighed up for every case. For the wider context of this particular study, we briefly explore some commonly used techniques. Other methods such as the Allison scanner [72] are well described in the literature.

3.2.1 Slit Plate and Pepper-pot Methods

A beam may be split into so-called 'beamlets' by propagation through a plate covered in slits or a grid of holes (pepper-pot) with fixed apertures [73–75]. Detection and intensity measurements of the beamlets on a monitor (e.g. phosphor screen) further downstream provides information on the beam distribution. Because of the known aperture positions and widths, the angular distribution of the beamlets, x', may be reconstructed at the screen using a simple calculation, e.g:

$$x' = \frac{(x_1 - x_2)}{L}, \tag{3.1}$$

where x_1 is the horizontal position of the hole or slit the beamlet passed through, x_2 is the beamlet's horizontal position on the screen and L is the distance between the plate and the screen. Knowing these values for all beamlets allows one to reconstruct the angular distribution for the entire beam at the position of the grid or pepper-pot plate. The main difference between the slit and grid methods is that the grid can provide information on both the x and y planes simultaneously by simply summing intensities in each plane.

Using these methods the angular distribution and hence emittance of the entire beam may be reconstructed, however because of varying amount of beam losses based on the geometry of the plates, values for the real, slit and pepper-pot emittances are always different. Slit and pepper-pot methods are only suitable for use along linear machines or transport lines since the equipment must be placed in the beam's path before a measurement can be made. A pepper-pot monitor is limited

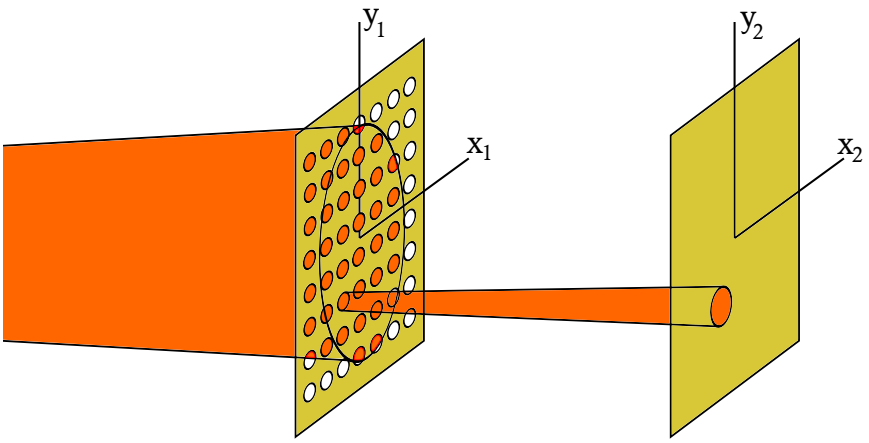

FIGURE 3.1: Representation of the pepper-pot method. Only one beamlet is shown for simplicity.

also by the spot resolution of the screen being used. The screen resolution is less significant with increasing L, and so a compromise must be made with available space.

Additionally to the schemes described above, more advanced and complex variations of these methods have been developed. For example, using two pairs of slits separated along the beamline allows the user to define the position of a beamlet and scan over an area [76, 77]. The entire phase space can be systematically scanned whilst measuring only the resultant intensity for discrete steps in (x, x') or (y, y'), creating a phase space map. Step size depends on the resolution of the intensity monitor.

3.2.2 Wire and Laser Wire Scanners

Similarly to a scraping device, a wire scanner system [78, 79] works by moving a thin wire quickly and transversally through a circulating beam and creating and measuring the intensity of a shower of secondaries proportional to the beam intensity. By scanning perpendicularly to the wire's length and comparing the secondary shower intensity with the wire's position, a beam profile in the plane of scanning motion can be obtained. Alternatively, the charge deposited on the wire may be used in place of the shower intensity.

Wire scanners are useful because they are only semi-invasive as the remaining particles in the beam may continue to circulate the machine. The beam however, will typically experience an increase in emittance due to scattering increasing the angular spread of the beam. Wire scanners may be used typically for mid to high energy range (i.e. >100 MeV) accelerators since at lower energies and intensities less intense secondary showers become difficult to detect. The emittance increase associated with wire scanners is also greater at lower energies [80]. As with many methods presented here, including scraping, wire scanners are also time dependent as they do not sample the beam instantly. This may also lead to errors in measurement.

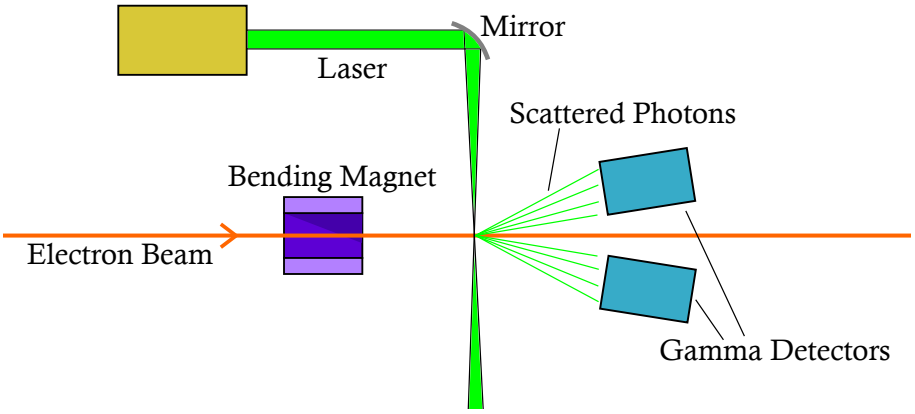

FIGURE 3.2: Diagram illustrating a laser wire scanner system with detectors in the adjacent configuration. The beam would be bent into and out of the page with the bending magnet.

Laser wire scanners [81, 82] work on the same basic principle as standard wire scanners, however the material wire is replaced with a narrowly focused laser beam, around one wavelength in diameter. As a result, laser wire scanners are considered non-destructive. The laser beam may be split from its source and used to scan either horizontally or vertically across the aperture with the use of mirrors. A signal is produced when particles interact with the laser through inverse Compton scattering, sending photons in the direction of beam propagation. The beam may then be bent away from this path allowing for the scattered photons to be detected and measured as an intensity signal. Alternatively, the particle beam may continue on its path and adjacent detectors may measure some flux of photons, as seen in

Fig. 3.2. As an alternative to laser movement, the beam may be moved through a stationary laser beam using a bending magnet.

The Compton differential cross-section, which gives a measure of the likelihood of interaction, is inversely proportional to the square of the rest mass of the particle. This means that inverse Compton scattering is suppressed for more massive particles, such as the proton. As a result, too few photons arrive at the detectors when scanning beams of more massive particles, and so the technique is saved for electron and positron beams.

3.2.3 Triple Measurement Matrix Methods

This technique is particularly useful for linacs and transport lines as it gives the emittance from a single shot. It is still being commonly used and developed with the event of linac dependent laser-plasma wakefield accelerators and X-ray free electron lasers [83, 84].

It is possible to calculate the horizontal transverse emittance as $\epsilon_x = \sqrt{det\sigma_{\mathbf{x}}^{\mathbf{0}}}$, where $\sigma_{\mathbf{x}}^{\mathbf{0}}$ is the 2×2 beam matrix [85] defined as:

$$\sigma_{\mathbf{x}}^{\mathbf{0}} = \begin{pmatrix} \sigma_{x,11}^{0} & \sigma_{x,12}^{0} \\ \sigma_{x,21}^{0} & \sigma_{x,22}^{0} \end{pmatrix} = \begin{pmatrix} \langle x^2 \rangle - \langle x \rangle^2 & \langle xx' \rangle - \langle x \rangle \langle x' \rangle \\ \langle x'x \rangle - \langle x' \rangle \langle x \rangle & \langle x'^2 \rangle - \langle x' \rangle^2 \end{pmatrix}, \tag{3.2}$$

for the beam at z_0. Here for simplicity we describe in terms of the horizontal plane x, however the methods may be applied for the vertical plane, y, too. It is not possible to directly measure all of the quantities within the matrix in one instant, however the first term $\sigma_{x,11}^{0}$ may be calculated simply from the beam width at z_0. Using this knowledge we may take several measurements of the first terms at different positions along z to infer the other matrix terms at z_0.

A similar matrix $\sigma_{\mathbf{x}}^{\mathbf{1}}$ may describe the beam at a different position along the beamline, z_1. Additionally we may consider a transfer matrix $\mathbf{R}$ capable of transforming $\sigma_{\mathbf{x}}^{\mathbf{0}}$ to $\sigma_{\mathbf{x}}^{\mathbf{1}}$:

$$\mathbf{R} = \begin{pmatrix} R_{11} & R_{12} \\ R_{21} & R_{22} \end{pmatrix}, \tag{3.3}$$

so that:

$$\sigma_{\mathbf{x}}^{\mathbf{1}} = \mathbf{R}\ \sigma_{\mathbf{x}}^{\mathbf{0}}\ \mathbf{R}^{T}. \tag{3.4}$$

Assuming that there is no transverse position offset of the beam, or that the offset is static and we redefine our co-ordinates around it, we may say that $\sigma_{x,12} = \sigma_{x,21}$. With this assumption we may then use Eq. 3.4 to express $\sigma_{x,11}^{1}$ in terms of the matrix $\sigma_{\mathbf{x}}^{\mathbf{0}}$:

$$\sigma_{x,11}^{1} = R_{11}^{2}\sigma_{11}^{0} + 2R_{11}R_{12}\sigma_{12}^{0} + R_{12}^{2}\sigma_{22}^{0}. \tag{3.5}$$

We may use this equation, or combine measurements from several variants of it to calculate all elements within the target matrix, $\sigma_{\mathbf{x}}^{\mathbf{0}}$. For example, the beam width may be calculated at two additional z positions downstream from z_0 with only drift spaces between, leading to a pair of equations which may be solved for σ_{12}^{0} and σ_{22}^{0};

$$\sigma_{x,11}^{1} = \sigma_{11}^{0} + 2L_1\sigma_{12}^{0} + L_1^{2}\sigma_{22}^{0}, \tag{3.6}$$

$$\sigma_{x,11}^{2} = \sigma_{11}^{0} + 2L_2\sigma_{12}^{0} + L_2^{2}\sigma_{22}^{0}, \tag{3.7}$$

where the transfer matrix $\mathbf{R}$ has been replaced with a drift matrix in each case;

$$\mathbf{R_d} = \begin{pmatrix} 1 & L_i \\ 0 & 1 \end{pmatrix} \tag{3.8}$$

where L_i is a drift length for the ith position measurement.

Whilst the drift method is suitably straightforward to introduce the concept, a more commonly used application of triple matrix analysis would be as follows. Instead of changing the transfer matrix by having different drift lengths, a quadrupole may be placed downstream from z_0. Different quadrupole strengths give different transfer matrices. Measurements of the beam waist at a fixed position downstream for different quadrupole strengths provides a set of equations, similar to those above, from which the emittance at z_0 can be extracted. Additionally, setting z_0 to a position where the beam is at a waist gives $\sigma_{12}^{0} \approx 0$ and simplifies the calculation further [86].

3.2.4 Optical Transition Radiation

Optical Transition Radiation (OTR) measurements work on the principle that particles passing a boundary between two media of differing dielectric constants emit optical radiation. It is possible to exploit this by placing a sheet of material in the beam's path and measuring the radiation generated as the beam passes from vacuum to the material, and again as it leaves the material. By rotating the sheet 45° around x or y, OTR may be generated centred around 90° from the beam's direction as particles enter the sheet, and also around the beam's direction upon re-entering vacuum, Fig 3.1. Because it is a surface phenomenon, very thin sheets may be used resulting in minimal impact and scattering of the beam, especially when compared with scintillating screens.

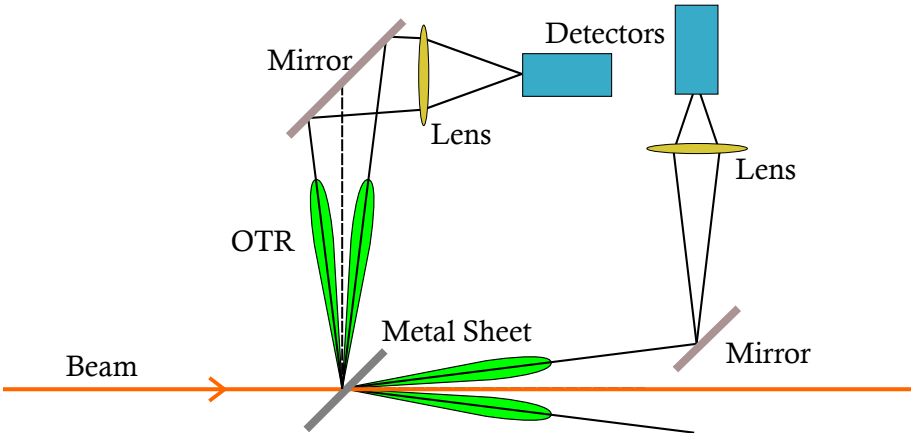

FIGURE 3.3: An example equipment layout when measuring OTR for beam diagnostics.

The radiation generated by OTR is in the form of two cones offset at equal angles from the line of reflection of the beam's path with the material. Detailed analysis of the radiation allows reconstruction of the RMS beam size. The clarity of the signal received is proportional to the Lorentz factor, γ_l, of the beam and so the technique is best applied to lepton or high energy hadron beams.

An extension this technique is known as OTR interferometry, or OTRI [87–89] and may be used to measure the emittance of the beam. An OTRI experimental set up would be similar to Fig. 3.3 with a second thin metal sheet with the same orientation slightly downstream from the first. The intention is that the second

new sheet also creates upward propagating OTR whilst reflecting upwards the forward propagating radiation from the first sheet. The two signals would interfere and a resultant interference pattern would be detected by the detector above. The characteristics of the interference pattern, such as spacing and visibility provide extra information on the beam, particularly the x and y angular spread, or divergence. This allows one to gain insight into the transverse phase space of the beam and careful analysis of the interference pattern allows for the reconstruction of the emittance of the beam. OTR and OTRI are typically used in linear machines and transport lines due to repeated loss and beam degradation as it passes through the thin metal sheet many times in a circular machine.

3.2.5 Beam Scraping

Beam scraping allows one to probe the transverse phase space of the beam by either moving a scraper blade transversally into the path of the beam, or creating a local orbit bump using steering magnets to progressively shift the beam into a fixed position blade. An example of the latter is the BEAMSCOPE used on the PS Booster at CERN [90]. Since this approach is less conventional and the new algorithms were developed for the moving blade scheme, we focus here on that approach [91].

The movement of the scraper blades is slow in comparison to the beam's revolution frequency to ensure all particles with a maximum amplitude equal to, or greater than, the scraper's position are eliminated. As the beam is intercepted, the intensity of the subsequently generated secondary particle shower is measured as a function of the position of the scraper blade. By taking the intensity of this particle shower as an indicator for the intensity of the beam along the corresponding scraper position, the transverse phase space density for the direction of the scraper's movement can be obtained. An example of the resultant distribution may be seen in Fig. 3.4. The emittance and other useful information may then be inferred through analysis, for example; by estimating the 95% beam width as in the AD system (Section 5.4), or by making a fit to the data assuming a Gaussian beam profile.

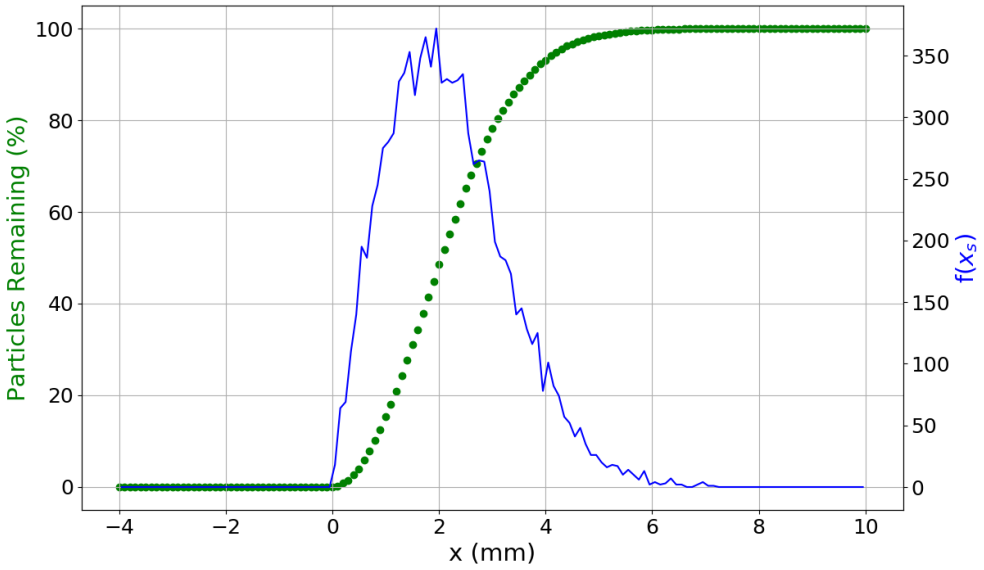

FIGURE 3.4: An example of a distribution that may be obtained via beam scraping. Beam intensity is represented by green dots. The scraper blade is coming from positive x. The data has been converted to a probability distribution function (PDF), $f(x_s)$, shown as a blue line.

Because of their high dynamic range, beam scrapers are able to investigate beam halos and low intensity long tails. They have been used to do so in various high energy machines such as the Tevatron, the Large Electron-Positron collider (LEP) and, more recently, the Large Hadron Collider (LHC) [92–94]. Additionally, scrapers may be held stationary at various aperture sizes in order to act as a more conventional collimator.

Although scraping destroys the beam being measured, it has the advantages of being simple to use and is suitable for low energy and low intensity machines. For these reasons it was chosen as the primary emittance and transverse profile diagnostic for the Antiproton Decelerator (AD) at CERN [95, 96]. After many years successful usage in the AD, a scraper system was also chosen for use in the ELENA ring [42].

3.3 About the Scraper System in ELENA

The main hardware comprising the scraping system in ELENA consists of two scraper blade windows at right angles to each other, each attached to a motorised arm, four Micro Channel Plate detectors (MCPs), two scintillator detectors, the stainless steel vacuum tank, and the associated support structures.

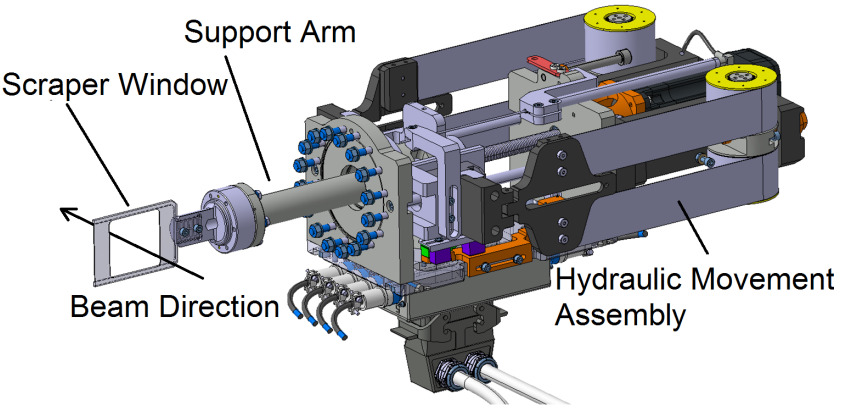

FIGURE 3.5: CAD model of the horizontal scraper window and movement system.

3.3.1 Scraper Arm

The scraping component which intercepts the beam is made from an aluminium plate with a 66 x 66 mm window in the centre as seen in Fig. 3.5. The window configuration allows one scraper arm to scrape from both sides, with the beam passing through the centre of the window at the start of scraping. During runs when scraping does not occur the aluminium window may be fully retracted to entirely clear the beamline aperture.

An actuation system is used to control scraper movement. The arms are guided by two linear ball bushings and powered by a brushless DC motor. In a similar manner to systems used for the LHC collimators two constant force springs ensure auto retraction of the blades in case of motor failure [97].

3.3.2 MCPs

The four MCPs are installed around the two scraper blades as seen in Fig. 3.6. Two are positioned upstream of the scraper blades and two downstream to ensure sufficient secondary detection regardless of the directions of both the primary beam and secondary showers. The MCPs are present to detect the secondary electrons generated when the primary beams of either H^- or protons interact with the scraper blades. Since the secondary electrons will not escape the vacuum chamber, the MCPs must be installed within its walls and so only the readout plates are visible from the outside.

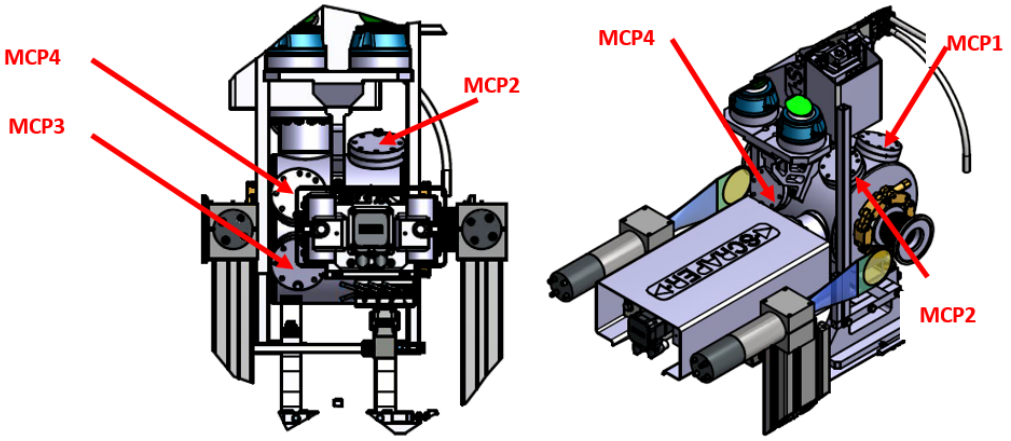

FIGURE 3.6: Positions of the MCP detectors in the scraper's vacuum tank. The scintillating detectors (scintillating surface in yellow) are also displayed on either side of the protective casing covering the actuation system.

The MCP's front face is made from a highly resistive material containing an array of micrometer ($\approx$10 μm) diameter scale tubes, microchannels, all offset by a small angle from normal to the surface. The plate is held at a high voltage, typically around 2.5 kV for ELENA, to allow the tubes to act as continuous-dynode electron multipliers.

Electrons enter the microchannels and due to the angle offset, they will impact the tube walls. When this happens more electrons are generated through secondary emission. The electron multiplication process continues along the tube until the electrons exit the opposite end and are collected on an anode, as a now amplified signal of the original electron. Because the electrons have cascaded, there are many of them but at low energy. Hence the anode is held at high positive voltage,

around 3 kV for the ELENA MCPs, specifically. The amplified signal is recorded as a function of time and correlated with the scraper position readout, giving beam density as a function of position. Diagrams illustrating the equipment and processes are displayed in Fig. 3.7.

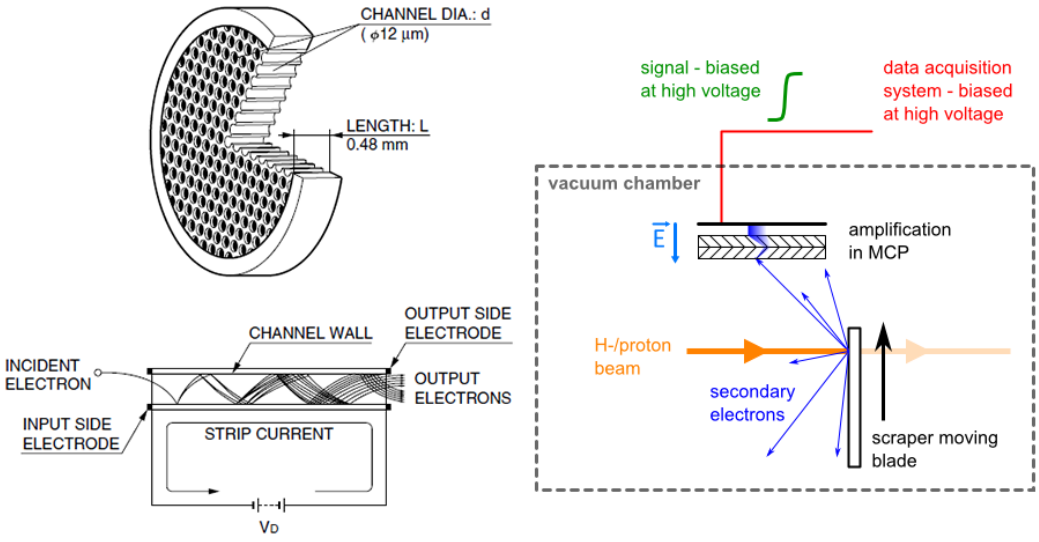

FIGURE 3.7: The diagrams on the left display a typical MCP front face and illustrate the cascading effect. On the right-hand side, a schematic diagram shows how the device is integrated into the scraper system, including the read-out. Image courtesy of Pierre Grandemange.

3.3.3 Scintillating Detectors

The concept and operation of scintillators for the detection of particles is well known. Typically a piece of scintillating material will serve as the detecting surface. As ionizing particles are incident their energy is absorbed and re-emitted as photons. The scintillating material is connected to an electronic light sensor, in ELENA it is a photomultiplier tube (PMT). The amplified signal is then read out from the PMT, and is proportional to the number of particles incident on the scintillating surface. The process is represented schematically Fig. 3.8.

In the case of ELENA the scintillating detectors are primarily used to detect the secondary pions generated from proton-antiproton annihilation within the scraper blade or on the beam-pipe walls. For this purpose, two circular shaped scintillating detectors were mounted on paddle shaped arms and placed both upstream and

downstream of the scraper vacuum tank to ensure forward- and back- scattered showers may be detected. The original design positions are displayed in Fig. 3.6.

During the design stage, GEANT4 tests were carried out to determine the flux of secondary particles. The results showed that for the planned scintillator positions and at the end of scraping, within the beam core, the count rate would be over 1 MHz. At this rate there would be a possibility of saturating the PMTs so the diameter of the circular scintillating surfaces was reduced from the nominal 100 mm to 80 mm. The signal was still shown to be sufficient after installation and testing so the exact positioning of the scintillators could then be adjusted for the mechanical convenience of other equipment. The upstream scintillator was adjusted from its design position to underneath the actuator system's protective casing. The readout end of the PMT can be seen highlighted by a white circle in Fig. 3.8 to give an indication of its current position.

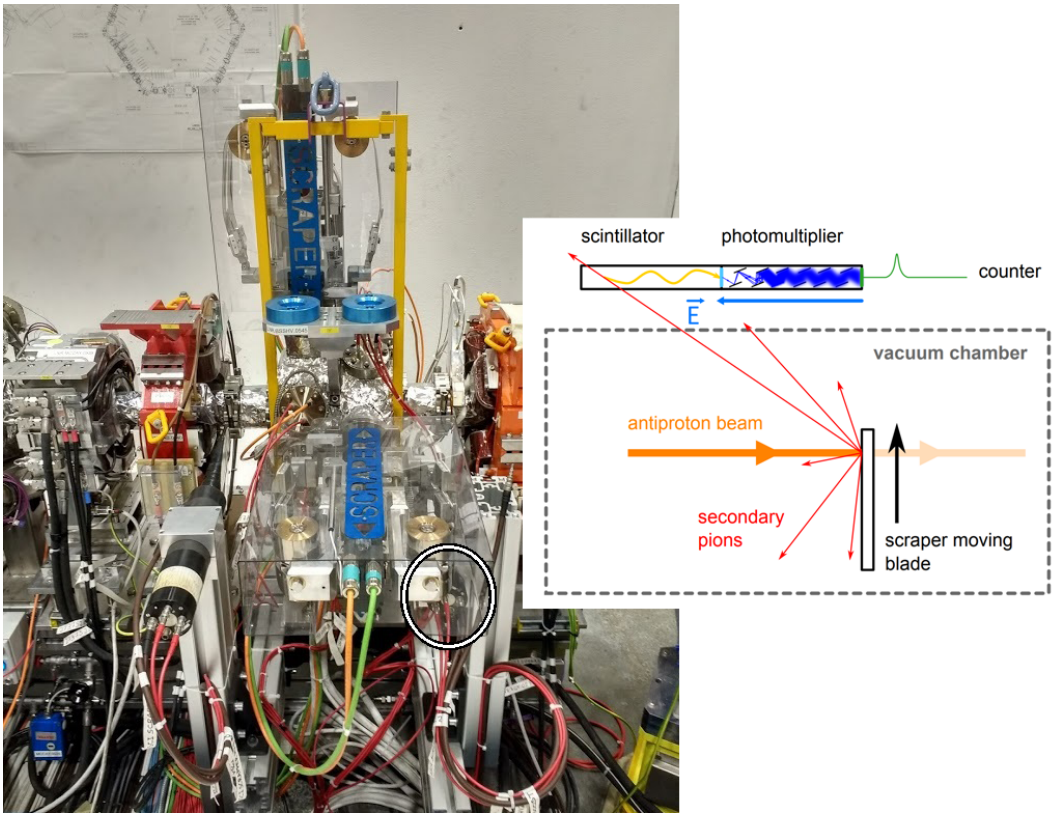

FIGURE 3.8: A photograph taken in May 2018 showing the full scraper assembly, with a white circle highlighting the position adjusted scintillator. On the right a schematic diagram (courtesy of Pierre Grandemange) illustrates the detection process in the context of the scraper.

3.3.4 Scraper Position

The scraper is positioned in Section 5 of the ELENA lattice. Table 3.1 shows the optics at the scraper's position for the various configurations considered. In the original design it was positioned closer to the centre of the section, with transverse beta function and dispersion listed as configuration C1 in the table. The ratio of the horizontal beta function against horizontal dispersion gives a measure of the impact longitudinal momentum spread will have on the scraped beam profile. For example, in configuration C1 the ratio is relatively low, with lower β_x giving horizontally thin beams and higher D_x allowing the momentum spread to contribute more to the horizontal displacement, i.e. smearing, of particles.

TABLE 3.1: Optics parameters at the position of the scraper for 4 different configurations of the machine. C1: Original layout. C2: Original layout quadrupoles with adjusted for tune. C3: Predicted optics at new scraper position. C4: Values measured in the machine.

Configuration	C1	C2	C3	C4
β_y (m)	2.92	3.00	2.70	2.97
β_x (m)	0.664	0.688	3.48	3.21
D_x (m)	1.18	1.292	0.87	1.38
β_x/D_x	0.492	0.533	4	2.33
s (m)	22.56	22.56	23.44	23.44

During the simulation process, the optics of the machine were adjusted to give the machine a more stable tune and the resultant configuration is listed as configuration C2 in the table. A discussion of the adjustment may be found in the simulations chapter, Section 5.3.1. The section also contains plots showing the simulated optics of the ring for configurations C1 and C2.

To reduce the impact of the momentum spread, the design scraper position was moved 88 cm upstream to a region with values calculated and listed as C3 in the table. The scraper was installed in this position, as seen in Fig. 3.9. The new ratio allows the beam to be wider at the scraper whilst the distribution is less affected by the momentum spread.

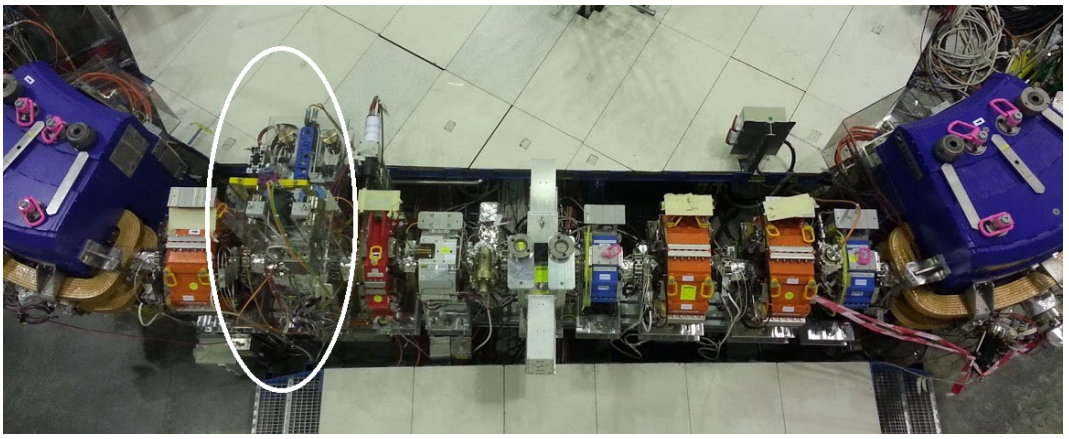

FIGURE 3.9: A photograph showing the scraper positioned in section 5 of the ELENA ring. November 2017.

As well as the change in position, the configuration of the optics has changed several times during commissioning to account for various factors, such as adjustments in the injection line optics and further tune adjustments. The most recent available lattice parameters at the position of the scraper were estimated based on the strengths of optical lattice elements around the ring. Figure 3.10 shows a screenshot taken in the ELENA control room during commissioning with a plot of the calculated optics. The scraper parameters are listed in Table 3.1 as C4. For the scraper simulations presented later, both configurations C2 and C4 were used, primarily to allow for comparisons between high and low β_x/D_x ratios. Further details and discussion of this may be found in the simulations chapter, Section 5.3.1.

3.3.5 Longitudinal Momentum Spread Measurement

The longitudinal momentum spread may be measured using the set of 20 BPMs installed around the ELENA ring. The signals detected for a coasting beam may be summed around the ring, making corrections for time of flight between pickups and allowing for the data to be analysed as a single Schottky pickup measurement. The signal may then undergo a fast Fourier transform (FFT) resulting in a spectral density distribution, with Schottky peaks at harmonic frequencies. Averaging to account for the 20 BPMs, an estimate for the longitudinal momentum spread may

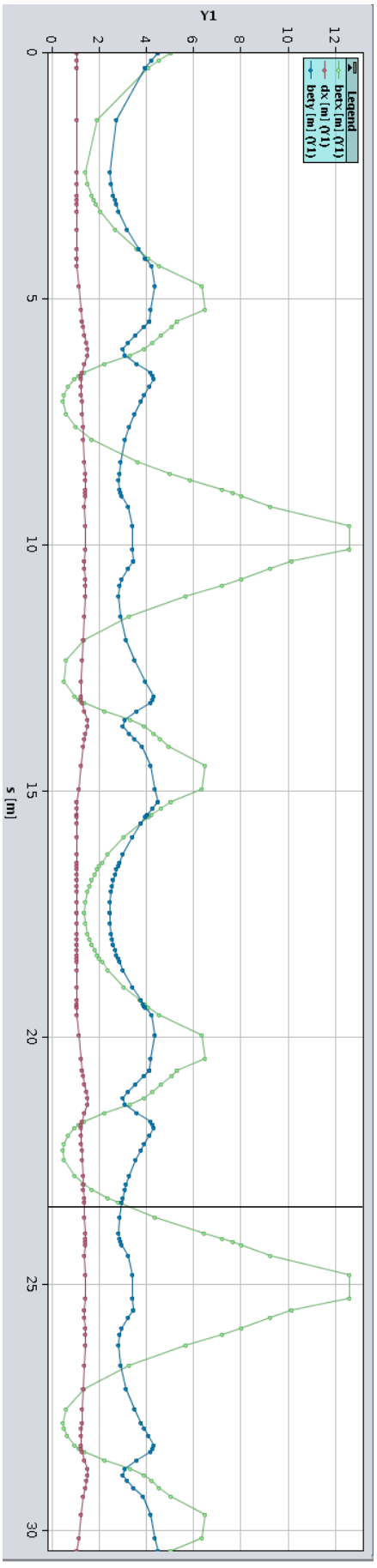

FIGURE 3.10: Optics calculated from ELENA field strengths with a vertical black line marking the position of the scraper. β_x is marked by a green line, β_y a blue line and D_x with a red line.

be made by measuring the RMS of a frequency peak in the data, Δf_h, of known harmonic number, h:

$$\sigma_\delta = -\frac{1}{\eta}\frac{\Delta f_h}{f_h} \tag{3.9}$$

where η is the frequency dispersion or phase slip factor and f_h is the centre frequency of the peak [98]. In ELENA the system will be able to measure up to $h = 111$, and where possible a higher harmonic will be selected to allow for more frequent measurements, since the required acquisition time is inversely proportional to h [99].

3.4 Challenges Presented for ELENA

Scraping systems and other similar emittance diagnostic devices are typically placed in regions of zero dispersion to simplify measurements. As explained in Section 2.2.4, the phase space distribution of a beam is affected by the longitudinal momentum spread proportionally to the dispersion at any given location in the machine. In the AD, for example, the scraper system is placed in a dispersion free region and hence the impact of large momentum spreads on the measurement is zero or negligible. In ELENA there is no region with zero dispersion so this effect is unavoidable.

The impact of the effect on the transverse phase space depends on a combination of the ratio of transverse beta function with dispersion at the position of the scraper and the longitudinal momentum spread of the beam. If the dispersion is large and beta small, with a higher momentum spread, the transverse phase space could be significantly affected. This could be to such a degree that an uncorrected measurement of the RMS beam width could translate to an incorrect emittance value by several factors. This is explored in Section 5.4 when using the basic AD algorithm.

During machine operation the beam will undergo intra-beam scattering (IBS). Since the growth rates introduced by IBS are inversely proportional to the fourth

power of the Lorentz factor, γ_l^4, they are much more significant for lower energy machines such as the AD or ELENA. Depending on growth rates and scraper speed, the beam may experience a change in emittance during the scraping process. This possibility is something to be considered when designing the system. Additionally, corresponding scraper measurements for the two scan algorithm should be performed at the exact same time during the cycle to minimise the impact of IBS growth on the emittance values. It may be possible to measure the magnitude and rate of this effect by scraping at different times during the cycle and comparing emittance values.

In order to counter the diffusion effects mentioned above, an electron cooler will be employed in ELENA. As shown in Section 2.3.3, the effects of the electron cooler are expected to give the beam a non-Gaussian beam distribution. Simulations show that the beam could be described as a bi-Gaussian distribution, however depending on the electron cooler field distribution and perhaps due to unforeseen effects, the beam profile could take any shape. Using Gas Electron Multiplier (GEM) beam profile monitors [100, 101], beams in the AD have been shown to take on non-Gaussian transverse beam distributions, particularly with dense cores and long tails. This is attributed to the beam cooling process which, in the AD, is a mixture of stochastic and electron cooling.

These non-Gaussian beam distributions will cause problems for the scraping process in ELENA as typically the algorithms are based on the assumption of Gaussian beams. Similarly to the dispersion consideration, the impact of this effect when using the Gaussian AD method is investigated in Section 5.4. It is expected that the beam will appear more non-Gaussian than the AD beam due to its relatively low energy. A-priori estimates of a function which best describes the beam distribution would have to be made, or an algorithm developed to reconstruct the emittance for arbitrary beam distributions. Another complication due to electron cooling may arise from a transversally non-uniform field seen by the electrons. Electrons at higher amplitude could take larger velocities which could lead to an emittance-momentum offset correlation and further pollute the shape of the beam distribution. The magnitude of this property of the electron

beam is uncertain and may later be indirectly measured through observations of the antiproton beam.

An additional source of error could arise from the transmission of antiprotons through the scraper blade itself. Since the horizontal speed of the scraper blade will be very low most particles will come into contact with the very tip of the blade. There is a possibility that in this region antiprotons may scatter from the side of the scraper blade and continue circulating in the machine causing an incorrect measurement of the phase space density. Although the impact of this effect is minor, the possibility may be investigated using simulations.

Several sources of error have been described in this section. The impact of some is known more precisely than others but there is enough information to determine that standard scraping algorithms will not be sufficient. The main two factors that are expected to have the biggest impact are non-zero dispersion and non-Gaussian beam profiles. Separately these problems may be dealt with using slightly modified traditional methods however in combination the beam quickly becomes complicated and difficult to diagnose. Assuming that some of the additional potential complications have a significant impact on the scraping profile too, it is of utmost importance that these main two effects be dealt with effectively first. In the next chapter two new algorithms are introduced, one for scraping a Gaussian beam in a region on non-zero dispersion, and the second to perform the same task for non-Gaussian beams.

Chapter 4

Algorithms

4.1 Introduction

The purpose of this chapter is to introduce the new emittance reconstruction algorithms developed for ELENA [53]. The focus is on the derivation of the algorithms from theory including introducing some additional quantities that may be estimated using them.

An algorithm for accurately reconstructing the transverse emittance and estimating with great accuracy the longitudinal momentum spread of a Gaussian beam in a dispersive region has been developed. In addition to this, an algorithm capable of reconstructing the emittance and other useful quantities of a beam of arbitrary profile shape, also in a dispersive region will be introduced. Although developed for the specific case of ELENA, the algorithms are presented for use in other storage rings which might include similar conditions and challenges.

4.2 New Algorithms

Due to the numerous different definitions for emittance, it should be clearly stated that these algorithms are for the purpose of determining the RMS geometric transverse emittance. It is introduced in Section 2.2.5, but for convenience and clarity,

here it may be defined statistically as:

$$\epsilon_{rms} = \langle J \rangle \equiv \frac{1}{2}\langle A^2 \rangle, \tag{4.1}$$

where A is the amplitude of the particles in phase space, and J is the action variable, $(\gamma x^2 + 2\alpha x x' + \beta x'^2)/2$.

4.2.1 Basis of Derivations

To establish the theory necessary to develop scraping algorithms suitable for the challenges presented in Section 3.4, we begin by considering a scraper blade moving slowly into the beam from the $+x$ direction as seen in Fig 4.1. Considering the revolution frequency of the beam, we may assume the scraper blades travel into the beam at a low enough velocity that particles with a maximum amplitude, A_{max}, equal to scraper's position, x_s, are lost immediately. This leads to the condition that the beam intensity is equal to the fraction of the beam within the aperture defined by the scraper's position.

A phase space plot of the traces of three particles in a region with positive dispersion[1], D, can be seen in Fig 4.1. The particles have different emittances but all have the same maximum oscillation amplitude, equal to x_s. Assuming they all have the same closed orbit, x_0, we see how the dispersion shifts the phase space ellipses in x based on their momentum offsets, and why this would complicate the scraper measurement process.

We begin by considering a beam in normalised phase space:

$$X_\beta = \frac{x_\beta}{\sqrt{\beta}}, \qquad X'_\beta = x'_\beta\sqrt{\beta} + \frac{x_\beta \alpha}{\sqrt{\beta}}, \tag{4.2}$$

where X_β and x_β are the normalised and non-normalised particle betatron positions respectively, X'_β and x'_β are the normalised and non-normalised divergence angles respectively, and β and α are the Twiss parameters in the corresponding transverse plane. Combining these quantities gives the normalised amplitude in phase space, which may also be described in terms of the action variable, J:

[1]Here D represents non-zero dispersion in the plane being considered, without the x subscript for generality.

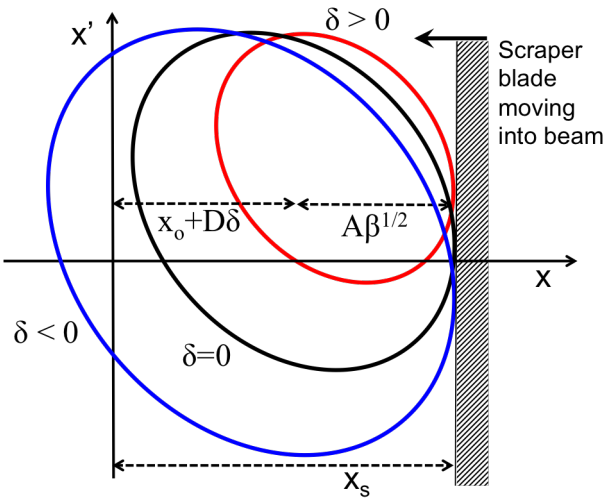

FIGURE 4.1: Representation of the phase space traces of three particles passing a scraper. The ellipses represent particles with negative momentum offset (blue), zero momentum offset (black) and with positive momentum offset (red).

$$A = \sqrt{X_\beta^2 + X_\beta'^2} \equiv \sqrt{2J} = \sqrt{x_\beta^2\gamma + 2x_\beta x'_\beta\alpha + x_\beta'^2\beta}, \tag{4.3}$$

where $\gamma = (1+\alpha^2)/\beta$.

If the scraper is located within a dispersive region, and the beam has a relative momentum offset, $\delta = \Delta p/p$, the total position and angle may be described in terms of the betatron and dispersive contributions:

$$x = x_0 + x_\beta + D\delta \tag{4.4}$$

$$x' = x'_0 + x'_\beta + D'\delta \tag{4.5}$$

where $D' = \mathrm{d}D/\mathrm{d}s$, x_0 and x'_0 are the contributions due to the closed orbit offset.

Particles whose momentum dependent closed orbits are greater than the position of the scraper, $x_0 + \delta D \geq x_s$, are lost at the scraper. Hence, the momentum spread acceptance of a beam is given by:

$$\delta_{max} = \frac{(x_s - x_0)}{D}. \tag{4.6}$$

When $\delta < \delta_{max}$ the transverse acceptance of the beam is given by the difference between the scraper position and the momentum dependent closed orbit, $x_s - (x_0 + D\delta)$. This effect can be seen in Fig 4.1 where particles with a lower and higher

momentum offset than on momentum particles have larger and smaller transverse acceptances, respectively. Therefore, if a horizontal scraper blade is coming from the positive x-axis and in a determined measurement stage it is at position x_s, the condition for a particle to stay in the machine is:

$$x_0 + \delta D + \beta^{1/2} A < x_s, \tag{4.7}$$

We may summarise the above in terms of the maximum oscillation amplitude as a function of the momentum offset:

$$A_{max} = \begin{cases} \frac{x_s - x_0 - D\delta}{\sqrt{\beta}} & \text{for } \delta \leq \delta_{\max}, \\ 0 & \text{otherwise.} \end{cases} \tag{4.8}$$

For clarity, these limits are represented in longitudinal and transverse phase space in Fig. 4.2.

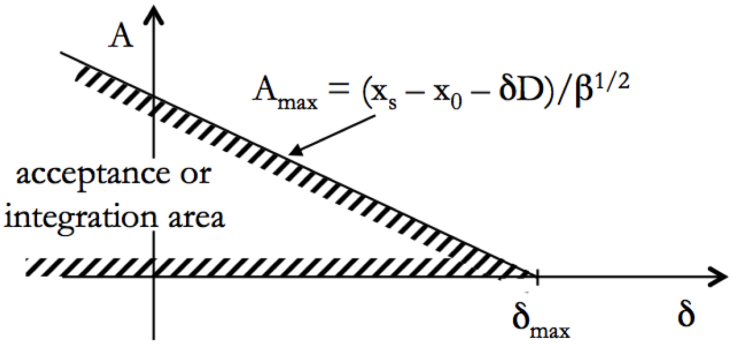

FIGURE 4.2: Representation of acceptance for particles in the presence of a scraper blade. Image courtesy of Christian Carli.

Generally, a beam may be characterised as a distribution density:

$$\rho(\delta, A) = \rho_p(\delta)\rho_T(\delta, A) \tag{4.9}$$

where $\rho_p(\delta)$ is the synchrotron amplitude distribution as a function of the relative momentum offset, and $\rho_T(\delta, A)$ is the transverse amplitude distribution, which depends on both A and δ as described above.

The phase space density may be normalised as follows:

$$\int_{-\infty}^{+\infty} \rho_p(\delta)\ \mathrm{d}\delta \ = \ 1, \tag{4.10}$$

$$\int_{0}^{+\infty} 2\pi A \rho_{\mathrm{T}}\left(\delta, A\right)\ \mathrm{d}A \ = \ 1. \tag{4.11}$$

For the scraper measurement a coasting beam with no coupling between the two transverse planes is assumed. The measurements will typically take place between deceleration ramps, and in order to see and account for longitudinal momentum spread effects they must be carried out with the RF systems off.

The remaining fraction of the beam with dispersion $D > 0$ may be calculated using the acceptance limits described in Eq. 4.8:

$$F_+(x_s) = \frac{N_+(x_s)}{N_0} = \int_{-\infty}^{\delta_{max}} \rho_p(\delta)\ \mathrm{d}\delta \int_0^{A_{max}} \ 2\pi\ A\ \rho_{\mathrm{T}}(\delta, A)\ \mathrm{d}A, \tag{4.12}$$

where $N_+(x_s)$ is the number of particles left in the machine when the scraper is at x_s and N_0 is the number of particles in the machine before scraping. Similarly, if the scraper is coming from the negative x-axis, we obtain:

$$F_-(x_s) = \frac{N_-(x_s)}{N_0} = \int_{\delta_{max}}^{+\infty} \rho_p(\delta)\ \mathrm{d}\delta \int_0^{-A_{max}} \ 2\pi\ A\ \rho_{\mathrm{T}}(\delta, A)\ \mathrm{d}A. \tag{4.13}$$

The integrals above give the cumulative distribution functions (CDFs) of the beam loss. Taking the derivatives of these quantities gives the corresponding probability density functions (PDFs) projected along x_s:

$$f_\pm = \pm\frac{\mathrm{d}F_\pm(x_s)}{\mathrm{d}x_s}. \tag{4.14}$$

To do this we begin by making the substitution:

$$n(\delta, x_s) = \begin{cases} \rho_p(\delta) \int_0^{A_{max}} 2\pi A \rho_{\mathrm{T}}(\delta, A)\ \mathrm{d}A & \text{for } \delta \leq \delta_{max}, \\ 0 & \text{for } \delta > \delta_{max}, \end{cases}$$

which gives:

$$F_+ = \int_{-\infty}^{\delta_{max}} \ n(\delta, x_s)\ \mathrm{d}\delta. \tag{4.15}$$

The density probability function f_+ defined as the derivative of F_+ with respect to x_s becomes:

$$f_+(x_s) = \int_{-\infty}^{\frac{x_s - x_0}{D}} \rho_p(\delta) 2\pi \frac{x_s - D\delta - x_0}{\beta} \times \rho_{\mathrm{T}} \left(\delta, \frac{x_s - D\delta - x_0}{\sqrt{\beta}} \right) \mathrm{d}\delta. \tag{4.16}$$

Similarly we may calculate the function for a scraper moving into the beam from the negative x direction:

$$f_-(x_s) = \int_{\frac{x_s - x_0}{D}}^{+\infty} \rho_p(\delta) 2\pi \frac{D\delta + x_0 - x_s}{\beta} \times \rho_{\mathrm{T}} \left(\delta, \frac{D\delta + x_0 - x_s}{\sqrt{\beta}} \right) \mathrm{d}\delta. \tag{4.17}$$

An example of a CDF and its corresponding PDF for a Gaussian distribution are shown in Fig. 4.3.

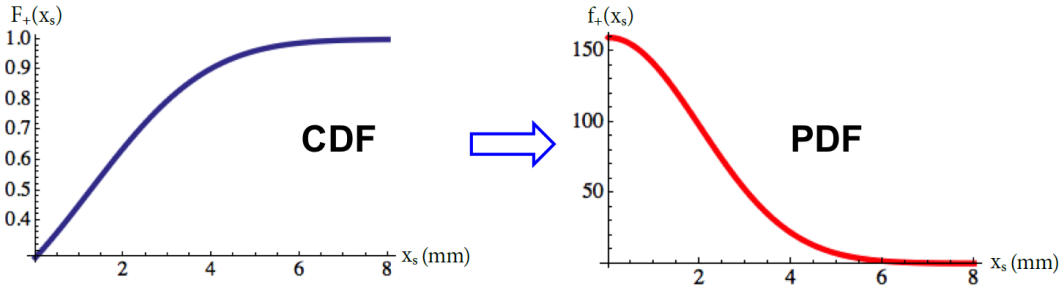

FIGURE 4.3: Example of a CDF and PDF for a Gaussian distribution.

4.3 Gaussian Case Algorithm

We may calculate $F_\pm$ and $f_\pm$ for the specific case that the beam passing the scraper in a dispersive region has a Gaussian distribution. This would be useful to test the validity of our simulations since Gaussian is the most simple beam profile to generate and evaluate, and the method only requires scraping once per measurement. Additionally, this approach gives an estimation for the longitudinal momentum spread of the beam, which is not possible once we also begin considering non-Gaussian beam distributions. In practice in ELENA, if the beam could be approximated as Gaussian this method could be useful as a quick check of beam quality and to provide a rough estimation of the longitudinal momentum spread.

We may begin by describing the beam as a combination of densities (Eq. 4.9):

$$\rho_p(\delta) = \frac{1}{\sqrt{2\pi}\sigma_\delta} e^{-\frac{\delta^2}{2\sigma_\delta^2}} \quad \text{and} \quad \rho_{\mathrm{T}}(\delta, A) = \frac{1}{2\pi\epsilon_{\mathrm{rms}}} e^{-\frac{A^2}{2\epsilon_{\mathrm{rms}}}}, \tag{4.18}$$

where A is defined in Eq. 4.3, and the mean momentum offset is equal to zero, i.e. $\langle\delta\rangle = 0$. Substituting the densities, Eq. 4.18 into Eqs. 4.12 and 4.13, and solving the corresponding integrals, one obtains expressions for the Gaussian case CDFs:

$$\begin{aligned} F_\pm(x_s) &= \frac{1}{2}\left[1 \pm \mathrm{erf}\left(\frac{A_0}{\sqrt{2\epsilon_{\mathrm{rms}}}|d|}\right)\right] \\ &- \frac{1}{2\sqrt{1+d^2}} e^{-\frac{A_0^2}{2(1+d^2)\epsilon_{\mathrm{rms}}}} \left[1 \pm \mathrm{erf}\left(\frac{A_0}{\sqrt{2\epsilon_{\mathrm{rms}}}|d|\sqrt{1+d^2}}\right)\right], \end{aligned} \tag{4.19}$$

where $d = D\sigma_\delta/\sqrt{\beta\epsilon_{\mathrm{rms}}}$, $A_0 = (x_s - x_0)/\sqrt{\beta}$ and $\mathrm{erf}(x) = \frac{2}{\sqrt{\pi}} \int_0^x e^{-t^2}\, \mathrm{d}t$ is the error function. Note that the absolute value $|d|$ in the argument of the error function arises from the fact that changing the sign of the dispersion does not alter the result since zero mean momentum offset allows one to exchange particles with positive and negative momentum offset. Figure 4.4 shows an example of how the expression changes for different values of d due to different momentum spreads.

This function forms the basis of the Gaussian only algorithm and may be used by performing a fit to the cumulative losses in the scraper data, taking the emittance as a variable. Additionally, d may be taken as a second variable during fitting to allow for an estimation of the momentum spread, and the term x_0 may also be estimated simultaneously.

By differentiating these functions with respect to x_s, as in Eq. 4.14, we may obtain the corresponding PDFs:

$$\begin{aligned} f_\pm(x_s) &= \frac{d}{\sqrt{2\pi\beta\epsilon_{\mathrm{rms}}}(1+d^2)} e^{-\frac{A_0^2}{2\epsilon_{\mathrm{rms}} d^2}} \\ &\pm \frac{A_0 e^{-\frac{A_0^2}{2(1+d^2)\epsilon_{\mathrm{rms}}}}}{2(1+d^2)^{3/2}\sqrt{\beta\epsilon_{\mathrm{rms}}}} \left[1 \pm \mathrm{erf}\left(\frac{A_0}{\sqrt{2\epsilon_{\mathrm{rms}}}|d|\sqrt{1+d^2}}\right)\right]. \end{aligned} \tag{4.20}$$

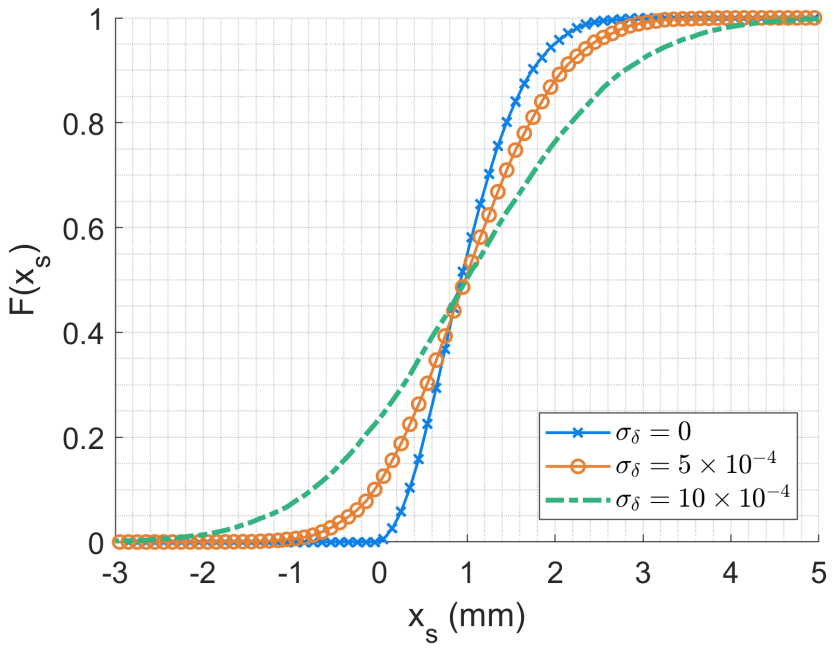

FIGURE 4.4: Effect of longitudinal momentum spread on the CDF obtained from scraping.

4.4 General Case Algorithm

In the case that a Gaussian approximation is not possible and the scraper blades remain in a position of non-zero dispersion, we must develop a method for RMS emittance reconstruction regardless of the beam distribution.

4.4.1 Algorithm Derivation

We begin by expressing the second moment of $(x_s - x_r)$ in terms of density functions $f_{\pm}(x_s)$, Eqs. 4.16 and 4.17, where x_r has been introduced as an estimate for the central orbit, x_0. Considering the cases of scraper blades coming from the positive and negative x directions simultaneously:

$$\langle (x_s - x_r)^2 \rangle_{\pm} = \int_{-\infty}^{+\infty} (x_s - x_r)^2 f_{\pm}(x_s)\, \mathrm{d}x_s, \tag{4.21}$$

where $\langle ... \rangle$ denotes the expectation value of the quantity in the parenthesis.

Using the following;

$$\int_{-\infty}^{+\infty} x_s^2 f_\pm(x_s)\ \mathrm{d}x_s = \bar{x}_\pm^2 + {\sigma_\pm}^2, \tag{4.22}$$

$$\int_{-\infty}^{+\infty} x_s f_\pm(x_s)\ \mathrm{d}x_s = \bar{x}_\pm, \tag{4.23}$$

$$\int_{-\infty}^{+\infty} f_\pm(x_s)\ \mathrm{d}x_s = 1, \tag{4.24}$$

where $\bar{x}_\pm$ is the mean value of the measured distribution and $\sigma_\pm^2$ is the variance, we me rewrite this quantity as:

$$\langle (x_s - x_r)^2 \rangle_\pm = \bar{x}_\pm^2 + \sigma_\pm^2 - 2\bar{x}_\pm x_r + x_r^2. \tag{4.25}$$

Simultaneously we may expand the left hand side and use the substitution $x_{s\pm} = x_0 + \delta D \pm \sqrt{\beta} A$ to obtain:

$$\begin{aligned} \langle (x_s - x_r)^2 \rangle_\pm &= \langle ((x_0 - x_r) + \delta D \pm \sqrt{\beta} A)^2 \rangle_\pm \\ &= (x_0 - x_r)^2 + 2(x_0 - x_r)\langle\delta\rangle D \pm 2(x_0 - x_r)\sqrt{\beta}\langle A\rangle \\ &\quad + \langle\delta^2\rangle D^2 \pm 2D\sqrt{\beta}\langle\delta A\rangle + \beta\langle A^2\rangle. \end{aligned} \tag{4.26}$$

Considering the definitions $\bar{\delta} = \langle\delta\rangle$, $\bar{A} = \langle A\rangle$, $\sigma_\delta^2 = \langle(\delta - \bar{\delta})^2\rangle$, the statistical definition of the geometric transverse emittance shown in Eq. 4.1, and the usual normalisations of phase space density, Eqs. 4.10 & 4.11, we may rewrite Eq. 4.26:

$$\begin{aligned} \langle (x_s - x_r)^2 \rangle_\pm &= (x_0 - x_r)^2 + D^2(\bar{\delta}^2 + {\sigma_\delta}^2) + 2\beta\epsilon_{rms} + 2(x_0 - x_r)D\bar{\delta} \\ &\quad \pm 2(x_0 - x_r)\sqrt{\beta}\bar{A} \pm 2D\sqrt{\beta}\langle\delta A\rangle. \end{aligned} \tag{4.27}$$

These expressions allow us to put $\langle (x_s - x_r)^2 \rangle_\pm$ in terms of the RMS transverse emittance ϵ_{rms} and the dispersive contribution $D\sigma_\delta$. However, the additional terms $\langle A\rangle$ and $\langle A\delta\rangle$ make the evaluation difficult even for a known closed orbit centre x_0. We can perform a combination of measurements from both the positive and negative x_s-axis in order to solve this problem. Summing terms for positive and

negative scraper scans in Eqs. 4.25 and 4.27 we may write:

$$\begin{aligned} &\langle (x_s - x_r)^2 \rangle_+ \\ +\langle (x_s - x_r)^2 \rangle_- &= 2(x_0 - x_r)^2 + 2D^2(\bar{\delta}^2 + {\sigma_\delta}^2) + 4\beta\epsilon_{rms} + 4(x_0 - x_r)D\bar{\delta} \\ &= \bar{x}_+^2 + \bar{x}_-^2 + {\sigma_+}^2 + {\sigma_-}^2 - 2x_r(\bar{x}_+ + \bar{x}_-) + 2x_r^2. \end{aligned} \tag{4.28}$$

Further transformation yields:

$$\begin{aligned} 2 \quad & (x_0 + D\bar{\delta} - x_r)^2 + 2D^2\sigma_\delta^2 + 4\beta\epsilon_{rms} = \\ 2 \quad & (\frac{\bar{x}_+ + \bar{x}_-}{2} - x_r)^2 + \frac{1}{2}(\bar{x}_+ - \bar{x}_-)^2 + {\sigma_+}^2 + {\sigma_-}^2. \end{aligned} \tag{4.29}$$

Given that the momentum depended closed orbit is equal to the mean particle position,

$$x_0 + D\bar{\delta} = \frac{(\bar{x}_+ + \bar{x}_-)}{2}, \tag{4.30}$$

we may rearrange equation Eq. 4.29 for the emittance:

$$\epsilon_{rms} = \frac{1}{4\beta}\left[\sigma_+^2 + \sigma_-^2 + \frac{(\bar{x}_+ - \bar{x}_-)^2}{2}\right] - \frac{D^2\sigma_\delta^2}{2\beta}, \tag{4.31}$$

which contains only values that can be obtained from the scraper data or otherwise measured and estimated. This equation forms the basis of the algorithm.

The contribution from longitudinal momentum spread in Eq. 4.31 can clearly be seen as the rightmost dispersive dependent term, and may be set to zero when scraping in the vertical plane, where typically $D = 0$.

Calculating the emittance using this result requires two separate scraper scans from opposing directions, e.g. positive and negative x. In this case the machine must cycle twice, so beam stability between shots is very important. The impact of beam stability, as well as other challenges and sources of error, are investigated in the following chapter.

4.4.2 Additional Quantities

Because we perform scraping from both sides it is possible to extract further information on the beam by comparing the difference in the two results. For example, Eq. 4.30 may be used to obtain an estimate for the mean amplitude of the particles.

Performing a subtraction, as opposed to the addition in Eq. 4.28, we find:

$$\begin{aligned} &\langle (x_s - x_r)^2 \rangle_+ \\ -&\langle (x_s - x_r)^2 \rangle_- &&= 4(x_0 - x_r)\sqrt{\beta}\bar{A} + 4D\sqrt{\beta}\langle \delta A \rangle && (4.32) \\ &&&= \bar{x}_+^2 - \bar{x}_-^2 + {\sigma_+}^2 - {\sigma_-}^2 - 2x_r(\bar{x}_+ - \bar{x}_-), && (4.33) \end{aligned}$$

which may be rearranged to make it possible to compare the coefficients of x_r,

$$\begin{aligned} &4(x_0 + D\bar{\delta})\sqrt{\beta}\bar{A} + 4D\sqrt{\beta}\langle (\delta - \bar{\delta})A \rangle - 4x_r\sqrt{\beta}\bar{A} \\ &\qquad = \bar{x}_+^2 - \bar{x}_-^2 + {\sigma_+}^2 - {\sigma_-}^2 - 2x_r(\bar{x}_+ - \bar{x}_-), && (4.34) \end{aligned}$$

leading to an estimation for the mean amplitude using measurable quantities:

$$\bar{A} = \frac{\bar{x}_+ - \bar{x}_-}{2\sqrt{\beta}}. \tag{4.35}$$

We may use this result combined with Eq. 4.30 to further rearrange Eq. 4.34 allowing us to measure a quantity which would describe the magnitude of the correlation between momentum spread and the maximum amplitude of the particles:

$$\langle (\delta - \bar{\delta})A \rangle = \frac{{\sigma^2}_+ - {\sigma^2}_-}{4D\sqrt{\beta}}. \tag{4.36}$$

This quantity will be referred to as the emittance-momentum spread correlation coefficient since it will later allow us to investigate such a correlation brought about by the effects of the electron cooler.

4.4.3 Data Analysis

Assuming that the signal received from the detectors is given as cumulative loses and transformed to $F_{\pm}(x_s)$, as for the AD and ELENA scintillators, then differentiation must be performed to obtain the beam size variance, $\sigma_{\pm}^2$, and the mean x position of the intercepted particles, $\bar{x}_{\pm}$, required by the algorithm. Since the algorithm is designed for non-Gaussian beams, it is unlikely that an expression for the data will be known and hence symbolic differentiation will not be possible. Two alternate methods are available for consideration: spline interpolation and simplified numerical approximations.

Comparisons of the methods may be found in Section 5.6.1. Here we present the simplified numerical method, which was found to be a sufficient approximation for these purposes, assuming a data acquisition rate of 400 Hz.

We may begin by assuming a set of CDF values, i.e. the tabulated function $F_{\pm}(x_s)$, with corresponding scraper positions, x_s, for every data point, i. Using finite difference approximations it is possible to get estimations for the tabulated PDF, $f_{\pm}(x_s)$, for all points, i:

$$f_{i,\pm} = \frac{F_{\pm,i} - F_{\pm,i+1}}{|x_{\pm,i} - x_{\pm,i+1}|}. \tag{4.37}$$

The following integral may be approximated by a midpoint Riemann sum:

$$\int_{-\infty}^{+\infty} f_{\pm}(x_s)\ \mathrm{d}x_s \approx \sum_{i=1}^{n} (f_{i,\pm}(|x_{\pm,i} - x_{\pm,i+1}|)), \tag{4.38}$$

where n is the number of entries in the data set, into which we may substitute Eq. 4.37 to provide a simple expression for use in the algorithm:

$$\int_{-\infty}^{+\infty} f_{\pm}(x_s)\ \mathrm{d}x_s \approx \sum_{i=1}^{n} (F_{\pm,i} - F_{\pm,i+1}). \tag{4.39}$$

This result may then be used to obtain an approximation for the distribution variance:

$$\sigma_{\pm}^2 = \int_{-\infty}^{+\infty} f_{\pm}(x_s)(x_s - \bar{x}_{\pm})^2\ \mathrm{d}x_s \approx \sum_{i=1}^{n} (F_{\pm,i} - F_{\pm,i+1})(x_{\pm,i,mid} - \bar{x}_{\pm})^2, \tag{4.40}$$

where $x_{\pm,i,mid}$ is the midpoint between $x_{\pm,i}$ and $x_{\pm,i+1}$, and the value $\bar{x}_\pm$ is obtained using similar approximations for Eq. 4.23:

$$\bar{x}_\pm \approx \sum_{i=1}^{n} (F_{\pm,i} - F_{\pm,i+1}) x_{\pm,i,mid}. \tag{4.41}$$

It would also be possible to use trapezoidal Riemann sums in order to increase the accuracy of the algorithm, however with the relatively small step sizes used between measurement points it is not necessary to do so here.

4.5 Summary

The two new scraper algorithms have been introduced. One is capable of scraping a Gaussian beam in a region of non-zero dispersion, and the other under the same conditions but for an arbitrary beam profile distribution. The arbitrary distribution method requires two scraper measurements from opposing directions. In the next chapter, the algorithms are verified through the use of simulations. Additionally, several sources of error, some of which were discussed in Section 3.4, are investigated through simulations and error tolerances are established.

Chapter 5

Scraper Simulations

5.1 Introduction

The primary goal of this chapter is to use simulations to test the emittance reconstruction algorithms derived in the previous chapter. The various methods used in performing the simulations are presented in detail such that the results may be reproduced by the reader.

The effects of systematic errors on the accuracy of the non-Gaussian algorithm are investigated, and the use of the algorithm to determine additional quantities such as the emittance-momentum spread correlation is performed. The chapter begins with an investigation into the transmission of particles through and out the side of the aluminium scraper blade, to ensure later assumptions in simulations are adequate.

5.2 Transmission Through Scraper Blade

An investigation into the stopping power of the scraper blade was performed. Particle physics Monte Carlo simulation package FLUKA [102, 103] was used to track particles incident on the scraper blade.

In an unpublished CERN note regarding the material choice for an AD scraper blade renovation (2016), an investigation is performed using GEANT4 for the several different beam energy plateaus in the AD cycle. The report includes results

for the lowest energy case, 5.3 MeV, which is the injection energy for ELENA. This energy plateau will form the basis of these studies since it is the most pessimistic case in terms of scraper blade transmission.

In the report, 10,000 antiprotons are incident on a wide bulk block of material, to allow no particles to escape the edges. For 10,000 cases at 5.3 MeV in GEANT4 the mean penetration depth for the antiprotons into a block of aluminium, the ELENA scraper blade material, was given as 0.22 mm. All other materials tested, with the exception of titanium, had smaller penetration depths at this energy. To benchmark simulations, the first FLUKA simulation investigated the penetration depth of 5,000 antiprotons into a bulk block of aluminium. Fig. 5.1 shows the results, where a clear agreement with the GEANT4 simulation result can be seen. Analysis of the data gives a value for the mean as 0.22 mm which further confirms the GEANT4 and FLUKA packages used are in agreement. The standard deviation of this value is 8.40 μm, leading to the assumption that no antiprotons will make it entirely through the bulk of the 1 mm aluminium scraper blade for any ELENA energy.

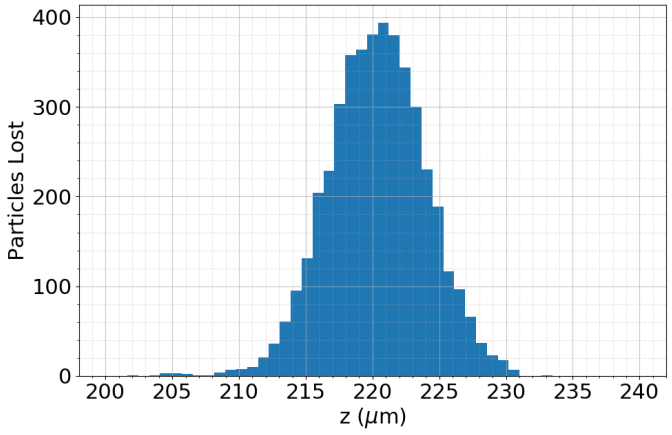

FIGURE 5.1: Penetration depth for antiprotons in aluminium, as simulated in FLUKA.

5.2.1 Side Scattered Particles

The next stage was to investigate the likelihood that antiprotons would enter the bulk of the scraper blade but escape the edge and continue in the machine or

annihilate downstream and hence not be detected. The simulations were carried out using a very simple geometrical configuration with positive z defined as the direction of beam propagation. The scraper element is a rectangular (10 mm x 10 mm) sheet of aluminium, with a thickness of 1 mm in the z direction. It is placed such that its front face is at z=0 mm, and offset into positive x to align its edge with $x = 0$ mm.

Non-divergent rectangular antiproton beams were chosen to determine the significance of a particle's x position at impact on the likelihood and nature of transmission through the scraper. The beams were run from z = -50 mm and were also aligned such that their edge was at $x = 0$ mm and they extended into positive x, like the scraper blade. Behind the scraper is a large cuboid detector, positioned such that all transmitted particles would be incident on its front face.

A beam of 5,000 particles and energy 100 keV was run to determine the transmission at lowest possible energy. To allow for maximum transmission (i.e. highest possible particle density at the edge of the scraper blade), the horizontal beam size was chosen to represent the smallest possible scraper movement during one revolution of the beam:

$$\Delta x_s = \frac{v_s}{f} \tag{5.1}$$

where v_s is the nominal velocity of the scraper, 40 mm/s, and f is the revolution frequency of the beam, in Hertz, calculated from its energy.

For 100 keV, $\Delta x_s = 277.7$ nm. Of 5,000 antiprotons incident within this range, zero were detected behind the scraper blade leading to the conclusion it is more than adequate at such low energies.

For the highest energy case of 5.3 MeV, $\Delta x_s = 38.3$ nm. Of 5,000 particles incident within this range from the edge of the blade, 69.88% were detected behind the scraper blade, a significant difference from the low energy configuration. As expected, no particles were transmitted directly through the scraper blade, only scattered out the side. This can be seen in Fig. 5.2.

Although the majority of particles incident in this thin slice passed out of the side of the scraper blade, it is likely that they would leave the scraper with low energy, be scattered at such an angle that they would not continue in the machine,

or be annihilated in a region close to the detectors and still show as a signal on the detectors. To determine the likelihood that side scattering would cause a problem for the scraping process, the energy and divergence, x', of the particles were studied.

Figure 5.3 shows the energy distribution of the particles. The centre of the

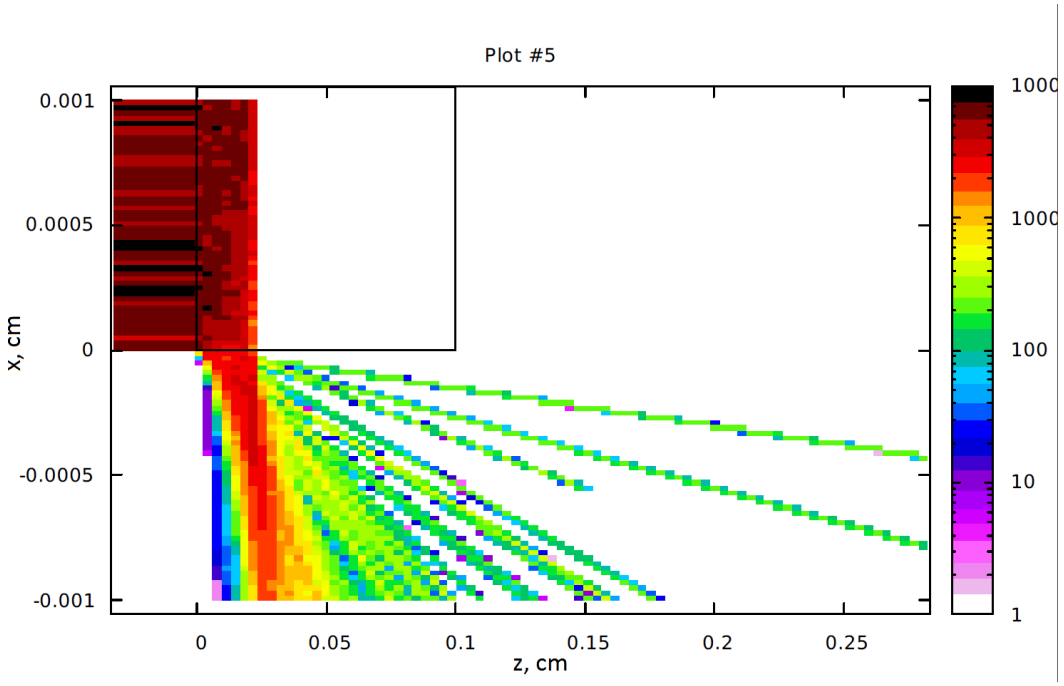

FIGURE 5.2: FLUKA plot showing the relative density of particle tracks through the scraper blade. The scaling of the axes, to fit in the width of both the beam and the scraper blade, gives the impression of large angle scattering.

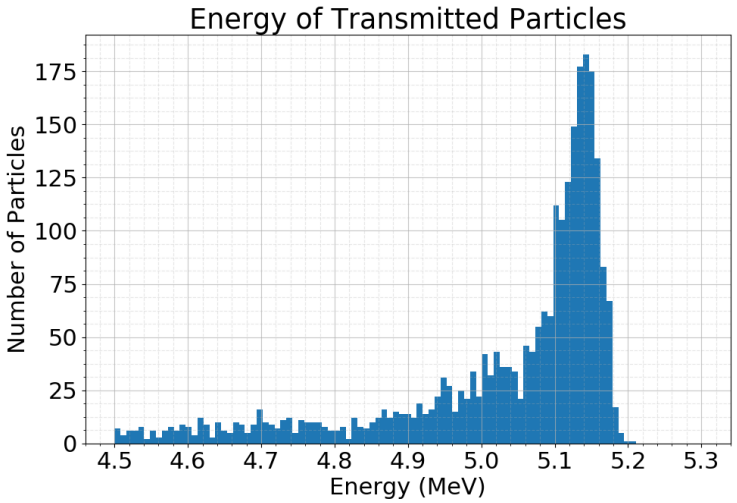

FIGURE 5.3: Energy distribution of side scattered particles at 5.3 MeV on impact.

peak lies at 5.143 MeV, and no particles with an energy greater than 5.21 MeV were detected. The peak at 5.143 MeV corresponds to a momentum spread of 3.29% which is around 100 times greater than the nominal momentum spread for the machine.

The divergence of the scattered particles is displayed in Fig. 5.4, showing a peak lying at -6.7×10^{-3}, with the majority of particles having an even greater angle. For comparison, an optically matched particle with emittance 1 mm mrad at the position of the scraper has a maximum divergence of around $\pm 1.5 \times 10^{-3}$. Because of the sudden change in angle, scattered particles would be unmatched to the lattice, and if surviving around the machine, would undergo filamentation to a larger perceived emittance. Considering the unlikely case that a particle would scatter to this divergence and remain matched to the lattice, its minimum possible emittance would be 19.8 mm mrad. This, combined with the loss in energy leads to the conclusion that almost all scattered particles would instantly or very quickly become unstable and be lost in the machine or contact the bulk of the scraper in the next several turns.

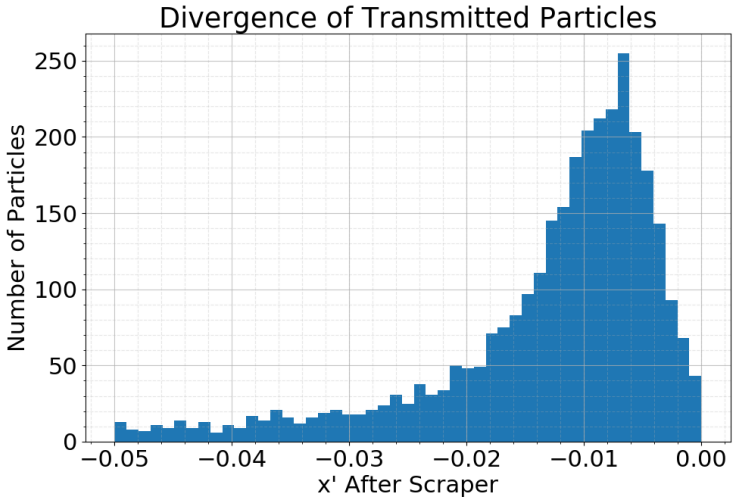

FIGURE 5.4: Divergence of side scattered antiprotons from the scraper blade.

Additionally, because of betatron oscillations, particles are not always incident on the scraper blade when it first moves to their maximum amplitude. It may take many revolutions before a particle is at, or close to, its maximum oscillation amplitude at the position of the scraper, and intercepted. To account for this, the

simulation was run for a beam extending 40 μm in x, a distance that corresponds to ≈1,000 turns of the beam. It can be seen in Fig. 5.5 that the likelihood of side scattering is reduced to negligible levels for 1,000 turns. Given that the desired position accuracy of the scraper is 0.1 mm, which corresponds to around 2600 turns, side scattering effects for antiprotons at any ELENA energy may be deemed negligible.

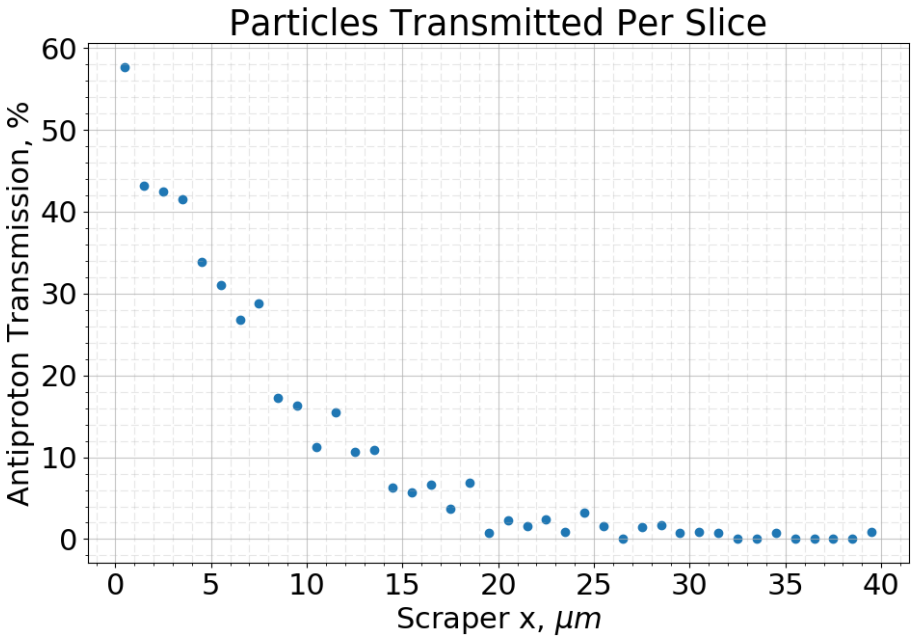

FIGURE 5.5: Number of antiprotons transmitted through the scraper blade as a percentage of the total antiprotons incident in 0.1 μm slices along x.

5.3 Simulating the Scraping Process

5.3.1 Tracking Methods

MAD-X (Methodical Accelerator Design) [104] is a multi-purpose code developed, used and maintained primarily by CERN. It is used for the study and design of the charged particle optics that make up modern linear and circular accelerators and beam transport lines, and is the successor to MAD-8. MAD-X allows the user to define a series of accelerator elements and an input beam and will calculate useful quantities such as the Twiss parameters at each location or the tune and chromaticity, to name a few.

MAD-X also contains the symplectic integrator PTC (Polymorphic Tracking Code) library developed by E. Forest [105], which was the primary tool used for these simulations. PTC allows the user to track individual particles and beam distributions through all of the accelerator elements that make up the lattice defined in MAD-X. The user may specify the number of steps and integration type allowing the flexibility to find a balance between accuracy and processing power dependent simulation time.

The lattice was constructed according to the Technical Design Report specifications [42] and updated as adjustments were made during the construction phase of the ring. In order to ensure a stable beam, the tune of the lattice was adjusted using MAD-X's matching module on the three families of quadrupoles. The tune was moved away from systematic resonances at $Q_x = 2.3$ and $Q_y = 1.5$, the lattice in Fig. 5.6, to $Q_x = 2.35$ and $Q_y = 1.44$, as seen in Fig. 5.7. The tune adjustment made a small difference in the β_x/D_x ratio.

A general overview of the lattice may be found in Section 1.4 and the optics calculated by MAD-X and used in these simulations are presented in Fig. 5.8. The figure also highlights the position of the scraper, which is represented by

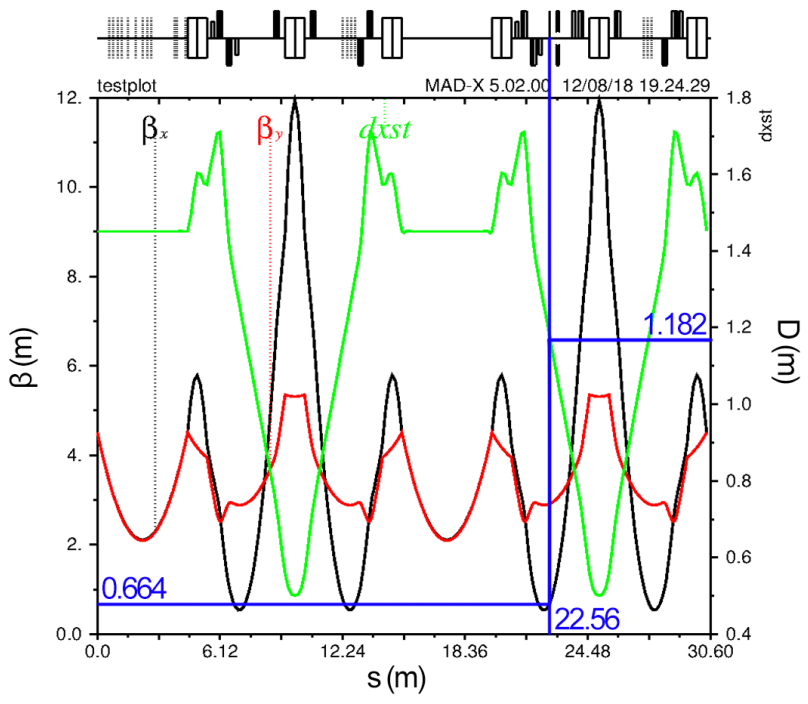

FIGURE 5.6: The lattice before tune adjustment. Blue lines and numbers highlight the β_x, D_x and distance from injection, s, of the scraper blade.

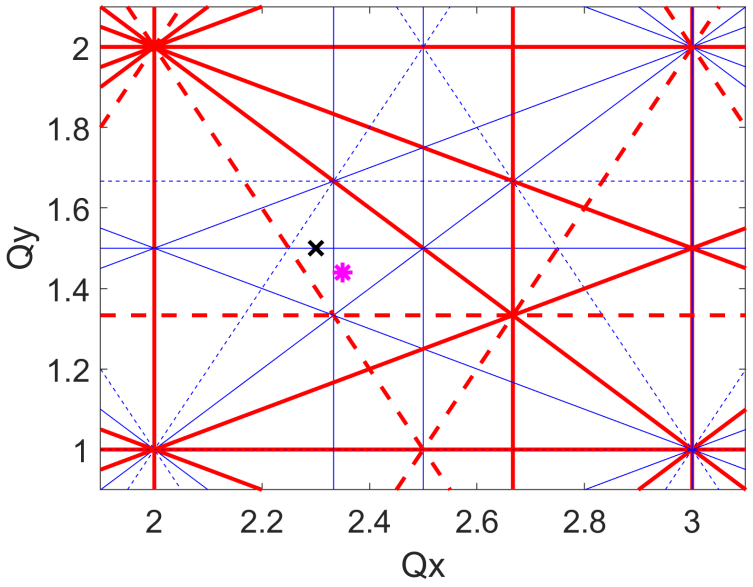

FIGURE 5.7: The tunes used in the ELENA MAD-X simulations. The black x represents the previous tune value, whilst the magenta asterisk marks the updated values.

a vertical blue line. These are the optics presented in Chapter 3, Table 3.1 as configuration C2. Before the majority of the MAD-X simulations were run, the state of the lattice was frozen to allow for consistency in the simulations. With these parameters, the effect of the dispersion on the beam is more pronounced, providing better (more pessimistic) conditions for testing the performance of the algorithms and showing their versatility for use in future machines.

Configuration C4 in the same table gives the expected values of β_x and D_x based on the most recent measured optics in ELENA. The configuration includes a small move upstream of the scraper resulting in a higher β_x/D_x ratio. Further simulations and analysis were also performed with these optics to allow for analysis and estimations of errors in the specific case of ELENA, and to investigate how the ratio affects different aspects of the scraping process. For clarity and ease of reference, C2 and C4 are presented in Table 5.1.

Distributions of 10,000 macro-particles were generated using a Python script (described in Section 5.3.2) and tracked around the ring at an energy of 100 keV using PTC. Since the particles of a beam are tracked individually, collective effects such as IBS and rest gas scattering were not included directly in the simulation,

TABLE 5.1: Horizontal optics parameters used by the simulations. C2 is based on the original design and C4 is the most recent measured values.

Configuration	C2	C4
β_y (m)	3.00	2.97
β_x (m)	0.688	3.21
D_x (m)	1.292	1.38
β_x/D_x	0.533	2.33
s (m)	22.56	23.44

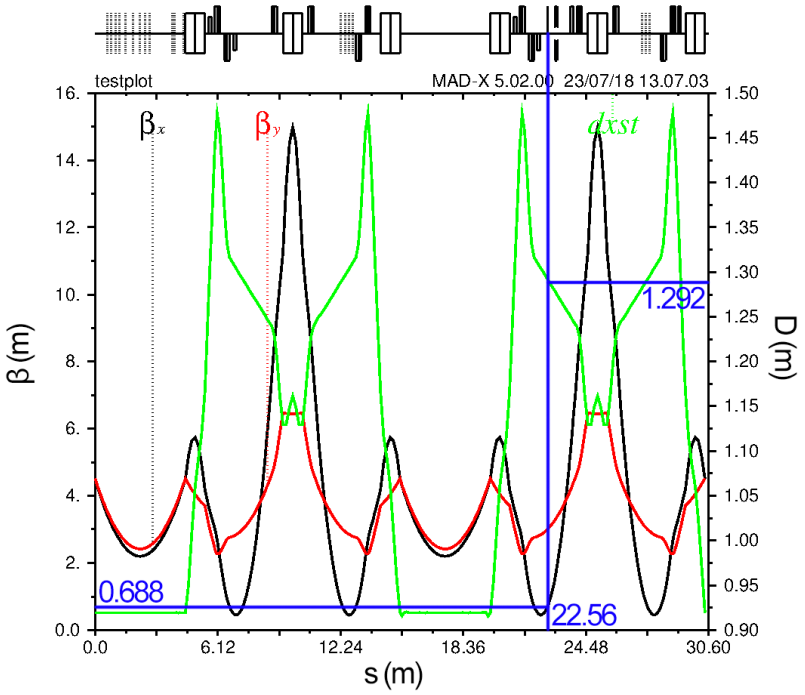

FIGURE 5.8: The optics calculated by MAD-X for the lattice used in the scraper simulations, corresponding to configuration C2.

however some injected beams contained characteristics related to these phenomena such as the bi-Gaussian distributions.

A quadrupole with zero length, zero strength and a rectangular aperture was defined to act as a collimator element. It was introduced to the lattice to simulate the scraper blade and will hence be referred to as the scraper. The scraper has a square aperture 100 mm in diameter, larger than the actual diameter of the scraper blades at 66 mm. The discrepancy is of no consequence since the beam in these simulations does not stray far from the closed orbit, or reach a transverse beam size close to 33 mm.

A Python script was used to control, automate and save the output from the simulations, as MAD-X was executed many times over the course of a simulation, each time adjusting the scraper position. The scraper was moved into the beam in steps of 0.1 mm. For a beam with energy 100 keV this corresponds to a scraper movement every 360 turns. The scraper blade was moved in these discrete steps to allow simulations to run faster and 0.1 mm was chosen based on the predicted scraper position resolution. An investigation into the impact of the step size on the reconstructed emittance values was performed and can be found with the simulation results in Section 5.6.3.1.

To scrape from positive x, the collimator was centred vertically at $y = 0$ mm. The horizontal position was calculated such that $x_{col} + r_{col} > A_{max}$ by around 1 mm, where r_{col} is the scraper radius, x_{col} is the position of the centre of the collimator and A_{max} is maximum amplitude of the largest emittance particle in the distribution. This allowed for only several hundred beam revolutions before scraper interception to cut down total simulation run time. In some cases, for example when testing with a poorly matched beam, more time was given to allow the beam to stabilise after filamentation.

After each 360 revolution MAD-X simulation, a copy of the output beam was saved for imaging and analysis, and the distribution was automatically reformatted to be injected into the following simulation. The process was repeated until the scraper reached the designated amplitude. The beam distributions at each step could be imaged and shown in rapid succession to create an animation of the destruction of the beam, in real and phase space. This was useful for debugging the codes and for observing how the scraping process changed under different conditions. Figure 5.9 shows the horizontal phase space of beam at four stages during scraping.

5.3.2 Beam Generation

5.3.2.1 Gaussian Beams

For the beam generation process we first assume a Gaussian beam, and then later adapt the code for other distributions. For these simulations we use five input

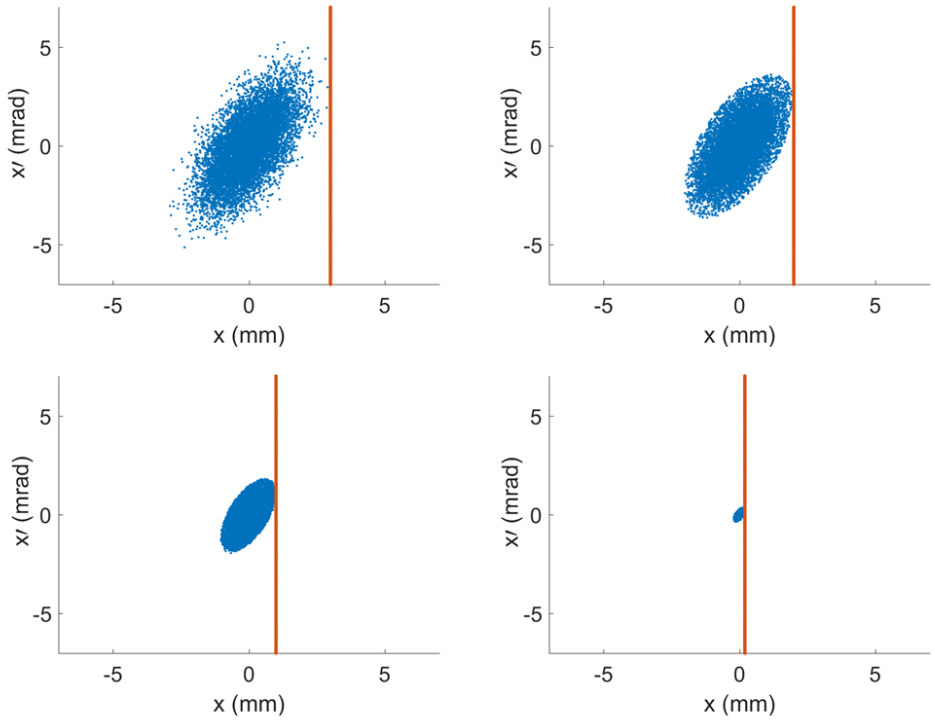

FIGURE 5.9: Horizontal phase space plots of a beam of 10,000 macroparticles for different stages of the scraping process.

co-ordinates to describe a particle's position in the beam:

$$(x, x', y, y', \delta) \tag{5.2}$$

where δ is the longitudinal momentum offset of the particle. Considering only the horizontal transverse co-ordinates, we begin with the equation for an ellipse in the $x - x'$ plane:

$$A^2\beta = x_\beta^2 + (\alpha x_\beta + \beta x'_\beta)^2 \tag{5.3}$$

Make a transformation to normalise for a constant radius in order to simplify beam generation:

$$X_\beta = x_\beta \tag{5.4}$$

$$X'_\beta = \alpha x_\beta + \beta x'_\beta \tag{5.5}$$

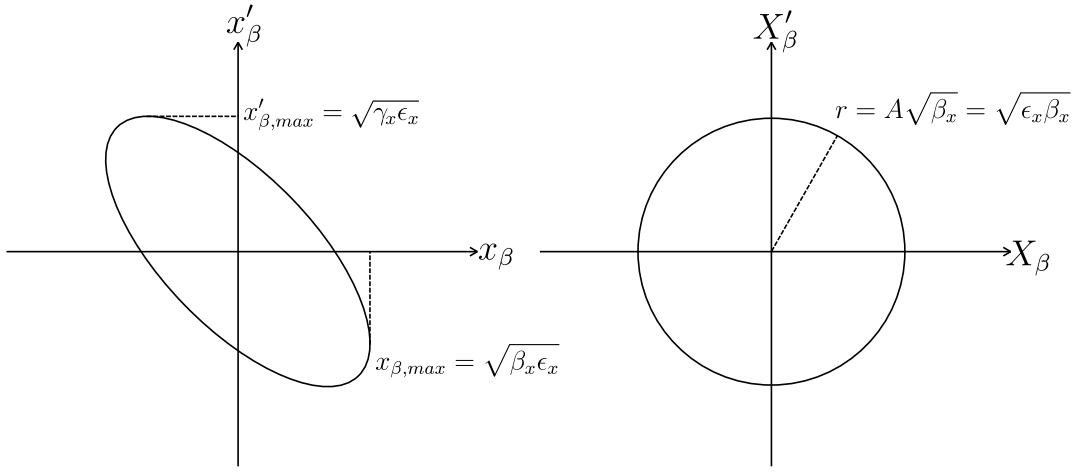

FIGURE 5.10: Phase space ellipses for a particle in standard and normalised phase space.

In normalised phase space the radius, r, of the circle traced out by a particle is given by $r = X_{\beta,max} = x_{\beta,max} = \sqrt{\epsilon\beta}$. It can be seen from Fig. 5.10 that $X'_{\beta,max} = \sqrt{\epsilon\beta}$ also, due to the constant radius. Using these relations, we may then begin generating N values of X_β and X'_β, where N is the total number of macroparticles to be used in the simulation. This may be done using the random Gaussian number function available in most modern scientific codes [106]:

$$X_{\beta,n} = G[0, \sqrt{\epsilon\beta}]_1, \tag{5.6}$$

$$X'_{\beta,n} = G[0, \sqrt{\epsilon\beta}]_2, \tag{5.7}$$

where the subscript n refers to the n^{th} macroparticle, and $G[\mu, \sigma]_i$ represents a random value picked from a Gaussian shaped probability distribution, with a mean, μ, and a standard deviation, σ, and where i denotes separate callings of the function per particle.

For input into the simulation it is necessary to transform back to x and x'. There is a dependence of x'_β on x_β hence it is important to generate the values simultaneously for each particle. Using Eqs. 5.4 & 5.5 and the values previously

generated for each particle we may use:

$$x_{\beta,n} = X_{\beta,n}, \tag{5.8}$$

$$x'_{\beta,n} = \frac{X'_{\beta,n} - \alpha x_{\beta,n}}{\beta}, \tag{5.9}$$

to obtain the horizontal phase space co-ordinates for N particles in a Gaussian beam.

Additionally a longitudinal momentum spread may be introduced. Using the same methods and notation as in Eqs. 5.4 & 5.5, we obtain N longitudinal momentum offsets, δ:

$$\delta_n = G[0, \sigma_\delta]_3, \tag{5.10}$$

where σ_δ is the desired RMS momentum spread of the beam. This value is only generated once per particle and is used for both the x and y co-ordinates. These values will be accepted by MAD-X, however the effect of the momentum spread on the transverse positions of the macroparticles must also be accounted for.

Multiplying the values for longitudinal momentum offset by the dispersive terms at injection, $D_{x,y}$ & $D'_{x,y}$, and using the process described above to obtain co-ordinates for the vertical $y - y'$ plane, we finally arrive at:

$$x_n = x_{\beta,n} + \delta_n D_x, \tag{5.11}$$

$$y_n = y_{\beta,n} + \delta_n D_y, \tag{5.12}$$

$$x'_n = x'_{\beta,n} + \delta_n D'_x, \tag{5.13}$$

$$y'_n = y'_{\beta,n} + \delta_n D'_y, \tag{5.14}$$

for N macroparticles. In the MAD-X simulations, N was taken as 10,000 as a compromise between statistical significance and simulation running time. It is also worth mentioning that when working in MAD-X for low energy (not highly relativistic) machines one should divide input $D_{x,y}$ & $D'_{x,y}$ by relativistic β_{rel} to counteract assumptions made by the program [107]. Calculated values of dispersion by MAD-X and PTC must also be multiplied by β_{rel} for the same reasons.

5.3.2.2 Bi-Gaussian Beams

The generation of a bi-Gaussian beam was based on the beam dynamics investigations presented in Section 2.3.3. Bi-Gaussian beams were simply generated as a combination of two Gaussian beams of different properties, with $N/2$ particles each.

From BETACOOL simulations, a scaling factor, n_{inc}, between the RMS width of the two Gaussian distributions, σ_1 and σ_2, was obtained, $\sigma_2 = \sigma_1 n_{inc}$. Using $\sigma^2 = \epsilon\beta$ we may express the relation between the two Gaussian beams in terms of the emittance of each:

$$\epsilon_2 = \epsilon_1 n_{inc}^2. \tag{5.15}$$

Assuming we have an equal number of particles in each Gaussian beam, $N_1 = N_2$, we may write an expression for the resultant emittance when the two distributions are combined, ϵ_{out}:

$$\epsilon_{out} = \frac{N_1\epsilon_1 + N_2\epsilon_2}{N_1 + N_2} = \frac{\epsilon_1 + \epsilon_2}{2}. \tag{5.16}$$

Substituting Eq. 5.15 into Eq. 5.16 and rearranging for ϵ_1 we arrive at:

$$\epsilon_1 = \frac{2\epsilon_{out}}{1 + n_{inc}^2} \tag{5.17}$$

which in combination with Eq. 5.15 allows us to easily calculate the two values of emittance from the desired values of n_{inc} and ϵ_{out}.

The Gaussian beam generation process described above was used to generate two separate beams each with $N/2$ macroparticles, using ϵ_1 and ϵ_2 as input values. The beams were combined to form the bi-Gaussian beams used in these simulations. In these simulations a bi-Gaussian beam has $n_{inc} = 3.25$ based on the result from the study presented in Section 2.3.3.

5.3.3 Transverse Phase Space Scraper Simulations

To check how the two scan algorithm performs on different beam distributions, various Twiss parameters and with different sources of error, an analysis program

was written in Python. The purpose of the program is to analytically simulate the scraping process without having to track around the ELENA lattice thousands of times per particle thus speeding up the process. The program was used to support and build upon data gathered from MAD-X simulations.

First a beam is generated using the methods in Section 5.3.2 with the desired Twiss parameters at the scraper, as opposed to at ELENA injection for the MAD-X beams. From the phase space co-ordinates of each particle given in Eqs. 5.8 & 5.9, the emittance of the particle is calculated using:

$$\epsilon_x = \gamma x^2 + 2\alpha_x x x' + \beta_x x'^2 \tag{5.18}$$

and similarly for y. Using this emittance and the longitudinal momentum offset given by Eq. 5.10, the maximum and minimum particle amplitudes are calculated and saved for each particle:

$$x_{max} = \delta D_x + x_0 + \sqrt{\beta_x \epsilon_x} \tag{5.19}$$

$$x_{min} = \delta D_x + x_0 - \sqrt{\beta_x \epsilon_x} \tag{5.20}$$

and again similarly for y. Assuming the beam is well optically matched to the machine, it may be scraped using these values. Assigning a finite step size to the scraper blade, the program sequentially removes all particles with a maximum amplitude greater than the current scraper blade position when scraping from positive x. The number of scraped particles is saved. When scraping from negative x, the minimum (most negative) amplitude is used. The data may then be saved for analysis, once the scraper blade has moved through the desired distance.

The program does not track the particles around the machine since it assumes that all particles are scraped at their maximum (or minimum) amplitude, and that the beam is optically matched to the machine. Whilst this is a simplification of the MAD-X simulations, benchmarking confirmed it returned the same results with the same accuracy for well matched beams of the same parameters. The code allows for much higher statistical data to be collected over a much shorter time scale than with the MAD-X approach and was particularly useful when considering

systematic errors. The program is also capable of quickly changing the Twiss parameters at the scraper, and producing plots of the beam distributions, CDFs and PDFs quickly. It includes a section for algorithm analysis of the scraping data and so is self contained and hence may be used for parameter scans of beam input, Twiss and algorithm properties.

5.4 AD Code Comparison

The scraper system in the AD works using a more basic method for determining the emittance of the beams. The system assumes a Gaussian beam in a dispersion free region. In contrast with the algorithms developed for ELENA which calculate the RMS emittance, the AD algorithm calculates the 95% emittance. This choice of which emittance to use is preferential, here the 95% technique was chosen due to the simplicity of the calculation.

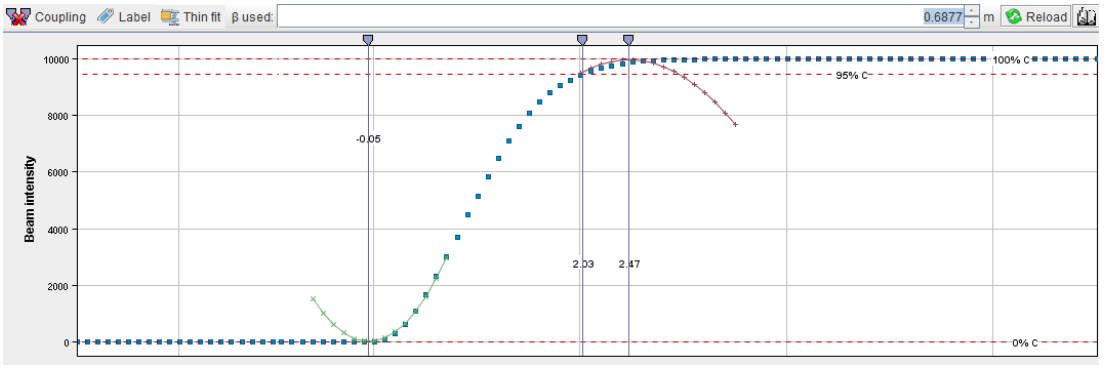

FIGURE 5.11: A screenshot of the CDF displayed within the AD analysis GUI.

The algorithm begins by aligning the scraper time and position with the scintillator time data in order to make the standard intensity versus scraper position comparison. Once the beam has been scraped and the data aligned, a CDF is produced. The algorithm then makes an estimate for the intensity on the scintillators at 100%, 0% and then with a linear fit of the intensities, 95% of the beam's intensity. Using these values, a parabola of around 16 points is fit to the core (rising edge of CDF), x_{cent}, and outer edge of the beam (CDF plateau), x_{outer}, to determine the corresponding scraper positions. The process is the same in the vertical, y, plane but for brevity the process is described in terms of x. The parabolas

TABLE 5.2: Results from the AD scraper algorithm.

Input			$\beta_x/D_x = 0.533$		$\beta_x/D_x = 2.33$	
$\epsilon_{RMS,in}$	σ_δ ($\times 10^{-4}$)	n_{inc}	$\epsilon_{95\%,out}$	Difference (%)	$\epsilon_{95\%,out}$	Difference (%)
1	0	1	6.28	4.816	6.12	2.15
1.5	0	1	9.34	3.93	8.95	0.414
3	0	1	17.11	4.81	17.36	3.42
1	3	1	10.88	81.6	7.98	33.2
1	10	1	59.23	888	20.25	237
1	0	3.25	8.52	42.2	8.26	37.9
1	3	3.25	14.19	137	10.67	78.1

can be seen in the algorithm's GUI display and an example is shown in Fig. 5.11. Horizontal lines mark the calculated intensities with vertical lines showing their corresponding positions. The 95% position is found by iterating through the intensity data and finding the nearest point to the computed intensity value from the linear fit.

Using these three values of the positions at the different intensities, the acceptance A_{AD} and 95% emittance, $\epsilon_{95\%}$, are computed using the beta function, β_x, at the scraper:

$$A_{AD} = \frac{(x_{cent} - x_{outer})^2}{\beta_x}, \tag{5.21}$$

$$\epsilon_{95\%} = \frac{(x_{cent} - x_{95\%})^2}{\beta_x}, \tag{5.22}$$

and similarly for the vertical, y, plane.

To test how the algorithm performs in the conditions presented in ELENA, and to demonstrate the need for the new algorithms, ELENA simulation data was run through this algorithm. A range of beams were run to investigate the impact of different effects for the two different β_x/D_x ratios at the scraper, and the results may be seen in Table 5.2.

The input beams were generated based on ϵ_{RMS} values so that the input is consistent with tests of the new algorithms. Additionally, a beam may have various distributions and momentum spreads but the same RMS emittance. This gives a measure of the beam quality as opposed to being only proportional to the width of the beam, as with the 95% emittance. If a beam is Gaussian, with no dispersive

effects, then it is possible to compare the RMS and 95% emittances using:

$$\epsilon_{RMS} = \frac{\epsilon_{95\%}}{-2\ln 0.05}. \tag{5.23}$$

The table displays the 95% emittances output by the algorithm directly and percentage errors calculated using Eq. 5.23 to compare the results with the RMS input. This approach is justifiable as for the trials in the top three rows where only emittance is being adjusted the equation is correct. In all other cases where the equation is an approximation because of complicating factors such as non-Gaussian beams or momentum spread, the RMS emittance is held constant and so relative comparisons in the algorithm's output may be made.

For the top 3 rows we can see that the algorithm returns accurate values, within the 10% accuracy limit set for the new ELENA algorithms. The beams are Gaussian with no momentum spread. In the next two rows the momentum spread of the beam has been increased. As a result, the transverse width of the beam has increased despite the RMS emittance remaining the same. This is reflected in the results where we see a huge increase in the output 95% emittance, particularly for the low β_x/D_x case. This translates to an extreme percentage difference from the top row case with the same RMS emittance.

A trial with no momentum spread but a bi-Gaussian beam was performed. Again this led to an increase in the transverse beam width, and is reflected in the results. The final trial was for the expected beam quality in ELENA, with nominal momentum spread and the value of n_{inc} used in the majority of simulations presented here. The result returned by the algorithm is again much different for a Gaussian beam with no momentum spread and same RMS emittance.

The comparisons here highlight how the AD algorithm provides little more than a scaled measurement of the beam width. Whilst this is useful, it does not account for the overall mean beam quality. Because of the additional complicating factors presented by ELENA, analysis of the beam would need to be more sophisticated. As demonstrated in the table, beams may have several different properties, but the same RMS emittance. The new algorithms seek to measure this RMS emittance and to return additional quantities which help to further characterise the beam. It

will of course also be possible to simply perform a measurement of the 95% beam width if desired.

5.5 Gaussian Only Algorithm Results

5.5.1 Scraping Results Analysis

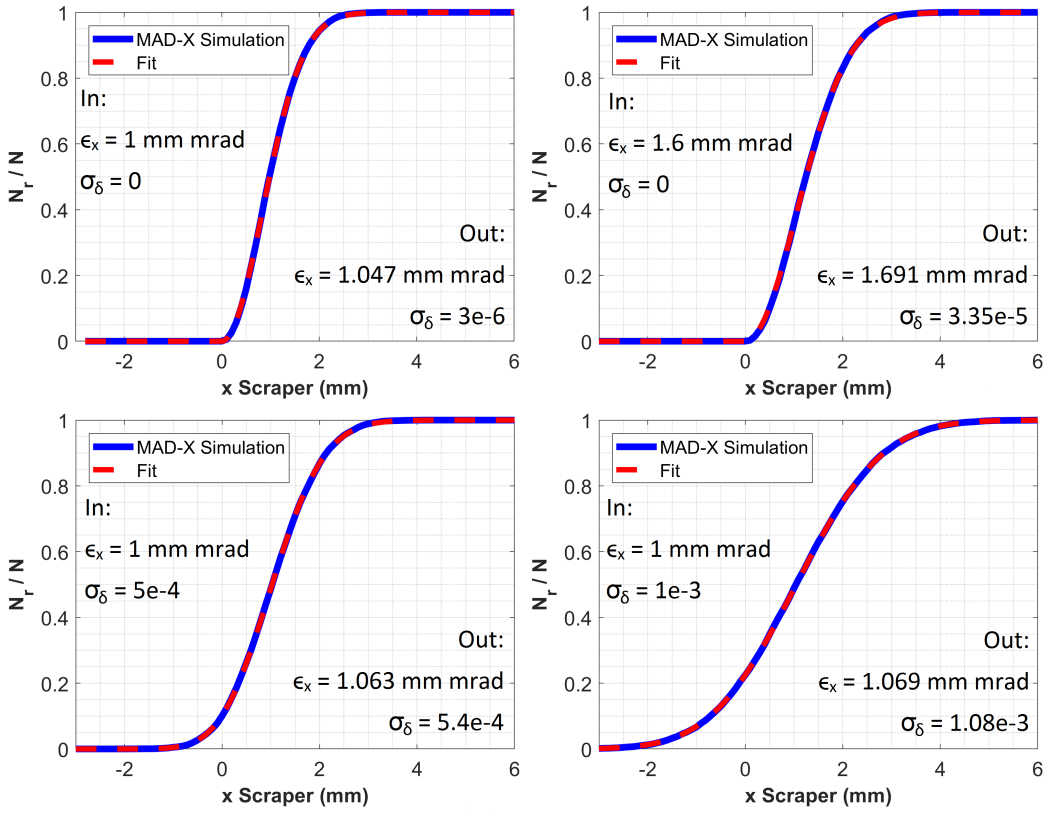

FIGURE 5.12: Intensity data for beams of varying parameters overlaid with the Gaussian algorithm fit.

To check the simulations were working properly, the single scrape Gaussian algorithm was applied first. Since the algorithm incorporates well established scraping techniques it is a better candidate for benchmarking and testing the simulations.

The first simulations were performed for the most simple input. Gaussian beams with emittances of 1 μm and 1.6 μm, with no momentum spread, $\sigma_\delta = 0$, were scraped. The scraper blade moved from positive x and the resultant distribution was saved as $F_+(x_s)$. The top two plots in Fig. 5.12 show the resultant

cumulative probability curves obtained, overlaid by the fit from the algorithm, Eq. 4.19, using MATLAB's custom equation fitting tool and taking both ϵ_x and σ_δ as free parameters. The numerical results from the algorithm are also included and it can be seen for both emittances, there is good agreement with the input values, well within the target accuracy of 10%. The estimations for momentum spread are small enough that they could be considered negligible and are a good estimation for an input value of zero. The error on the results could be attributed to statistical fluctuations and/or the discreet scraper steps of 0.1 mm.

The Gaussian beam was run again, with non-zero values of momentum spread. The results may also be seen in Fig. 5.12, where again the algorithm agrees with the input values to a satisfactory level. The estimations for longitudinal momentum spread are within 10% of the respective input values. This is more accurate than the expected accuracy of the Schottky diagnostic device ($\approx 20\%$) and hence this method could be used to determine the momentum spread in combination with such a device, in the circumstances that the beam may appear Gaussian enough. An investigation into the accuracy of this method for momentum spread estimation of non-Gaussian beams can be found later in this section. In addition to the potential sources of error mentioned above, taking the momentum spread as a free parameter as opposed to knowing its exact value also contributes to the small inaccuracy in reconstructed emittance value.

5.5.2 Momentum Spread Estimation

The Python analysis code was used to generate beam scraping profiles with n_{inc} starting at 1, a Gaussian beam, up to $n_{inc} \approx 3$, around the expected value after electron cooling in ELENA. The output scraping data was then analysed by the Gaussian reconstruction algorithm taking emittance and momentum spread as free parameters. To minimise statistical fluctuations, this was done 4 times for each value of n_{inc} and the mean and standard deviation in the results were calculated. The process was carried out using the same values of β_x and D_x as for the previous simulations, C2, which give dispersive effects more impact on the beam quality.

It was also then repeated for values which are closer to the expected values in the scraper's current position in ELENA, C4, which minimise the impact of D_x.

In Fig. 5.13, it can be seen that as n_{inc} increases, the error in the reconstructed emittance value also increases as expected. Using the gradient from a very simplified linear fit to compare the results it can be seen that the larger β_x/D_x ratio has little to no impact on the effectiveness of the algorithm. The error quickly grows above 10% for values of n_{inc} around 1.7 in both cases. It would not be recommended that the algorithm be used for emittance reconstruction in the presence of electron cooling. However, if the beam is injected and operators can ascertain how Gaussian it is, based on for example profiles measured by the BTV screen along the injection line, the algorithm could still be used for emittance reconstruction in ELENA.

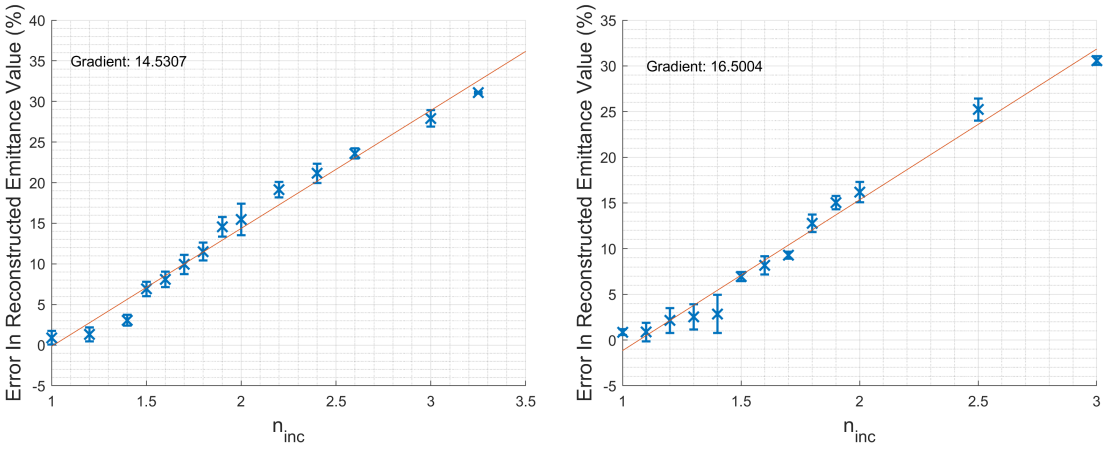

FIGURE 5.13: Error on reconstructed emittance values from the Gaussian fit algorithm based on increasingly bi-Gaussian beams. The plot on the left shows the results for the simulation standard values of $\beta_x = 0.688$ m and $D_x = 1.29$ m. The plot on the right has $\beta_x = 3.21$ m and $D_x = 1.38$ m, closer to the expected values at the new scraper position.

The same analysis for the reconstructed momentum spread values can be seen in Fig. 5.14. Here the difference between the two cases of differing Twiss parameters can be seen much more clearly, the gradient of the approximate line fit is more than 2.5 times greater for the higher β_x/D_x ratio case, C4. This result could be expected since a higher β_x/D_x ratio gives the scraper profile less of a momentum spread related tail at the core of the beam, and hence this momentum spread related characteristic of the distribution does not influence the fitting algorithm as

much. It would be recommended that a local adjustment of Twiss parameters to reduce the β_x/D_x ratio should be applied if using this algorithm for the purpose of acquiring the momentum spread of the beam. Additionally, the algorithm should not be used for this purpose if the profile shows strong bi-Gaussian effects after electron cooling.

A second set of simulations were performed with the same conditions, but only taking the momentum spread as an unknown value. The emittance could be accurately calculated from the two scan method instead. The results showed that even inputting the exactly correct emittance into the algorithm does not improve the momentum spread estimation performance with respect to increasing n_{inc} for either case.

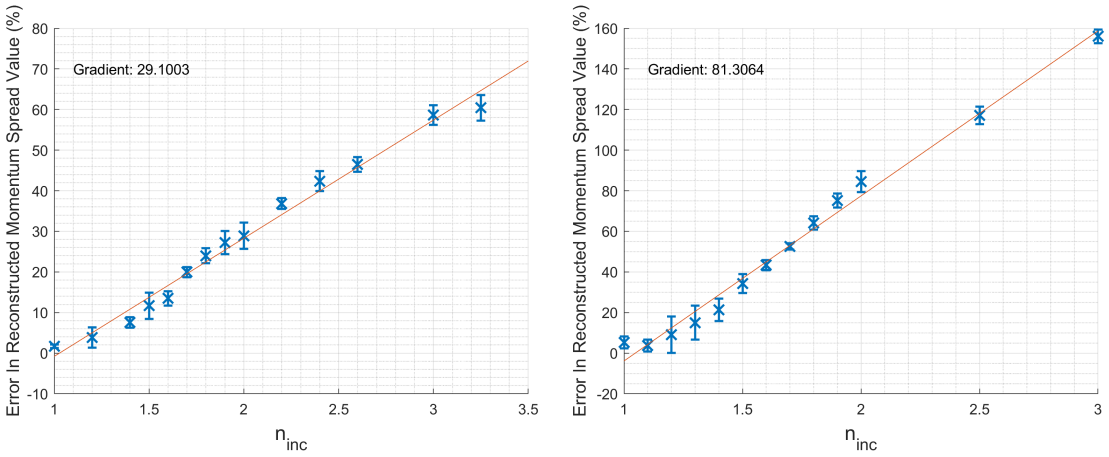

FIGURE 5.14: Reconstructed momentum spread values based on increasingly bi-Gaussian beams. Left plot: $\beta_x = 0.688$ m and $D_x = 1.29$ m. Right plot: $\beta_x = 3.21$ m and $D_x = 1.38$ m.

5.6 General Case Algorithm Results

5.6.1 Spline and Reimann Sums

The next stage of simulations dealt with the general case algorithm. As described in the previous chapter, two methods for handling the data were considered: spline fitting and differentiation by approximate numerical methods (e.g. Riemann sums

for differentiation). To determine the most suitable method, the same scraper distribution was analysed using both. For the spline fitting test, MATLAB's piecewise polymorphic spline interpolant [108] was used and the Riemann based method (Section 4.4.3) was compared with it.

The input beam had $\epsilon_x = 1.2$ mm mrad, and for the spline and Riemann sum methods, the algorithm returned 1.935 mm mrad and 1.941 mm mrad, respectively. Figure 5.15 shows the resultant PDFs, $f(x_s)$, produced by each method, and it is clear to see why the output values are in such good agreement.

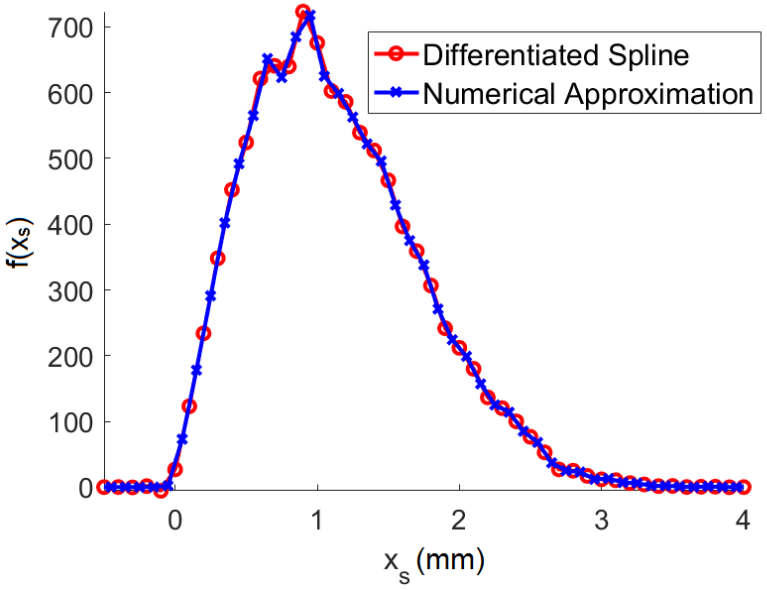

FIGURE 5.15: Reconstructed PDFs for both methods of processing the raw scraper data.

Since the Riemann sum method is much less computationally complex but is just as accurate, it is suggested that this is the most appropriate approach for the algorithms and is the one used in all analysis here. The spline method may need to be employed for a data acquisition rate of $\ll 400$ Hz, or for much smaller beams than are practically considered in this study.

5.6.2 Ideal Conditions Results

Matched beams were run in MAD-X and were scraped once from positive x then again from negative x. Scraping simulations were not performed for the y-plane since zero dispersion is equivalent to scraping in x with zero momentum spread.

The results of the first tests are displayed in Fig. 5.16. Initially, the most simple case was tested, plots a) and b) display the results for a well matched Gaussian beam with zero momentum spread. The transverse emittances, ϵ_x, ϵ_y for beam generation were set as 1 mm mrad each. The horizontal emittance of the resultant distribution was calculated to be 0.9987 mm mrad. The closed orbit of the beam can easily be seen to be at $x = 0$, where both sets of scraping data drop to $F(x_s) = 0$, at the core of the beam. The output emittance value from the algorithm was 0.9930 mm mrad which equates to a 0.57% error. Similarly to the Gaussian algorithm tests, this error could be contributed to statistical functions.

Figures c) and d) show the resultant distributions for a beam with the same input parameters, but for a bi-Gaussian distribution, with $n_{inc} = 3.25$. For a matched input beam with a calculated horizontal emittance obtained from the macroparticle distribution of 1.004 mm mrad, the algorithm returned $\epsilon_x = 1.012$ mm mrad, a negligible difference of 0.83%. This confirms that the algorithm works for arbitrary beam distributions, and that it would also work for bi-Gaussian beams when scraping in the vertical plane because $D_y = 0$.

The simulations were then run for beams with non-zero momentum spread. Figures e) and f) show an example of the resultant distributions for beams with non-zero momentum spread. The dispersive effect can be seen where the CDFs do not drop to zero at the closed orbit of the beam, where instead they cross each other, and the distribution appears to continue on the other side of the beam core. The reason for this is clearly illustrated in Fig. 2.3 in the beam dynamics chapter, where two sets of particles were run with and without momentum spread, and their phase space ellipses plotted. The dispersive effect shifts the ellipses in x based on the sign and magnitude of their momentum spread, and hence the beam appears to be 'smeared' during scraping. A comparison of plots e) and f) with those above them shows how significantly the dispersion can affect the result. Considering that all beams in the top six plots have the same emittance, it is clear why the double scan algorithm is needed for non-Gaussian beams.

A range of distributions were scanned, holding the momentum spread constant whilst adjusting the emittance and vice versa. The momentum spread was held

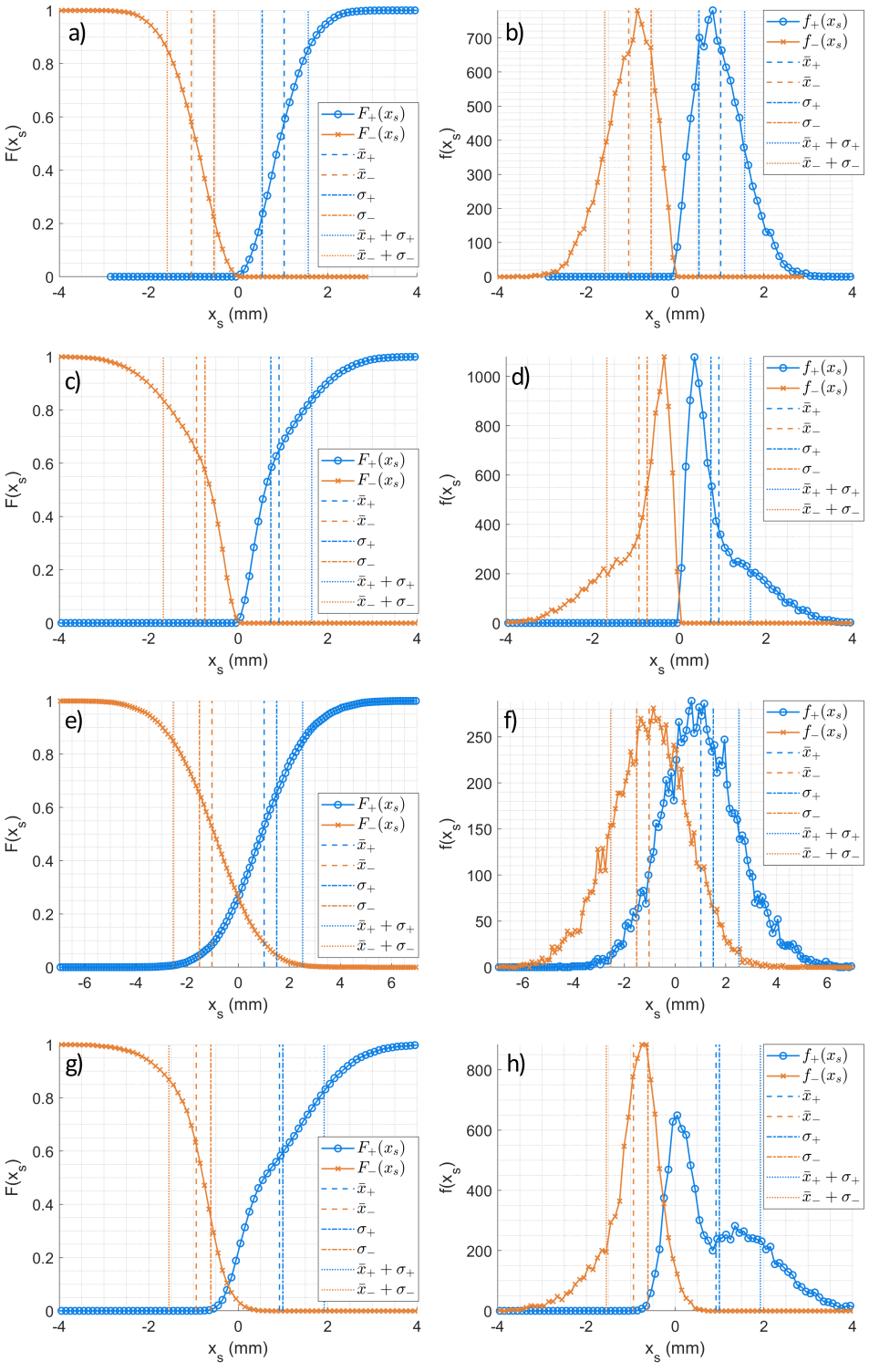

FIGURE 5.16: CDFs, $F(x_s)$ left plots, and their corresponding PDFs, $f(x_s)$ right plots, generated when scraping beams from both positive and negative x. a) and b), and c) and d) correspond to Gaussian and bi-Gaussian beams respectively. Both sets have $\epsilon_x = 1$ mm mrad and no momentum spread. e) and f) have $\epsilon_x = 1$ mm mrad and $\sigma_\delta = 1 \times 10^{-3}$. g) and h) have an emittance-momentum spread correlation and are discussed in Section 5.6.4.

TABLE 5.3: Reconstructed emittances and errors for bi-Gaussian beams with $\sigma_\delta = 3 \times 10^{-4}$.

$\epsilon_{x,in}$ (mm mrad)	$\epsilon_{x,out}$ (mm mrad)	ϵ_x Error (%)
0.4	0.4042	1.05
0.6	0.6060	1.01
0.8	0.8095	1.19
1.0	1.0127	1.27
1.2	1.2164	1.37
2	2.0343	1.72
4	4.0815	2.04
6	6.1385	2.31
8	8.1561	1.95
10	10.192	1.92

TABLE 5.4: Reconstructed emittances for beams with input ϵ_x= 1 mm mrad and various momentum spreads.

Gaussian		
$\sigma_\delta(\times 10^{-4})$	$\epsilon_{x,out}$ (mm mrad)	ϵ_x Error (%)
1	0.9937	0.634
3	0.9945	0.546
5	0.9960	0.401
10	1.0045	0.450
Bi-Gaussian		
$\sigma_\delta(\times 10^{-4})$	$\epsilon_{x,out}$ (mm mrad)	ϵ_x Error (%)
1	1.0120	1.20
3	1.0127	1.27
5	1.0143	1.43
10	1.0132	1.32

at the nominal value, $\sigma_\delta = 3 \times 10^{-4}$, whilst the horizontal emittance was scanned from 0.4 mm mrad to 10 mm mrad. The results are presented in Table 5.3, and it can be seen that the highest error is 2.31%. For beams up to 10 mm mrad the algorithm is well within the desired accuracy limit (10%), and for beams much greater than 10 mm mrad the emittance wouldn't need to be known to such an exact value.

Table 5.4 shows the results when running the algorithm on beams of differing momentum spreads. An increase in the error observed for bi-Gaussian beams compared with Gaussian beams may be observed. However, the error on the reconstructed emittance values remains very low even up to pessimistic input parameters for both types of beam distribution.

The results from the MAD-X simulations for bi-Gaussian beams appear to show that the algorithm tends to overestimate the emittance, and that this effect may possibly scale with the magnitude of the momentum offset. To investigate this with high statistics, beam scraping distributions for 100,000 particles in each scraper direction were generated for a range of momentum spreads using the Python scraping code. For each momentum spread, 10 sets of distributions were generated and analysed by the two scan algorithm.

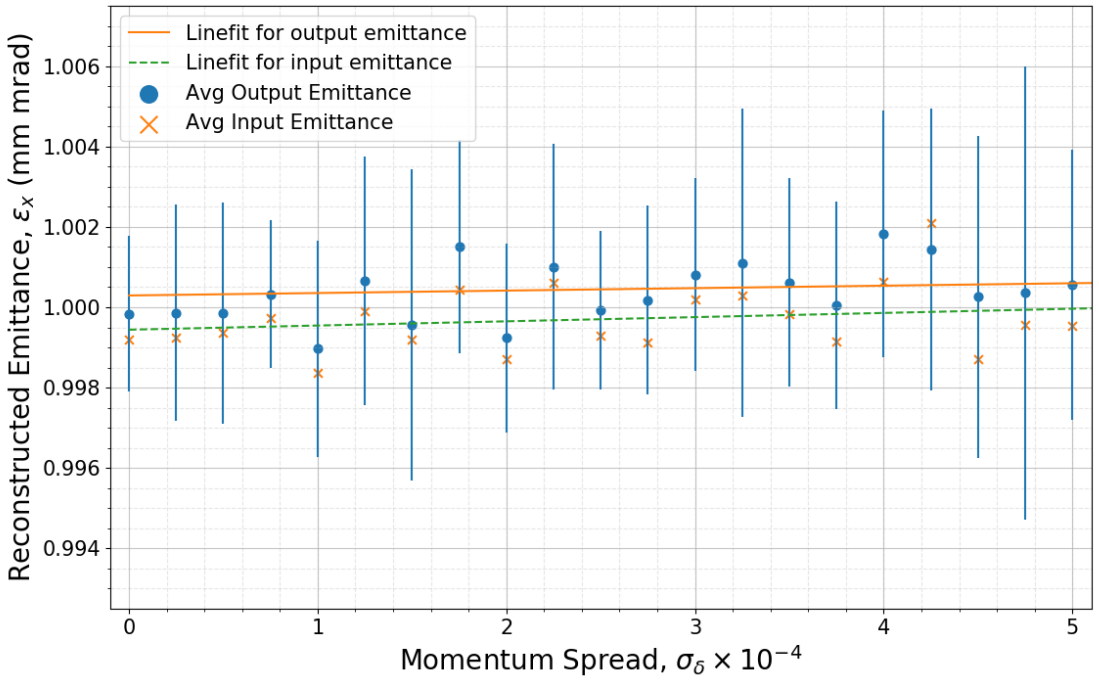

FIGURE 5.17: Python script simulations for 100,000 macroparticle beams with increasing momentum spread. 10 simulations were performed for each momentum spread value.

The results are presented in Fig. 5.17. The average of the emittance of the 20 input beams (10 for positive and negative scraping directions each) used at each momentum spread value are shown with the average of the 10 results from the algorithm. An increase of generated beam emittance with momentum spread can be seen from the gradients of the data fits, but is statistically insignificant. There does appear to be a small but noticeable overestimation by the algorithm for all but one data point. Whilst this effect is small enough to be ignored for the purposes of testing the algorithm, it is attributed to the scraper position resolution, which

is investigated in Section 5.6.3.1. No significant trend of an overestimation of the emittance with increasing momentum spread is observed.

So far the simulations have shown that the two scan algorithm works well for beams with a range of emittances and momentum spreads up to pessimistic values. These results, however, make the assumption that there are no systematic errors, for example, an incorrect momentum spread estimation. The next section investigates how such errors may affect the accuracy of the reconstructed emittance values.

5.6.3 Sources of Errors

5.6.3.1 Scraper Blade Position Resolution

It is expected that the resolution of the scraper blade arm position will be around 0.1 mm. In the simulations presented here, the beams are scraped in 0.1 mm steps and analysed with the same resolution. To investigate how the scraper position resolution may affect the accuracy of the algorithm, Python simulations were run with varying scraper step size. The beams used were bi-Gaussian with $n_{inc} = 3.25$, with nominal momentum spread, $\sigma_\delta = 3 \times 10^{-4}$, and with lattice parameters C2, $\beta_x/D_x = 0.533$. The scraper step size is more significant for a thinner beam, hence testing with the low beta case and $\epsilon_x = 1$ mm mrad.

Figure 5.18 shows the results when running 20 simulations of 10,000 particles each per scraper step size, and taking the mean value. As expected a clear trend can be seen where the reconstructed emittance values become more inaccurate with the scraper step size. The plot also reveals that decreased scraper position resolution leads to an overestimation of the emittance, rather than a random error in either direction.

To determine the impact of the effect in the region around the resolution being used for the simulations and in practice, 10 beams of 100,000 particles each were run for each scraper step size, between 0.01 mm and 0.2 mm. The results may be observed in Fig. 5.19. A polynomial fit to the data shows that there may be a slight overestimation for 0.1 mm which could explain the small discrepancies observed with earlier results. Taking into account the scale of the error bars and the scale of

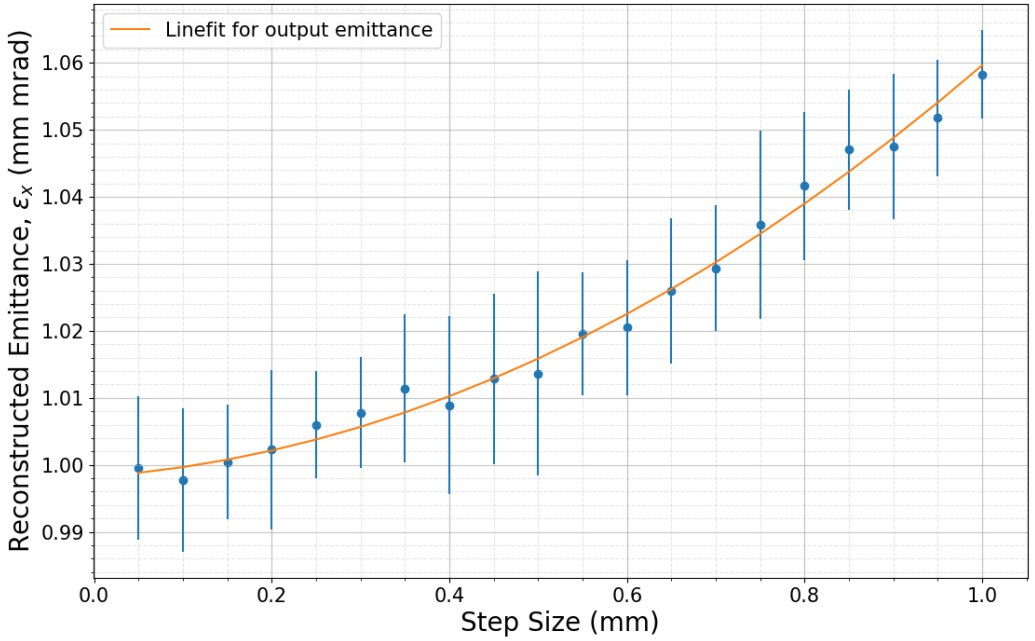

FIGURE 5.18: Effect of simulation scraper step size on reconstructed emittance values for an input beam of $\epsilon_x = 1$ mm mrad.

the y-axis, the overestimation may be deemed negligible for the purposes of these simulations, and also in practice.

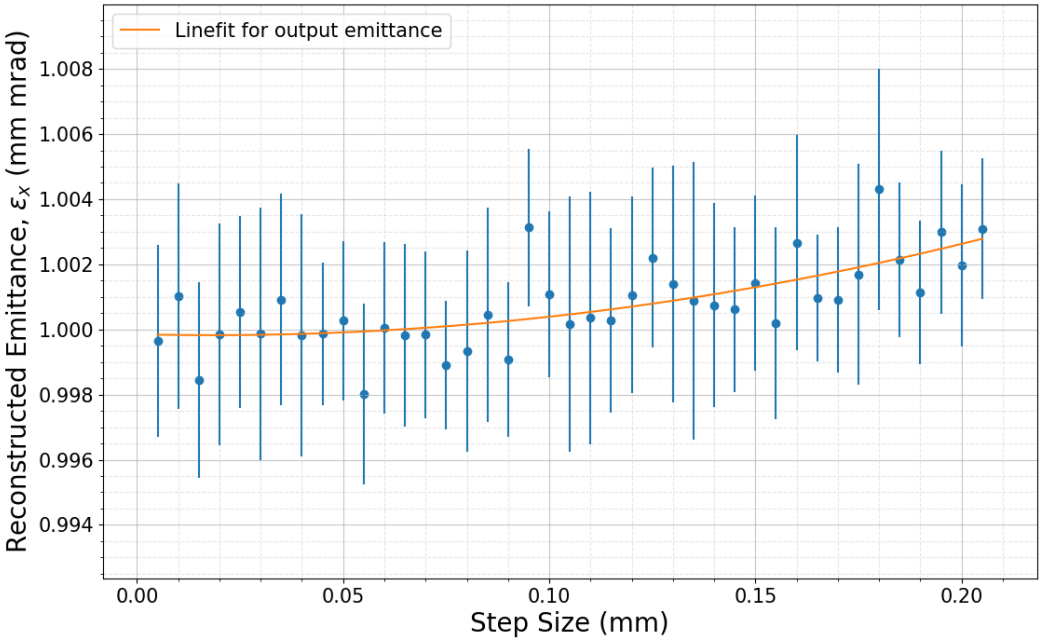

FIGURE 5.19: Effect of scraper step size on algorithm results.

5.6.3.2 Momentum Spread Estimation

The two scan algorithm requires an estimation for the longitudinal momentum spread in order to calculate the emittance. In ELENA, this value is measured using Schottky diagnostics on a coasting beam. It is expected that the method could be inaccurate by up to 20%. To investigate how this has an impact on the resultant emittance, the algorithm was run with varying degrees of incorrect momentum spread.

An estimation for the errors was derived from Eq. 4.31,

$$\frac{\Delta\epsilon_{rms}}{\epsilon_{rms}} = \frac{-1}{2\beta} D^2 {\sigma_\delta}^2 \left(2\left(\frac{\Delta\sigma_\delta}{\sigma_\delta}\right) + \left(\frac{\Delta\sigma_\delta}{\sigma_\delta}\right)^2 \right) \frac{1}{\epsilon_{rms}}, \tag{5.24}$$

and is displayed alongside MAD-X simulation results in Fig. 5.20.

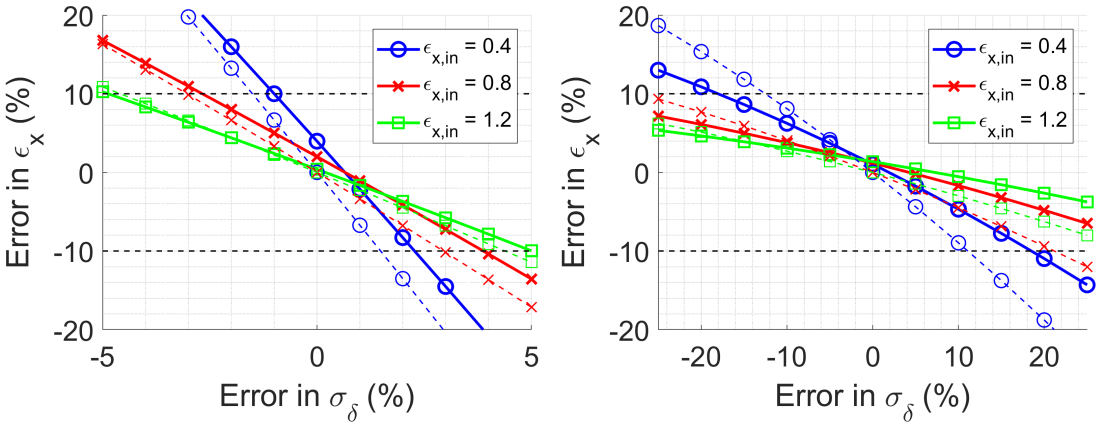

FIGURE 5.20: Error in reconstructed emittance based on inaccuracies in momentum spread estimation. Theoretical estimations are represented by dashed lines. Left plot $\sigma_\delta = 1{\times}10^{-3}$, right plot $\sigma_\delta = 3{\times}10^{-4}$.

The plots show that the derived equation is in good agreement with simulation results. It should be noted that there are small statistical errors resulting in the simulation lines not crossing the origin exactly.

For a pessimistic momentum spread of ($\sigma_\delta = 1 \times 10^{-3}$), and the smaller β_x/D_x ratio at the scraper, the algorithm is very sensitive to estimation errors. Performing the same analysis for the nominal momentum spread ($\sigma_\delta = 3 \times 10^{-4}$) shows that in fact the algorithm will return the emittance within the defined error value of 1 mm mrad for a momentum spread inaccuracy of up to ±20%. It may be expected that the higher the momentum spread is, the more likely the reconstructed

emittance will be affected by a percentage error, since the error is quantitatively larger for higher momentum spreads, i.e. 10% of 1×10^{-3} is larger than 10% of 3×10^{-4}. A similar argument may be made when observing the percentage error on resultant emittances based on their input values.

After confirming its suitability with simulations, dispersion and beta values predicted at the new position of the scraper, C4, were used in the equation to determine the impact of the error when using this algorithm for the specific case of ELENA. The results for a beam with 1 mm mrad and the nominal momentum spread predict emittance inaccuracies of -1.175% and 0.961% for momentum spread input errors of 20% and -20%, respectively, indicating this source of error will not be a significant problem for the current ELENA lattice configuration. In fact, for an input error of -100% (corresponding to $\sigma_\delta = 0$) the error estimation equation, Eq. 5.24, levels off at an emittance error of 2.67%. To create an error of -10%, the RMS momentum spread must be overestimated by 118%.

It is also worth mentioning that an error on the dispersion would take the same form as Eq. 5.24. The errors due to a dispersion mismatch can therefore be calculated in the same manner as above and the same percentage tolerances apply for both β_x/D_x ratios presented. When calculating the error on measurements, contributions from both momentum spread and dispersion should be considered.

5.6.3.3 Closed Orbit Offset

Another source of error may be found in a non-zero closed orbit offset, x_0. The algorithm calculates the area of the two PDFs determined by scraping, but more importantly here takes into account their relative position. Since a closed orbit offset consistent between two scraper scans would see no change in the relative PDF positions, the algorithm returned values with the same accuracy as for $x_0 = 0$, as expected.

A complication may arise however if the closed orbit changes between scraper scans. This effect is also analogous to an inaccurate measurement of the relative distance between the two scraper blades, so the effects could be investigated in parallel. Beams were run first being scraped from $+x$ side with $x_0 = 0$, and when

scraping from the opposite side the closed orbit was shifted by increasing amounts. The results may be seen in Fig. 5.21. Equation 4.31 was again rearranged to find an expression for the predicted impact of this error and plotted with the simulation data:

$$\frac{\Delta\epsilon_{rms}}{\epsilon_{rms}} = \frac{-1}{8\beta\epsilon_{rms}}(2(\bar{x}_+ - \bar{x}_-)\Delta\bar{x}_- - (\Delta\bar{x}_-)^2). \tag{5.25}$$

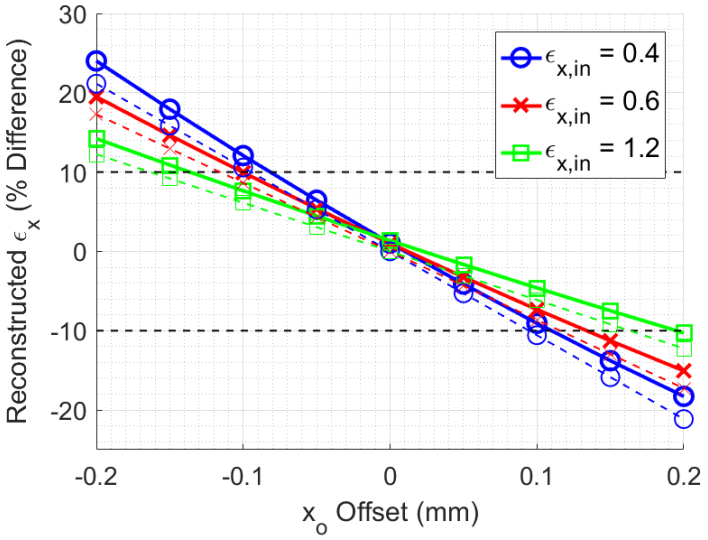

FIGURE 5.21: Error in reconstructed emittance as a result of a closed orbit offset between scraper scans. Input beams of were bi-Gaussian with $\epsilon_x = 1$ mm mrad and $\sigma_\delta = 3 \times 10^{-4}$. Theoretical estimations are plotted as dashed lines.

The plot shows that again the theoretical and simulated results are in agreement. A closed orbit offset or relative scraper blade position uncertainty of more than 0.1 mm would result in reconstruction errors higher than desired for beams of around 1 mm mrad for the pessimistic case, C2. The equation was used with the expected Twiss values at the scraper in ELENA, C4, and it was found that the closed orbit difference or blade uncertainty should be no more than 0.315 mm for that particular configuration.

5.6.3.4 Beta Function and Dispersion Inaccuracy

The algorithm relies on an estimation of the beta function at the position of the scraper blade. Similarly to the momentum spread estimation investigation, the simulation and algorithm were run with varying degrees of error in the input value of β_x, and for different input emittances. Again, a theoretical relation was derived

from Eq. 4.31 and was plotted with the data in Fig. 5.22:

$$\frac{\Delta\epsilon_{rms}}{\epsilon_{rms}} = \left(1 + \frac{\Delta\beta}{\beta}\right)^{-1} - 1. \tag{5.26}$$

The simulation data and theoretical prediction are in excellent agreement. It can be seen in the plot that the error has no dependence on the emittance of the input beam, as expected from Eq. 5.26. The error is also independent of the magnitude of β_x and so we may assert that for any Twiss parameters at the scraper, using the simulation-benchmarked equation, the error tolerances for 10% emittance reconstruction error are: $-9.091\% \leq \Delta\beta_x \leq 11.111\%$.

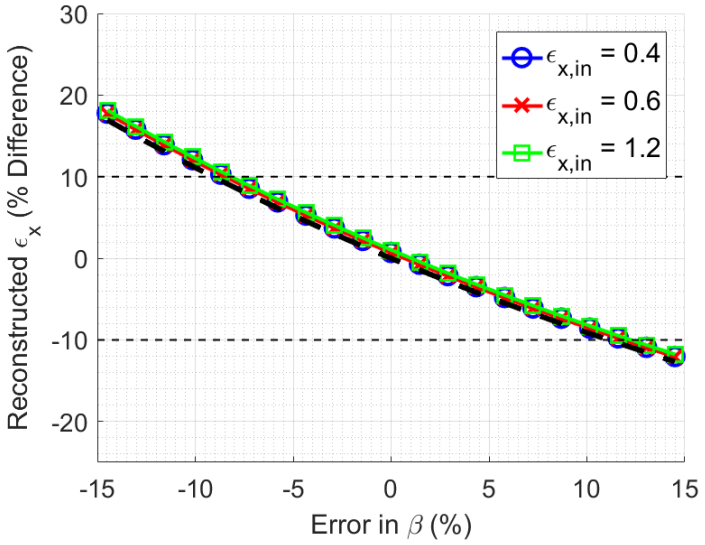

FIGURE 5.22: Errors in reconstructed emittance for varying degrees of error in $\beta_{x,y}$ estimation at the scraper. Input beams of were bi-Gaussian with $\epsilon_x = 1$ mm mrad and $\sigma_\delta = 3 \times 10^{-4}$. Theoretical estimations are plotted as dashed lines.

5.6.3.5 Scraper Blade Tilt

It is possible that a tilt misalignment in the scraper blades may cause an error in the scraper measurement. Because the scraper blades are attached to each other via the window configuration, both scraper blades were tilted through the same angle during these simulations. Both the x and y planes were considered for this error and so longitudinal momentum spread was set to zero to allow for a better comparison of the two planes. Tilt testing in x was performed with and without

the momentum spread and it was confirmed that there was negligible impact on the magnitude of the error.

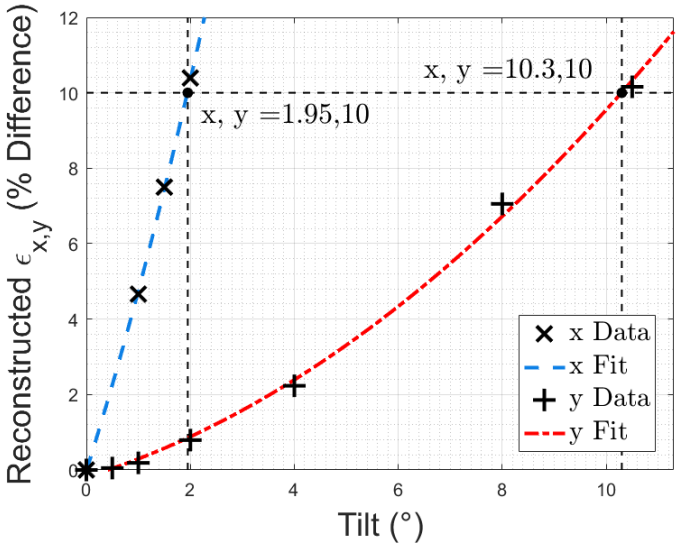

FIGURE 5.23: Effect on the reconstructed emittance due to tilt errors on the x and y scraper blades for a bi-Gaussian beam with $\epsilon_x = 1$ mm mrad and $\sigma_\delta = 0$.

The results of the simulations can be seen in Fig. 5.23. A trend was observed for both planes and simple polynomial fits were made in order to ascertain error tolerances. No theoretical estimation was made as the complex nature of considering four dimensions in phase space, as opposed to two previously, was deemed unnecessary for this application.

It can be seen that the vertical scraping was much more tolerant to a tilt misalignment. This is because the beta functions used were $\beta_{x,y} = 0.688, 3.001$ m, and a wider beam distribution is less affected by the error. The effects of this error may be considered negligible for the ELENA scraper since the tilt misalignment thresholds are much greater than what may be expected in practice, even for the most pessimistic case. Comparing the ratios of beta, $\frac{\beta_x}{\beta_y} = 0.23$, and the 10% emittance reconstruction tolerance, $\frac{1.95°}{10.3°} = 0.19$, suggests the error could decrease linearly with β.

5.6.4 Momentum-Emittance Correlation

As particle beams are decelerated they undergo adiabatic-like growth in transverse phase space. Additionally, due to the low energy of the beam, space charge effects

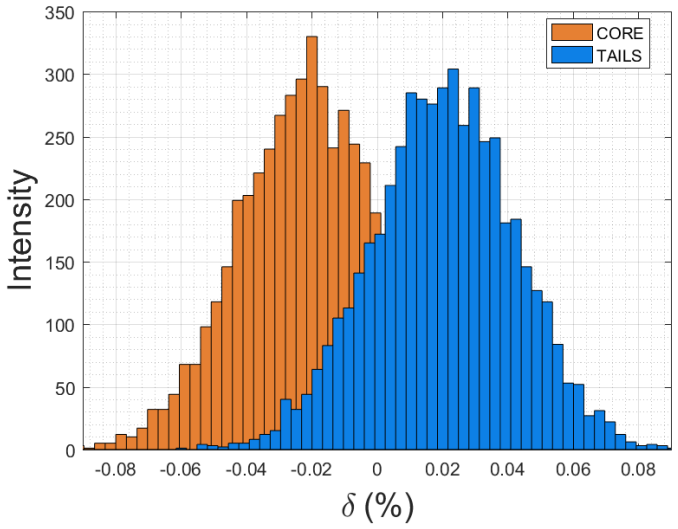

FIGURE 5.24: Distribution of momentum offsets for particles in a beam made to approximate the emittance-momentum spread effects of electron cooling. The difference in mean momentum between the core and tails is $\Delta\delta = 0.04\%$, with an average $\delta = 0$. The σ_δ of the core and tails is equal and adjusted such that the entire distribution has $\sigma_\delta = 3 \times 10^{-4}$.

such as IBS contribute to the growth in emittance. To counteract these effects it is necessary for electron cooling to be applied between deceleration ramps, at the energy plateaus of 0.65 MeV and 0.1 MeV. It is expected that the velocity distribution of the electron beam, v_{e^-}, will be parabolic in shape, centred on $x, y = 0$. As a result, it is likely that a correlation between higher emittance particles and a larger momentum offset will occur.

To investigate how the effects of an emittance-momentum offset correlation impacts the performance of the algorithm, beams were generated to approximate this effect. Bi-Gaussian beams with the same parameters as used previously were given a different mean δ at their core and tails. Figure 5.24 shows an example of the momentum distribution of one such beam. The momentum spread offsets were calculated such that their mean values have a defined separation, $\Delta\delta$, which may be adjusted to investigate how the strength of the correlation effects the performance of the algorithm.

The beam generation process also ensured that the entire beams have a nominal RMS momentum spread of $\sigma_{\delta,beam} = 3 \times 10^{-4}$, whilst the mean momentum offset of the entire beam is zero, to provide consistency with previous simulations. This

was done using:

$$\sigma_{\delta,C,T} = \sqrt{\sigma^2_{\delta,beam} - \Delta\delta^2} \tag{5.27}$$

$$\delta_C = -\frac{1}{2}\Delta\delta \tag{5.28}$$

$$\delta_T = \frac{1}{2}\Delta\delta \tag{5.29}$$

where $\sigma_{\delta,C,T}$ is the RMS momentum spread of the core and tails, δ_C indicates the mean momentum offset of the core and δ_T the tails.

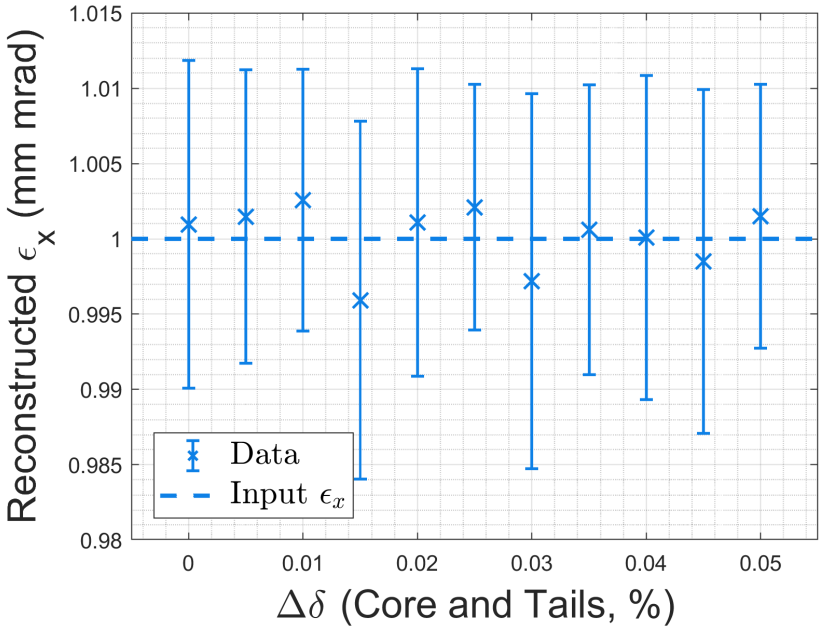

FIGURE 5.25: Effect of the emittance-momentum spread correlation on the accuracy of the algorithm.

The characteristic asymmetric CDF and PDF shapes generated by scraping such a distribution can be seen in Fig 5.16, g) & h). There is a shift of the core to negative x and the tails to positive x which may be observed in the distributions. It is clear to see this when scraping from positive x, and particularly so for the CDF, f_+, (h).

The impact of the emittance-momentum spread correlation on the reconstructed

emittance values can be seen in Fig. 5.25. Each point represents the mean reconstructed emittance from 20 simulations with that particular $\Delta\delta$. Statistical fluctuations are observed, however no significant trend of increasing error may be observed. The algorithm was tested up to momentum spreads differences above which the beam appears to be unphysical using this approximation ($\Delta\delta >> \sigma_{\delta,beam}$), and hence the impact of the effect on the accuracy of the algorithm may be deemed negligible.

5.7 Extra Beam Information

5.7.1 Emittance-Momentum Spread Correlation Coefficient

We may compute an emittance-momentum spread correlation coefficient which gives an indication of the strength of this effect. The term will henceforth be referred to as simply the "correlation coefficient", and is described by:

$$\langle(\delta_p - \bar{\delta_p})A\rangle = \frac{\sum_{i=1}^{2}(N_i\sqrt{\frac{\epsilon_{rms,i\pi}}{2}}(\bar{\delta_i} - \bar{\delta}_{beam})^2)}{\sum_{i=1}^{2} N_i}, \tag{5.30}$$

where the subscripts $i = 1, 2$ refer to the core and tails of the beam. It is also possible to split the beam into more than two parts in order to simulate a more continuous correlation effect, however here two parts are adequate for showing the algorithm works. The correlation coefficient may be reconstructed using known quantities and those obtained for the algorithm:

$$\langle(\delta_p - \bar{\delta_p})A\rangle = \frac{{\sigma^2}_+ - {\sigma^2}_-}{4D\sqrt{\beta}}. \tag{5.31}$$

Figure 5.26 shows the output from the algorithm after simulations and a plot of the analytically computed function. There is an excellent agreement between the two which confirms the algorithm may be used to further characterise the beam. In fact, measurements of this quantity may be used to provide insights into the effects of the electron cooler.

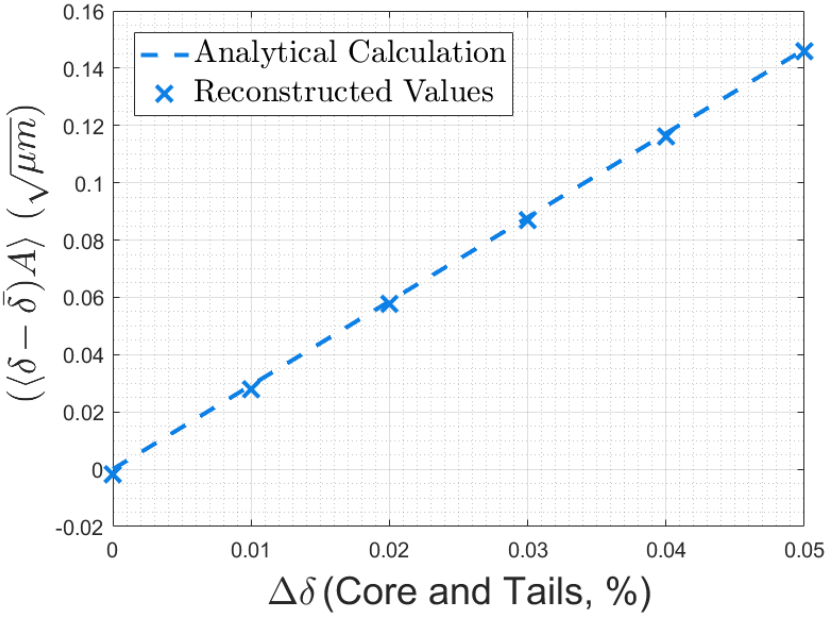

FIGURE 5.26: Algorithm estimates for the correlation coefficient compared with the analytical predictions.

One possible way to investigate the electron cooler would be to use simulation tools, such as BETACOOL, to obtain the resultant beam distributions for different v_{e^-} profiles in the electron cooler. The correlation coefficient could be computed for various cases and results could then be compared with measurements of the real beam over different time periods.

5.7.2 Closed Orbit

One of the useful expressions to come out of the derivation of the algorithm gives the magnitude of the momentum-dependent closed orbit:

$$x_0 + D\bar{\delta} = \frac{(\bar{x}_+ + \bar{x}_-)}{2}. \tag{5.32}$$

To test the accuracy of this algorithm, two sets of simulations were run using the Python script, with the pessimistic β_x/D_x ratio C2, and bi-Gaussian distributions with the usual σ_δ and n_{inc}. Firstly, the average momentum offset, $\bar{\delta}$, was held at zero whilst the closed orbit, x_0, was increased incrementally. For each value of x_0, 10 simulations of 10,000 particles were run. The quantity on the right-hand side of Eq. 5.32 was calculated from the algorithm, and the difference between this

value and the input value were calculated and averaged over all simulations. The results are shown in Fig. 5.27 and confirm that the algorithm will estimate the closed orbit offset with very high accuracy.

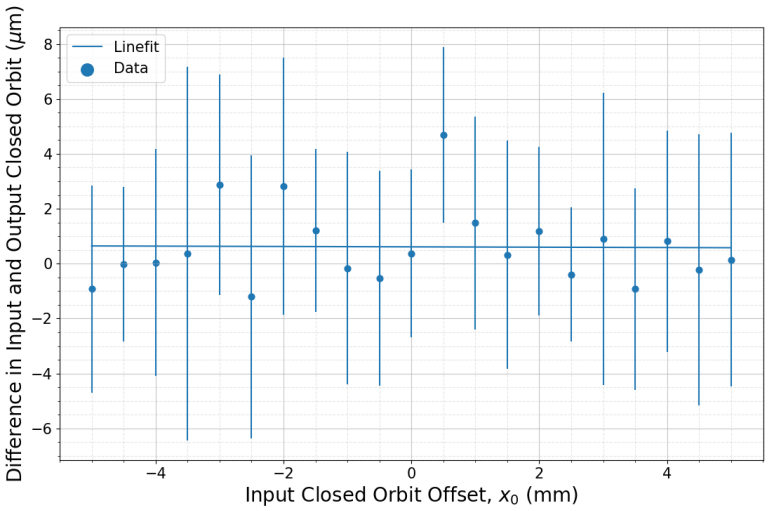

FIGURE 5.27: Accuracy of the algorithm when estimating the closed orbit offset.

Secondly, the closed orbit offset was held at zero whilst adjusting the mean momentum offset of the beams. The offset was adjusted such that it would give a transverse shift of the same order as the range for the closed orbit offset trials. The quantity returned by Eq. 5.32 was divided by D_x at the scraper, and the difference from the input $\bar{\delta}$ was found and averaged over the simulations. The results are shown in Fig. 5.28 and again show that the accuracy reconstructs the transverse offset extremely well.

Further testing was performed to ensure that the algorithm correctly calculates the transverse offset when a combination of both imperfections is present. As expected, the returned quantities were around the same level of high accuracy as with the individual tests.

5.8 Summary

In this chapter, simulations have been performed to test the effectiveness of the scraping algorithms. First, an investigation into errors arising from transmission

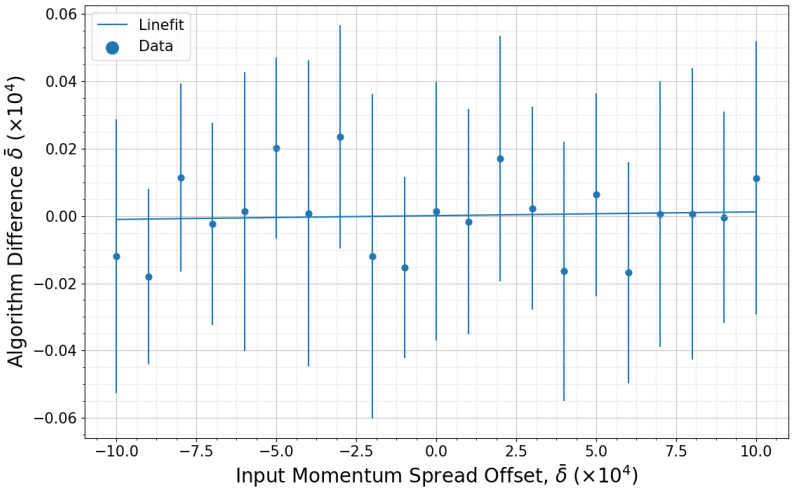

FIGURE 5.28: Difference in values of input and calculated momentum offset values.

through the scraper blade using FLUKA was performed and found the 1 mm thick aluminium blades to be suitable. The methods for tracking and scraping the beam in MAD-X were presented including a description of beam generation for bi-Gaussian beams. Similar simulation methods using a custom Python script were also presented.

The code currently used for the AD scraper was tested on results from MAD-X scraper simulations in ELENA for beams of varying degrees of a bi-Gaussian nature and momentum spread. The tests were performed for two different β_x/D_x ratios and found that in both cases the AD algorithm is not suitable for use within ELENA.

The Gaussian only fitting algorithm was shown to work for Gaussian beams with various momentum spreads. When considering its use for bi-Gaussian beams it was found that the algorithm could reconstruct the emittance to within a 10% error for values of around $n_{inc} = 1.7$. This means the algorithm could provide a rough estimate for the emittance in the case only one direction measurement is available and beams appear to the operators to be approximately Gaussian. Similarly, the algorithm was used to estimate the momentum spread of a beam at various values of n_{inc} showing larger errors for a higher β_x/D_x ratio. Again this method could be used as a rough estimate for the momentum spread if the beam

does not appear to be strongly non-Gaussian.

For the two scan arbitrary beam profile method, a comparison of spline fitting and Reimann sums for treating data was performed and showed that computationally less expensive Reimann sums were just as suitable for differentiating the data. The algorithm was shown to work to well within the desired error tolerance of 10% in all cases in the absence of errors i.e. for a non-Gaussian beam with momentum spread in a dispersive region, and an emittance-momentum offset correlation. Error tolerances for the algorithm were determined for a range of errors and none were found to cause any significant problems. Finally, the algorithm was shown to accurately reconstruct an emittance-momentum offset correlation for a range of values and to accurately estimate the closed orbit of the beam.

This chapter has shown through the use of simulations that both algorithms work well under the conditions they were developed for and has investigated error tolerances. In the next chapter, the algorithms are put to use on data taken from ELENA at the end of the commissioning run in 2018.

Chapter 6

Measurements

6.1 Introduction

Numerous scraper measurement campaigns were made during ELENA commissioning in 2018, which were then analysed using a combination of the two new scraping algorithms. A total of 18 individual scraper measurements are used for analysis here. These were taken in all four scraper directions at three different times during the ELENA cycle, along the intermediate and ejection cooling plateaus.

In this chapter, the details of the data acquisition process are presented, followed by an explanation of how the collected data is treated and then analysis of the measurements. The chapter concludes with a discussion of all results, including summary tables containing all measured and reconstructed quantities.

6.2 Collecting Data

The user interface to control the scraping system is presented in Fig. 6.1 [109]. In the top right, a plot shows the ELENA deceleration cycle. The operator may set the scraper movement start time by adjusting the vertical slider or by entering a time lag in ms, here it is set to 6400 ms, corresponding to the start of the first cooling plateau for this particular cycle.

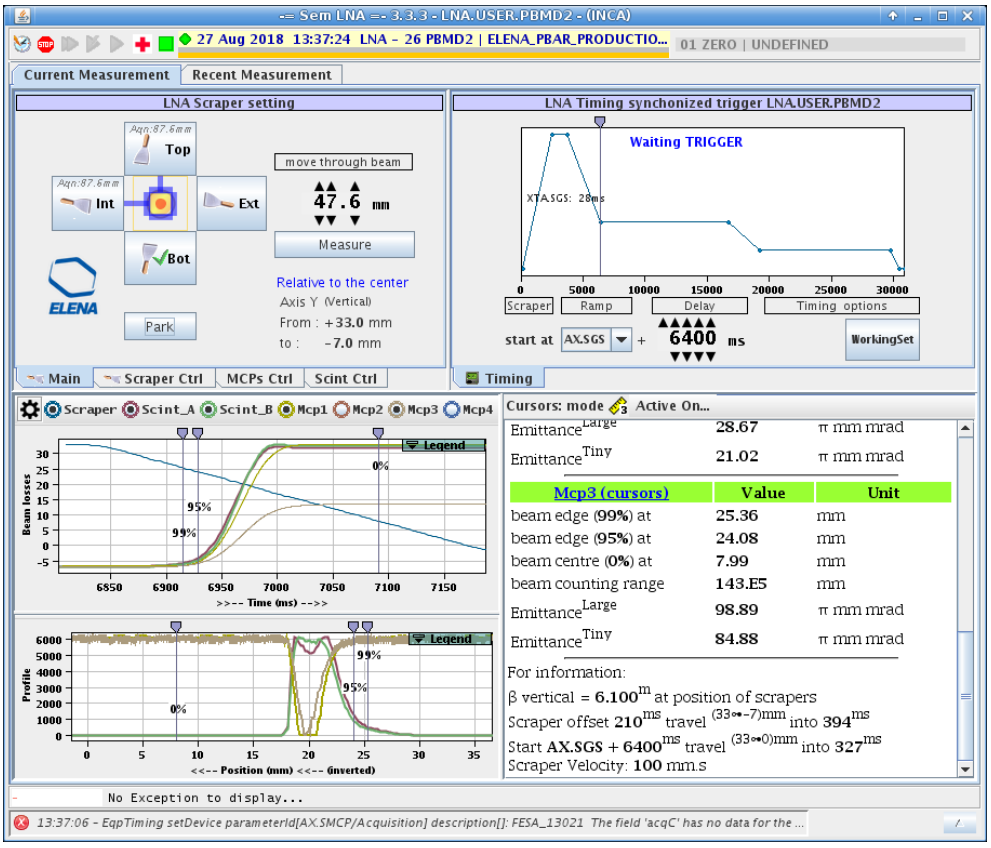

FIGURE 6.1: The ELENA scraper GUI.

The scraper blade start point is at a fixed value, corresponding to ±33 mm depending on the direction of the scraper blade. The user may set the end point by adjusting the value in the top left of the GUI currently set to 47.6 mm. This value corresponds to the total extension of the scraper blade arm and is corrected and displayed in terms of the centre orbit position below the "Measure" button. Typically the default setting is to scrape from ± 33 mm to ∓ 7 mm, however to effectively scrape the entire beam it is suggested to move the scraper to ∓ 27 mm. As a fail-safe precaution, the system causes the scraper blade arms to fully retract and become inoperable if they are extended too far and have a danger of contacting the opposing side of the vacuum chamber, so caution is required when scraping beyond this value.

The GUI allows the operator to adjust the voltages on the MCPs allowing to compensate for sensitivity to signal and similarly scintillator acquisition parameters may also be adjusted. The operator may select a scraper blade by clicking on one of the four buttons in the top left, and then prime it to scrape the beam

during the next cycle by clicking the "Measure" button. The scraper blade will then perform the action at the designated time in the cycle.

The bottom left quarter of the GUI panel displays the data from the most recent measurement, with the option to select which detectors to plot. The top plot shows the cumulative beam losses as a function of time, and the bottom plot shows the signal as a function of the scraper position. The display is useful for gaining a quick insight into the beam quality and position. To the right of this, calculations for the beam edges, centre and emittance similar to those performed for the AD scraper are displayed.

Once the beam has been scraped, the raw data from the detectors and scraper system combined with general information such as time, beam type and settings, are saved in a single file containing previous measurements in JSON (JavaScript Object Notation, [110]) format. The data may then be accessed using the same GUI at a later date. Selected variables useful for analysis in the JSON files are displayed in Table 6.1.

Table 6.1: Selected contents of JSON scraper file.

Parameter Name	Example	Notes
particule	'PBAR'	Particle type
startScraperDelay	6800	Measurement start time (ms)
scraperDirection	'Ext'	Possibilities: 'Int', 'Ext', 'Top', 'Bot'.
scraperY	1×1499 double	Array of scraper positions (mm)
scraprXms	1×1499 double	Corresponding array of scraper times (ms)
scintY	2×749 double	Array of scintillator signal intensities (arb.)
scintXms	1×749 double	Corresponding array of scintillator times (ms)
mcpsY	4×3099 double	Array of MCP signal intensities (arb.)
mcpsXms	1×3099 double	Corresponding array of MCP times (ms)

6.3 Data Processing and Analysis

The mathematical theory for calculating the emittance of the beam based on two scraper measurements is explained in Section 4.4.1, however the process of converting raw data to an emittance measurement requires several careful steps.

Here the process is explained in detail, with a particular focus on the practical considerations made when dealing with real-world measurements.

6.3.1 Scraper and Detector Correlation

Once the raw data is acquired the scraper position must be correlated with the intensity signals from the detectors. The analysis process beings by taking the maximum and minimum position values of the scraper to determine the start and end points of movement. As the scraper does not instantly accelerate to its maximum velocity, a threshold of 2 mm is set. Data points between 2 mm from the start and end positions of the scraper's movement are selected.

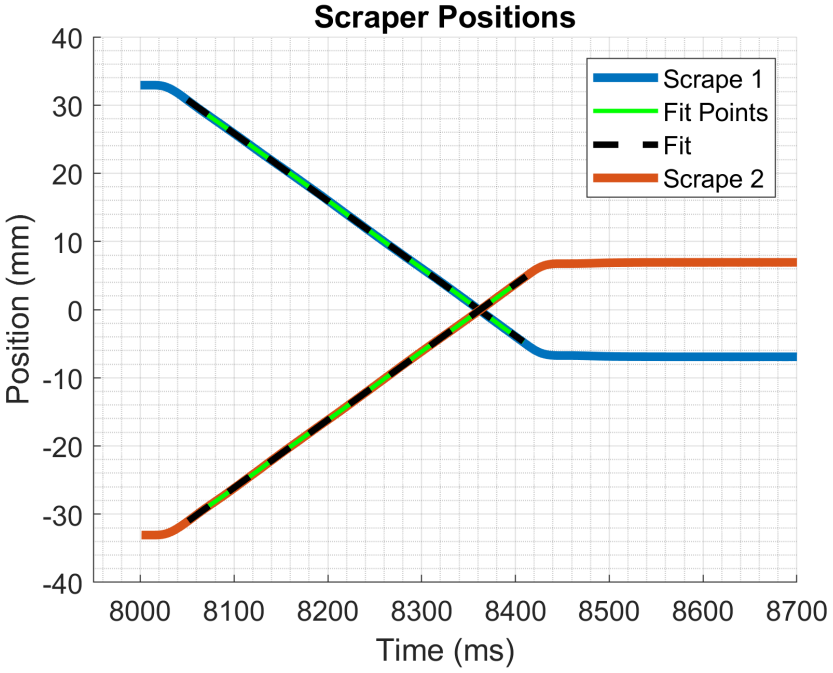

FIGURE 6.2: Scraper positions as a function of time, with highlighted fit points and corresponding linear fits.

A linear fit of these data points gives an equation to describe the scraper's position as a function of time. The fit points, fit and raw data can be seen in Fig. 6.2, for two separate scraper measurements in opposite directions. Figure 6.3 shows the scraper velocities obtained through simple finite difference differentiation. The fit points are highlighted and emphasise why the 2 mm threshold is necessary to negate scraper acceleration and deceleration. This plot may be monitored when using different scraper speeds in order to adjust the threshold if necessary.

The scraper velocity may be extracted from the gradient of the line fit and compared with the velocity setting at the time of the measurement. In the examples when scraping horizontally, shown in Figs. 6.2 & 6.3, the velocity was calculated to be -99.032 mm/s and 99.656 mm/s for a 100 mm/s input. Discrepancies are typically of this magnitude and are inconsequential since only the real (measured) velocity has an impact on the analysis, and is used.

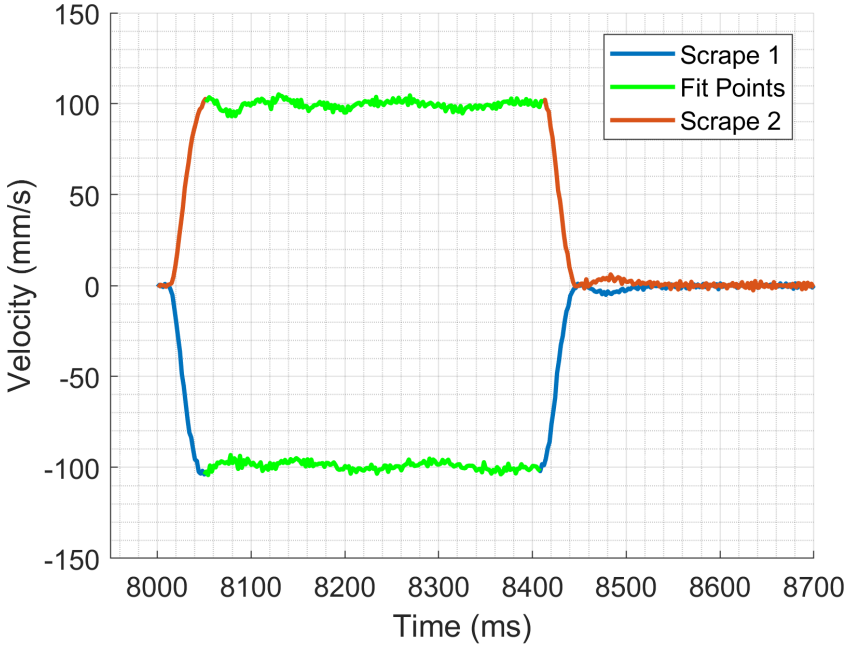

FIGURE 6.3: Calculated scraper blade velocity when scraping horizontally in opposite directions.

Figure 6.4 shows the velocities calculated for two vertical scraper movements. When compared with the horizontal data larger fluctuations are observed for both vertical directions. This could be due to the weight of the scraper blade acting along the same axis as the actuation system. Despite the noise, the averaged velocities are within ±1.2 mm/s of the 100 mm/s setting. In fact, the small deviation in average velocity could also be described by the geometry of the scraper arm; when scraping from the top (dropping arm down) the average velocity is consistently greater than the input velocity, and from below (pulling arm up) is consistently smaller. Figure 6.5 displays the velocities calculated for several measurements in

each direction at different times in the ELENA cycle. Consistencies in the direction and magnitude of the velocity offset and size of errors due to noise can clearly be seen for each direction.

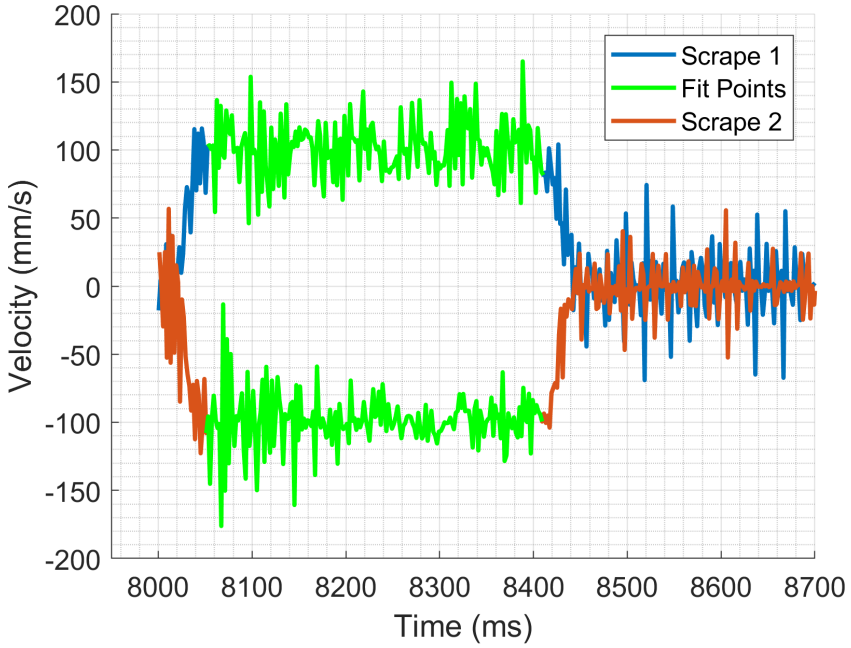

FIGURE 6.4: Calculated scraper blade velocity when scraping vertically in opposite directions.

Table 6.2 summarises the data taking the mean of all scraper velocities in each direction. Errors are propagated from 95% confidence intervals from the linear polynomial fit to the scraper position and time. Larger errors on the vertical scraping directions are consistent with the discussion above.

TABLE 6.2: Scraper velocities

	Ext	Int	Top	Bot
Calculated Speed (mm/s)	99.073	99.655	101.194	99.000
Error (mm/s)	0.017	0.016	0.036	0.023
Standard Deviation (mm/s)	0.045	0.013	0.064	0.036
Number of Measurements	9	7	12	8

Detector signal times are input into the linear polynomial resulting in an array of scraper positions associated with the array of detector intensities. These data sets then form the basis of the analysis. Figure 6.6 shows raw scintillator signals as

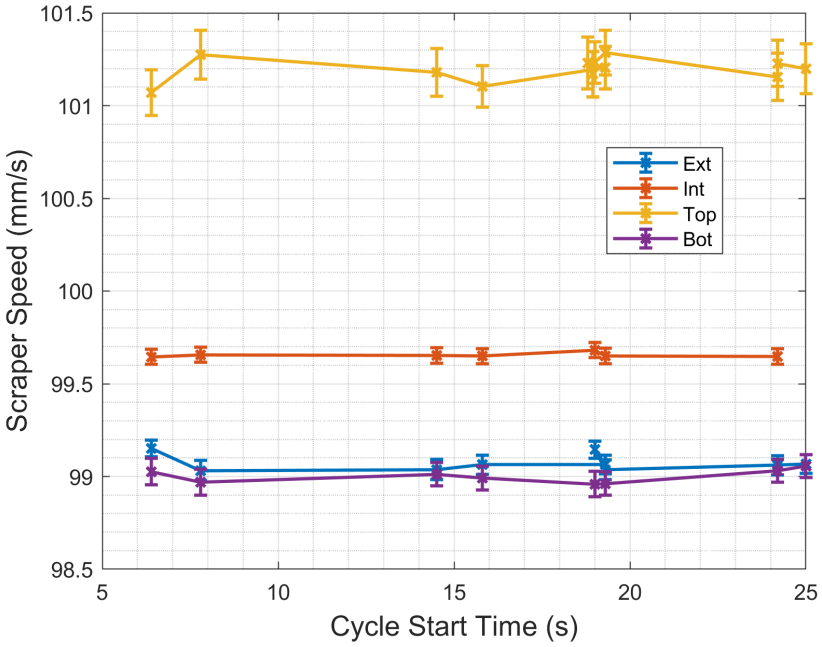

FIGURE 6.5: Scraper speed calculations for several measurements in each direction.

a function of time, and the same signals as a function of scraper position after the process described above. The plots show signal from both scintillators taken from two separate shots, scraping from opposite directions. Mirroring of the scintillator data when scraping from positive x can be seen as expected. Observing that signals drop to zero at the same point (or slightly overlapping if considering dispersive effects) in the position plot is a good check to ensure the conversion process has worked correctly, and should correspond to the position of the core of the beam.

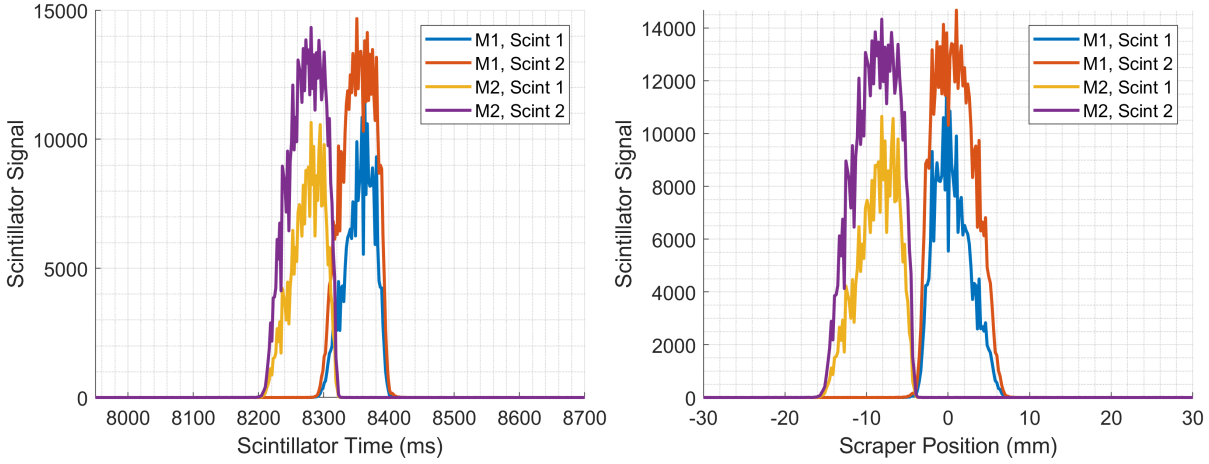

FIGURE 6.6: Scintillator signals as a function of time (left) and position (right).

6.3.2 Emittance Calculations

Figure 6.7 is a visual representation of the calculation process to aid with an understanding of the structure of the analysis program. The emittance reconstruction equation for the two scrape reconstruction method (Eq. 4.31) is shown with a green border.

6.3.2.1 Quantities Obtained Through Scraper Measurements

Now that the detector signals can be transformed into terms of scraper position the data may be mathematically analysed to reconstruct the emittance. The first step is to determine which quantity to reconstruct and for when, i.e. horizontal or vertical emittance and how far along the cycle. The analysis program can load two scraper measurements from opposing directions, in the same transverse plane, and both taken at a specific time. After transforming detector data in terms of scraper position, it is useful to plot the signals from all or several detectors, depending on particle type. This allows one to determine which signals appear clearest for this measurement and to determine a single detector for use in the analysis program. It is necessary to apply cuts to the data to ensure that noise detected before or after the measurement is not incorrectly included as large amplitude particles in the calculations. Typically for these measurements data was clipped within ± 25 mm.

Scintillator and MCP data is given as signal intensity at a specific time and is not cumulative. The intensities for scintillators and MCPs have arbitrary units due to their sensitivity settings being adjustable. Although intensities on the same detector may be compared under different conditions to indicate relative beam intensities (and would give a rough estimate at best), the arbitrary units of the detectors are not relevant to the analysis process. Working with a single measurement direction at a time, the first analysis step is to convert the detector data to a cumulative signal by a simple summing function. All values in the cumulative signal array are then divided by the total sum in order to normalise and give a cumulative distribution function (CDF), $F(x_s)$. (Here x_s indicates

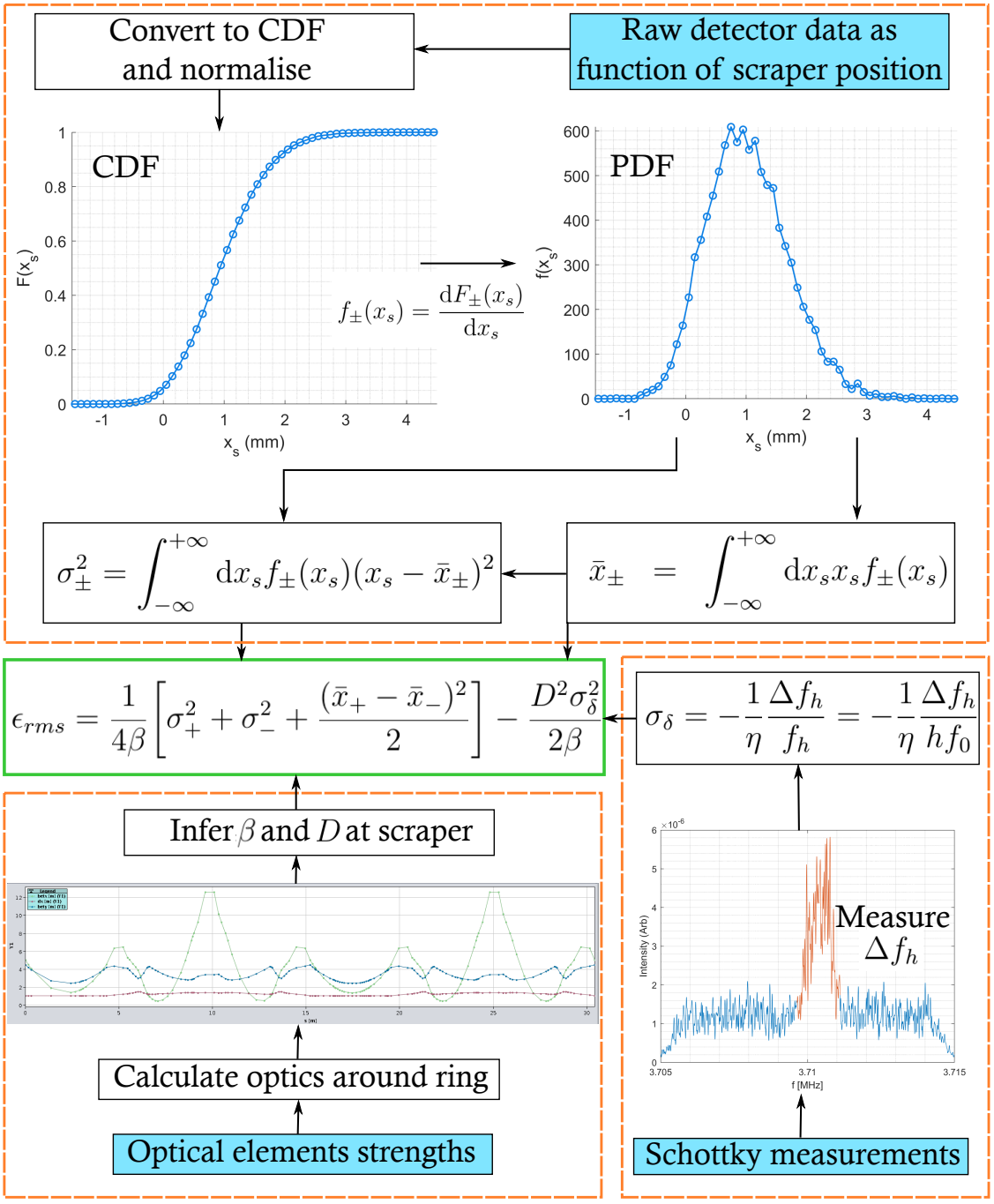

FIGURE 6.7: Schematic diagram of the emittance calculation process. Three inputs are highlighted in blue, their associated calculation schemes are separated by dashed orange borders and the emittance equation is highlighted in green.

horizontal transverse measurements, however, vertical analysis is identical when replacing all x with y.)

The CDF may then be converted to a probability density function (PDF), $f(x_s)$, by differentiation through the finite difference approximations. Although

the resultant PDF has the same distribution as the raw data, the new scaling of the PDF is crucial for the algorithm. From here the algorithm follows the mathematical steps laid out in Section 4.4.3 to arrive at values for the beam variance σ^2 and $\bar{x}$ for this particular scraper direction. This process is repeated for the scraper measurement in the opposite direction resulting in $\sigma_{\pm}^2$ and $\bar{x}_{\pm}$ for each direction (+ or −) which may then be inserted directly into the emittance reconstruction equation.

6.3.2.2 Quantities Obtained Without Scraping

Referring back to the two scan equation (Eq. 4.31) or Fig. 6.7, we see other quantities which may not be determined through scraper measurements. The beta function, β, and the dispersion, D, both for the appropriate transverse plane, are estimated at the position of the scraper. To do this the optics around the ring are calculated using the strength settings of the elements at the time of the scraper measurement. The values may then be read from the resultant plot or data table and input into the equation.

The final value to obtain is the RMS longitudinal momentum spread, σ_δ. As discussed earlier, the value must be calculated from Schottky data taken at the same time in the cycle as the scraper measurement. The equation presented in Section 3.3.5 is shown again here for convenience:

$$\sigma_\delta = -\frac{1}{\eta}\frac{\Delta f_h}{f_h} \tag{6.1}$$

where f_h is the centre frequency of the peak in the Schottky data, Δf_h is the RMS width of the peak, h is the harmonic number and η is the frequency dispersion or phase slip factor.

Here the raw Schottky data is taken from a single transverse pickup and a spectral density distribution is acquired from a spectrum analyser. The system summing over all pickups will be implemented during LS2. Figure 6.8 shows an example of such data, taken during the intermediate cooling plateau and scanning around the 10th harmonic, $h = 10$, with respect to the revolution frequency of $f_0 = 371$ kHz.

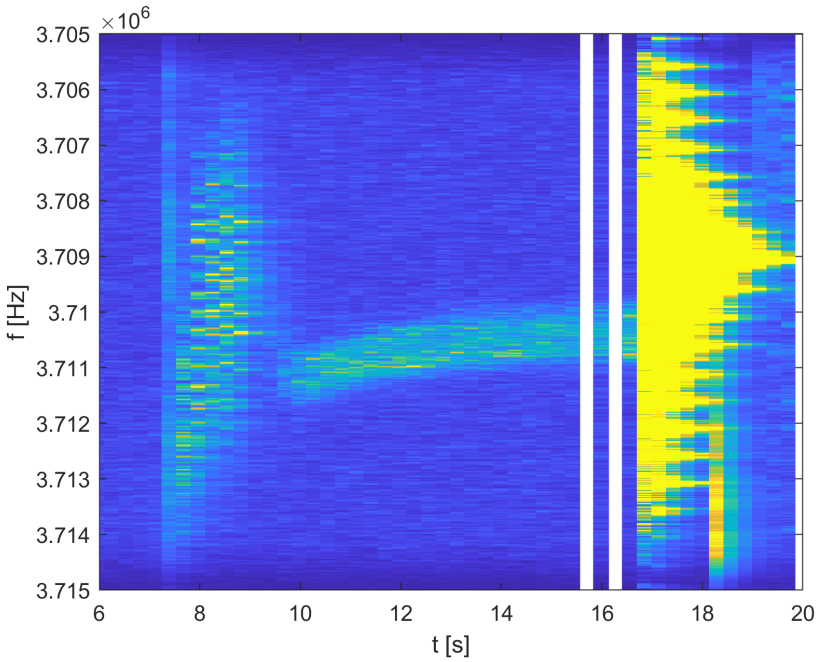

FIGURE 6.8: Spectral density distribution for Schotty measurements along the intermediate cooling plateau.

Rebunching may be observed to the far right side of the figure where the signal appears to be saturated. Only when the beam is coasting, a coherent signal useful for analysis may be observed which may be seen to the left of the rebunching signal. On the far left of the plot a more convoluted signal may be seen, where the beam is debunched and cooled. This data may also be used to obtain an estimate for the momentum spread at these times but with larger uncertainties than for the clear signal at the centre of the plot.

To begin the analysis, a "slice" of the data corresponding to a specific time is selected, represented in the plot between two vertical white lines. A measurement of the RMS width of the signal gives Δf_h for this particular time whilst the centre point of the peak gives f_h. Figure 6.9 shows the intensity of the raw signal at this particular time. The signal distinguished from noise by an orange highlight is used for the RMS and centre point calculations.

The phase slip factor, η, may be estimated from an accurate simulation of the lattice, similarly to the estimates for the β functions and dispersion, D. A MAD-X simulation of the ELENA optics corresponding to those during measurements gave $\eta = -0.7304$ for the intermediate cooling plateau energy, which is the value used

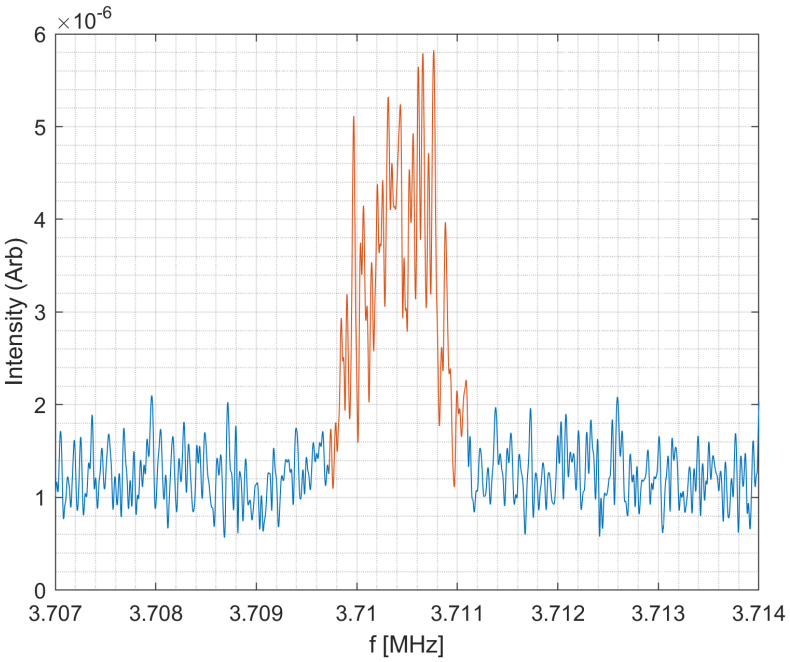

FIGURE 6.9: Raw data "slice" of Schotty measurements.

in the calculations performed here. The RMS longitudinal momentum spread may then be calculated from Eq. 6.1 for all points with Schottky data during coasting beam. As with scraping from several directions, it is assumed that the cycle and beam are set up and behave in the same manner for each measurement, so it is recommended that the Schottky data be taken the cycle before, in between or the cycle after scraper measurements to ensure a most accurate estimate.

6.4 Error Calculations

The effect of errors and error tolerances on the reconstructed emittance were covered in detail in the previous chapter. Here the actual magnitudes of errors are considered for application to these results. It was determined that all sources of error were within accuracy tolerance limits so the main sources of error considered here are the most significant sources in the emittance reconstruction equation: $\beta_{x,y}$ function estimates, when scraping horizontally the error on σ_δ and D_x and finally horizontal and vertical closed orbit fluctuations between shots, Δx_0, Δy_0.

To determine an error value for D_x and the $\beta_{x,y}$ functions a MAD-X simulation of the optics was created. A parameter scan was performed by adjusting the

strengths of the three families of quadrupoles by the same percentage. This was done to both simulate a systematic error in the estimation of magnetic fields based on current, and to assume a pessimistic case in a random error scenario i.e. errors don't cancel. The optics at the scraper, $\beta_{x,y}$ and D_x specifically, were recorded.

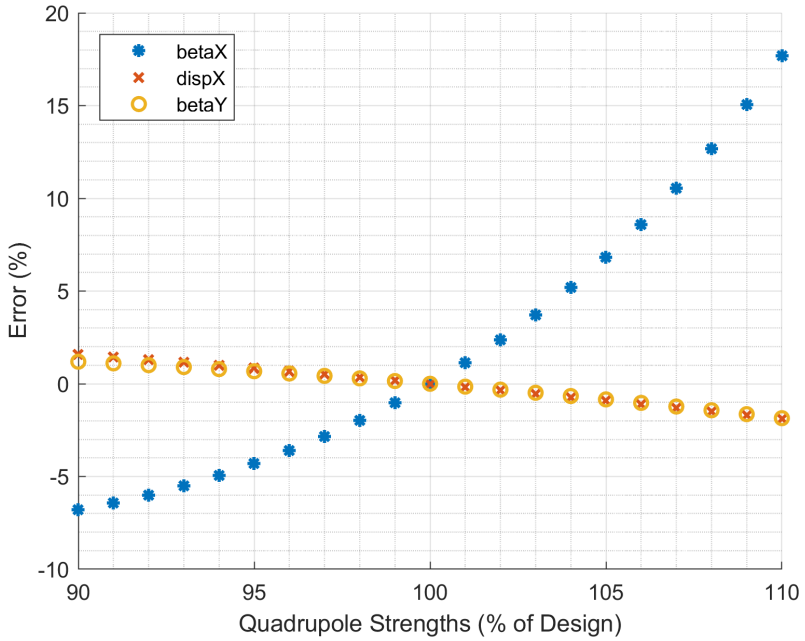

FIGURE 6.10: Quadrupole scan results on optics at the scraper.

Figure 6.10 shows the results from the parameter scan. It is clear that β_y and the dispersion, D_x, are not significantly affected by magnet strength uncertainties. The horizontal β_x, however, appears to be relatively sensitive to incorrect estimations of quadrupole field strengths. Fitting to the results and making a conservative estimate of $\pm 5\%$ error on quadrupole field measurements, errors in β_x of 6.81% and -4.31% were determined. Similarly, errors for β_y and D_x were calculated. The results are summarised in Table 6.3.

TABLE 6.3: Uncertainties in optics at the scraper.

	β_x	β_y	D_x
Assumed Value (m)	3.21	2.97	1.38
+5% Field Uncertainty Error (%)	6.81	-0.84	-0.92
-5% Field Uncertainty Error (%)	-4.31	0.68	0.85

For the momentum spread estimates, σ_δ, methodical errors associated with integration techniques were recorded when measuring the RMS widths, Δf_h and centre points, f_h of the Schottky signals from raw data. An error on the phase slip factor, η, was estimated at 5% based on the method used to attain it from a MAD-X simulation of the optics. These errors were then propagated through Eq. 6.1. The magnitudes of the resultant errors are presented with the measured values in the following section and are around 10%.

To account for errors on the dispersion-dependent closed orbit offset (henceforth referred to as just the closed orbit), Δx_0, Δy_0, repeat measurements were examined. Due to limited beam time only two repeat measurements were made and so it was assumed that those repeat measurements show typical per-shot fluctuations in beam position. Repeat measurements were made once for the vertical plane, in the "Top" direction, and once in the horizontal plane in the "Ext" direction. The repeat measurements were not made immediately after each other and in fact, were separated by around half an hour and 8 - 10 other measurements each.

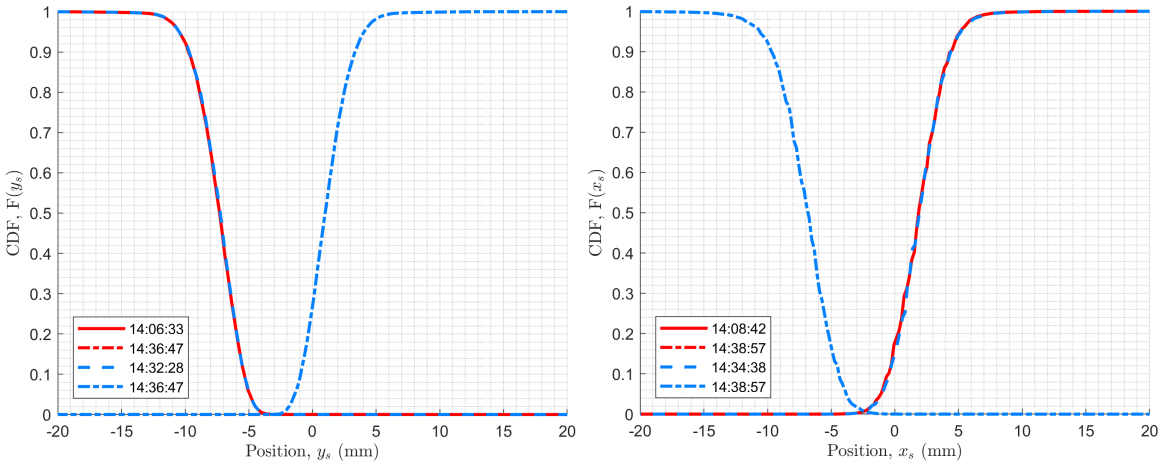

FIGURE 6.11: Repeat measurements for the vertical (left) and horizontal (right) scraper directions. The times the measurements were taken is shown in the legend to highlight consistency over time (*hh:mm:ss*).

Figure 6.11 shows plots of the data for both directions, as well as the single corresponding measurement in the opposite direction. Visually it is apparent that the scraping profiles and positions do not change in a significant manner for either horizontal or vertical measurements. The mean value of the PDFs, $\bar{x}$, was

calculated from the measurements and compared between repeat measurements. Table 6.4 shows the results of these calculations. Because these are the only these

TABLE 6.4: Mean position of all particles for two scraper measurements in the same directions.

	Top	Ext
Run 1 (mm)	-7.46	1.94
Run 2 (mm)	-7.43	1.98
Difference (mm)	0.03	0.04

two repeat measurements, the differences were used as guide values and so the errors on vertical and horizontal closed orbit offsets were set at 0.03 mm and 0.04 mm, respectively. The errors are propagated through the two scan emittance equation, affecting $\bar{x}_{\pm}$ and $\sigma_{\pm}$, and combined with other sources of error determined above. The errors are around 10% of the maximum tolerance value calculated in Chapter 5 (0.315 mm).

All sources of error were combined to determine an error on the measured emittance. It is clear from this analysis that, as expected, the errors on horizontal measurements are much more significant than vertical due to a combination of larger β_x errors, uncertainties in momentum spread and a slightly larger Δx_0.

6.5 Results

All measurements were made during energy plateaus (injection, intermediate cooling and ejection plateaus) with RF off in order to allow for a coasting beam which is necessary for the algorithms and Schottky measurements. Figure 6.12 shows times at which scraper measurements were made along an ELENA antiproton commissioning cycle.

Measurements taken at injection and at the start of the ejection plateau were not suitable for analysis with the two scan algorithm. A bug in the code which saves the scraper arm positions affected some measurements at these times, at least once in each plane. Additionally, during horizontal measurements at injection, which were not affected by this bug, the scraper blade did not entirely move

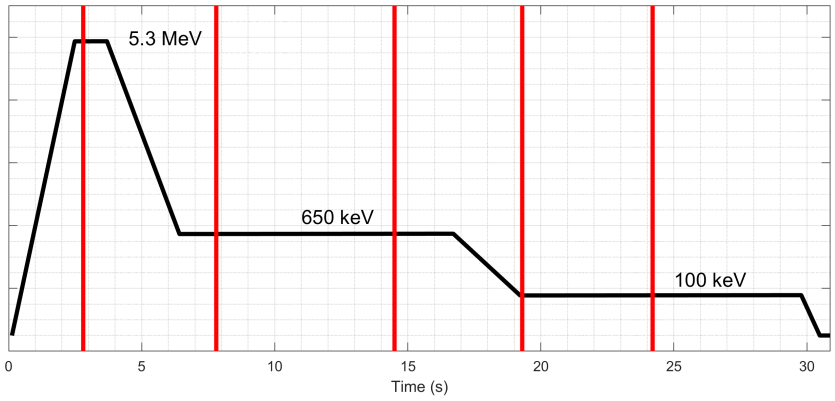

FIGURE 6.12: Times at which scraper measurements were made during an ELENA antiproton commissioning cycle, marked by vertical red lines. The y-axis does not have units as the plot is representational. Three energy plateaus are labelled.

through the beam, resulting in no information at the core (a plot showing the raw data may be found in Fig. A.1).

The only Schottky data available for the scraper measurements was taken during the intermediate plateau where, fortunately, the scraper system was fully operational and so these sets of measurements could be used to test the algorithm and investigate the effects of electron cooling. Measurements at the start of the ejection plateau were not affected by the scraper arm bugs, however a lack of Schottky data gives higher priority to intermediate plateau measurements. The unaffected ejection plateau measurements still proved useful, containing the repeat measurements that formed the basis of the closed orbit error estimations above.

The two sets of measurements (4 directions at each time) taken along the 650 keV intermediate plateau were made at times along the cycle of $t = 7.8$ s and $t = 14.5$ s. This sub-section begins with analysis of the vertical measurements followed by a discussion of the available Schottky data and corresponding scraper measurements. Additional scraper measurements for an energy of 100 keV were also made during a different cycle with a slightly longer repetition rate, and are discussed after the measurements made for the cycle shown.

6.5.1 Intermediate Plateau: Cooling at 650 keV

6.5.1.1 Vertical Measurements

Measurements were taken along the intermediate plateau. This is the first cooling plateau and so the measurements serve to check the cooling efficiency. The nominal operating parameters of ELENA's electron cooler may be found in Table. 2.1.

First, scraper measurements in the vertical plane are considered since $D_y = 0$ m and hence longitudinal momentum spread does not need to be accounted for. This simplifies the analysis making it a good place to start. Figure 6.13 shows the raw signal as a function of position for both vertical scraping directions on the two scintillators. There appears to be a loss of signal at high intensity on scintillator 2, possibly due to saturation effects. This effect can be seen for both times of the intermediate plateau and is also present at other times and directions. To ensure best quality measurements, scintillator 1 was chosen to be used for analysis.

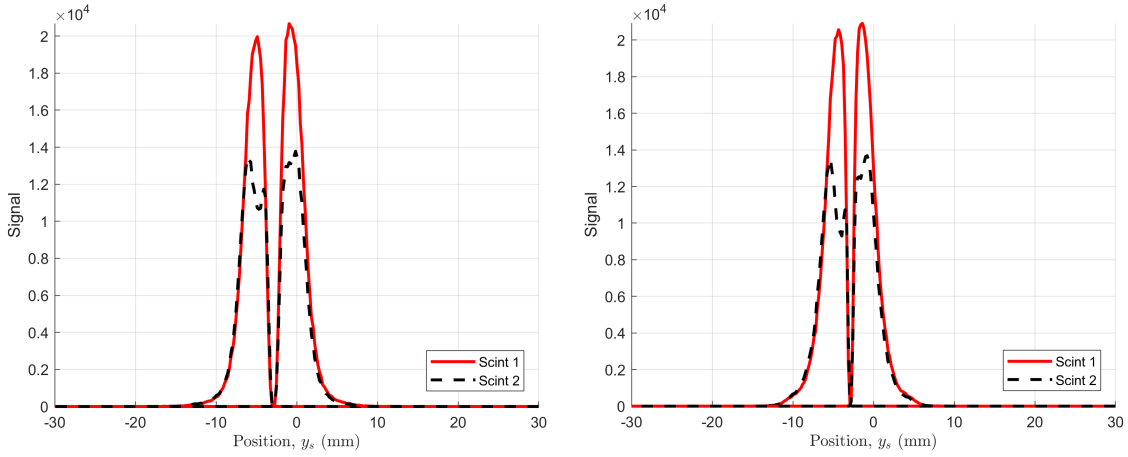

FIGURE 6.13: Scintillator signals as a function of position for the vertical plane along the intermediate plateau. The left plot corresponds to $t = 7.8$ s and the right to $t = 14.5$ s.

The two scan algorithm was used to determine the vertical emittances, ϵ_y at both times resulting in emittances of 1.59 ($\pm$0.02) mm mrad and 1.15 ($\pm$0.02) mm mrad for $t = 7.8$ s and $t = 14.5$ s, respectively. This shows the first evidence of electron cooling in ELENA, with a reduction in emittance of 28 ($\pm$2)% of the initial value over 6.7 seconds. A slight change in the separation of the two CDFs generated when scraping can be seen for the two different times along the plateau in Fig. 6.14, which is consistent with the emittance reduction.

Figure 6.14 also displays the CDFs generated when simulating the scraping of Gaussian beams with the calculated emittances from the data. Generally, there is a good match between simulation and data but closer inspection could reveal some insight into the effects of the electron cooler on the distribution shape. It appears that the beam may be better described by the Gaussian simulation at $t = 7.8$ s and less so after some cooling. This can be seen by observing a thinner core with more significant tails at $t = 14.5$ s than the corresponding simulation. Additional evidence for this is in comparing the data taken; whilst the bulk and core of the beam appear to be affected by cooling, less significant differences are observed in the tails. Further incremental (in time) measurements would allow a more thorough investigation of this possible effect by the electron cooler. The vertical plane is most suited for such an investigation since dispersive effects do not convolute the beam distribution.

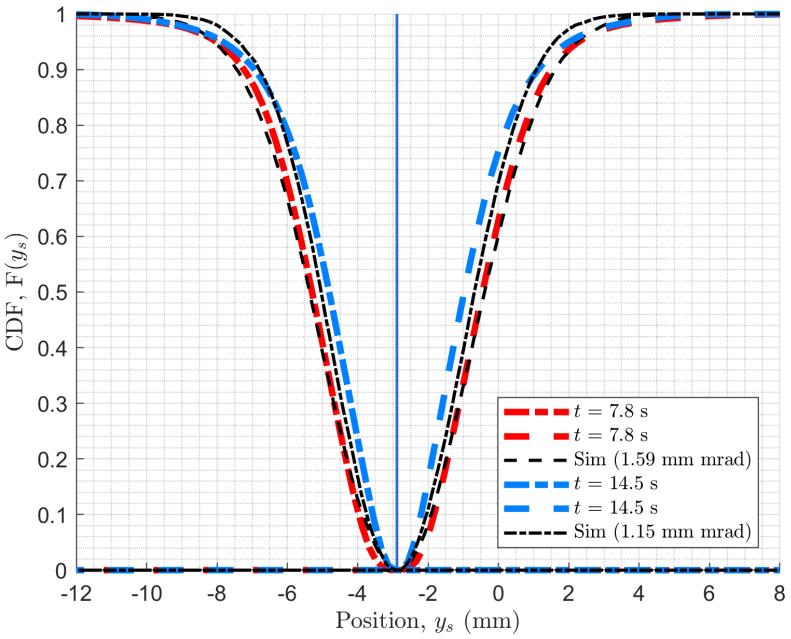

FIGURE 6.14: CDFs for vertical scraper measurements along the intermediate cooling plateau. Two vertical lines (overlaying) represent calculated closed orbits for the two times and are correspondingly coloured, whilst Gaussian simulations ("Sim") based on reconstructed emittance values are plotted in back.

The closed orbit of the beam was extracted from the measured quantities according to Eq. 4.30 and is also displayed in Fig. 6.14. The results show no significant change in closed orbit during electron cooling with measured values of -2.88

(±0.03) mm and -2.89 (±0.03) mm at 7.8 s and 14.5 s, respectively. The offset from $y = 0$ mm could be due to a calibration issue with the scraper as all vertical measurements are offset by a similar magnitude in this direction. Alternatively, there could be a consistent closed orbit offset during the cycle. Calibration tests during LS2 would determine which one of these possibilities is more significant.

TABLE 6.5: Comparison of results from the single scan Gaussian algorithm with the two scan method.

	Two Scan	Single Scan "Top"	Single Scan "Bot"
$t = 7.8$ s, ϵ_x (mm mrad)	1.59 (±0.02)	1.40 (−11.95%)	1.45 (−8.81%)
$t = 14.5$ s, ϵ_x (mm mrad)	1.15 (±0.02)	0.97 (−15.7%)	0.97 (−15.7%)

The single scan Gaussian algorithm (Eq. 4.19) was tested with the data since comparisons with Gaussian simulations showed they were a good approximation. The closed orbit estimates from the two scan method were input into the algorithm and the momentum spread set to zero. The results are summarised in Table 6.5, percentages in brackets after the single scan results give the difference between these values and those calculated from the two scan method. Whilst there appears to be a systematic underestimation, larger disagreement on the $t = 14.5$ s data further suggests the beam has become less Gaussian during electron cooling. Figures A.2, A.3, A.4 and A.5 in the appendix show the fits with the data, where again the tails at $t = 14.5$ s deviate from Gaussian. The horizontal scraper measurements were dealt with next.

6.5.1.2 Horizontal Measurements

To begin analysis of the horizontal scraper measurements, the RMS momentum spread of the beam was calculated first. The RMS widths, Δf_h and mean values, f_h, were calculated for each slice of the Schottky data before rebunching at around cycle time $t = 15.7$ seconds to give an indication of its evolution during electron cooling. To do this first the background level, estimated from the mean value of several noise samples, was subtracted from the signals. Numerical integration was then used across each sample to determine the mean value and variance. Figure 6.15 shows the estimates for both f_h and Δf_h on top of the raw data. Scraper measurement trigger times are also displayed as vertical green lines.

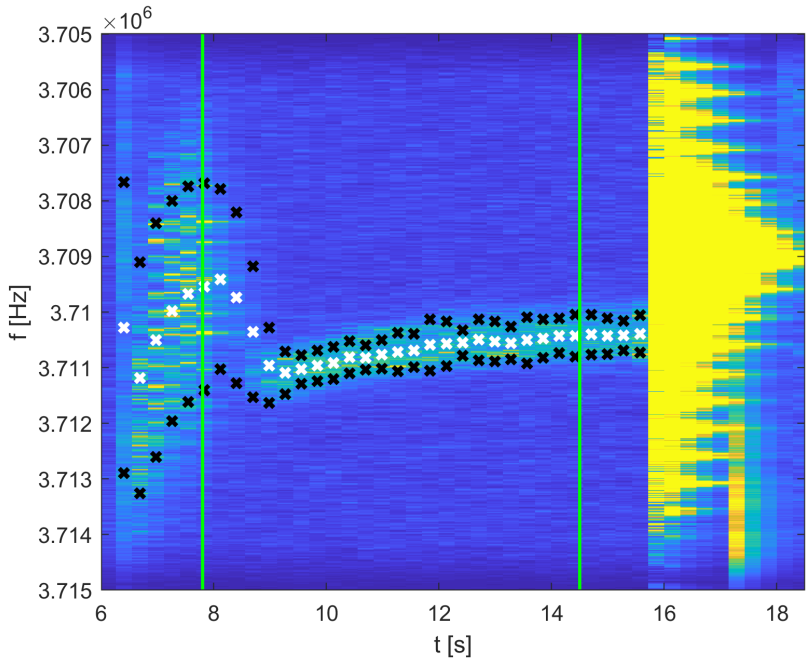

FIGURE 6.15: Estimates for the mean (white crosses) and width (black crosses) of signal in the raw Schottky data during the intermediate cooling plateau. The times of initial scraper movement are represented by green vertical lines.

Equation 6.1 was used to estimate the momentum spread at each time, with errors determined by propagating uncertainties on f_h, Δf_h and η through it. The results are displayed in Fig. 6.16 and show a dramatic decrease in the longitudinal momentum spread at the start of cooling followed by a plateau where it is expected an equilibrium is reached with beam heating effects such as IBS. As with Fig. 6.15, vertical green lines indicate scraper measurement trigger times. Using raw data containing the scintillator signal and corresponding cycle time, it was possible to establish when exactly the scraper blade reached and interacted with the beam. The time windows when signal from the beam was observed are indicated on the plot between two pairs of vertical red lines. It should be noted that this scraper blade "travel time" is important when considering a beam with rapidly changing properties, such as the momentum spread in this case. As a result of these considerations, estimates for the momentum spread were made at $\sigma_\delta = 1.1\ (\pm 0.16) \times 10^{-3}$ and $\sigma_\delta = 0.22\ (\pm 0.03) \times 10^{-3}$ for the measurements with triggers at $t = 7.8$ s and $t = 14.5$ s, respectively.

For the horizontal emittance evolution along the intermediate plateau, the two

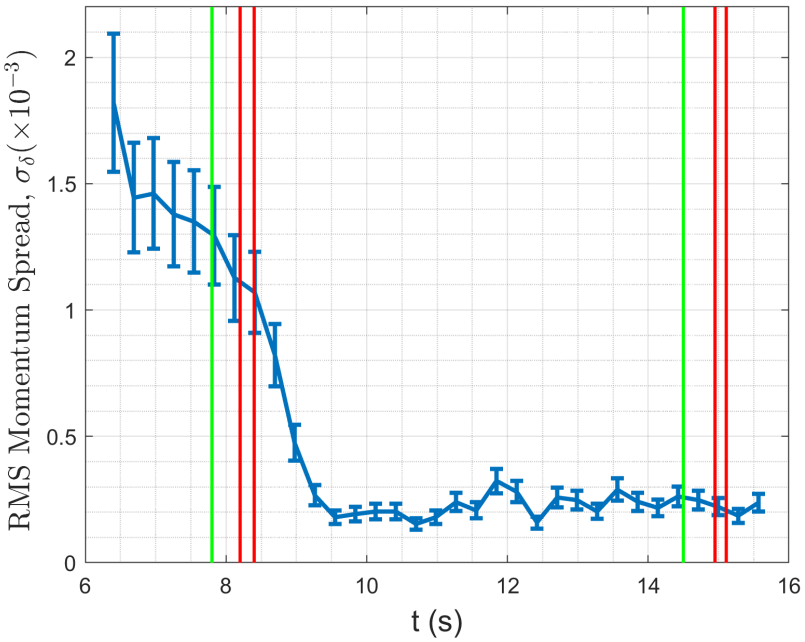

FIGURE 6.16: Evolution of the longitudinal momentum spread of the beam during the intermediate plateau. Green vertical lines mark scraper trigger positions with two pairs of red vertical lines showing times between which scintillator signal was observed.

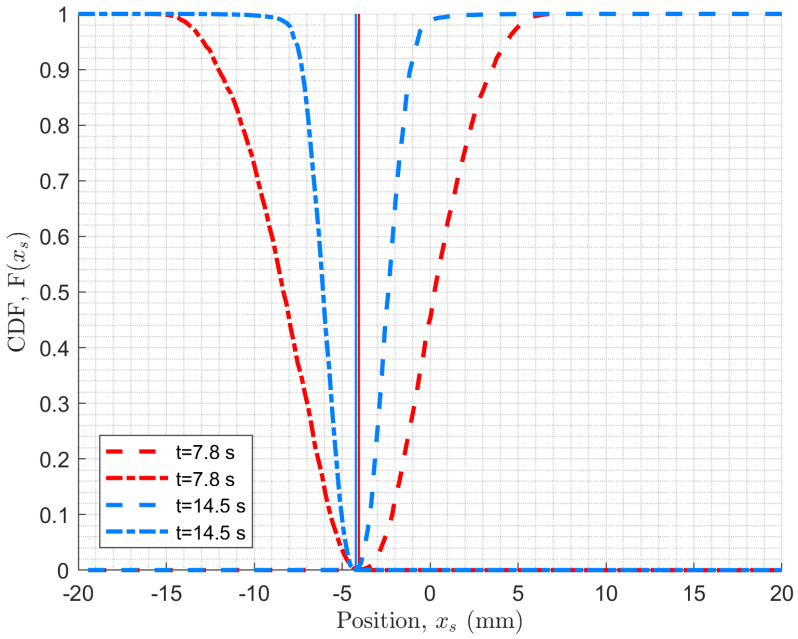

FIGURE 6.17: CDFs for horizontal scraper measurements along the intermediate cooling plateau. Closed orbits are represented by appropriately coloured vertical lines.

scan algorithm was used with the RMS momentum spread values calculated from the Schottky data. Figure 6.17 shows the normalised CDFs extracted from the scraper data, corresponding to horizontal emittance values, ϵ_x, of 3.6 ($\pm$0.27) mm mrad and 0.7 ($\pm$0.05) mm mrad for for t = 7.8 s and t = 14.5 s, respectively. Assuming the momentum spread estimations are accurate, the electron cooler has reduced the emittance by 81 ($\pm$10)% of the value at the start of cooling, consistent with a large observable difference in the separation of CDFs.

Similarly to the vertical measurements, closed orbit calculations showed a consistent offset towards negative x. There was some small change between the estimates, also visible in Fig. 6.17, with values of -4.05 ($\pm$0.04) mm and -4.22 ($\pm$0.04) mm measured for the start and end of the plateau, respectively. This could be explained by a change in the mean momentum offset of the beam, $\Delta\bar{\delta}$, affecting the horizontal amplitude of the particles through dispersion. In fact differences in f_h and x_0 at each scraper measurement could be used to calculate the dispersion at the scraper ($\Delta x_0 = D_x \Delta\bar{\delta}$). This would require Schottky measurements at a much higher harmonic (i.e. better time resolution in the spectral density distribution) to allow for a more accurate estimation of f_h for the measurement at t =7.8 s. Conversely, the change in momentum offset may be calculated from Δx_0 and the measured D_x, here it was found to be $\Delta\bar{\delta} = -1.2\ (\pm 0.3) \times 10^{-4}$.

Whilst closely inspecting the core region of the CDFs at t =7.8 s an observation may be made: that they do not show the characteristic crossing above $F(x_s) = 0$ expected when dispersive effects are present. To compare the expected crossing point two simulations were plotted against the data. One simulation plotted the emittance calculated taking the Schottky momentum spread (σ_δ =1.1$\times 10^{-3}$: $\epsilon_x = 3.6 \times 10^{-3}$ mm mrad), and another with the emittance calculated using no momentum spread (σ_δ =0$\times 10^{-3}$: $\epsilon_x = 4$ mm mrad). Figure 6.18 shows the comparison for the entire distribution whilst Fig. 6.19 shows a zoom on the core (the simulations are plotted against the data separately in the appendix, for clarity: Fig. A.6 & Fig. A.7).

It is clear that the simulation based on an assumption of no momentum spread is in much better agreement with the data. It does not necessarily mean that the

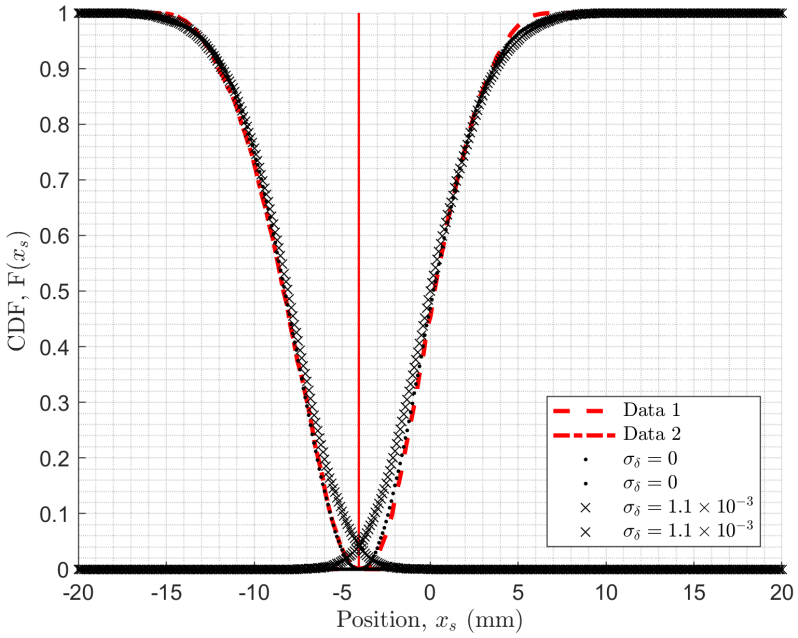

FIGURE 6.18: Comparison of CDFs obtained from data with simulations of beams with σ_δ =1.1×10^{-3}, $\epsilon_x = 3.6 \times 10^{-3}$ mm mrad and σ_δ =0×10^{-3}, $\epsilon_x = 4$ mm mrad.

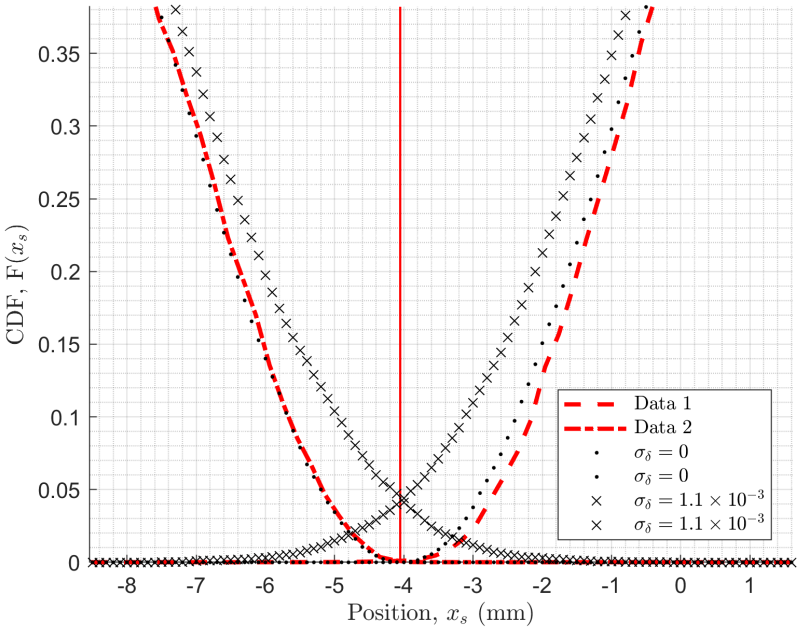

FIGURE 6.19: Zoom on the core region of Figure 6.18.

no momentum spread assumption is correct though; even if the Schottky data is not reliable it is extremely unlikely that the beam has zero momentum spread at the start of the intermediate plateau. It is possible that an error in the value of

dispersion at the scraper D_x is responsible, however it would have to be essentially equal to zero for a discrepancy of this magnitude. This would be very far outside of the uncertainty range.

More complicated factors could be the cause of this unexpected result. As seen in the vertical comparisons, the electron cooler appears to be more effective at the centre of the beam than at the tails. This could also be the case with longitudinal cooling, where the momentum spread of particles with smaller oscillation amplitudes is more effectively reduced. Particles with larger emittances would then contribute to the Schottky signal. It is possible that this could reduce the crossing effect at the centre of the CDFs, even for a scraper measurement at t =7.8 s, since the beam had already been exposed to electron cooling for >1 s before scraping.

Another explanation could be due to an optical mismatch of beam and lattice parameters, either at injection or after the deceleration ramp. Simulations scraping a beam undergoing filamentation showed a marked decrease in the crossing point of CDFs with an increasing degree of optical mismatch. Figure. 6.20 shows the CDF pairs resulting from 3 simulations of beams with varying degrees of optical mismatch. The mismatch was brought about by adjusting the x' of every particle by some degree during injection into the ring. Figure A.8 shows horizontal (x, x') phase space plots at different times during a simulation with $\Delta x' = 1$ mrad to illustrate the beam's behaviour. A less dense particle distribution at the core region may be observed due to beam oscillations around $(x, x' = 0)$. Whilst these simulations do not match the exact conditions of the data taken, they serve to offer a potential mechanism for the discrepancy. It would be useful to perform scraper measurements with known optical mismatches upon injection, or alternatively with various optical configurations of the ring during and after the first deceleration ramp to test this supposition.

A similar comparison with the data at t = 14.5 s shows a less obvious discrepancy due to the measured momentum spread already being relatively low. Figure A.9 shows the comparison with simulations using reconstructed emittance values of: $\epsilon_x = 0.71$ (± 0.05) mm mrad for $\sigma_\delta = 0$, and 0.7 (± 0.05) mm mrad for $\sigma_\delta = 0.22$ (± 0.03) $\times 10^{-3}$. It is expected the reasons for the discrepancy here are

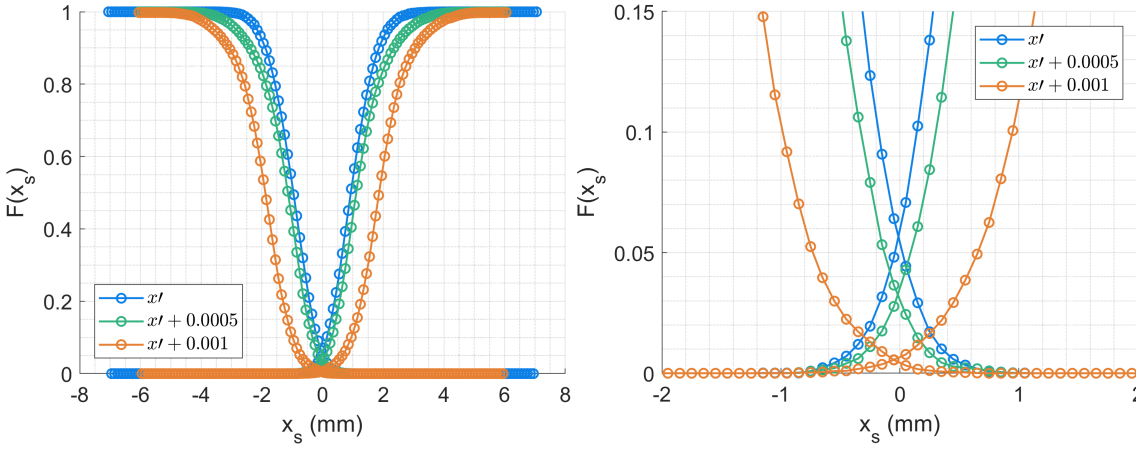

FIGURE 6.20: Comparison of beam scraping distributions for 3 beams of varying degrees of mismatch at injection.

the same as for the t =7.8 s measurement.

The Gaussian scan algorithm was tested for both horizontal measurements at t = 14.5 s. As expected the unexplained deviation in the shape of the CDFs caused results inconsistent with Schottky measurements and two scan method. Further measurements would be necessary to thoroughly explain this observation.

6.5.2 Ejection Plateau: Cooling at 100 keV

As mentioned previously, a second set of measurements were made during the 100 keV ejection plateau for an ELENA cycle with a longer repetition rate. The measurements were again made in all four directions, but this time an important distinction must be pointed out: The measurements were made twice at the same cycle time t=28.875 s, with electron cooling on and off. Whilst this approach is somewhat different, it again allows for investigation into the effects of the electron cooler. Electron cooling began at the start of the plateau at t= 24.897 s and so the measurements highlight the effects of 3.888 s of electron cooling compared with a coasting beam subject only to collective effects such as IBS.

6.5.2.1 Vertical Measurements

Analysis of the vertical data using the two scan algorithm gave emittances of 2.55 ($\pm$ 0.03) mm mrad and 0.53 ($\pm$ 0.01) mm mrad, without and with cooling respectively. After 3.9 s of electron cooling at 100 keV the vertical beam emittance

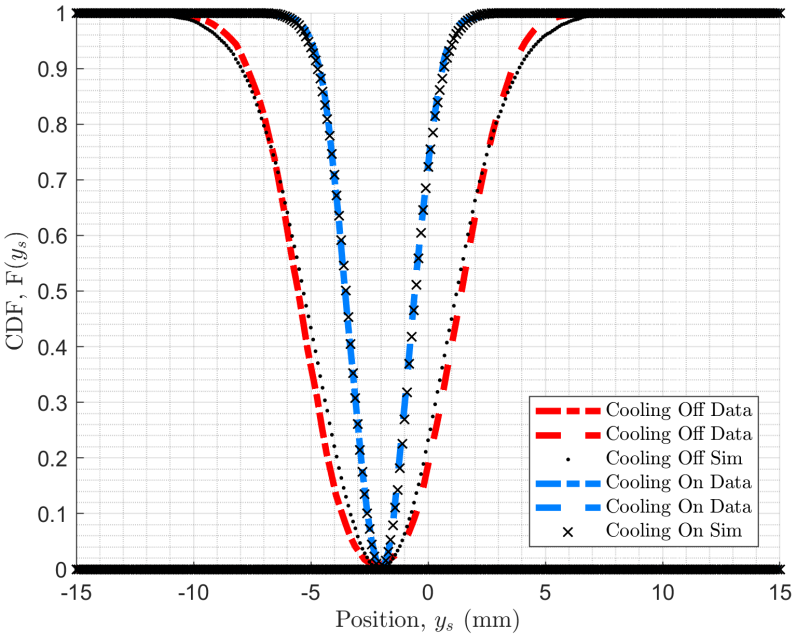

FIGURE 6.21: CDFs compared with simulations for vertical scraper measurements along the ejection plateau. Both sets of data are taken at the same time in the cycle, with and without electron cooling.

is significantly reduced by 79 (± 2) % of that without. The data showed negligible changes in the closed orbit offset with values of -2.08 (±0.03) mm and -2.03 (±0.03) mm calculated without and with electron cooling, respectively.

Similarly to the previous section, Fig. 6.21 shows a comparison of the data with simulations, yet this time more obvious deviations from a Gaussian distribution are observed for the beam with no cooling. Another difference is that the beam has a wider core than the Gaussian approximation compared with a thinner core after cooling during the intermediate plateau. This distribution could be explained by the fact that the beam has been measured 3.9 seconds after the end of the deceleration ramp with no cooling. The more dense region at the core may have expanded faster than at the tails during this time due to IBS being more significant at higher intensities. After cooling the beam is well approximated by a Gaussian distribution, perhaps due to the cooling being more effective at the core and correcting for more IBS at the core. Also, when the beam size is eventually smaller so is the deviation in electron velocities interacting with the beam, resulting in more even cooling across the entire beam.

6.5.2.2 Horizontal Measurements

Due to no Schottky data being available for this plateau it was necessary to make an estimate of the longitudinal momentum spread in order to use the two scan algorithm. Preliminary analysis of the data showed that indeed there was a crossing of CDFs above zero in this plane. Measurements at this final plateau were not taken on the same day as for the intermediate plateau but current readings for the 3 quadrupole families showed negligible changes in the optical configuration. It is possible that injection conditions were different. This would support the optical mismatch hypothesis when trying to understand the absence of a raised crossing point in the CDFs taken at $t = 7.8$ s, assuming a more well optically matched beam for these measurements, however as previously stated, further measurements are required.

After confirming that the Gaussian fit algorithm is accurate for determining the emittance for vertical measurements, and combined with its capability to accurately estimate momentum spread for simulation results, it was used to make an estimate for the longitudinal momentum spread of the beam. This was done first using the data for an uncooled beam, since vertical measurements along the intermediate plateau suggested the beam becomes less Gaussian with cooling.

The Gaussian fit algorithm was run twice, once for each direction and results were compared. When scraping from the "Ext" direction, the momentum spread estimate had extremely large uncertainty values (based on the goodness of the fit) and so the estimation was discarded. The fit can be seen in Fig. A.10. The estimations from the "Int" direction returned $\sigma_\delta = 9.4\ (\pm 0.2) \times 10^{-4}$. The fit is displayed in Fig. 6.22, showing an excellent agreement at the tails but some small deviation towards the core, suggesting an underestimation. The error on the value, based on the goodness of the fit, was deemed acceptable for this method to form the basis for the estimate of the momentum spread. The uncertainty of the estimate was increased to 20% ($\pm 1.9 \times 10^{-4}$) to account for the uncertain nature of this method, and was carried through to the error on the reconstructed emittance.

The two scan algorithm was run with this estimation and returned an emittance of 2.5 (± 0.2) mm mrad. For the case with cooling present an RMS momentum

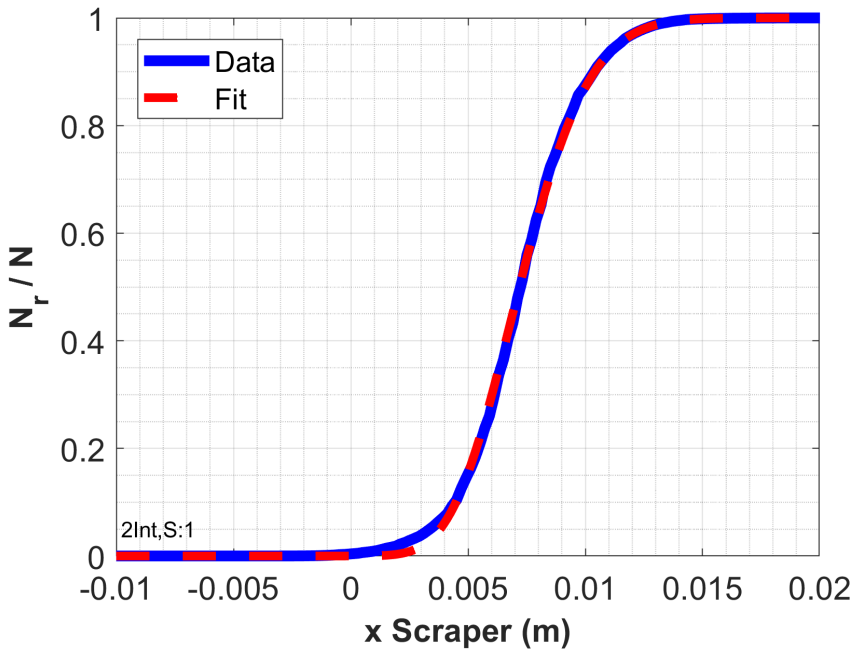

FIGURE 6.22: Application of the single scan Gaussian fit algorithm to a horizontal measurement along the ejection plateau in the absence of electron cooling. Data has been mirrored about $x = 0$ mm to accommodate the fitting algorithm, this process does not affect the result.

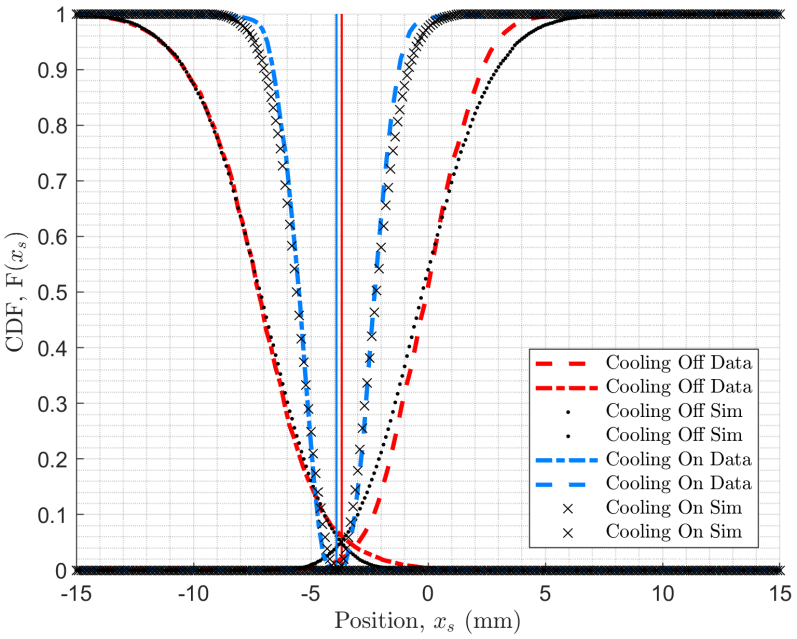

FIGURE 6.23: Data vs Gaussian simulations for the ejection plateau.

spread of 0 ($\pm 2 \times 10^{-4}$) was estimated, based on the Gaussian only algorithm estimating values of the order 10^{-7} for both directions. With this input, the two

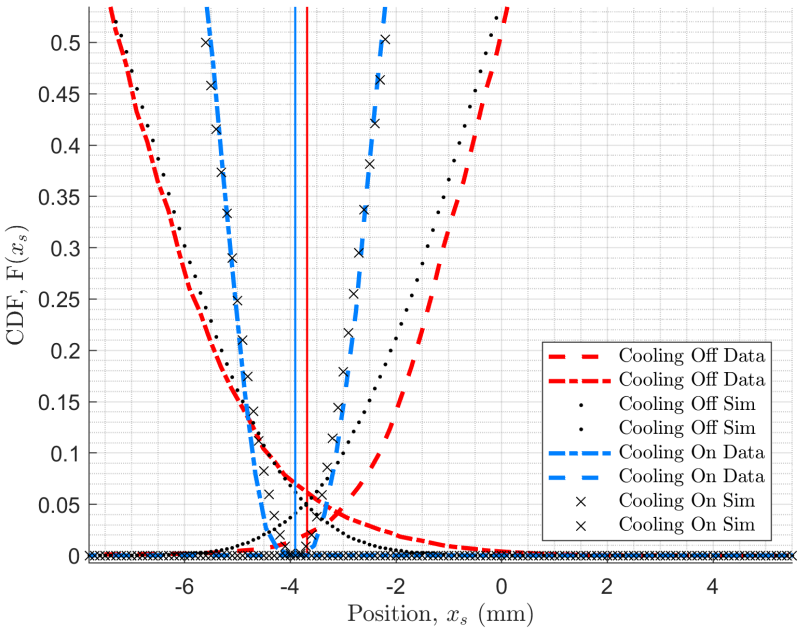

FIGURE 6.24: Zoom on beam core region for data vs Gaussian simulations along the ejection plateau.

scan method returned an emittance of 0.55 (±0.04) mm mrad, a change of 78 (±10) % of the emittance at this time without electron cooling. Again, a shift in the closed orbit of −0.24 (±0.08) mm was seen, suggesting that because the mean momentum offset of the beam has changed due to electron cooling, so has the closed orbit through dispersion. Using the same method as for the intermediate plateau ($\Delta x_0 = D_x \Delta\bar{\delta}$), the change in momentum offset with and without electron cooling was calculated at $\Delta\bar{\delta} = -1.7\ (\pm 0.3) \times 10^{-4}$. (It was $\Delta\bar{\delta} = -1.2\ (\pm 0.3) \times 10^{-4}$ for the intermediate plateau.)

The data and Gaussian simulations based on the two scan algorithm result are shown in Figs. 6.23 and 6.24. Again there appears to be good agreement with the Gaussian simulations, and this time the crossing height of the CDFs is much closer to the data for the non-cooling case. The Gaussian simulation for the non-cooling case serves well to highlight an asymmetry in the measured distribution. Such asymmetries were observed during the simulation phase (Section 5.7.1) when investigating correlations between momentum offset and emittance and so the correlation coefficient was investigated next.

6.5.3 Emittance-Momentum Offset Correlation

The emittance-momentum offset correlation was introduced in Section 4.4.2 and explored through simulations in Section 5.7.1. It would arise from a parabolic transverse distribution in electron velocities with a minimum at the centre of the beam pipe $(x, y = 0)$. It would be the case that antiprotons with a smaller emittance, those populating the core of the beam, have a more reduced momentum offset than those at the tails after some exposure to electron cooling.

This effect should not be confused with the bi-Gaussian effect whereby electron cooling is more effective at the core of the beam due to a higher density of electrons. Although these two effects are related by the parameters of the electron beam, they must be considered separately. This is possible with scraper measurements since the bi-Gaussian effect influences both transverse planes, whereas the emittance-momentum offset correlation effects only horizontal measurements. Additionally, unlike bi-Gaussian beam distributions, the emittance-momentum offset correlation manifests through asymmetrical scraper measurements and so careful comparisons can separate the effects.

An emittance-momentum offset correlation coefficient, henceforth referred to as the correlation coefficient, was derived. To highlight the nature of such a quantity, the expression to determine the correlation coefficient for a simulated bi-Gaussian beam is repeated below;

$$\langle(\delta - \bar{\delta})A\rangle = \frac{\sum_{i=1}^{2}(N_i\sqrt{\frac{\epsilon_{rms,i}\pi}{2}}(\bar{\delta_i} - \bar{\delta}_{beam})^2)}{\sum_{i=1}^{2} N_i},$$

where in simulations the subscripts $i = 1, 2$ refer to the core and tail Gaussian distributions whose superposition comprises the beam. The quantity is obtained generally through the algorithm using;

$$\langle(\delta - \bar{\delta})A\rangle = \frac{{\sigma^2}_+ - {\sigma^2}_-}{4D\sqrt{\beta}},$$

where $\sigma_{\pm}^2$ are the variances of the PDFs from each scraping direction. To ensure that the coefficient gives an accurate measure of the correlation between the

emittance of individual particles and their momentum offsets, the quantity is normalised to the overall emittance of the beam by dividing by $\sqrt{\epsilon_x}$. This accounts for scaling of the quantity with overall transverse beam size, and we may define the normalised correlation coefficient as $\phi_{\epsilon\delta} = \langle(\delta - \bar{\delta})A\rangle\epsilon_x^{-1/2}$, for the sake of brevity.

TABLE 6.6: Calculated correlation coefficients for horizontal scraper measurements at both energy plateaus. The bottom row displays the difference in values, $\Delta\phi_{\epsilon\delta}$, and associated errors.

	Int		Ext	
	$t = 7.8$	$t = 14.5$	No Cooling	Cooling
$\phi_{\epsilon\delta}$ ($\times 10^{-5}$)	-5.4	1.0	-16	0.3
Error $\phi_{\epsilon\delta}$ ($\times 10^{-5}$)	2.5	1.1	3.1	0.9
$\Delta\phi_{\epsilon\delta}$ ($\times 10^{-5}$)	6.4 $\pm$3.6		16.3 $\pm$4	

The correlation coefficient was calculated for both horizontal measurements along both energy plateaus and the results are displayed in Table 6.6. Large uncertainties arise from a combination of large error contributions from β_x and ϵ_x combined with errors on $\sigma_\pm^2$. It should be noted that this quantity is quite abstract in nature and single measurements do not offer much insight into a beam's qualities, aside from observations of its sign ($\pm$). It is better served as a comparative quantity, monitoring how it evolves over time or in different conditions. A positive change in $\phi_{\epsilon\delta}$ for beams after more exposure to electron cooling does, in fact, indicate a shift in the correlation. Particles with smaller emittance have a reduced momentum offset compared with an increase for those at higher amplitudes.

The negative initial $\phi_{\epsilon\delta}$ indicates that already a negative correlation exists, perhaps brought about by deceleration, which it seems is unintentionally corrected for by electron cooling. The next obvious step for this investigation would be to measure $\phi_{\epsilon\delta}$ at injection and monitor how it evolves throughout the entire cycle. It would be worth measuring the quantity after extended exposure to electron cooling to see if it continues to positively increase.

The quantity was calculated for the vertical measurements to investigate whether indeed it is a good measure of the effect of momentum spread on the beam. It should be clearly stated that when doing so, D_y was set to 1.38 m, the same as D_x purely for the purposes of comparing the magnitude and evolution of the quantity in both planes. The quantities calculated for y are hence for benchmarking the

method only and do not serve to supply any information on the beam. The results of this benchmarking exercise are presented in Table. 6.7 using the same units as for the horizontal table for ease of comparison.

TABLE 6.7: Calculated correlation coefficients for vertical scraper measurements at both energy plateaus. Results presented in this table are purely for benchmarking purposes only.

	Int		Ext	
	$t = 7.8$	$t = 14.5$	No Cooling	Cooling
$\phi_{\epsilon\delta}$ ($\times 10^{-5}$)	0.3	-0.5	0.5	0.7
Error $\phi_{\epsilon\delta}$ ($\times 10^{-5}$)	0.3	0.3	0.2	0.2
$\Delta\phi_{\epsilon\delta}$ ($\times 10^{-5}$)	-0.7 $\pm$0.6		0.2 $\pm$0.4	

Clearly the values obtained for $\Delta\phi_{\epsilon\delta}$ in the two different planes show that the effect is restricted only to the horizontal plane, as changes in the vertical plane are negligible by comparison and by their uncertainties. It is then asserted that $\phi_{\epsilon\delta}$ may indeed an indicator of more complex beam behaviour than has previously been measured through scraper measurements alone, and its application should be further investigated.

6.6 Discussion and Summary

Despite some technical challenges relating to hardware and limited beamtime during machine commissioning, scraper measurements have been made and analysed for two points along the intermediate plateau, in the presence of electron cooling, and twice during the extraction plateau, with and without cooling. Larger errors on horizontal measurements were calculated due to dispersive effects, as expected. Tables 6.8 and 6.9 display all parameters used and reconstructed from the data for both plateaus. Estimates used for momentum spread based on the Gaussian algorithm results are presented in the ejection plateau and hence have large uncertainties.

A comparison of emittance differences for each plateau and plane is displayed in Fig. 6.25, complete with the rate of change based on each pair of measurements' exposure time to electron cooling. The rate of change is included only as a guide value, indicating the slowest possible rate of change, since it is highly likely that

TABLE 6.8: Intermediate plateau summary table. Note: changes in emittance are expressed as percentages of initial emittance.

	t=7.8	Error	t=14.5	Error	Change	Error
ϵ_y(mm mrad)	1.59	0.02	1.15	0.02	28%	2%
y_0 (mm)	-2.88	0.03	-2.89	0.03	-0.01	0.06
ϵ_x (mm mrad)	3.6	0.27	0.70	0.05	81%	10%
x_0 (mm)	-4.05	0.04	-4.22	0.04	-0.17	0.08
σ_δ ($\times 10^{-3}$)	1.10	0.16	0.22	0.03	-0.88	0.19
$\phi_{\epsilon\delta}$($\times 10^{-5}$)	-5.4	2.50	1.00	1.10	6.40	3.6

TABLE 6.9: Ejection plateau summary table."e$^-$C. Off" and "e$^-$C. On" refer to the status of the electron cooler. Note: changes in emittance are expressed as percentages of initial emittance.

	e$^-$C. Off	Error	e$^-$C. On	Error	Change	Error
ϵ_y (mm mrad)	2.55	0.03	0.53	0.01	79%	2%
y_0 (mm)	-2.08	0.03	-2.03	0.03	0.05	0.06
ϵ_x (mm mrad)	2.5	0.20	0.55	0.04	78%	10%
x_0 (mm)	-3.67	0.04	-3.91	0.04	-0.24	0.08
σ_δ ($\times 10^{-4}$)	0.94	0.19	0.0	0.2	-0.94	0.39
$\phi_{\epsilon\delta}$($\times 10^{-5}$)	-16	3.1	0.3	0.9	16.3	4

it is not linear. The effects of electron cooling on the emittance show a clear reduction in both directions for both plateaus, a promising result considering the measurements were taken shortly after the installation and during commissioning of the electron cooler. In fact, the emittance reduction at the extraction plateau shows good agreement with BETACOOL simulations performed previously at the same energy, with a coasting beam [111]. For comparison, the simulations had initial emittances of $\epsilon_{x,y} = 2.8$ mm mrad, being reduced to $\epsilon_x = 0.52$ mm mrad and $\epsilon_y = 0.33$ mm mrad after 2 seconds. The cooling rate appeared to reach equilibrium with IBS after this time in the simulations.

Although the linear fit might suggest the cooler is much more horizontally efficient along the intermediate plateau, it is not known whether both emittances had reached equilibrium points with IBS earlier than the second ($t = 14.5$ s) measurement. Despite IBS being proportional to $1/\gamma_l^4$, smaller "final" emittances for the ejection plateau could be the result of a lower overall beam intensity (less resistance from collective effects), since during commissioning the RF was not yet optimised and losses were common during deceleration. Many more incremental

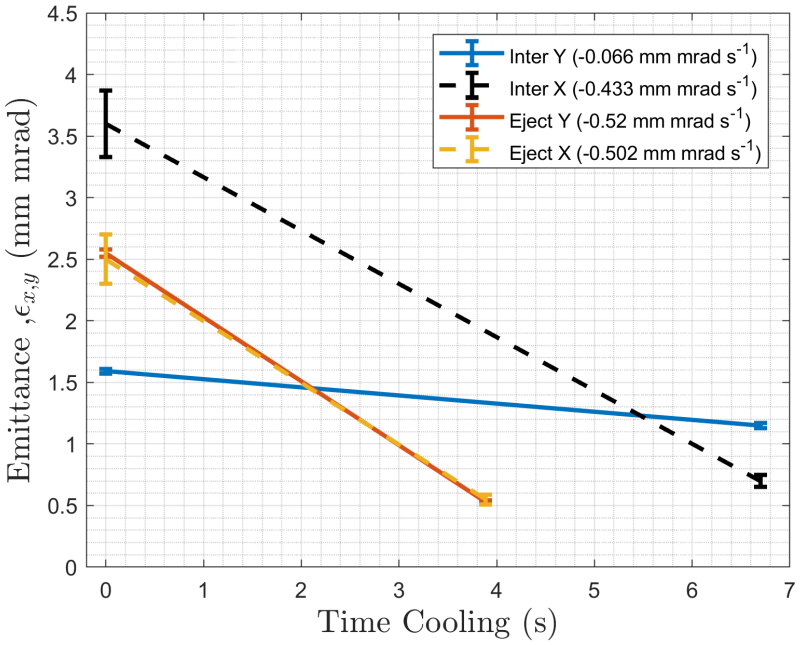

FIGURE 6.25: Effects of electron cooling on horizontal and transverse emittances. Here "Inter" and "Eject" refer to intermediate and ejection cooling plateaus, respectively.

measurements are required to map the curve of emittance reduction and determine the equilibrium point with collective effects in all cases. For a direct comparison of cooling between plateaus, measurements should also be taken on the same day with the same cycle length, whilst monitoring and correcting for intensity differences.

Table. 2.1 presents the nominal parameters of the electron cooler. It is seen that $\beta_{x,y}$ is expected to be roughly equal at the centre of the cooler and optics simulations based on quadrupole current strengths showed small deviations ($\approx$10%) in opposite directions (smaller β_x) from these values. Calculations for the horizontal RMS beam width at the electron cooler ($\sigma_{RMS} \approx \sqrt{\beta\epsilon}$) gave values of 2.6$\pm$0.3 mm and 2.3$\pm$0.3 mm at t=7.8 s and with no cooling at the ejection plateau, respectively. Estimations of horizontal beam widths encapsulating $\approx$99.7% ($\approx 3\sigma_{RMS}$ using the empirical rule) of around 7.8$\pm$0.9 mm and 6.9$\pm$0.9 mm could be large enough to be affected by the parabolic distribution of electron velocities within the cooler. Work done previously to determine optimised lattice functions for electron cooling [112, 113] could be expanded upon into this next generation of low energy antimatter beams by using this new two scan algorithm for ELENA. This

new scraping algorithm combined with variations in the β_x/D_x ratio at the cooler whilst maintaining other conditions could provide a more detailed look into the unexpected strong influence of dispersion contributing towards decreased cooling times previously seen in these studies.

Closed orbit estimations show consistent offsets in the negative direction for both planes and plateaus. It would be beneficial to test the calibration of the scraper arms during LS2, to ensure that the co-ordinate system aligns with that of the beam due to consistent offsets towards negative x, y. In the vertical plane, the closed orbit does not deviate outside its uncertainty levels for both measurements at either plateau, showing a stable beam. Horizontally, deviations are observed and were attributed to changes in the mean momentum offset of $\Delta\bar{\delta} = -1.2\ (\pm 0.3) \times 10^{-4}$ and $\Delta\bar{\delta} = -1.7\ (\pm 0.3) \times 10^{-4}$ for the intermediate plateau and ejection plateaus, respectively.

Comparisons with simulations showed that indeed beams appeared to be non-Gaussian, particularly after some time exposed to electron cooling during the intermediate plateau where the core has been cooled more efficiently. This was more apparent for vertical measurements which were free of dispersive effects. It is likely that the effects of IBS are observed at the extraction plateau where, in the absence of cooling, the beam core is larger than the Gaussian approximation. This would be explained by more significant IBS due to a higher beam intensity at the core.

The non-Gaussian nature of the beams did not, however, appear to be significant enough to completely render the single scan Gaussian fit algorithm useless, and in fact it was shown that the algorithm could be used, with careful consideration, to estimate the vertical emittance of the beam. It would be very beneficial to compare Schottky measurements and momentum spread estimates from the single scan Gaussian algorithm to benchmark the technique as a viable fast estimation option or for when Schottky data is not available. It would also be of interest to make repeat Schottky measurements to ascertain the level of fluctuations between shots. Of course, Schottky measurements at each plateau are necessary and analysis in combination with the incremental emittance evolution study suggested

above would build a complete picture of the beam's behaviour and quality from 5.3 MeV to 100 keV.

An investigation of the emittance-momentum offset correlation was performed using the (emittance normalised) correlation coefficient, $\phi_{\epsilon\delta}$, extracted from the algorithm. The method was benchmarked against vertical measurements which showed negligible change as expected. Horizontally, although large uncertainties were observed due primarily to uncertainties in ϵ_x and β_x, comparisons between the quantities with and without cooling certainly suggest the electron cooler is contributing towards such a correlation. To further examine this effect, it would be useful to make measurements at the same time in the cycle whilst adjusting electron cooler settings such as the e^- beam energy, density or crucially, the radius. Furthermore, $\phi_{\epsilon\delta}$ unexpectedly appeared to be largely negative after both deceleration ramps.

This chapter has shown that the two scan algorithm is indeed appropriate when considering low energy beams in the presence of electron cooling. The algorithm has determined emittances to within desired uncertainty limits for both planes along both cooling plateaus. Further measurements are required to fully understand the evolution of the beam emittance, distribution shape and momentum spread due to electron cooling effects. It is also proposed that measurements at different times during the plateaus with no electron cooling could be performed to obtain emittance growth rates due to IBS. The measurements and analysis have thoroughly explored the practical considerations needed for the two algorithms to be successfully employed. Additionally, detailed analysis of the limited available measurements has exposed numerous potential studies to be carried out in continuation from this work and from similar related studies e.g. lattice optimisation for electron cooling. The potential gains from combining opposing scraper measurements are clear, with particular emphasis on studying $\phi_{\epsilon\delta}$.

Finally, a measurement of the beam profile during the last plateau in the presence of electron cooling has been made. In the following chapter, the results of this analysis will be used to best approximate the beam distribution and to track it through a realistic model of the 37.4 m long transport lines to the ALPHA

experiment. This will provide the best possible estimation for beam quality at the handover point, and aid in determining an optimised transport lines configuration.

Chapter 7

Transfer Lines

7.1 Introduction

In order to transport cooled 100 keV antiprotons to the six experiments currently operating in the AD hall, electrostatic transport lines will be used. The elements for the transport lines have already been manufactured and at the time of writing are already being assembled during CERN's second long shutdown, LS2. Antiproton operations resume in 2020.

The use of electrostatic elements in such a large configuration is a relatively recent practice and much less common compared with the use of their magnetic counterparts. For example, the racetrack shaped electrostatic storage ring ELISA [114] was the first of its kind and was constructed as recently as 1998 in Denmark. It has since inspired other facilities to duplicate its design, such as ELASR constructed in Saudi Arabia between 2014 and 2015 [115].

As the the field of low energy antimatter research expands with new facilities planned or under construction, for example FLAIR at GSI [116, 117], the use of electrostatic elements will become more prevalent. To understand why they are so desirable for such applications we may compare the efficiency of electrostatic and magnetic elements by inspecting their magnetic and electrostatic rigidities:

$$\rho E = \frac{2E_k}{q}, \quad \rho B = \frac{1}{q}\sqrt{2mE_k}$$

where ρ is the bending radius, E is the electric field, B the magnetic field, E_k is the kinetic energy of the particles, m the mass and q the charge of the particles [118].

It can be seen that the electrostatic rigidity is independent of mass, so electrostatic elements become more desirable for low energy ion beams than their magnetic counterparts. Because of the dependence on the square root of the kinetic energy for the magnetic elements, they become much more efficient for medium to high energy particles which explains their prevalence in conventional set-ups.

The main goal of the work in this chapter is to develop realistic and computationally fast simulation methods for low energy beam transport using electrostatic elements, whilst simultaneously investigating and optimising the beam quality along ELENA's transfer lines, building upon previous studies [119]. To achieve these goals a 3D simulation of the longest transfer line, connecting ELENA and ALPHA, was created in G4Beamline [120]. Although numerous other 3D beam transport codes exist (such as BEAMPATH [121] or TRACK3D [122]), G4Beamline has been chosen since it is still actively maintained and updated and is based in a GEANT4 [123] environment.

Connected antimatter experiments such as ALPHA, ASACUSA and AEGIS [124] use GEANT4 in simulations thanks to its wide range of ever updating libraries. Whilst some contention exists regarding discrepancies between FLUKA and GEANT4, G4Beamline's accelerator oriented perspective lends itself to these particular simulations. Efforts are continually made by experiments to provide experimental observations as input to improve the accuracy of GEANT4 [125, 126], the benefits of which may then be easily implemented here. This opens the possibility to directly interface the G4Beamline model with existing experimental simulations and guarantees access to the most up to date low-energy antiproton physics packages.

The transport line simulation may be validated and compared with existing simulations and also benchmarked against real measurements taken once the line begins operation after LS2. The simulation may then be used to ascertain and optimise beam quality at the handover point to the ALPHA experiment. Additionally, the simulation is used to transport distributions based on the most recent

beam measurements in ELENA with the scraper, and along transport lines to GBAR, taken at the end of commissioning in 2018 to predict beam quality at the handover point.

7.2 ELENA to ALPHA Transport Line

Fig. 7.1 shows a drawing of the planned layout of the ELENA transfer lines, with a focus on the ELENA to ALPHA configuration. One of the benefits of the ELENA ring is the ability distribute four bunches between experiments during the same cycle. The transport lines are vital in ensuring that the beam is distributed amongst the experiments whilst meeting certain requirements at the handover point to each. Optimisation of the optics and junction sections therefore must be performed with this in consideration. Here we consider the ALPHA configuration where the beam sees an extraction kicker, a fast kicker & static deflector combination and finally a static deflector, as well as the periodic quadrupole assemblies. The total length of this path is 37.4 m.

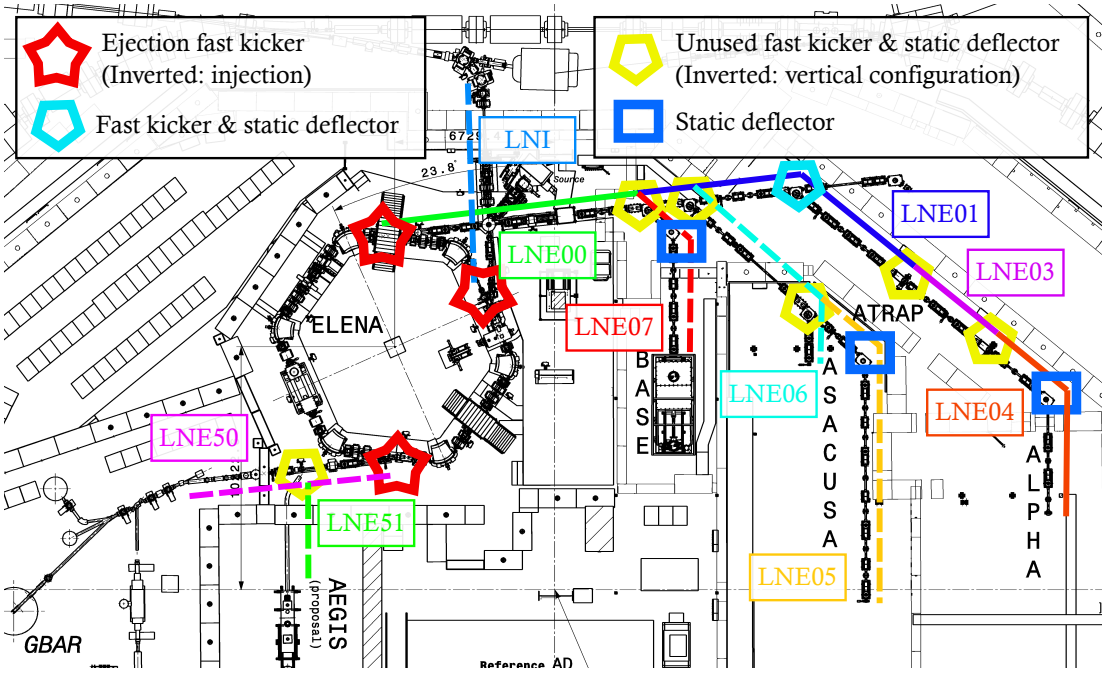

FIGURE 7.1: Layout and naming scheme of the ELENA transfer lines. The path from ELENA to ALPHA is marked with unbroken lines with all other sections being marked by dashed lines (elements marked "Unused" are unused specifically when transporting to ALPHA). The position of all experiments is also included (note: ATRAP is located above LNE03).

The transfer lines to all experiments are built in a modular fashion i.e. they are constructed mostly from repetitions of the same several elements. The main focusing assembly is an electrostatic quadrupole doublet with horizontal and vertical corrector kickers situated between the quadrupole pair, seen in Fig. 7.2. The quadrupoles are 10 cm in length along the centreline, s, with a gap of 24.4 cm between their centres. The electrode radius, r_0, (radius of the circle drawn around $x, y = 0$ and touching the electrodes) is 30 mm. The correctors are both 3.7 cm in length and are situated symmetrically between the quadrupoles. The assembly is typically used in a FODO configuration with one focusing and one defocusing quadrupole, however sometimes in several consecutive assemblies only a single quadrupole (of alternating polarity per assembly) is active to create a larger FODO arrangement. Quadrupole assemblies are often immediately preceded or followed by a microwire beam position monitor (BPM) for online monitoring and tuning.

There are two main types of bending elements in the transport lines, a pulsed fast deflector (naming convention ZDFA) and static bending elements (three variations on one design to accommodate different angles, ZDS[A,B,C]). The fast deflector is designed for small angles (max 240 mrad) and acts as a fast switch with a rise and fall time $< 1\mu s$ to allow beams to either pass straight through or be diverted to another section. The static deflectors are used for larger angles ranging 33.16°– 77.4°, often directly after a fast deflector at junctions.

There are three fast deflectors within ELENA itself, one injection kicker and two acting as extraction kickers. The extraction kickers either take beam to the original experimental area via LNE00 or to the new area that houses GBAR via LNE50. It is expected that the position of AEGIS will be moved to also branch from LNE50 (LNE51) although at the time of writing the move is not confirmed. All other fast deflectors in the transfer lines network are placed at junctions and are followed by static deflectors. The fast deflectors all have a nominal bending angle of 220 mrad. Two fast deflectors bend vertically upwards in combination with vertical static deflectors to take the beam to the two ATRAP handover points above the transport line.

Three static deflector types were designed to be used in the beam transport

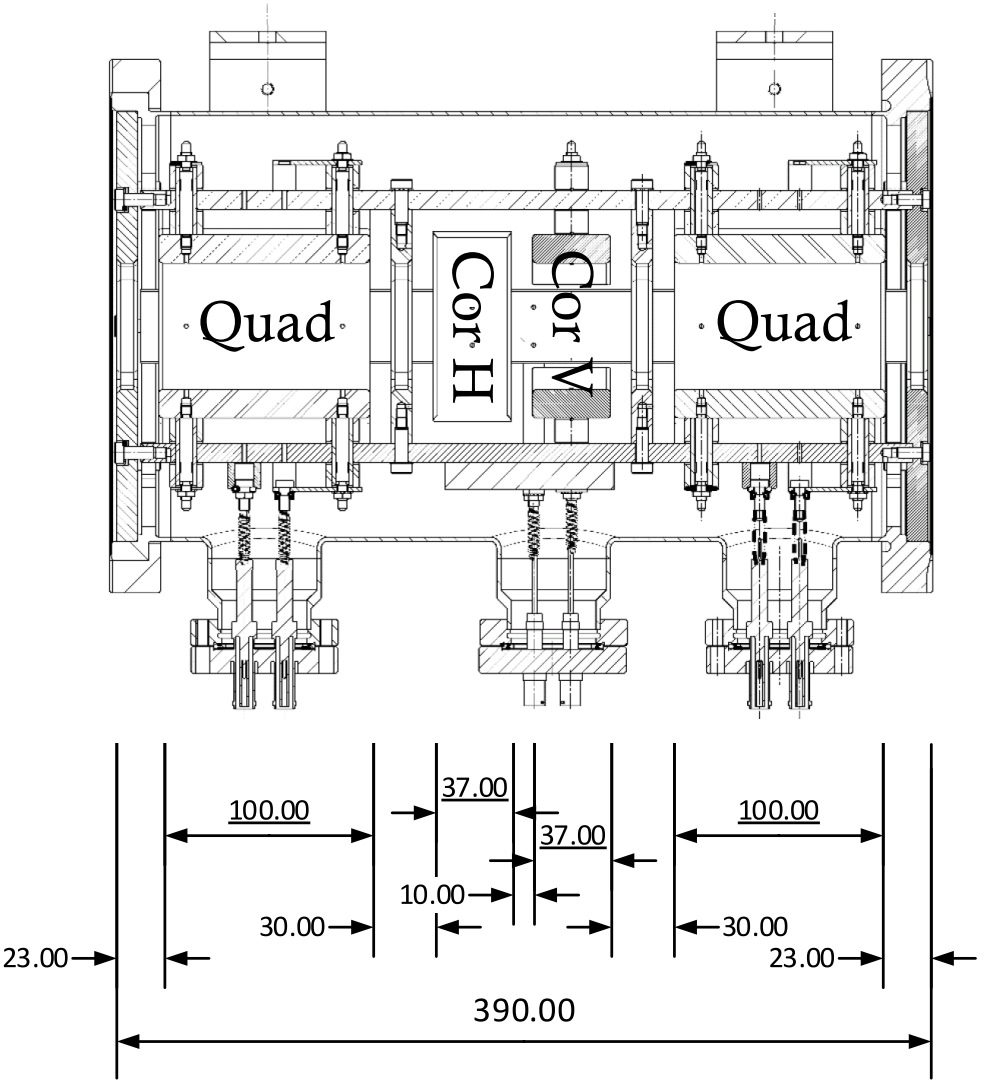

FIGURE 7.2: ELENA transport lines electrostatic quadrupole assembly showing horizontal ("H") and vertical ("V") correctors ("Cor") between a quadrupole ("Quad") doublet. Lengths and spacing of elements are expressed below in mm.

lines. One for use in combination with the fast horizontal deflector, ZDSA, one for standalone use, ZDSB, and one to be used in combination with vertical fast deflectors to bend vertically upward to ATRAP handover points, ZDSC. Because of the existing layout of the AD hall, it was not possible to design the transport lines system with just one required angle from each of these designs. The range of angles required for each deflector type is small enough such that each type has one specific electrode design to be used at differing operating voltages to accommodate the range of angles. This allows for simplified production of electrodes and is also beneficial when considering spare parts and repairs.

When transporting antiprotons from ELENA to ALPHA two fast kickers are used, including one for extraction. Additionally, two static deflectors are used, designs ZDSA and ZDSB, with the ZDSA model being used in conjunction with one of the ZDFA kickers. 21 sets of quadrupole doublets are used, although only five of those use both quadrupoles in the assemblies. Typically for longer straight sections, only one quadrupole per doublet is used to allow for a long phase ($\approx$3 m) repeating FODO arrangement.

7.3 Simulation Environment

G4Beamline is a GEANT4 based particle tracking code developed for the study of charged particle propagation through accelerator lattices, and was used as the basis for the simulations presented here. As well as the compatibility reasons mentioned in the introduction, it was chosen due to several features which allow the user to find a balance between detailed realism and efficiency within simulations.

To use the code a lattice may be constructed as a combination of predefined bending and focusing elements, regions of electromagnetic field defined by equations, or externally generated field maps. The lattice exists in 3D space, with (x, y, z) as (right handed) global co-ordinates, and similarly a set of centreline co-ordinates (x, y, s), with s being an axis which follows the lattice's bends. The input beam may be generated based on the input parameters used by G4Beamline or can be read in as an externally generated beam distribution, providing maximum flexibility.

In contrast with many commonly used tracking codes such as MAD-X, which uses calculated transport matrices for tracking through optical elements and drift space, the particles in these simulations are influenced by the electromagnetic fields they propagate through. A 6D beam distribution will propagate through voxelised 3D space and fields, with Runge-Kutta methods performing integrations for the particles' motion. Optical lattice parameters then arise from the motion of bunches through these fields naturally as opposed to particle movement based on calculated optics.

Whilst propagating through the 3D environment particles may be also subject to additional forces depending on the physics package being used. This allows the simulation to combine many effects, including fringe and inhomogeneous fields, stray magnetic fields from experiments, space charge effects, the heating effects on electrodes and more.

The GEANT 4 environment in which the simulations are based allows the user to choose from the extensive list of physics packages that have been developed and updated over many years, and which take into account experimental measurements. There is also the possibility to manually create physics lists. These options provide the possibility to simulate low energy hadron behaviour and to continue improving the simulations as new data becomes available.

The ability to quickly view lattices and primary and secondary particle tracks in a 3D visualisation is an extremely useful feature of the program. It allows for the quick identification of sources of error within the lattice definitions, for example; to determine which quadrupole may have the wrong position or strength, or to see the origin of beam loss. It also aids in the correct placement of field maps and other components of the lattice, particularly useful being the ability to visualise field lines within a defined volume.

Once a beam has been tracked through the lattice, the program may then calculate many useful accelerator physics quantities based on the beam's behaviour. For example, using the `profile` command one may quickly view the emittance and beta functions along the lattice, amongst other parameters. The `trace` command allows the user to record information on individual particles at defined steps, for example to check the field type, strength and direction seen by the particles as a function of s, or the dose deposition in beamline elements.

7.4 Electrostatic Quadrupoles

G4Beamline includes a set of predefined elements such as `genericquad`, `genericbend` and `sectorbend`. The `genericquad` command places a hollow cylinder with its length along the s direction at a specified point in the beamline to act as a

quadrupole. The dimensions of the object are fully customisable and it is possible to assign a material to it or set it to kill particles incident on its surface to act as a limiting aperture. The element includes a typical quadrupole shaped magnetic field (transversally $r^2 \cos(2\theta)$, in polar co-ordinates) of user-defined gradient with a customisable fringe field which is described below.

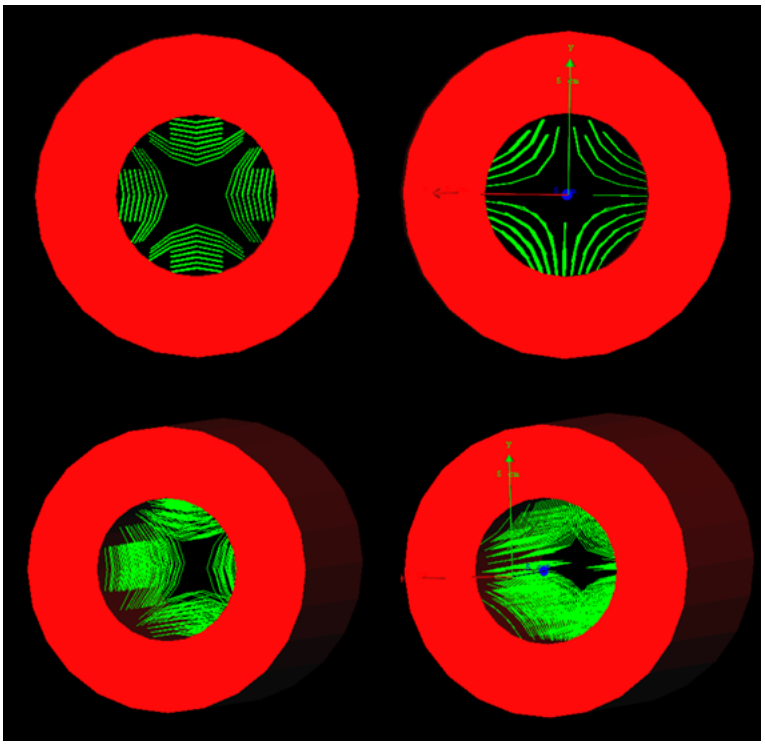

FIGURE 7.3: Side by side comparison of the magnetic (left) and electrostatic (right) quadrupoles as shown in the G4beamline visualisation. The red volume represents the inner and outer aperture of the elements.

In this simulation the quadrupoles are approximated by modified versions of these predefined `genericquad`s. At this stage of the simulations where the bending elements are represented by externally generated field maps, it is sufficient to represent the quadrupoles by these limiting apertures with well-defined uniform fields and fringe fields. Currently, field maps are being obtained through measurements of one of the ELENA quadrupoles in a collaboration established during the course of this work between the Cockcroft Institute, CERN and Technische Universität Wien using a novel sensor [127]. The results of the study will be used for benchmarking and it will be possible to implement the obtained field maps into these simulations.

The source code G4Beamline was modified to allow for easy implementation of electrostatic quadrupoles. The `genericquad` command was edited to allow the construction of magnetic and electrostatic quadrupoles using the commands `genericquadM` and `genericquadE`. `genericquadE` has the same field distribution but with an electrostatic field instead of magnetic, effectively creating a skew electrostatic quadrupole. Placement of the element into the lattice requires a 45° rotation around s to enable it to act as a standard focusing or defocusing quadrupole. The field lines shown by G4Beamline may be seen in Fig. 7.3.

Two beamlines based on the start of LNE00 were constructed using an electrostatic injection kicker at $z = 100$ mm followed by eight quadrupoles of each type, i.e. an all `genericquadM` lattice and a rotated `genericquadE` only lattice. The magnetic, G_M, and electrostatic, G_E, quadrupole gradients were calculated from the nominal integral focusing strengths, k, for each quadrupole, with the intention of creating two lattices of identical Twiss parameters. The gradients were input with G4Beamline units (Tm^{-1}, MVm^{-1}) from:

$$G_M = \frac{kp}{c \times 10^{-9}}, \quad G_E = \frac{G_M v}{10^6}, \tag{7.1}$$

where p is the momentum of the particles in the beam, v is the velocity of the beam particles and c is the speed of light in vacuum. The same optically matched Gaussian beam distribution, with $\epsilon_{x,y} = 2$ mm mrad, was run through the test lattices and the results were compared.

The resultant beta functions along the lattices are shown in Fig. 7.4. The two sets of quadrupoles clearly have the same focusing effect on the beam, and despite k not being fine tuned, both beams enter an almost identical FODO configuration. Some small difference can be seen towards the end of the lattice, and is highlighted in Fig. 7.5 which displays the horizontal phase space of the 1,000 particles tracked at the end of both lattices. The small difference in particles' positions could be explained either by the different effective field shape encountered by the particles, small rounding errors during the conversion from one gradient to the other, or a combination of both. The difference does not significantly affect the characteristics

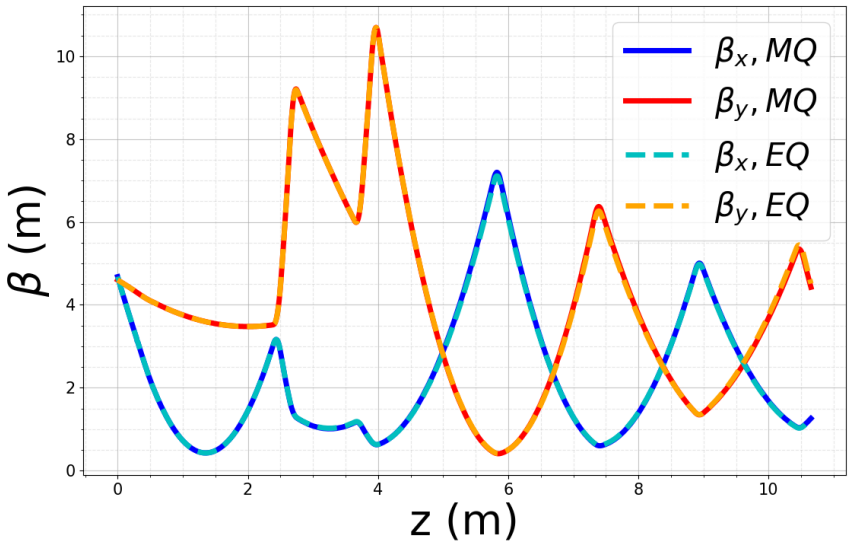

FIGURE 7.4: Overlaying comparison of horizontal and vertical beta functions for magnetic (MQ) and electrostatic (EQ) quadrupoles.

of the overall beam. Similarly, the longitudinal momentum spread is minimally affected, as seen in Fig. 7.6.

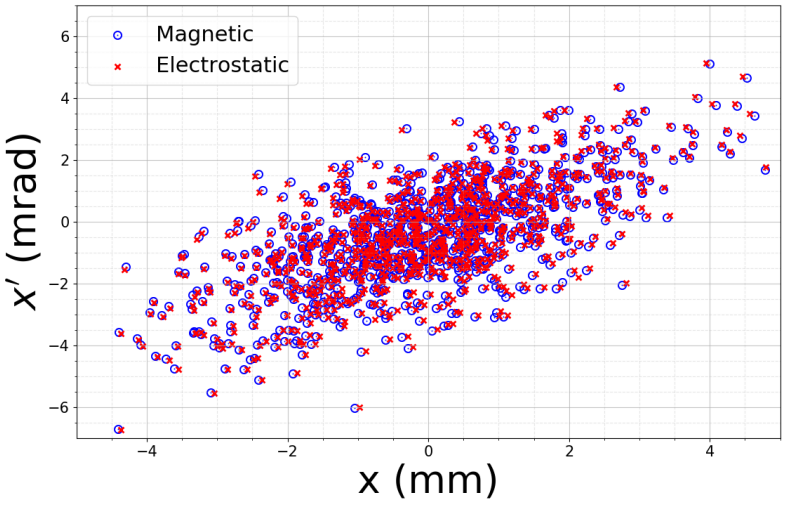

FIGURE 7.5: Horizontal phase space plot for two beams after tracking through magnetic and electrostatic versions of LNE00.

A model of the standard ELENA transport line quadrupole was created in CST Studio [128] using the technical report from CERN's Drawing Directory (CDD) [129]. A range of voltages were applied to the electrodes to ascertain the field gradient and inspect its shape throughout the quadrupole, seen in Figs. 7.7 & 7.8.

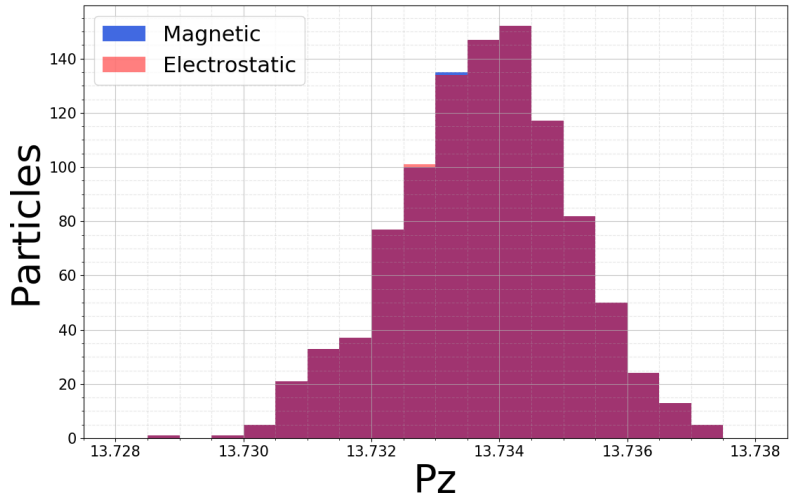

FIGURE 7.6: Longitudinal momentum distribution of particles after tracking through magnetic and electrostatic versions of LNE00.

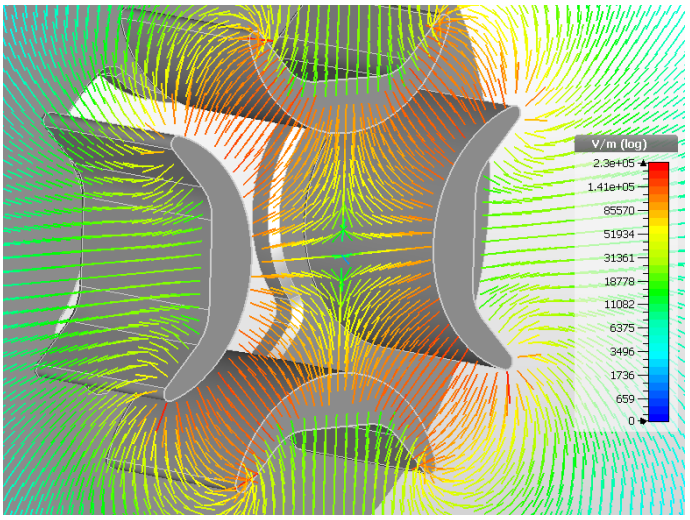

FIGURE 7.7: An x-y plane cross section of the CST quadrupole model. Field lines show the shape of the field and the electrodes and shielding are displayed behind.

The electrostatic potential, V, at $x = 20$ mm and $y = 20$ mm was exported to be used to characterise the fringe field shape. The custom equation in MATLAB's curve fitting tool was used to obtain 6 Enge function [130] coefficients, a_n. The function has the form:

$$Enge(z) = \frac{A}{1 + \exp(a_1 + a_2(z/D) + ... + a_6(z/D)^5)}, \tag{7.2}$$

where z is the distance perpendicular to the effective field boundary, D is the

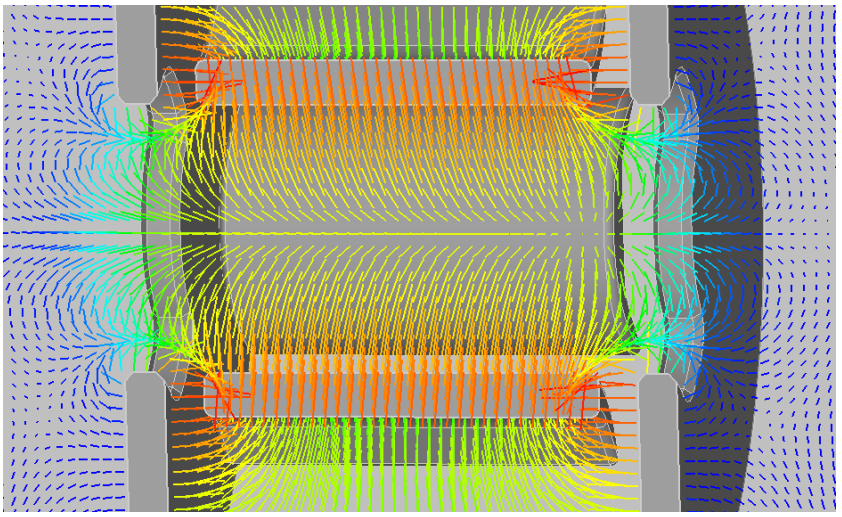

FIGURE 7.8: The field within the quadrupole along the y-z plane, offset by 14 mm in x.

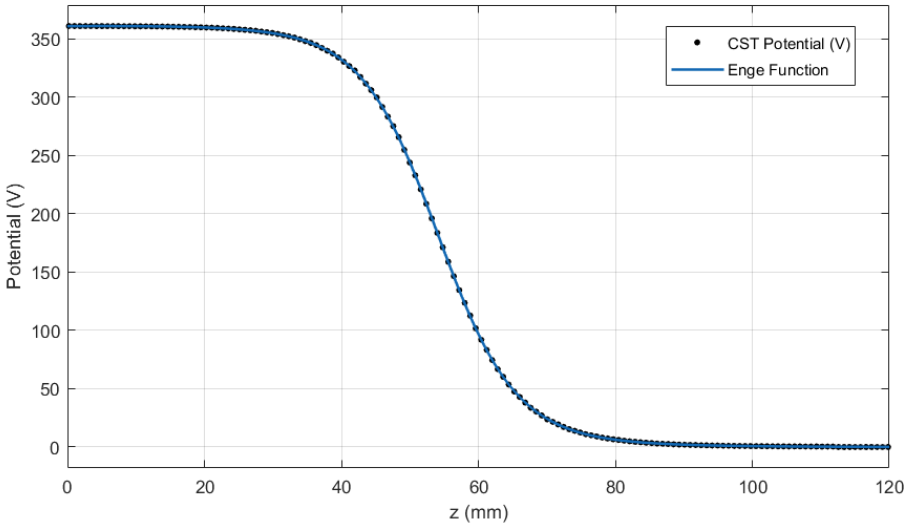

FIGURE 7.9: Enge function fitted to the quadrupole fringe field generated in CST.

full aperture of the element and A is a scaling factor. The line fit is displayed in Fig. 7.9 and the coefficients may be found in Table 7.1. The coefficients were used by G4Beamline to generate an accurate approximation of the fringe fields.

TABLE 7.1: Enge coefficients for Eq. 7.2.

A	a1	a2	a3	a4	a5	a6
362.4	-0.7233	10.39	1.003	-6.39	0.8186	2.049

7.5 Electrostatic Bending Elements

To model the electrostatic bending elements several approaches were tested and compared. The first element to be simulated was the ejection kicker which, situated within ELENA, is considered the start of the beamline. Its entrance is placed at $z = 100$ mm with the injection beam beginning at $z = 0$ mm to allow space for fringe field effects.

7.5.1 Field Expressions

It is possible to define an electrostatic or magnetic field based on either cartesian or cyclindrical expressions. An electrostatic field, E, perpendicular to the centre line of the electrodes was created using the following expressions:

$$E_x = E\cos\theta,\ E_y = 0,\ E_z = E\sin\theta \tag{7.3}$$

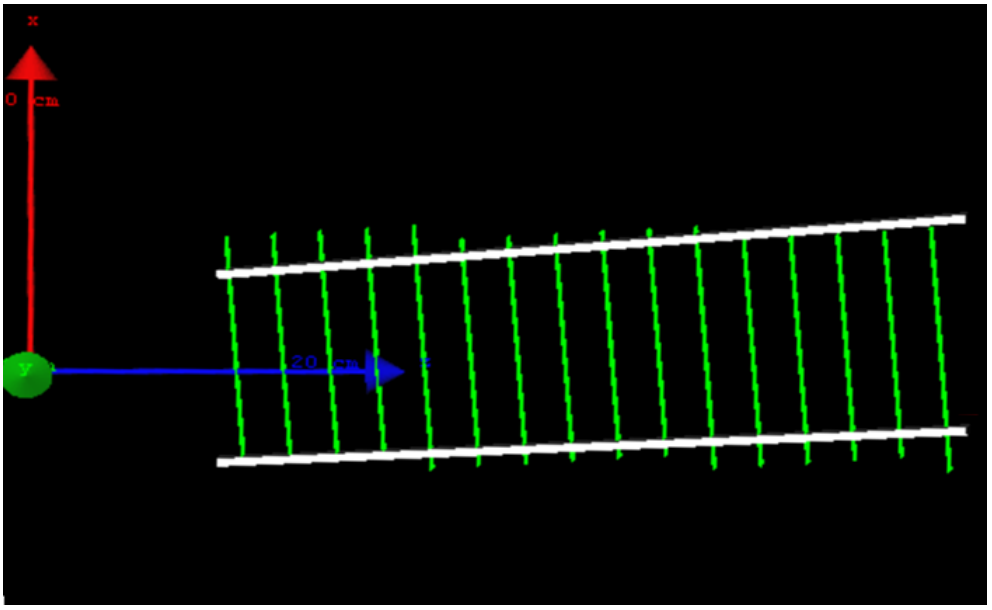

FIGURE 7.10: G4Beamline screenshot showing field lines (green) approximating the fast extraction kicker using field expressions. White volumes represent electrodes.

where θ is the angle between the centre line of the element and the z axis. Whilst this approach is fast and simple, it serves as a placeholder for more realistic models. The expression doesn't take into account fringe effects or the difference in

separation of the electrodes from the entrance to the exit. Fig. 7.10 shows the field lines in the simulation. As the field lines are always contained within a rectangular cuboid they cannot be made to fit the elements well and field leakage is observed. For elements that bend through much larger angles, field lines would not be perpendicular to s for the majority of the element. Regardless of the flaws, field expressions are useful for obtaining a quick approximation of what field strength to use and for tuning the fast deflectors in the beamline during the construction phase of the simulation. As a placeholder for the large angle static deflectors, a G4beamline magnetic sector bend was used during initial quadrupole placement.

7.5.2 Finite Element Methods

In order to realistically simulate the field distributions of the bending elements, field expressions were replaced with externally generated field maps. The field maps include realistic fringe fields plus field inhomogeneities due to the geometry of electrode placement e.g. angled edges and tapering of electrodes in the fast deflector or curved inner walls on the static deflector electrodes. G4beamline allows the placement of field maps through the `fieldmap` command, provided the map is in a grid format with a constant step in either $\{x, y, z\}$ or $\{z, r\}$.

Using technical drawings from the CERN Drawing Directory, CDD [131], CAD models of electrodes of the fast and two horizontal static deflector electrodes were created in CST Studio. The models were used to generate field maps by applying nominal operating voltages on the electrodes. The strengths of the fields could later be scaled and adjusted during the tuning process. Examples of CST models and placements in the beamline of the field maps may be found in Fig. 7.11. Tests using field maps with resolutions (spacing between points) of 1, 3 and 5 mm found a negligible difference in the resultant beam distribution between 1 and 3 mm and a larger discrepancy when reducing resolution to 5 mm. 3 mm was chosen for the majority of simulations as the best compromise between speed and accuracy. Later the field maps could be replaced by those with 1 mm spacing for most realistic final results.

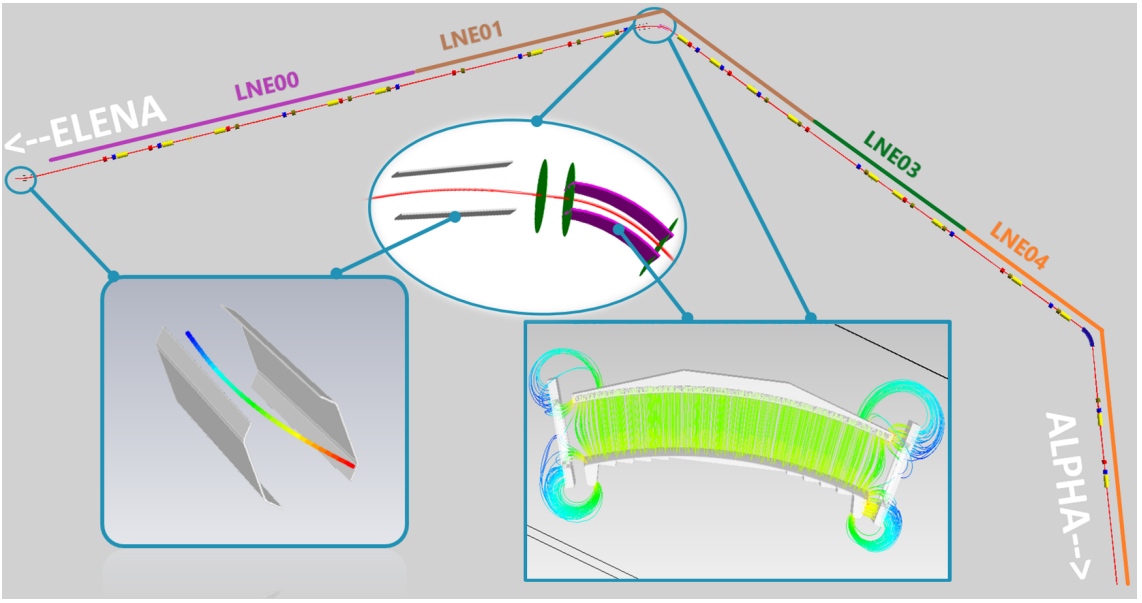

FIGURE 7.11: Full simulation of the transport line from ELENA to ALPHA. The red lines represent antiproton tracks. Focusing and defocusing quadrupoles are represented by red and blue elements respectively, and SEM profile monitor vacuum tanks are represented as yellow objects. Deflectors created in CST are shown as well as their placement within the beamline. Dark green disks are virtual detectors for monitoring beam properties during tuning.

7.6 Input Beams

Input beams were generated using the Python beam generation script developed for the scraper studies (Section 5.3.2) but modified for G4Beamline input format. Input Twiss parameters were matched to those used for a MAD-X simulation of the transport lines supplied by CERN. Macroparticles were generated for a Gaussian beam with $\epsilon_{x,y}$= 1 mm mrad and zero momentum spread for the testing and tuning of the beamline optics.

In Chapter 6 the coasting ELENA beam was measured in the presence of electron cooling along the extraction plateau. Analysis using the two scan method showed a beam with emittances ϵ_x =0.55 ($\pm$0.04) mm mrad and ϵ_y =0.53 ($\pm$0.01) mm mrad. There did not appear to be any significant emittance-momentum offset correlation and the transverse beam distributions were well described by a Gaussian distribution of the same input parameters.

After the point at which the measurements were taken, the beam is rebunched and extracted from ELENA. Since rebunching using the RF systems tends to

lead to a blow-up in transverse emittance and longitudinal momentum spread this process is performed also in the presence of electron cooling. Previous studies have shown that slow beam capture and compression, in around one second, with electron cooling can keep the RMS momentum spread at a suitable level, with an estimate of $\sigma_\delta = 4.2\times10^{-4}$ [132].

Profile measurements taken with an SEM grid around 3 m along the transport line to GBAR gave estimates for horizontal and vertical RMS beam widths of $\sigma_x =$ 5 mm and $\sigma_y = 2.5$ mm respectively. Converting to emittance values using simply $\epsilon = \sigma^2/\beta$, for $\beta_x = 6.5$ m and $\beta_y = 3.1$ m, gives extraction estimates of $\epsilon_x = 3.9$ mm mrad and $\epsilon_y = 2$ mm mrad. Although crudely calculated, these values are currently the best estimate for post-extraction emittance. Coupled with scraper measurements confirming cooling, showing no significant emittance-momentum offset correlation and a distribution well approximated by a Gaussian profile they form the basis of beam generation for beam quality studies. The RMS momentum spread is set to 4.2×10^{-4}. Distributions containing 10,000 macroparticles with these properties and matched Twiss parameters were generated to determine beam quality estimates at ALPHA.

7.7 Beamline Optics Tuning

The four different sections that make up the beamline were created and simulated independently before being merged together to create the entire 37.4 m long line to ALPHA. It was only after the separate sections were merged that the tuning process could begin properly, since initial beam conditions at each section depend on the end conditions of the previous.

7.7.1 Bending Elements

G4Beamline is capable of tuning bending elements and field maps by using a reference particle repeatedly travelling from s_0 to s_1 to calculate and minimise an expression at s_1, based on some variable property, typically an element's field strength. For example, to tune the extraction kicker the reference particle passes

through it, from $s_0 = 0$ m to $s_1 = 2$ m, adjusting the strength of the field map to minimise the x position of the particle at s_1. When the output satisfies the tolerance settings the field strength is saved.

This was done to set the strengths of all four bending elements to deflect the reference particle by the correct angle. Each time this automated tuning was performed, the reference particle was tracked from $s = 0$ m to ensure entry conditions into the bending element take into account all preceding effects. Because the horizontal static deflectors must achieve a range of bending angles for a single pair of electrodes, it was not possible simultaneously satisfy $x = 0$ m and $p_x/p_z = 0$ after a particle passes through them, i.e. a beam leaves the deflector at some horizontal displacement then passes the centre co-ordinate at s_1 and continues diverging (in the case of minimising x), or the beam will travel parallel to the centreline but at some displacement in x (in the case of minimising p_x/p_z). A very specific set of electrodes would have to be designed for each angle for a chance to satisfy these conditions. It is, however, necessary to satisfy both conditions at some point.

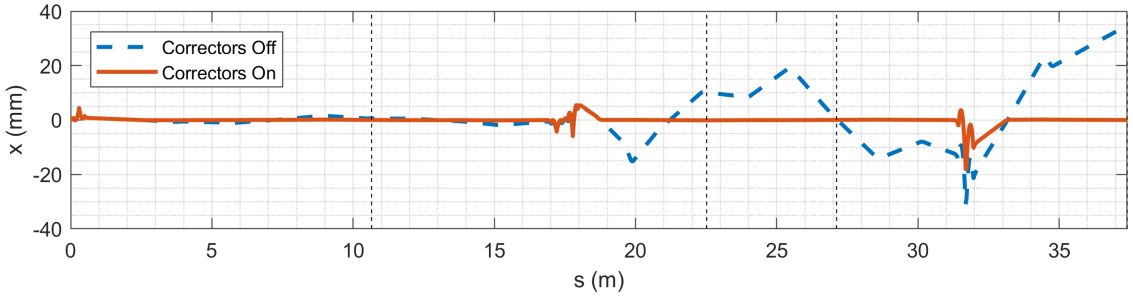

FIGURE 7.12: Closed orbit of the beam with correctors on and off. Vertical black lines mark the different sections: LNE00, LNE01, LNE03, LNE04. The closed orbit through deflectors appears unphysical (skewed 'M' shapes) due to G4Beamline defining reference centre orbit, s at corners with 3 points, whilst the beam travels in a smooth ark.

To achieve a centred and aligned beam after the two static deflectors, the condition was set to minimise x-position at the entrance of the following quadrupole assembly. All of the horizontal correctors in the quadrupole assemblies are set to use a reference particle from $s = 0$ m to minimise p_x/p_z 15 cm downstream from the centre of the assembly. This resulted in beams from deflectors entering following quadrupole assemblies at $x = 0$ but with some small angle and then being kicked to a non-divergent path, achieving the desired closed orbit of the beam.

Figure 7.12 shows a comparison. The maximum mean horizontal position of the beam, during FODO sections, without correctors is almost 20 mm and with is less than 1 mm, showing how essential the proper operation of the correctors is. The plot also highlights their necessity for delivering the beam on target.

7.7.2 Quadrupoles

MAD-X determined strength settings for the quadrupoles did not achieve similar beta functions because of differences due to fringe fields in both the quadrupoles and deflectors, and field inhomogeneities in field maps due to electrode geometry. G4Beamline does not offer a built in quadrupole tuning module. A wrap-around macro based on CERN's function minimization tool MINUIT [133] is packaged with the program, however it is not suitable for multi-variate and multi-objective problems, e.g. tuning several quadrupoles to simultaneously satisfy various beta function constraints.

Initially, manual quadrupole tuning was used to achieve stable beta functions, based on the MAD-X configuration i.e. variations starting with MAD-X quadrupole strengths to obtain similar beta functions. To aid in this (and to generally increase the functionality of these simulations) a GUI interface was developed in MATLAB [134]. The interface, pictured in Fig. 7.13, is capable of setting and changing input parameters such as individual quadrupole strengths, executing the program and displaying resultant properties, such as beta functions along the line, or 2D and 3D plots from 6D phase space information collected at virtual detectors. Sliders at the bottom of the GUI may be changed to adjust any input parameter of the simulation from within the source code. After re-running simulations with new settings it is possible to plot with previous results for direct comparisons.

Using this method a stable beta function configuration was achieved and several particularly effective quadrupoles for influencing beta functions were identified. The specific quadrupoles are listed in Fig. A.11 which also includes their positions along the line and their effects on beta functions. This information may

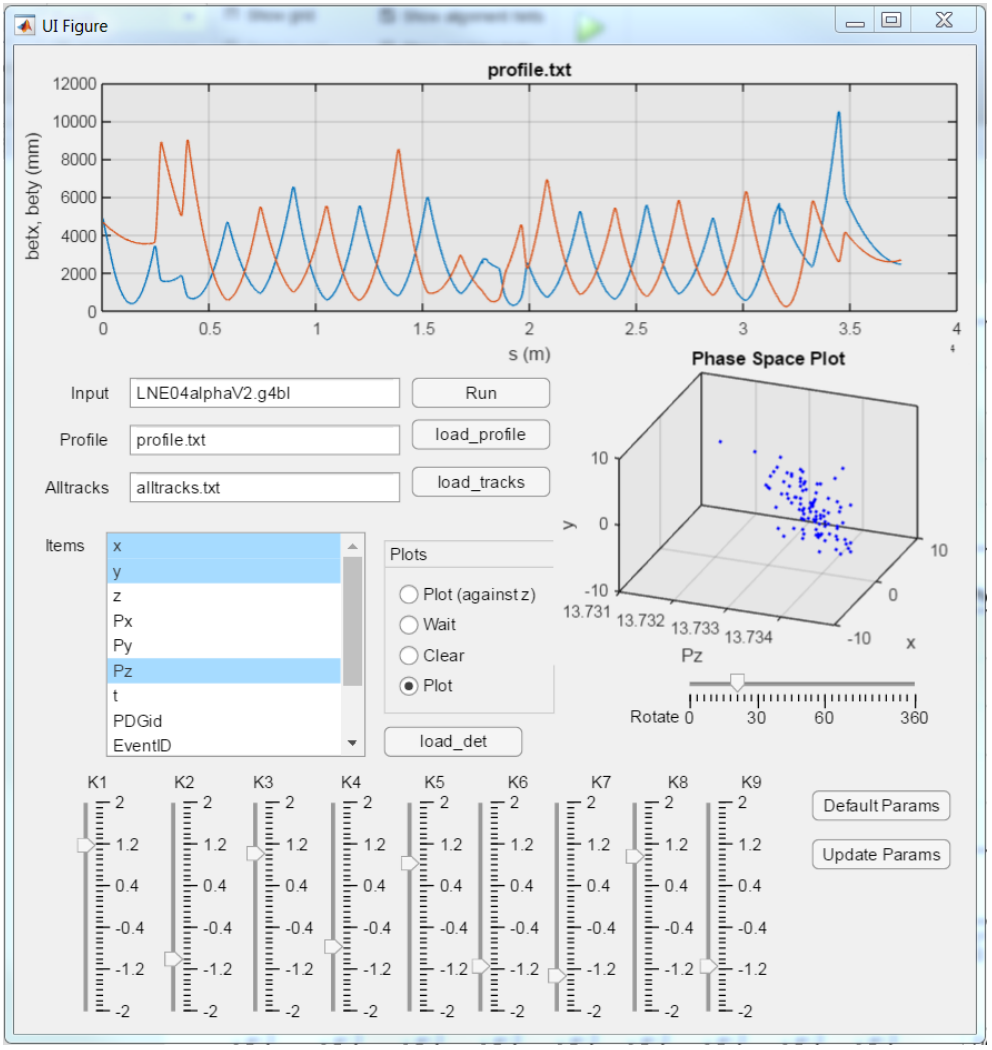

FIGURE 7.13: Screenshot of the GUI developed for use in tuning and optimising the beamline.

be especially useful during the set up of the transfer lines as it identifies useful tuning knobs for specific beta adjustments.

Figure. 7.14 shows a comparison of the beta functions for both G4Beamline and a MAD-X simulation based on that used by CERN during the design phase. Generally, there is good agreement between the two simulations, but it is seen that the final static bending element (at 31.5 m) appears to have different effects on the properties of the beam, particularly for the vertical case. This is unusual because the behaviour of the earlier static deflector around 18 m is much more consistent between the simulations. It is asserted that the G4Beamline simulation gives a more accurate description of the beam's behaviour since the particles here are tracked directly through a high resolution field map based on detailed electrode

geometry, rather than beta functions computed from a Taylor map extracted from a simplified electrode model. Indeed the extra step of Taylor map generation increases the likelihood of a miscalculation, a postulation which is supported by the agreement between the codes for the earlier static deflector.

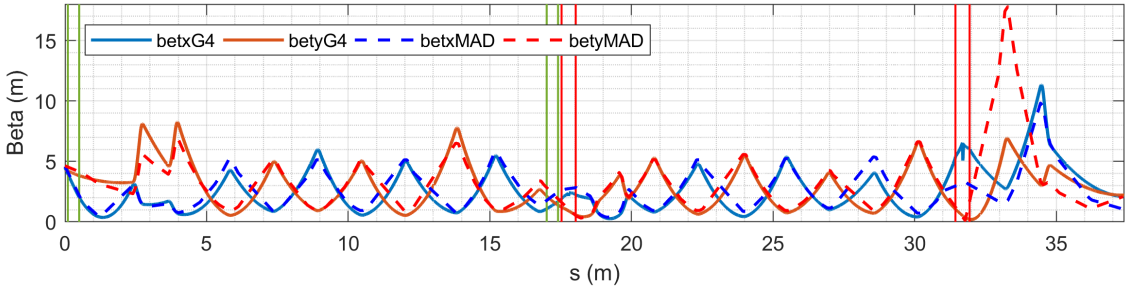

FIGURE 7.14: Comparison of beta functions for the G4Beamline simulation with the MAD-X values. Fast deflectors are positioned between pairs of green vertical lines and static deflectors between red.

Because MATLAB can interface with G4Beamline, by executing scripts and extracting results, it was possible to then automate this process using the available machine learning libraries. This functionality was demonstrated by using a pattern search algorithm [135] to minimise both beta functions (minimization objective: $\sqrt{\beta_x^2 + \beta_y^2}$) at the end of the transport line using four quadrupole strengths as variables. Pattern search was chosen as it works well for non-smooth problems at a smaller number of trials cost than some other non-smooth problem solving techniques, such as annealing or a genetic algorithm. The algorithm did cause larger beta functions earlier along the line to achieve its goal but due to strict restraints imposed on possible quadrupole strength ranges, large emittance beams would remain within the aperture. Fig. 7.15 shows the optical arrangement, with changes in selected quadrupoles highlighted. The final beta functions have been reduced by a factor of two, with a smaller reduction in RMS beam size due to $\sigma_{RMS} = \sqrt{\epsilon\beta}$. It is proposed that the beamline should be tuned to a stable configuration as in Fig. 7.14 and, if desired, pushed to achieve smaller spot size with the machine learning results as initial guide changes.

Some preliminary results using the paretosearch function [136], which is capable of multi-objective analysis, have shown promise and further experimentation with such techniques is ongoing. It is proposed that using G4Beamline simulations with

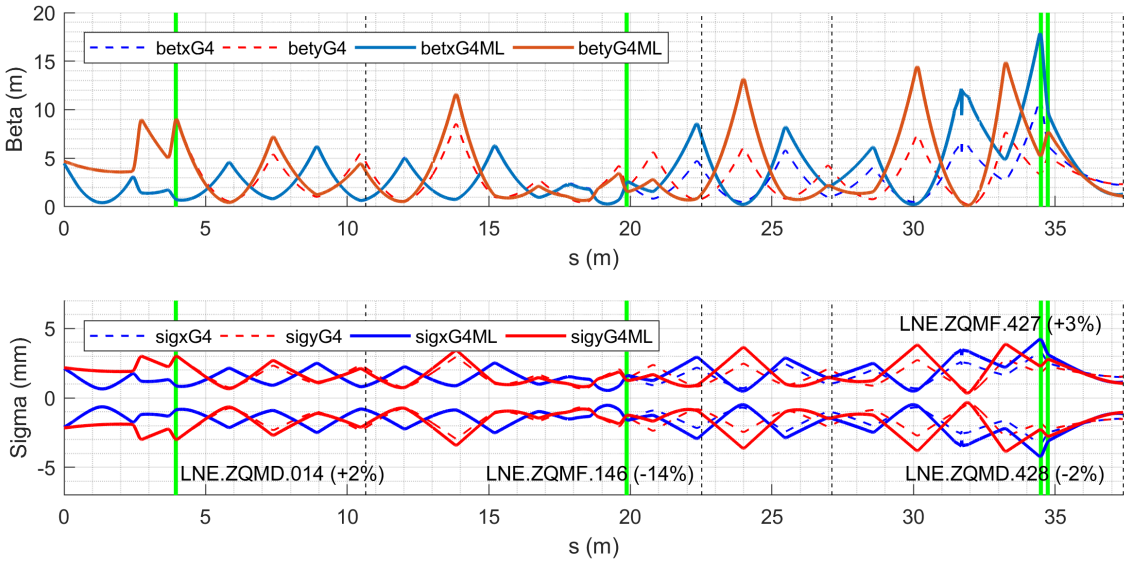

FIGURE 7.15: Comparison of beta functions and RMS beam width ('Simga') from the machine learning ('G4ML') results with the manually matched lattice. Varied qaudrupoles' centre positions are marked with green vertical lines next to their names located on the bottom plot.

a MATLAB machine learning wrap around would be extremely beneficial in the future design and optimisation of such transport lines. It is also noted that with enough computing power, numerous quadrupole strengths and positions could be set as variable parameters solving for a range of desired objectives, such as global maximum betas or a flat beta function at the handover point, to achieve settings for highly optimised beam transport. Such solutions would contain considerations for the large array of effects that G4Beamline is capable of including, for example the effects of stray magnetic fields on the beamline.

7.7.3 Dispersion

Unfortunately, G4Beamline is not equipped to either calculate or tune the dispersion along a beamline. This is an important flaw in the program when considering its use in quickly calculating lattice properties. To automate a tuning process which also includes dispersion would require extra macros running at least two reference particles – one on-momentum reference particle and one with a momentum offset, δ. The dispersion may then be calculated along the line using the

particle's horizontal shift due to it's offset: $D_x = \frac{\Delta x}{\delta}$. The results may then be used as tuning parameters.

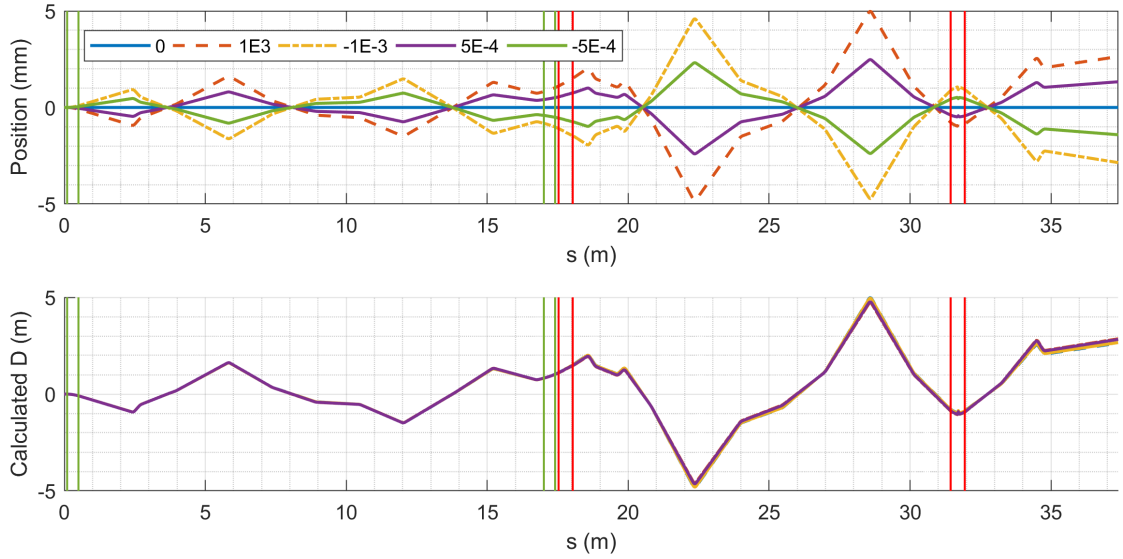

FIGURE 7.16: Horizontal offsets for particles of differing momentum offsets. The bottom plot shows the (overlaying) dispersion calculated from the paths of the four off-momentum particles. Fast deflectors are positioned between pairs of green vertical lines and static deflectors between red.

This process was performed manually for 5 different particles to determine the dispersion of the beta function-tuned lattice. The results may be seen in Fig. 7.16. As expected, all 5 particles gave very similar estimations for the dispersion along the line. Since there were some small differences, particles were run with positive and negative values of momentum offset and the dispersion at the handover point to ALPHA was calculated as a mean of the final values. It was given at $D_x = 2.74$ m and D'_x, calculated from the gradient between the last two data points (separated by 30 mm) was given as 2.25×10^{-4}.

7.8 Beam Quality

The first beam quality tests were performed with a Gaussian beam of $\epsilon_{x,y}$= 1 mm mrad with no momentum spread using the lattice pictured in Fig. 7.14. 10,000 macroparticles were tracked along the beamline with a minimum and maximum step size of 1 mm to ensure highest resolution results. Figure 7.17 shows a comparison of the beam distributions at ejection and at the handover point to ALPHA. It

can be seen that the beam has maintained its Gaussian distribution, and that it is at a waist at the handover point. Roughly equal transverse beta values seen at the handover point during the tuning phase are reflected in a circular x, y distribution. The RMS beam widths at the handover point are $\sigma_x = 1.6$ mm, and $\sigma_y = 1.7$ mm which fall within the target values of $\sigma_{x,y} = 2$ mm. Transverse emittances at the start and end of the beamline were calculated from particle distributions collected by virtual detectors and as expected a negligible change was observed.

The longitudinal momentum of the beam was affected along the transport line, however. At the end of the beamline, the mean momentum offset of the entire beam was $\delta = 6.4 \times 10^{-3}$ with an RMS momentum spread of $\sigma_\delta = 1.2 \times 10^{-4}$. The momentum offset distribution of the particles can be seen in Fig. 7.18, and may be well described by a Gaussian distribution. It is likely that this introduction of some momentum offset has been caused by the use of electrostatic deflectors since their effect is not necessarily perpendicular to a particle's motion, i.e. $\vec{F} = q\vec{E} + q\vec{v} \times \vec{B}$. In fact, the momentum increase can be seen incrementally at the end of each section with values of $\delta_p = 2.6,\ 4.9,\ 4.9,\ 6.4$ ($\times 10^{-3}$) at the ends of LNE00, LNE01, LNE03 and LNE04, respectively. No increase is seen at the end of LNE03 since the beam did not pass any deflectors during this section. Although the static deflectors' geometry is designed to minimise this effect, the results highlight this important difference between electrostatic and magnetic bending elements.

Running the beam based on most recent measurements with $\epsilon_{x,y} = 3.9$ and 2 mm mrad and $\sigma_\delta = 4.2 \times 10^{-4}$ again did not show any emittance increase as expected. The mean momentum offset was increased to the same offset as previously, 6.4×10^{-3}, with an RMS momentum spread slightly increased from input to $\sigma_\delta = 4.8 \times 10^{-4}$. With this particular beam it is not a significant change, but the results suggest the beamline will be sensitive to low quality (high emittance, large momentum spread) beams, larger momentum offsets lead to larger deviations in closed orbit, for example. It is therefore essential to minimise dispersion along the transport lines where possible and to maintain electron cooling during the rebunching phase in order to ensure beams reach the handover point in the best possible condition. RMS beam widths of $\sigma_x = 3.3$ mm and $\sigma_y = 2.4$ mm show that

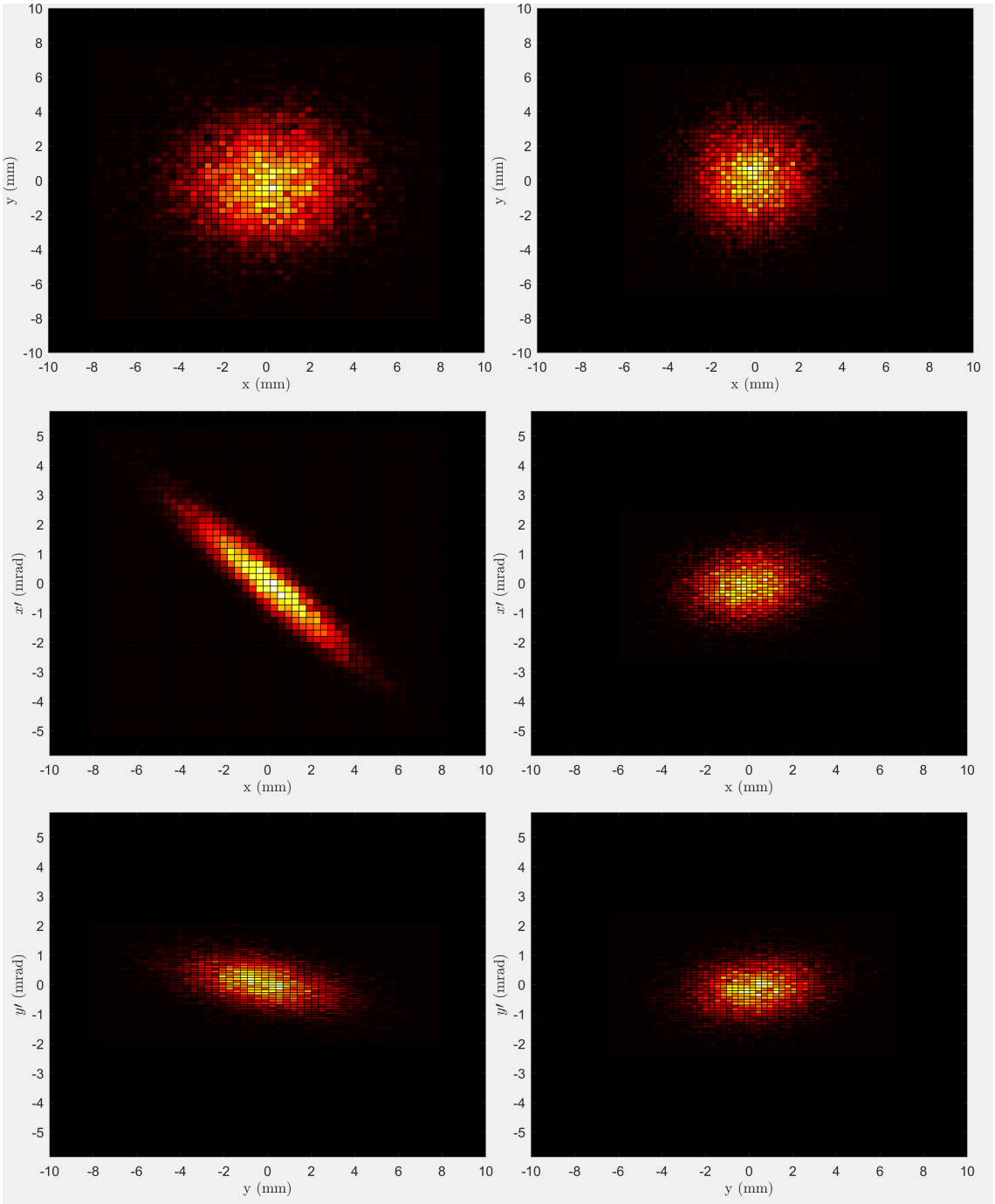

FIGURE 7.17: Transverse phase space plots for Gaussian beams of $\epsilon = 1$ mm mrad and $\sigma_\delta = 0$ at the start (left) and end (right) of the transport line to ALPHA.

at the end of commissioning in 2018 ELENA would already be delivering beams to close to their target quality of 2 mm RMS widths with this beamline configuration, despite ongoing issues with RF and and beam blow up during bunching before cooling.

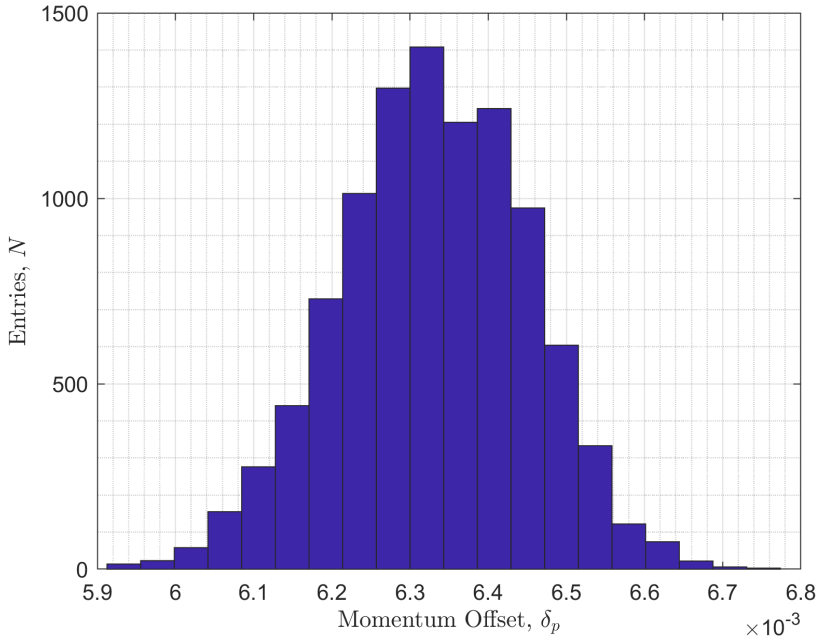

FIGURE 7.18: Momentum offset of 10,000 particles at the end of the beamline for an input beam of $\epsilon_x = 1$ mm mrad and $\sigma_\delta = 0$.

It should be noted again the importance of the correctors along the beamline. The beam spot size is increased slightly due to dispersion and RMS momentum spread, however the centre spot of the beam is well focused around $x, y = 0$ due to the correctors. If the correctors were not tuned using what is essentially a feedback loop with the reference particle (which also underwent a momentum offset increase), the momentum offset of the beam would cause a large horizontal shift in the beam spot through dispersive effects. Fortunately, it has been shown that this increase is consistent between shots and so the beamline can be corrected accordingly.

7.9 Errors

Monte Carlo methods were used to determine error tolerances along the beamline. Each effect investigated was the result of 20 random seed runs for 1,000 particles each.

To investigate the effect of quadrupole position offsets all quadrupoles were shifted independently. Because in practice the quadrupoles will not shift between

shots the correctors were allowed to automatically optimise for a reference particle before each random trial. This then simulates the best quality the beamline can provide after commissioning with the position offsets in place.

TABLE 7.2: Effects of quadrupole position offsets on closed orbit of beams.

RMS Position Offset	0.5 mm	1 mm	2 mm
Mean maximum (absolute) x_0	0.7	1.2	2.7
Standard Deviation	0.3	0.4	1.0

The only significant effect of this error was on the maximum deviation from closed orbit along the beam line. To characterise the effect the average maximum deviation was calculated for the 20 seeds at each different magnitude of position offset error. The results are summarised in Table 7.2. To keep the maximum deviation below 1 mm the quadrupoles should be installed to within 0.5 mm horizontal precision. The effect on the accuracy of beam delivery to the target is unaffected up to and above 2 mm thanks to the final sets of correctors.

TABLE 7.3: Effects of fast and static deflector position offsets on closed orbit of beams.

RMS Position Offset	0.5 mm	1 mm	2 mm
Mean maximum (absolute) x_0	0.7	1.4	2.2
Standard Deviation	0.4	0.8	1.2

Similarly to above, fast and static deflector offset trials were carried out with automatic corrector tuning. Although there are only 2 fast and 2 static deflector elements along the beamline compared with 26 quadrupoles, they obviously play a much larger factor in the horizontal position of the beam and so errors had a similar magnitude impact on the maximum closed orbit to those for the quadrupole offsets. The results are summarised in Table 7.3 whilst Fig. 7.19 highlights how closed orbit bumps are much more localised when considering deflector errors. It appears the final static deflector is the most sensitive to position errors, likely due to its much larger bending angle of 50.4° over a shorter distance than the earlier 33.16° counterpart. Considering that the large offsets following this element are in the region where beta functions may be maximised, with the aim to then tightly focus the beam to the handover point, its placement should be treated with most care.

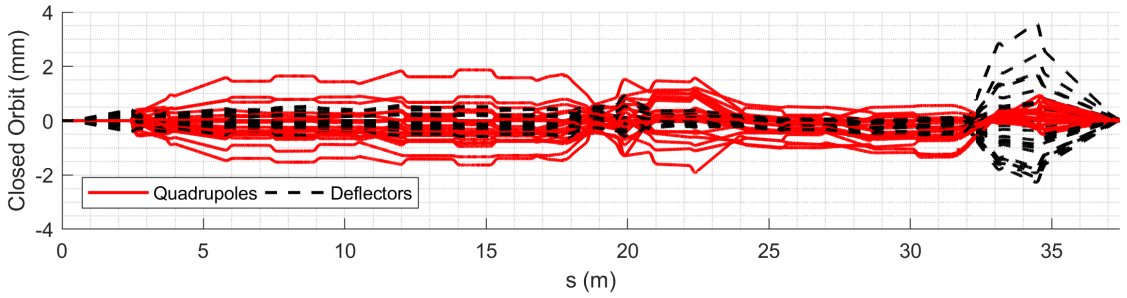

FIGURE 7.19: Comparison of the effect on closed orbit when varying quadrupoles and static deflectors randomly by RMS 1 mm for random 20 seeds.

Investigations into field uncertainties were carried out under the assumption of shot to shot fluctuations on power sources. For this reason the correctors were instead held at values optimised for ideal field strengths during all trial runs. The effects of quadrupole and deflector field fluctuations were carried out independently.

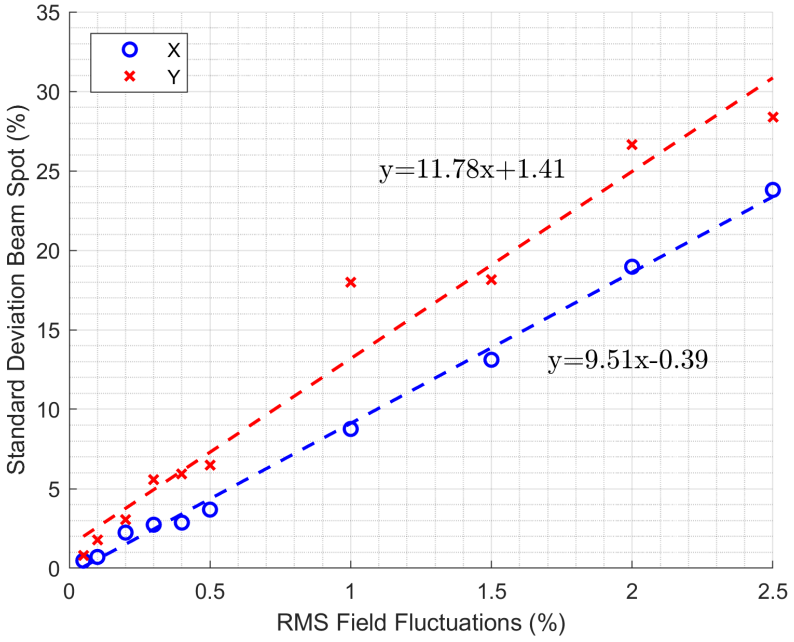

FIGURE 7.20: Beam size fluctuations based on quadrupole field strength errors.

Quadrupole fields were independently varied as a percentage of their original strengths and the standard deviation in beam size at the end of the line was calculated for 20 random seeds. The results are plotted in Fig. 7.20 with linear fits to inspect the relationship between error magnitudes and effect for each plane. Larger errors are observed vertically likely due to larger vertical beta functions at

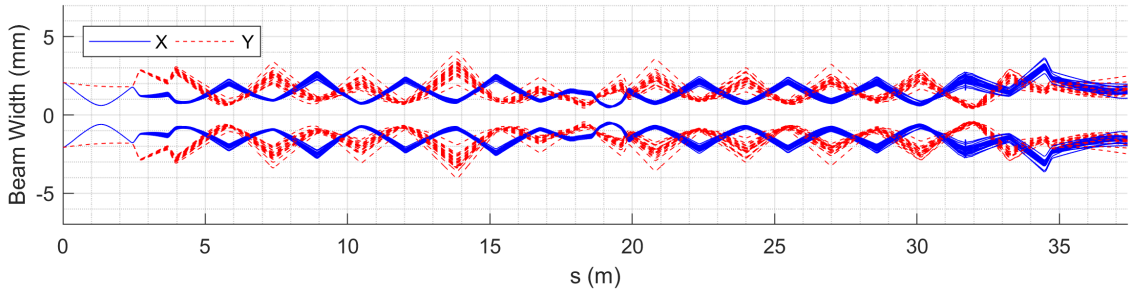

FIGURE 7.21: RMS beam widths along the transport line for field errors of 1.5%

the start of the line, as reflected in the beam widths early on, seen in Fig 7.21. An upper tolerance limit of 0.7% was given for quadrupole field strength fluctuations since beam spot size is affected up to around 10% in this error range. With very stable power sources, it is unlikely that this effect will have a significant impact on beam quality.

Deflector fields were also varied as a percentage of their original field strengths. The dominant effect on the beam was on the closed orbit, and because correctors were held at the same values to simulate shot-to-shot fluctuations this had a strong impact beam position at the handover point. Figure 7.22 shows the results for the horizontal position, since vertically the beam was affected negligibly. Again, a simple line fit is included to give a guide reference for the magnitude of this effect. To keep the beam on target to within 1 mm the field strengths should fluctuate no more than 0.028%, a significantly lower tolerance limit than established for quadrupole field fluctuations. This value serves to highlight the sensitivity issues when dealing with such low energy (100 keV) beams. Figure 7.23 shows two examples of the effect in action, with clear jumps in closed orbit offset after the two static deflectors. Larger orbit bumps after the second static deflector are likely caused by the cumulative impact of preceding errors and higher field strength to accommodate the sharper bending angle.

7.10 Summary and Outlook

A highly detailed and realistic G4Beamline simulation of the transport line from ELENA to ALPHA has been created with the aim of investigating and optimising

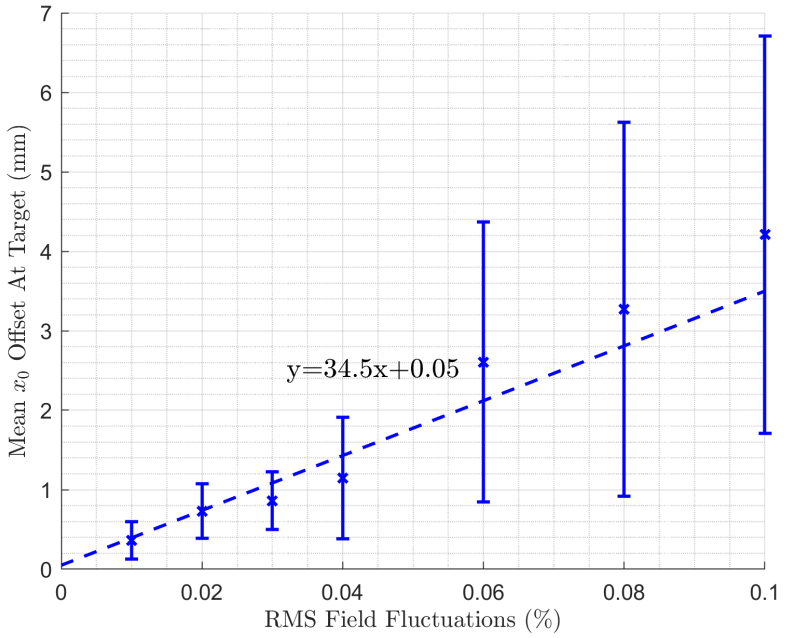

FIGURE 7.22: Mean absolute horizontal position at target as a function of deflector field strength fluctuations.

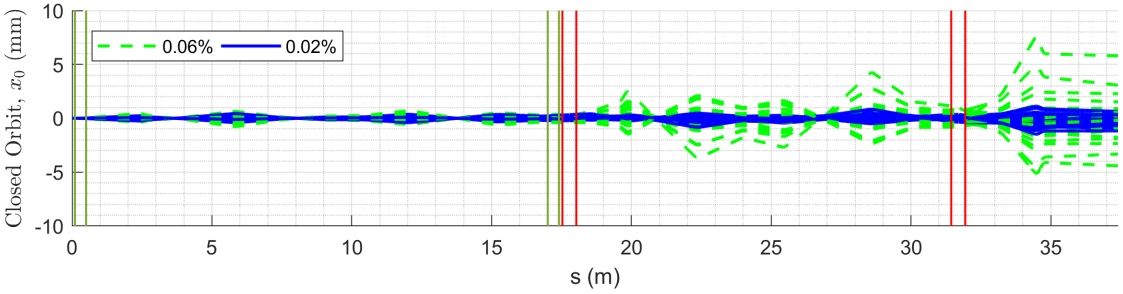

FIGURE 7.23: Horizontal closed orbit offsets as a function of deflector field fluctuations. Fast deflectors are positioned between pairs of green vertical lines and static deflectors between red.

beam quality at the handover point to the experiment. The source code of the program was modified to include electrostatic quadrupoles and realistic fringe fields based on a finite element model were implemented into the simulation with Enge functions. Field maps for the four bending elements were also generated using finite element methods and included in the simulation.

The field strengths of quadrupoles and bending elements were tuned to ensure stable beta functions and closed orbits along the lattice. A GUI was developed to maximise ease of use and productivity for current and future projects. Methods to apply machine learning to further aid in the tuning process were introduced and

it was suggested that these methods should be utilised in the future design and optimisation of beam transport lines.

Beam quality at the end of the beamline was investigated, using both an ideal beam and a beam based on the most recent observations with the scraper and beam profile monitors during commissioning of ELENA in 2018. It was found that an ideal beam with $\epsilon_{x,y} = 1$ mm mrad and no momentum spread would satisfy the spot size target of $\sigma_{x,y} = 2$ mm at the handover point. The more recent beam measurements suggested that after the transport lines the spot size would be larger than this target, although at the end of the commissioning period before LS2 there is still work to do to optimise the electron cooler and further reduce emittance during rebunching and extraction. It is also likely that the machine learning techniques introduced here will be able to further reduce the beta functions at the handover point without sacrificing beam quality along the transport line. An increase in longitudinal momentum offset was observed, likely introduced through the use of electrostatic bending elements. Whilst the change in energy at the eV scale is not relevant to experiments, it could cause issues related to dispersion along the beamline if unchecked and uncorrected for.

Monte Carlo methods were used to investigate error tolerances for this beamline. Upper tolerances of 0.5 mm for position offsets on both the quadrupoles and deflectors were determined individually. It was shown that quadrupole field strength fluctuations should not have any significant effect on beam quality, with a tolerance limit of 0.7%. Fast and static deflector field errors were much more sensitive with a value of 0.028% causing position fluctuations at the handover point of around 1 mm.

With over two years at the time of writing until the first antiproton beams pass through these transport lines, there is ample opportunity to expand this work. For example, the simulation may be enlarged to include additional branches of the transport lines and tailor beam parameters to individual experiments. The effects of stray magnetic fields from experiments could be investigated using these simulations, building upon previous studies [137], at higher resolution, to include the updated position of AEGIS, investigate for different lines and perhaps determine

a range of optimised parameter settings for when various magnets are in use by the experiments.

Further error studies could include an investigation into thermomechanical effects resulting from energy deposits on electrodes by importing the CAD models developed into Ansys [138]. Field maps generated based on these results could be implemented into the simulation. Ongoing work using a novel device to measure the electrostatic field generated by a quadrupole from these beamlines is currently underway. The resultant field distributions and errors could be easily included in these simulations.

Finally, the methods and software developed during this study collectively form a comprehensive simulation toolkit for the optimisation of future beam transport lines. Ongoing work into the applications of machine learning with these tools shows great promise for the future.

Chapter 8

Conclusions

8.1 Summary

Two new scraper algorithms for measuring the emittance of a beam in a region of non-zero dispersion have been developed and presented. One algorithm is capable of estimating the emittance and momentum spread of Gaussian beams through the use of a fitting algorithm. The other, involving two scraper measurements from opposing directions, can reconstruct the emittance for beams of arbitrary transverse beam profiles for scraper blades situated in dispersive regions. These algorithms improve greatly on existing techniques and go beyond the current state of the art for emittance measurements by scraping [90, 139].

The algorithms have been shown to work for a range of conditions and beam effects using a combination of MAD-X and custom Python simulations. An error study showed that the algorithms perform within desired accuracy limits in the presence of a number of errors. Error tolerances have been established for these effects which include errors in beta function and dispersion estimations, and fluctuations in closed orbit between measurements. Additionally, the two scan arbitrary profile algorithm has been shown to accurately reconstruct an emittance-momentum offset correlation coefficient with the simulations. This quantity may be used to investigate effects introduced by the electron cooler, brought about for example by a non-uniform electron velocity distribution.

The two scan arbitrary profile algorithm was applied to scraper measurements made during the intermediate and extraction energy plateaus of ELENA's deceleration cycle. The practical considerations and methods necessary when using the algorithm have been presented. Estimates for horizontal emittances were made in combination with longitudinal momentum spread measurements using Schottky data taken along the intermediate plateau. The vertical and horizontal emittances were shown to decrease by 28 (±2) % and 81 (±10) % respectively, over 6.7 s seconds of electron cooling along the intermediate plateau. At the extraction plateau measurements were made without cooling and then at the same time along the plateau after 3.9 seconds of cooling. Reductions of 79 (±2) % and 78 (±10) % were observed for the vertical and horizontal emittances respectively, in the presence of electron cooling. Comparisons with Gaussian distributions based on the measured results suggested that indeed the beams had taken on non-Gaussian profiles during cooling, although further measurements are required to ascertain the magnitude of this effect.

The emittance-momentum offset correlation was calculated for the horizontal plane and showed an increase from negative values after deceleration towards positive values during electron cooling. The method was benchmarked by similarly calculating the quantities for the vertical plane where, because there is zero vertical dispersion, no significant change was observed after cooling, as expected. The results confirm that indeed the two scan algorithm is an appropriate choice when measuring the beam quality in ELENA and other storage rings with non-zero dispersion and non-Gaussian beam profiles.

Beam profile measurements at the end of the extraction plateau were used in combination with profile measurements taken along the transport line to GBAR to create a beam distribution approximating that after extraction from ELENA. The distribution was tracked along a realistic 3D simulation of the 37.4 m long beam transfer line from ELENA to the ALPHA experiment.

The simulation includes a G4Beamline source code modification to implement electrostatic quadrupoles with realistic fringe fields. Four electrostatic bending elements are implemented as field maps generated in CST from geometrically

realistic electrodes. The closed orbit was tuned and stabilised through the use of tuning macros and correctors. Quadrupole adjustments were made to achieve stable beta functions along the transport line and machine learning methods have been implemented for optimisation of beam quality at the handover point. Further development of such techniques is ongoing.

Beam profiles based on an ideal beam and on the current beam quality at the end of commissioning in 2018 were obtained at the end of the transfer line. For the current beam quality upon extraction a slightly larger beam size than the target value of $\sigma_{x,y} = 2$ mm would be received by ALPHA with this configuration of the beamlines. For an ideal beam of $\epsilon_{x,y} = 1$ mm mrad the current configuration of the transport lines would satisfy the target beam size.

A range of systematic errors were investigated using Monte Carlo methods. Error tolerances on the fields strengths and positions of all elements were obtained, considering quadrupoles and bending elements separately. It was found that the deflectors were much more sensitive to field fluctuations in terms of beam quality at the handover point, with the final static deflector having the largest impact.

8.2 Outlook

Suggestions for further measurements and studies using the two scan scraper algorithm in ELENA have been proposed. These include taking pairs of scraper measurements in incremental time steps along each energy plateau to build up a more continuous picture of the emittance evolution in the presence of electron cooling. Similar measurements in the absence of cooling would allow an investigation into the significance and phase space growth rates introduced by intra-beam scattering. Additionally, the evolution of the emittance-momentum offset correlation coefficient could be measured for a range of electron cooler settings, particularly with changes to the density and radius of the electron beam.

Since the two new scraper algorithms have been shown to work through the use of simulations and used practically with scraper data taken from ELENA, it is proposed that they are suitable for use in other storage rings. Any machine with a scraper and non-zero dispersion around the lattice or at the position of the scraper

blades could well benefit from these algorithms. Although destructive to the beam, the ability of the two scan algorithm to reconstruct emittance for arbitrary beam distributions under these conditions is a significant improvement over the standard scraping techniques used currently. Other less invasive techniques are currently being investigated, for instance, supersonic gas jet monitors [140].

The methods developed during the creation of the electrostatic transport lines simulation form a comprehensive simulation toolkit which would be beneficial to the design and optimisation of future electrostatic facilities. The simulations may be extended to include transport lines to the other experiments in the AD hall and investigate further sources of error, such as the influence of stray magnetic fields on beam stability. Ongoing work to improve optimisation results using machine learning is expected to benefit beam quality at the handover points to all experiments. Measurements of the quadrupole field distribution currently being made using a novel electrostatic sensor [127] may be implemented into simulations, further building upon realism and accuracy of results. Finally, the simulations could be modified to extend beyond the interface with experiments, for example to include the degrader foils at ALPHA and its antiproton trap. Such an extension would allow a more comprehensive optimisation process and could further improve antiproton trapping efficiencies.

List of Figures

List of Tables

Appendices

Appendix A

Figures

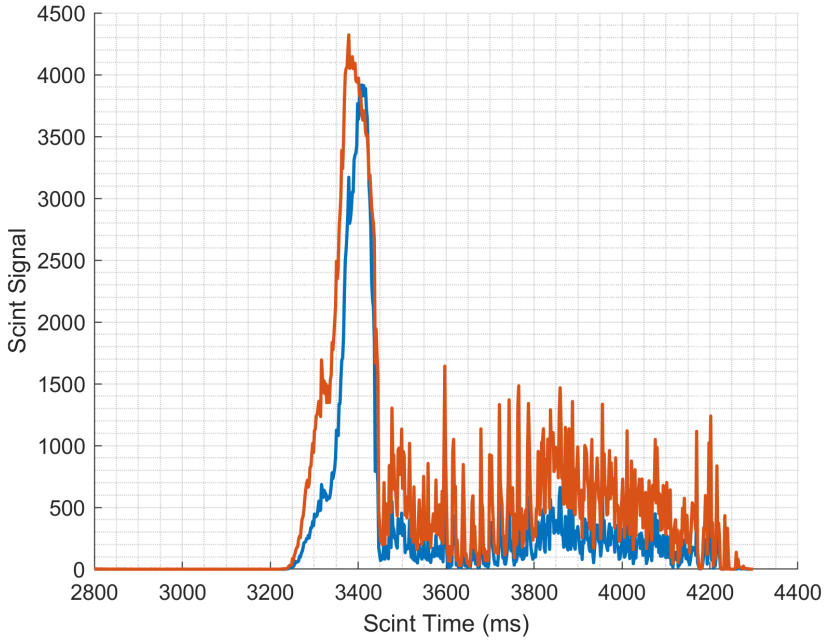

FIGURE A.1: Scintillator data gathered when the scraper stopped prematurely. The remaining circulating beam can be seen as loss signal over the remaining time of acquisition.

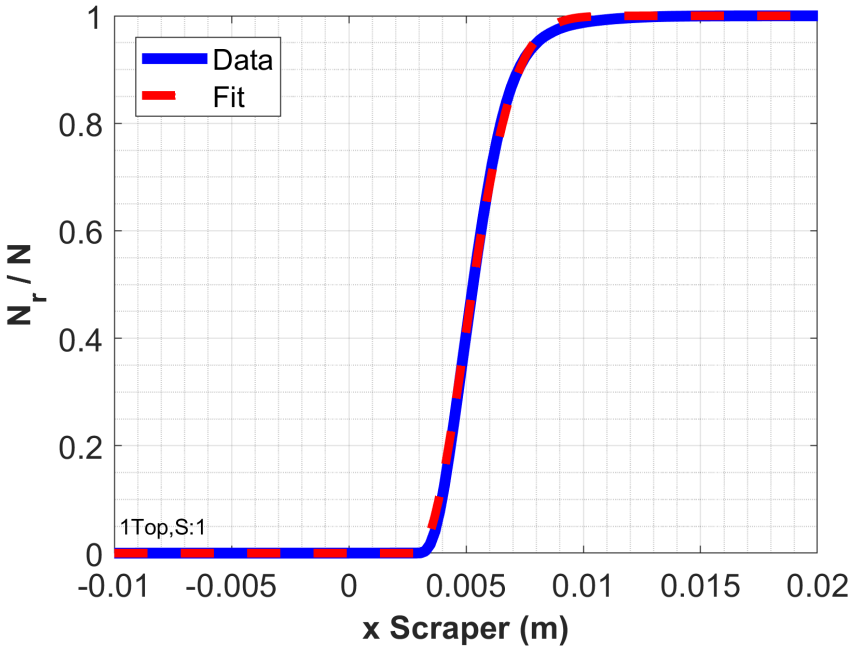

FIGURE A.2: Gaussian fit to data for the "Top" direction at t =7.8 s.

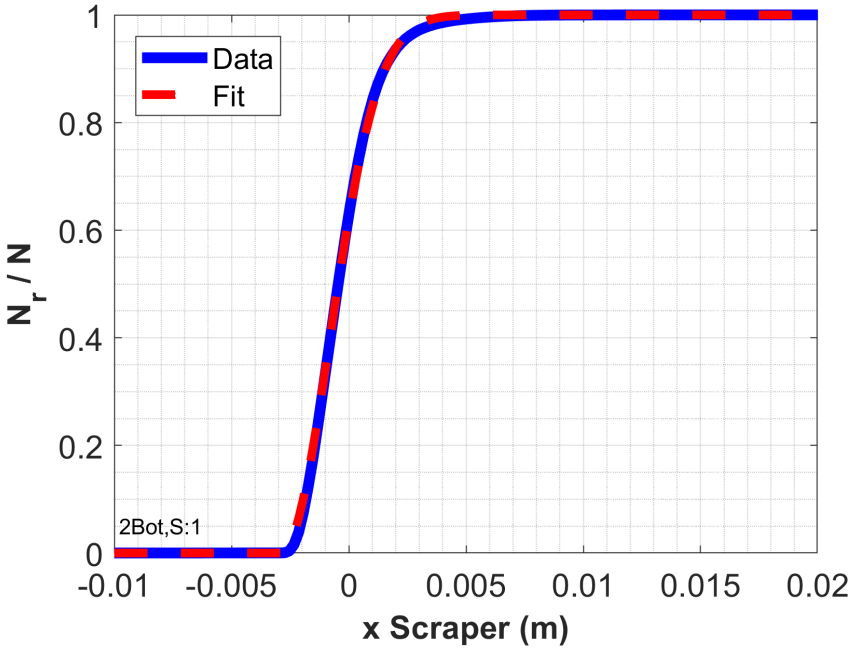

FIGURE A.3: Gaussian fit to data for the "Bot" direction at t =7.8 s.

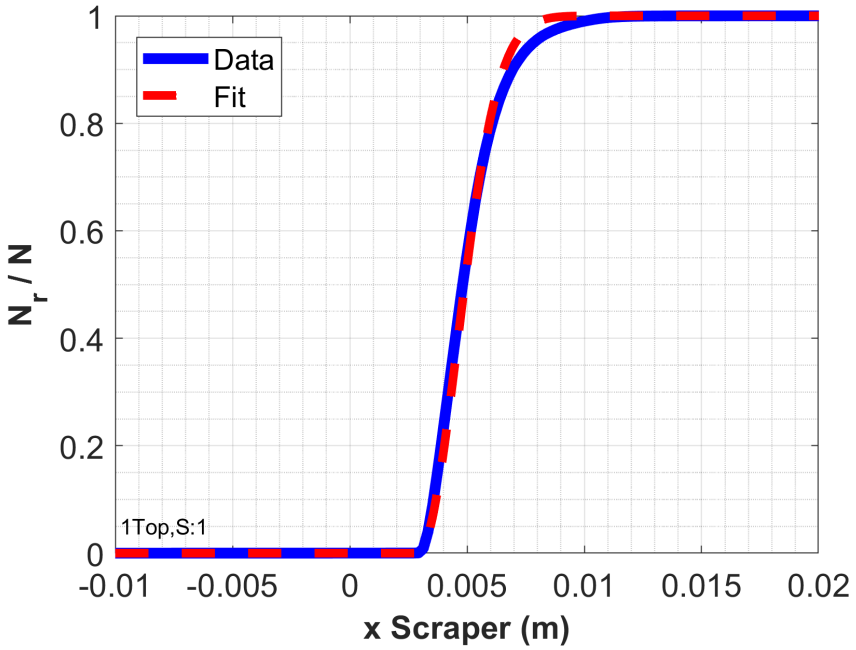

FIGURE A.4: Gaussian fit to data for the "Top" direction at t =14.5 s.

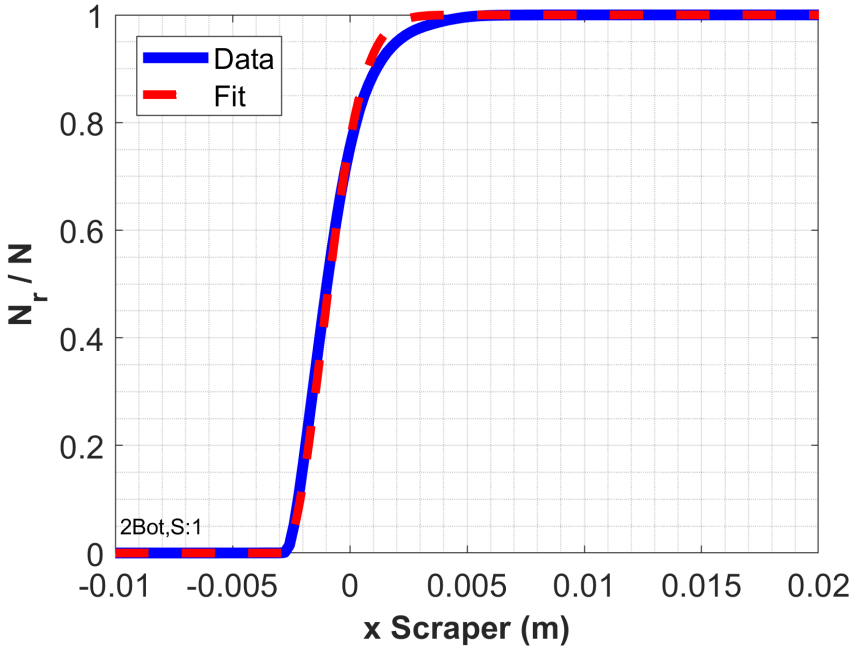

FIGURE A.5: Gaussian fit to data for the "Bot" direction at t =14.5 s.

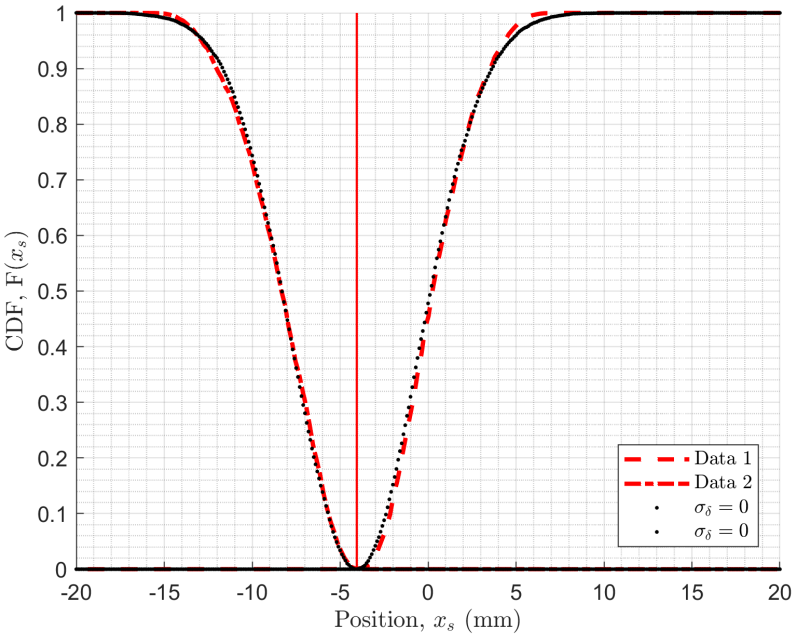

FIGURE A.6: Horizontal scraper measurements at $t = 7.8$ s compared with a simulation based on the results of the two scan algorithm with input σ_δ =0×10^{-3} resulting in $\epsilon_x = 4$ mm mrad.

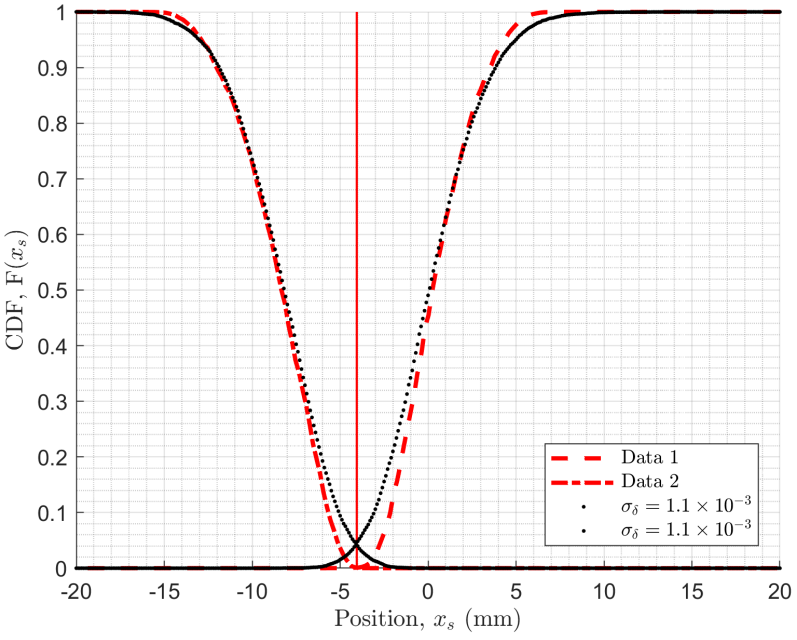

FIGURE A.7: Horizontal scraper measurements at $t = 7.8$ s compared with a simulation based on the results of the two scan algorithm with input from Schottky of σ_δ =1.1×10^{-3} resulting in $\epsilon_x = 3.6 \times 10^{-3}$ mm mrad.

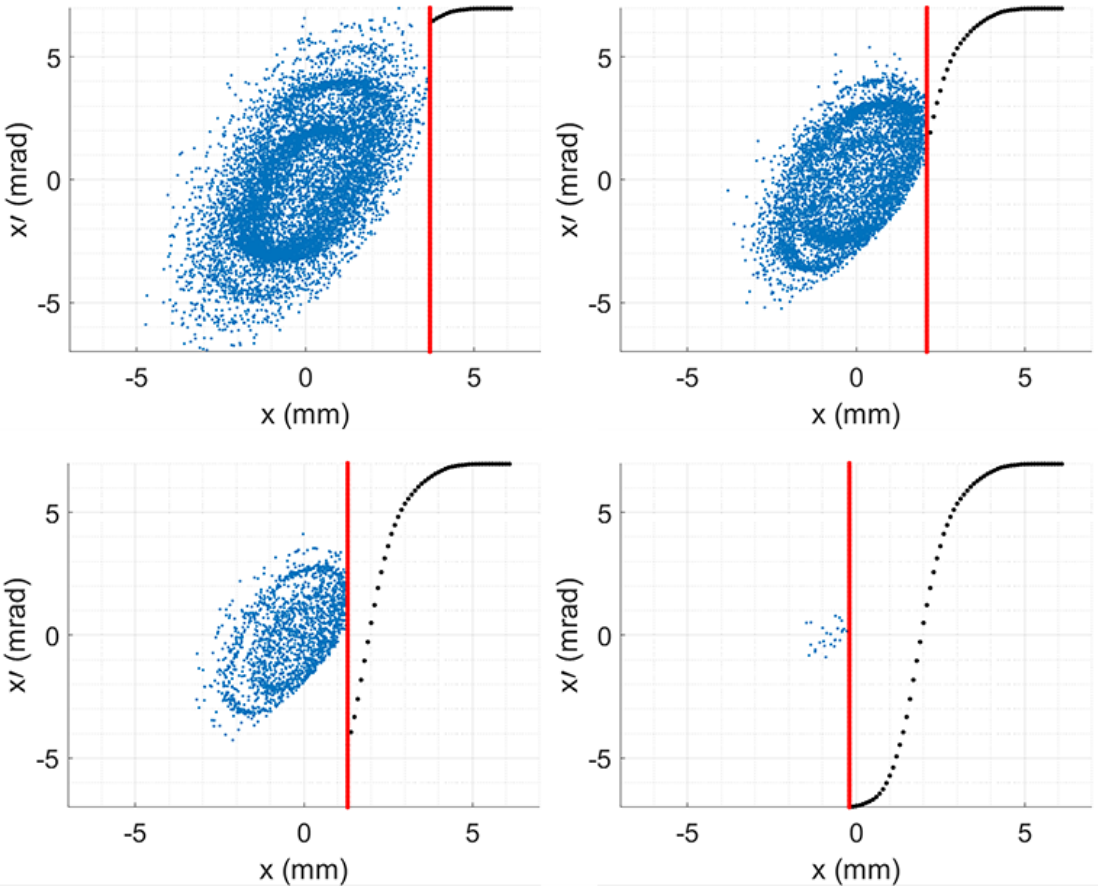

FIGURE A.8: Horizontal phase space plots for a simulation of scraping an optically mismatched beam. The scraper is represented by a vertical red line and the measured beam intensity as a function of scraper position is represented by a curve of black dots.

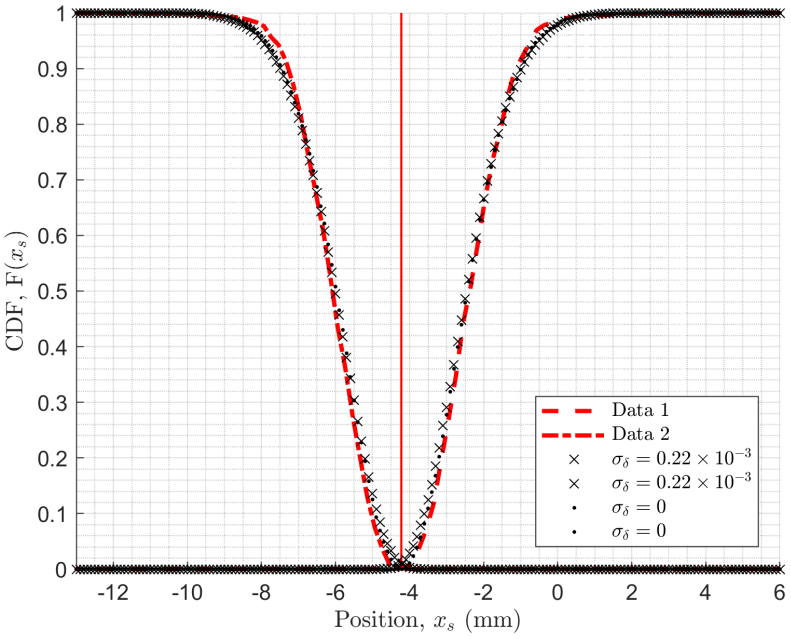

FIGURE A.9: CDFs for horizontal scraper measurements along the intermediate cooling plateau. The right plot displays a zoom on the core region of the same data.

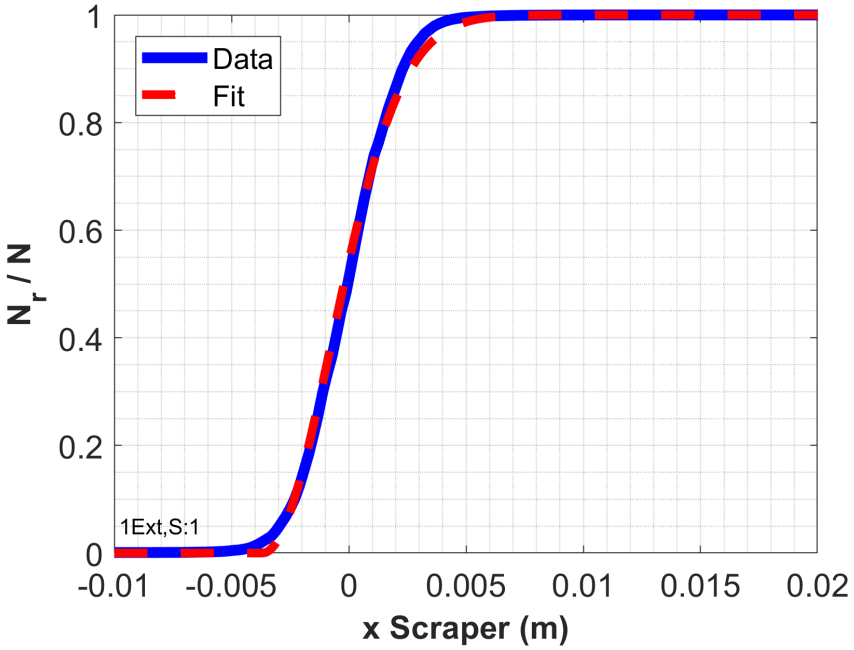

FIGURE A.10: Gaussian fit to a horizontal scrape during the ejection plateau with no electron cooling. Results showed an unacceptable uncertainty range for the σ_δ estimate.

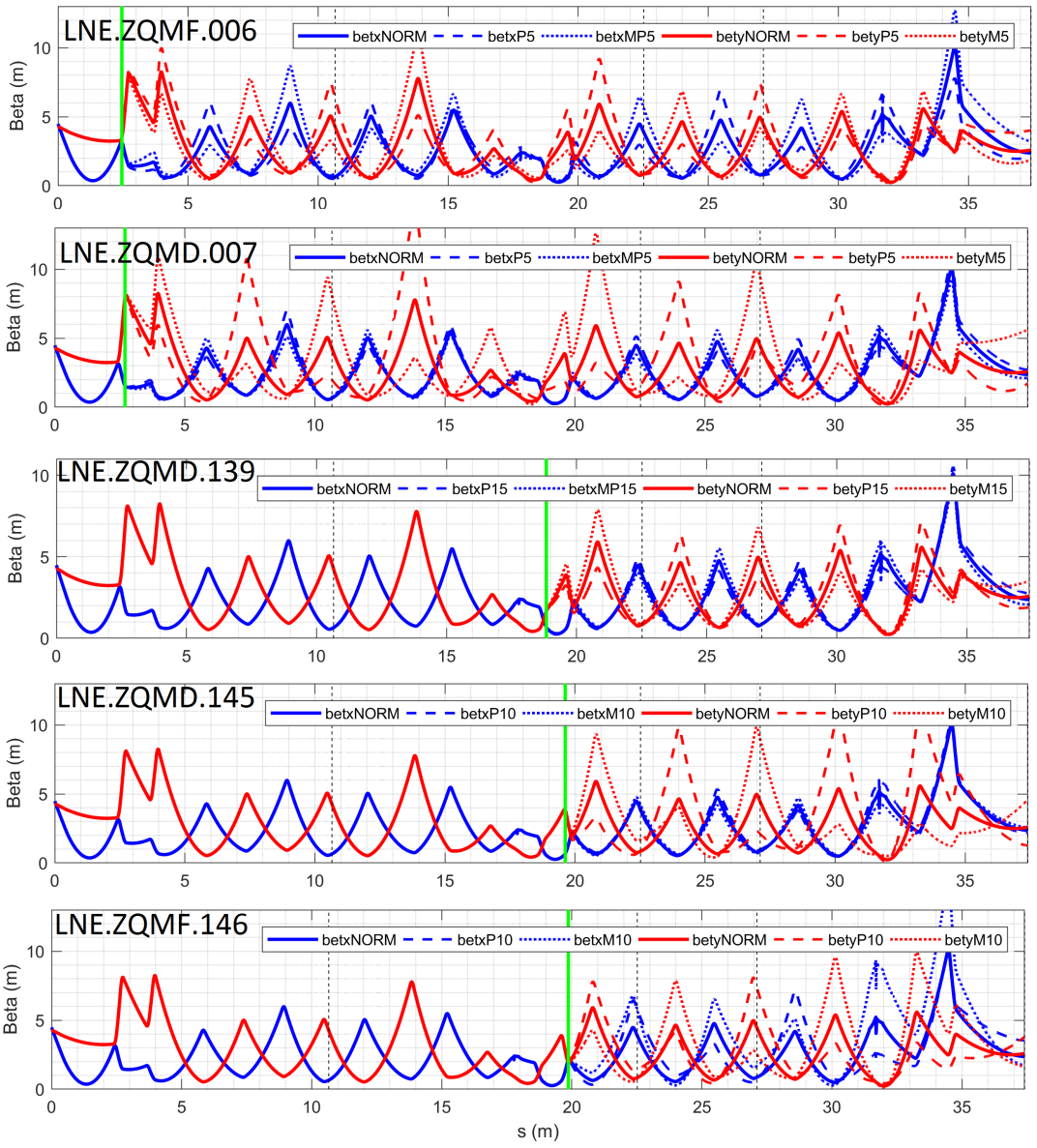

FIGURE A.11: Effect of five different quadrupoles on the beta functions along the transport lines to ALPHA. In the legend MX and PX refer to negative and positive changes in quadrupole strength by X percent.

Bibliography

[1] P. A. M. Dirac, "The Quantum Theory of the Electron. Part II," *Proceedings of the Royal Society A: Mathematical, Physical and Engineering Sciences*, vol. 118, no. 779, pp. 351–361, Feb. 1928.

[2] C. D. Anderson, "The Positive Electron," *Physical Review*, vol. 43, no. 6, pp. 491–494, Mar. 1933.

[3] O. Chamberlain *et al.*, "Observation of Antiprotons," *Physical Review*, vol. 100, no. 3, pp. 947–950, Nov. 1955.

[4] B. Cork *et al.*, "Antineutrons Produced from Antiprotons in Charge-Exchange Collisions," *Physical Review*, vol. 104, no. 4, pp. 1193–1197, Nov. 1956.

[5] T. Massam *et al.*, "Experimental observation of antideuteron production," *Il Nuovo Cimento A*, vol. 63, no. 1, pp. 10–14, Sep. 1965.

[6] D. E. Dorfan *et al.*, "Observation of Antideuterons," *Physical Review Letters*, vol. 14, no. 24, pp. 1003–1006, Jun. 1965.

[7] B. de Raad, "The CERN SPS Proton-Antiproton Collider," *IEEE Transactions on Nuclear Science*, vol. 32, no. 5, pp. 1650–1652, 1985.

[8] S. van der Meer, "Stochastic Cooling in the CERN Antiproton Accumulator," *IEEE Transactions on Nuclear Science*, vol. 28, no. 3, pp. 1994–1998, 1981.

[9] C. Rubbia, "The Discovery of the W and Z bosons," *Phys.Rept.*, vol. 239, pp. 241–284, 1994.

[10] R. Klapisch, "The LEAR Project and Physics with Low Energy Antiprotons at CERN (A Summary)," *Physica Scripta*, vol. T5, pp. 140–142, Jan. 1983.

[11] C. Habfast *et al.*, "The LEAR Electron Cooler: Recent Improvements and Tests," *Physica Scripta*, vol. T22, pp. 277–281, Jan. 1988.

[12] H. Poth *et al.*, "First results of electron cooling experiments at LEAR," *Zeitschrift fur Physik A Atomic Nuclei*, vol. 332, no. 2, pp. 171–188, Jun. 1989.

[13] B. Autin *et al.*, "The CERN Antiproton Collector Ring," *1st European Particle Accelerator Conference (EPAC 88)*, vol. C880607, pp. 308–310, 1988.

[14] E. Aker *et al.*, "The crystal barrel spectrometer at LEAR," *Nuclear Instruments and Methods in Physics Research Section A: Accelerators, Spectrometers, Detectors and Associated Equipment*, vol. 321, no. 1-2, pp. 69–108, Sep. 1992.

[15] A. Adamo *et al.*, "First results from OBELIX," in *AIP Conference Proceedings*, vol. 243. AIP, 1992, pp. 371–376.

[16] G. Baur *et al.*, "Production of antihydrogen," *Physics Letters B*, vol. 368, no. 3, pp. 251–258, Feb. 1996.

[17] G. Blanford *et al.*, "Observation of Atomic Antihydrogen," *Physical Review Letters*, vol. 80, no. 14, pp. 3037–3040, Apr. 1998.

[18] P. Belochitskii *et al.*, "LEIR Commissioning," in *Proceedings of EPAC 2006*, 2006.

[19] S. Maury, "The Antiproton Decelerator: AD," *Hyperfine Interactions*, vol. 109, no. 1/4, pp. 43–52, 1997.

[20] P. Belochitskii *et al.*, "Commissioning and first operation of the Antiproton Decelerator (AD)," in *Proceedings of the 2001 Particle Accelerator Conference (PACS2001)*, vol. 1. IEEE, 2001, pp. 580–584.

[21] K. S. Fine *et al.*, "The ATHENA antihydrogen experiment," in *AIP Conference Proceedings*, vol. 498, no. 1. American Institute of Physics, Mar. 1999, pp. 40–47.

[22] M. Amoretti *et al.*, "Production and detection of cold antihydrogen atoms," *Nature*, vol. 419, no. 6906, pp. 456–459, Oct. 2002.

[23] G. B. Andresen *et al.*, "Compression of Antiproton Clouds for Antihydrogen Trapping," *Physical Review Letters*, vol. 100, no. 20, p. 203401, May 2008.

[24] M. Charlton *et al.*, "Antihydrogen for precision tests in physics," *Contemporary Physics*, vol. 49, no. 1, pp. 29–41, Jan. 2008.

[25] N. Madsen, "Cold antihydrogen: a new frontier in fundamental physics," *Philosophical Transactions of the Royal Society A: Mathematical, Physical and Engineering Sciences*, vol. 368, no. 1924, pp. 3671–3682, Aug. 2010.

[26] G. Gabrielse *et al.*, "Driven Production of Cold Antihydrogen and the First Measured Distribution of Antihydrogen States," *Physical Review Letters*, vol. 89, no. 23, p. 233401, Nov. 2002.

[27] M. Hori *et al.*, "Buffer-gas cooling of antiprotonic helium to 1.5 to 1.7 K, and antiproton-to-electron mass ratio." *Science (New York, N.Y.)*, vol. 354, no. 6312, pp. 610–614, Nov. 2016.

[28] C. Malbrunot *et al.*, "The ASACUSA antihydrogen and hydrogen program: results and prospects," *Philosophical Transactions of the Royal Society A: Mathematical, Physical and Engineering Sciences*, vol. 376, no. 2116, p. 20170273, Mar. 2018.

[29] N. Kuroda *et al.*, "A source of antihydrogen for in-flight hyperfine spectroscopy," *Nature Communications*, vol. 5, no. 1, p. 3089, Dec. 2014.

[30] Y. Bylinsky, W. Pirkl, and A. Lombardi, "RFQD: A 'Decelerating' radio frequency quadrupole for the CERN anti-proton facility," in *Linac. Proceedings, 20th International Conference, Linac 2000*, vol. 1,2, Monterey, USA, 2000, pp. 554–556.

[31] G. B. Andresen *et al.*, "Trapped antihydrogen," *Nature*, vol. 468, no. 7324, pp. 673–676, Dec. 2010.

[32] G. B. Andresen *et al.*, "Confinement of antihydrogen for 1,000 seconds," *Nature Physics*, vol. 7, no. 7, pp. 558–564, Jul. 2011.

[33] G. Gabrielse *et al.*, "Trapped Antihydrogen in Its Ground State," *Physical Review Letters*, vol. 108, no. 11, p. 113002, Mar. 2012.

[34] M. Ahmadi *et al.*, "Observation of the 1S2S transition in trapped antihydrogen," *Nature*, vol. 541, no. 7638, pp. 506–510, Jan. 2017.

[35] M. Ahmadi *et al.*, "Observation of the 1S2P Lyman-α transition in antihydrogen," *Nature*, vol. 561, no. 7722, pp. 211–215, Sep. 2018.

[36] M. Ahmadi *et al.*, "Observation of the hyperfine spectrum of antihydrogen," *Nature*, vol. 548, no. 7665, pp. 66–69, Aug. 2017.

[37] P. Scampoli and J. Storey, "The AEgIS experiment at CERN for the measurement of antihydrogen gravity acceleration," *Modern Physics Letters A*, vol. 29, no. 17, p. 1430017, Jun. 2014.

[38] C. Smorra *et al.*, "A parts-per-billion measurement of the antiproton magnetic moment," *Nature*, vol. 550, no. 7676, pp. 371–374, Oct. 2017.

[39] P. Pérez *et al.*, "The GBAR antimatter gravity experiment," *Hyperfine Interactions*, vol. 233, no. 1-3, pp. 21–27, Aug. 2015.

[40] M. Holzscheiter *et al.*, "Relative Biological Effectiveness of Antiprotons the AD-4/ACE Experiment," in *Proceedings of the 12th International Conference on Low Energy Antiproton Physics (LEAP2016)*, vol. 18. Journal of the Physical Society of Japan, Nov. 2017, p. 011039.

[41] S. Sellner *et al.*, "The antiproton cell experimentdo antiprotons offer advantages over other particle beam modalities?" *Hyperfine Interactions*, vol. 213, no. 1-3, pp. 159–174, Dec. 2012.

[42] V. Chohan *et al.*, "Extra Low ENergy Antiproton (ELENA) ring and its Transfer Lines: Design Report," Tech. Report, CERN-2014-002, Apr. 2014.

[43] S. Maury *et al.*, "ELENA: the extra low energy anti-proton facility at CERN," *Hyperfine Interactions*, vol. 229, no. 1-3, pp. 105–115, Oct. 2014.

[44] T. Eriksson *et al.*, "ELENA-From Installation to Commissioning," in *Proceedings of IPAC2017*, Copenhagen, Denmark, 2017.

[45] W. Bartmann *et al.*, "The ELENA facility," *Philosophical Transactions of the Royal Society A: Mathematical, Physical and Engineering Sciences*, vol. 376, no. 2116, p. 20170266, Mar. 2018.

[46] T. Shirai *et al.*, "S-LSR, Cooler Ring Development at Kyoto University," in *AIP Conference Proceedings*, vol. 821, no. 1. AIP, 2006, pp. 103–107.

[47] G. Tranquille *et al.*, "The ELENA Electron Cooler," in *7th International Particle Accelerator Conference (IPAC 2016)*, 2016, p. TUPMR006.

[48] T. Eriksson *et al.*, "The ELENA Project: Progress in the Design," in *Proceedings of IPAC2012*, New Orleans, Louisiana, USA, 2012.

[49] O. Marqversen *et al.*, "The Orbit Measurement System for the CERN Extra Low Energy Antiproton Ring," in *6th International Beam Instrumentation Conference (IBIC2017)*, Grand Rapids, MI, USA, 2018.

[50] J. Bosser *et al.*, "New Beam Profile Monitor Based on GEM Detector for the AD Transfer and Experimental Lines," Tech. Report, CERN-AB-2004-089, 2004.

[51] M. Hori, "Parallel plate chambers for monitoring the profiles of high-intensity pulsed antiproton beams," *Nuclear Instruments and Methods in Physics Research Section A: Accelerators, Spectrometers, Detectors and Associated Equipment*, vol. 522, no. 3, pp. 420–431, Apr. 2004.

[52] M. Hori, "Photocathode microwire monitor for nondestructive and highly sensitive spatial profile measurements of ultraviolet, x-ray, and charged particle beams," *Review of Scientific Instruments*, vol. 76, no. 11, p. 113303, Nov. 2005.

[53] J. R. Hunt *et al.*, "Emittance measurements in low energy ion storage rings," *Nuclear Instruments and Methods in Physics Research Section A: Accelerators, Spectrometers, Detectors and Associated Equipment*, vol. 896, pp. 139–151, Jul. 2018.

[54] FLAIR, "Facility for Low-Energy Antiproton and Ion Research."

[55] C. P. Welsch and H. Danared, "FLAIR: a Facility for Low-energy Antiproton and Ion Research," in *Proceedings of EPAC 2006*, Edinburgh, Scotland, 2006.

[56] E. Widmann, "Low-energy antiproton physics and the FLAIR facility," in *9th International Conference on Nuclear Physics at Storage Rings, Sankt Goar, Germany*, Feb. 2015.

[57] R. Appleby, "Introduction to Beam Dynamics," Lecture Series, Daresbury, UK, 2017.

[58] H. Wiedemann, *Particle Accelerator Physics*, ser. Graduate Texts in Physics. Springer International Publishing, 2015.

[59] F. Zimmermann, "Measurement and Correction of Accelerator Optics," Tech. Report, SLAC-PUB-7844, 1998.

[60] J. Resta-López, J. R. Hunt, and C. P. Welsch, "Non-Gaussian beam dynamics in low energy antiproton storage rings," *Nuclear Instruments and Methods in Physics Research Section A: Accelerators, Spectrometers, Detectors and Associated Equipment*, vol. 834, pp. 123–131, Oct. 2016.

[61] J. Resta-López *et al.*, "Simulation studies of the beam cooling process in presence of heating effects in the Extra Low ENergy Antiproton ring (ELENA)," *Journal of Instrumentation*, vol. 10, no. 05, p. P05012, May 2015.

[62] A. Piwinski, "Intra-Beam Scattering," in *Proceedings of the 9th International Conference on High Energy Accelerators*, Stanford, CA, 1974, p. 405.

[63] A. Piwinski, "Intra-Beam Scattering," CERN Report 92-01, p. 226, 1992.

[64] M. Martini, "Intrabeam Scattering in the ACOL-AA Machines," Tech. Report ,CERN-PS-AA-84-9, 1984.

[65] J. Bjorken and S. Mtingwa, "Intrabeam scattering," *Particle Accelerators*, vol. 13, pp. 115–143, 1983.

[66] A. Sidorin *et al.*, "BETACOOL program for simulation of beam dynamics in storage rings," *Nuclear Instruments and Methods in Physics Research Section A: Accelerators, Spectrometers, Detectors and Associated Equipment*, vol. 558, no. 1, pp. 325–328, Mar. 2006.

[67] S. van der Meer, "Stochastic damping of betatron oscillations in the ISR," Tech. Report, CERN-ISR-PO-72-31, 1972.

[68] S. van der Meer, "Stochastic cooling and the accumulation of antiprotons," *Reviews of Modern Physics*, vol. 57, no. 3, pp. 689–697, Jul. 1985.

[69] D. Möhl *et al.*, "Physics and technique of stochastic cooling," *Physics Reports*, vol. 58, no. 2, pp. 73–102, Feb. 1980.

[70] G. I. Budker, "An effective method of damping particle oscillations in proton and antiproton storage rings," *Soviet Atomic Energy*, vol. 22, no. 5, pp. 438–440, May 1967.

[71] B. Veglia, "Photograph courtesy of Bianca Veglia," 2018.

[72] P. W. Allison, J. D. Sherman, and D. B. Holtkamp, "An emittance scanner for intense low-energy ion beams," *IEEE Transactions on Nuclear Science*, vol. 30, no. 4, pp. 2204 – 2206, 1983.

[73] U. Raich, "The Pepperpot Measurement Bench," CERN-BE-Note-2010-003, CERN, Geneva, 2010.

[74] F. Wenander *et al.*, "REXEBIS the Electron Beam Ion Source for the REX-ISOLDE Project," Tech Report. CERN-OPEN-2000-320, 1998.

[75] T. Nagatomo *et al.*, "Development of a pepper-pot emittance meter for diagnostics of low-energy multiply charged heavy ion beams extracted from an ECR ion source," *Review of Scientific Instruments*, vol. 87, no. 2, p. 02B920, Feb. 2016.

[76] H. Kashiwagi *et al.*, "A transverse emittance and acceptance measurement system in a low-energy beam transport line," *Review of Scientific Instruments*, vol. 85, no. 2, p. 02A735, Feb. 2014.

[77] A. Sosa *et al.*, "Beam instrumentation for the HIE Isolde linac at CERN," in *3rd International Particle Accelerator Conference*, New Orleans, LA, USA, May 2012, p. MOPPR048.

[78] C. Steinbach and M. van Rooij, "A Scanning Wire Beam Profile Monitor," *IEEE Transactions on Nuclear Science*, vol. 32, no. 5, pp. 1920–1922, 1985.

[79] V. Agoritsas *et al.*, "The fast wire scanner of the CERN PS," Tech. Report CERN-PS-95-06-BD-OP, 1995.

[80] P. Elmfors *et al.*, "Wire scanners in low energy accelerators," *Nuclear Instruments and Methods in Physics Research Section A: Accelerators, Spectrometers, Detectors and Associated Equipment*, vol. A396, pp. 13–22, Mar. 1997.

[81] T. Shintake, "Proposal of a nanometer beam size monitor for e+e linear colliders," *Nuclear Instruments and Methods in Physics Research Section A: Accelerators, Spectrometers, Detectors and Associated Equipment*, vol. 311, no. 3, pp. 453–464, Jan. 1992.

[82] T. Hofmann *et al.*, "Demonstration of a laserwire emittance scanner for hydrogen ion beams at CERN," *Physical Review Special Topics - Accelerators and Beams*, vol. 18, no. 12, p. 122801, Aug. 2015.

[83] C. Thomas, N. Delerue, and R. Bartolini, "Single shot transverse emittance measurement from OTR screens in a drift transport section," *Journal of Instrumentation*, vol. 6, no. 07, p. P07004, Jul. 2011.

[84] P. Bambade, "Betatron Phase Space Diagnostics In A Fodo Array," Tech. Report, SLAC-CN-367, 1988.

[85] K. Brown, "A First- and Second-Order Matrix Theory for the Design of Beam Transport Systems and Charged Particle Spectrometers," Tech. Report, SLAC-R-075, 1982.

[86] M. Ross *et al.*, "Automated emittance measurements in the SLC," in *PAC'87*, Washington, DC (USA), 1987, pp. 725–728.

[87] L. Wartski *et al.*, "Interference phenomenon in optical transition radiation and its application to particle beam diagnostics and multiplescattering measurements," *Journal of Applied Physics*, vol. 46, no. 8, pp. 3644–3653, Aug. 1975.

[88] M. A. Holloway *et al.*, "Multicomponent measurements of the Jefferson Lab energy recovery linac electron beam using optical transition and diffraction radiation," *Physical Review Special Topics - Accelerators and Beams*, vol. 11, no. 082801, 2008.

[89] R. Kieffer *et al.*, "Experimental Observation of Shadowing in Optical Transition Radiation," *Physical Review Letters*, vol. 120, no. 9, p. 094802, Feb. 2018.

[90] H. Schonauer, "Beamscope - A Novel Device for Measuring Emittances and Betatron Amplitude Distributions," *IEEE Transactions on Nuclear Science*, vol. 26, no. 3, pp. 3294–3296, 1979.

[91] S. J. Werkema, "Transverse Beam Profile Measurement Using Scrape Scans," Tech. Report, FERMILAB-PBAR-NOTE-665, Batavia, IL (United States), Sep. 2001.

[92] V. Lebedev and V. Shiltsev, Eds., *Accelerator Physics at the Tevatron Collider*, ser. Particle Acceleration and Detection. New York, NY: Springer New York, 2014.

[93] H. Burkhardt, I. Reichel, and G. Roy, "Transverse beam tails due to inelastic scattering," *Physical Review Special Topics - Accelerators and Beams*, vol. 3, no. 9, p. 091001, Sep. 2000.

[94] G. Valentino *et al.*, "Beam diffusion measurements using collimator scans in the LHC," *Physical Review Special Topics - Accelerators and Beams*, vol. 16, no. 2, p. 021003, Feb. 2013.

[95] S. A. Baird *et al.*, "Design study of the Antiproton Decelerator: AD," Tech. Report, CERN-PS-96-043-AR, 1996.

[96] M. E. Angoletta *et al.*, "Beam Measurement Systems for the CERN Antiproton Decelerator (AD)," in *19th IEEE Particle Accelerator Conference*, Chicago, IL, USA, Jul. 2001.

[97] A. Bertarelli *et al.*, "Analysis and Design of the Actuation System for the LHC Collimators (Phase I)," Tech. Report, CERN-EN-Note-2009-001, Aug. 2009.

[98] P. Forck, "Lecture Notes on Beam Instrumentation and Diagnostics," Joint University Accelerator School, GSI, Darmstadt, Germany, 2017.

[99] L. Søby *et al.*, "ELENA Orbit and Schottky Measurement Systems," in *6th International Particle Accelerator Conference*, Richmond, VA, USA, 2015, p. MOPTY056.

[100] S. D. Pinto *et al.*, "GEM-based beam profile monitors for the antiproton decelerator," *Journal of Instrumentation*, vol. 7, no. 03, p. C03001, Mar. 2012.

[101] J. Spanggaard *et al.*, "GEM detectors for the transverse profile measurement of low energy antiprotons and high energy hadrons," in *4th International Particle Accelerator Conference*, Shanghai, China, 2013, p. MOPWA036.

[102] T. Böhlen *et al.*, "The FLUKA Code: Developments and Challenges for High Energy and Medical Applications," *Nuclear Data Sheets*, vol. 120, pp. 211–214, Jun. 2014.

[103] A. Ferrari *et al.*, "FLUKA: A multi-particle transport code," Tech. Report, CERN-2005-010, SLAC-R-773, INFN-TC-05-11, 2005.

[104] L. Deniau *et al.*, "The MAD-X Program (Methodical Accelerator Design) User's Reference Manual," 2018.

[105] E. Forest, F. Schmidt, and E. McIntosh, "Introduction to the polymorphic tracking code," Tech. Report, CERN-SL-2002-044-AP; KEK-REPORT-2002-3, 2002.

[106] Python, "The Python Standard Library - Numeric and Mathematical Modules," https://docs.python.org/3/library/random.html.

[107] CERN, "MAD-X Pitfalls," http://mad.web.cern.ch/mad/madx.old/Introduction/pitfalls.html.

[108] MathWorks˜Inc., "spline," https://uk.mathworks.com/help/matlab/ref/spline.html.

[109] B. Dupuy, "ELENA Scraper GUI," private communication.

[110] JSON, "Introducing JSON," https://www.json.org/.

[111] J. Resta-López, J. R. Hunt, and C. P. Welsch, "Intra-Beam Scattering Effects in ELENA," in *6th International Particle Accelerator Conference, IPAC2015*, Richmond, VA, USA, 2015.

[112] J. Bosser *et al.*, "On the optimum dispersion of a storage ring for electron cooling with high space charge," *Nuclear Instruments and Methods in Physics Research Section A: Accelerators, Spectrometers, Detectors and Associated Equipment*, vol. 441, no. 1-2, pp. 60–63, Feb. 2000.

[113] J. Bosser *et al.*, "Optimum lattice functions for electron cooling," *Nuclear Instruments and Methods in Physics Research Section A: Accelerators, Spectrometers, Detectors and Associated Equipment*, vol. 532, no. 1-2, pp. 422–426, Oct. 2004.

[114] S. P. Møller, "ELISA, and electrostatic storage ring for atomic physics," *Nuclear Instruments and Methods in Physics Research Section A: Accelerators, Spectrometers, Detectors and Associated Equipment*, vol. 394, no. 3, pp. 281–286, Jul. 1997.

[115] M. O. El Ghazaly, "ELASR An electrostatic storage ring for atomic and molecular physics at KACST," *Results in Physics*, vol. 5, pp. 60–61, Jan. 2015.

[116] C. P. Welsch and J. Ullrich, "FLAIR a facility for low-energy antiproton and ion research," in *4th International Conference on Trapped Charged Particles and Fundamental Physics*. Berlin, Heidelberg: Springer Berlin Heidelberg, 2006.

[117] FLAIR, "Facility for Low-Energy Antiproton and Ion Research," http://www. flairatfair.eu.

[118] C. Glaessner *et al.*, "An Electrostatic Quadrupole Doublet with an Integrated Steerer," in *9th European Particle Accelerator Conference (EPAC 2004)*, Lucerne, Switzerland, 2004.

[119] M. Fraser *et al.*, "Beam Dynamics Studies of the ELENA Electrostatic Transfer Lines," in *6th International Particle Accelerator Conference (IPAC 2015)*, Richmond, Virginia, USA, 2015, p. MOPJE044.

[120] T. J. Roberts and D. M. Kaplan, "G4beamline simulation program for matter-dominated beamlines," in *IEEE Particle Accelerator Conference (PAC07)*. IEEE, 2007, pp. 3468–3470.

[121] Y. K. Batygin, "Particle-in-cell code BEAMPATH for beam dynamics simulations in linear accelerators and beamlines," *Nuclear Instruments and Methods in Physics Research Section A: Accelerators, Spectrometers, Detectors and Associated Equipment*, vol. 539, no. 3, pp. 455–489, Mar. 2005.

[122] C. R. Prior, "Simulation with space charge," in *AIP Conference Proceedings*, vol. 448, no. 1. American Institute of Physics, Mar. 1998, pp. 85–103.

[123] S. Agostinelli *et al.*, "Geant4 - a simulation toolkit," *Nuclear Instruments and Methods in Physics Research Section A: Accelerators, Spectrometers, Detectors and Associated Equipment*, vol. 506, no. 3, pp. 250–303, Jul. 2003.

[124] T. Ariga *et al.*, "Measuring GBAR with emulsion detector," *International Journal of Modern Physics: Conference Series*, vol. 30, p. 1460268, Jan. 2014.

[125] S. Aghion *et al.*, "Prospects for measuring the gravitational free-fall of antihydrogen with emulsion detectors," *Journal of Instrumentation*, vol. 8, no. 08, p. P08013, Aug. 2013.

[126] S. Chauvie, P. Nieminen, and M. G. Pia, "Geant4 Model for the Stopping Power of Low Energy Negatively Charged Hadrons," *IEEE Transactions on Nuclear Science*, vol. 54, no. 3, pp. 578–584, Jun. 2007.

[127] A. Kainz *et al.*, "Distortion-free measurement of electric field strength with a MEMS sensor," *Nature Electronics*, vol. 1, no. 1, pp. 68–73, Jan. 2018.

[128] CST, "Computer Simulation Technology," https://www.cst.com/.

[129] CERN, "CDD Web Home Page," http://edms-service.web.cern.ch/edms-serv ice/cdd.

[130] A. L. Septier, *Focusing of charged particles.* Academic Press, 1967.

[131] CDD, "ELENA Fast Deflector - Vacuum Chamber Assembly Horizontal," https:// edms.cern.ch/document/1365142.

[132] P. Belochitskii, "ELENA Project Status," in *COOL2013*, Murren, Switzerland, 2013.

[133] F. James and M. Winkler, "MINUIT Users Guide," CERN, Geneva, 2004.

[134] MATLAB, "GUI," https://uk.mathworks.com/discovery/matlab-gui.html.

[135] MATLAB, "patternsearch," https://uk.mathworks.com/help/gads/patternsearch.html.

[136] MATLAB, "paretosearch," https://uk.mathworks.com/help/gads/paretosearch.html.

[137] J. Jentzsch *et al.*, "Beam Dynamics Studies of the ELENA Electrostatic Transfer Lines in the Presence of Magnetic Stray Fields," in *7th International Particle Accelerator Conference (IPAC 2016)*, Busan, Korea, 2016, p. THPMB047.

[138] ANSYS®, "Academic Research Mechanical, Release 18.1," https://www.ansys.com/en-gb/academic/.

[139] G. Guignard, "Détermination par rabotage des faisceaux du profil vertical et de la luminosité avec application aux anneaux de stockage à intersections." Tech. Report, CERN-ISR-OP-73-28; ISR-OP-73-28, May 1973.

[140] V. Tzoganis *et al.*, "Design and first operation of a supersonic gas jet based beam profile monitor," *Physical Review Accelerators and Beams*, vol. 20, no. 6, p. 062801, Jun. 2017.